UiT The Arctic University of Norway

Faculty of Science and Technology

Department of Geosciences

Last Glacial Maximum – Holocene palaeoenvironment in Bessel Fjord and southwestern Dove Bugt, Northeast Greenland

Kevin Michael Zoller

Master's thesis in Geology GEO-3900 May 2020

Abstract

Marine studies reconstructing ice sheet conditions on the Northeast Greenland shelf and adjacent fjords since the Last Glacial Maximum (LGM) are sparse. As a result, the timing and origin of the deglaciation of the ice sheet over marine areas is not well constrained. This thesis aims to improve our understanding of the LGM, deglaciation, and Holocene ice dynamics of the Greenland Ice Sheet (GrIS) near the southern outlet of the Northeast Greenland Ice Stream (NGIS), as well as reconstruct the palaeoenvironment of this region since the LGM. Here, swath bathymetry data and the multi-proxy analysis of three sediment gravity cores from southwestern Dove Bugt and Bessel Fjord were integrated. Dove Bugt is an embayment that is positioned to the east of Storstrømmen, the southern outlet of the NGIS. Bessel Fjord is a W-E oriented fjord that lies south of Storstrømmen and is connected to southern Dove Bugt via the Store Bælt sound.

Bathymetric analysis of Dove Bugt revealed north-south oriented streamlined landforms which have been interpreted as the product of a fast-flowing, topographically bound branch of the NGIS that flowed southwards during the LGM. The sedimentology of a gravity core from southwestern Dove Bugt suggests that the NGIS may have retreat from the region around 11,190 cal. yr. BP, in conformity with previous onshore results. The presence of only a few, small retreat moraines implies that the deglaciation was rapid but may have had brief intervals of halting and/or readvancement. Sedimentation during the remainder of the Holocene is attributed to input from local ice caps and glaciers as well as mass wasting processes.

The bathymetry of Bessel Fjord reveals several basins and sub-basin that are separated by basin thresholds. The configuration of geomorphic features suggests that glacial ice may have conformed to the topography during ice expansion and reached the outer fjord. The position of recessional moraines suggests that ice had undergone multiple halts and/or readvances and was topographically bound during deglaciation. Sediments from a gravity core collected in the inner fjord reflect a gradual transition from ice proximal to ice distal settings and an absence of glacial ice after 7,160 cal. yr. BP. A gravity core collected from a mid-fjord basin contains a transition from mud to muddy sand layers at ~4,000 yr. BP, which is believed to be the result of increased

sediment input from nearby ice caps. This suggests that local ice caps in Bessel Fjord may have fluctuated with greater sensitivity to changing climatic conditions than the GrIS.

Acknowledgements

First, I would like to thank my main supervisor Jan Sverre Laberg for allowing me to work on this project and giving me fantastic guidance. I really appreciate your assistance and support throughout the writing process, as well as all the time you set aside for our interesting discussions. I'm truly grateful. Tom Arne Rydningen, thank you for devoting so much of your time to reading and discussing my thesis with me. Thank you, Katrine Husum, for your assistance with foraminifera species identification and general discussions about the project and Matthias Forwick for your assistance with processing X-Ray Fluorescence data. Also thank you to all those who were involved in the TUNU project for making this thesis possible.

I would also like to thank Trine Dahl, Karina Monsen and Ingvild Hald for your assistance in the Geology Laboratory at UiT. It was great working with each of you and I really appreciate all of the time you devoted to aid me. Thank you Juho Junttila for meeting with me to discuss sediment grain size analysis. Thank you to those operating the MICADAS at the Alfred Wegener Institut for processing my samples in a timely manner. I would also like to thank all the other students and academic staff who offered thesis-related advice when I needed it and have been friendly and welcoming since I first moved to Norway. These past two academic years in Tromsø have been an incredible experience and I have many of you to thank for that!

Emma, I don’t think I could have completed this thesis without your support and companionship. I appreciate everything, from the long hours we spent working together in the office and lab, to you taking the time to read over parts of my thesis before submission. I'm truly grateful for your help!

And finally, I would like to thank my family for their encouragement and support. Your messages and video chats made the long northern Norwegian winters much warmer than they otherwise would have been!

Table of Contents

1. Introduction 1

1.1 Purpose of the study and motivation 1

1.2 Objectives 2

2 Study Area 5

2.1 Physiographic setting 5

2.2 Bedrock geology 8

2.3 Shelf lithostratigraphy 13

2.4 Geomorphology 17

2.5 Glaciology 20

2.6 Climate 21

2.7 Oceanography 25

3 Background 30

3.1 Glacial history of Northeast Greenland: LGM and deglaciation 30

3.2 Holocene paleoclimate of East Greenland 35

4 Material and Methods 38

4.1 Swath Bathymetry 38

4.2 Sediment Cores 41

4.2.1 Laboratory Work 42

4.2.2 X-Ray Photography 44

4.2.3 Sediment Core Splitting and Logging 44

4.2.4 XRF Scan 45

4.2.5 Radiocarbon Dating 46

4.2.6 Sediment Grain Size Analysis 49

5 Results 51
5.1 Swath Bathymetry 51
5.1.1 Bessel Fjord 52
5.1.2 Dove Bugt 85
5.2 Lithostratigraphy 95
5.2.1 Lithostratigraphic overview 95
5.2.2 Gravity Core HH17-1290-GC-TUNU (Inner Fjord) 96
5.2.3 Gravity Core HH17-1289-GC-TUNU (Mid-Fjord) 106
5.2.4 Gravity Core HH17-1309-GC-TUNU (Southwest Dove Bugt) 117
6 Discussion 130
6.1 Palaeoenvironment of Dove Bugt 130
6.1.1 Stage I: Last Glacial Maximum (LGM) 130
6.1.2 Stage II: Deglaciation 135
6.1.3 Stage III: Holocene (Post-Ice Stream Deglaciation) 148
6.1.4 Model of Dove Bugt 154
6.2 Palaeoenvironment of Bessel Fjord 158
6.2.1 Stage I: Last Glacial Maximum (LGM) 158
6.2.2 Stage II: Deglaciation 162
6.2.3 Stage III: Holocene 170
6.2.4 Model of Bessel Fjord 176
7 Conclusion 182
8 Future Work 183
References 185
Appendix A 207

Appendix B 208

1. Introduction

1.1 Purpose of the study and motivation

This study focuses on Bessel Fjord and southwestern Dove Bugt in Northeast Greenland – an area of Greenland that has been scarcely studied due to its inaccessibility (Fig. 1.1). Historically, Northeast Greenland is covered by sea ice throughout most of the year, however, a decrease in sea ice in recent years has allowed for a greater number of geoscientific cruises into the area (Arndt, et al., 2015). Dove Bugt is an embayment which lies south of Germania Land and is bound by the island of Store Koldewey to the east (Fig. 1.2). Bessel Fjord is a tributary fjord that connects to southern Dove Bugt through a water way referred to as Store Bælt (Fig.1.2). Store Bælt is a sound that is bound by Store Koldewey to the east and the landmasses Ad. S. Jensen Land and Dronning Margrethe II Land to its west. Based on the absence of marine based studies in Bessel Fjord and the surrounding area (e.g. Fig. 1.2), this master's thesis aims to construct a more precise picture of how the Greenland ice sheet (GrIS), Northeast Greenland Ice Stream (NGIS) and local glaciers and ice caps responded to climatic changes during the Last Glacial Maximum (LGM) through the Holocene in fjord and inner shelf environments.

Fjords provide an excellent means of studying paleoenvironments and paleoclimates on the margins of Greenland. Glaciers are responsible for the development of fjord systems and are particularly sensitive to climatic changes. As the outlet glaciers on Greenland's coast fluctuate throughout time, they shape the fjord's seabed, creating submarine landforms, which can reveal their dynamic behavior. Fjords also act as a particularly good sediment trap, collecting glacially derived material, as well as sediments from mass wasting and fluvial activity. Therefore, the examination of geologic and geophysical data collected from Bessel Fjord and southwestern Dove Bugt, can provide an insight into the glacial and sedimentological history of the area and reveal details about the region's paleoclimate.

1.2 Objectives

During a cruise arranged by the TUNU-program in 2017, swath bathymetry data and three gravity cores were collected by the *R/V Helmer Hanssen* in Bessel Fjord and southwestern Dove Bugt. This data has been used in this project to address multiple objectives that have been established for the study area. These objectives include:

- The reconstruction of ice dynamics within Bessel Fjord and southern Dove Bugt during the Last Glacial Maximum (LGM), the subsequent deglaciation, and succeeding periods of warming and cooling.
- The utilization of geologic data to gain a better understanding of the Holocene paleoenvironment.
- Understand the dominant sedimentary processes within the fjord and lower bay.
- Comparing findings from this study to other bodies of work in Northeast Greenland to gain a boarder understanding of how the GrIS, NGIS and local glaciers and ice caps reacted to climatic changes from the LGM through the Holocene.

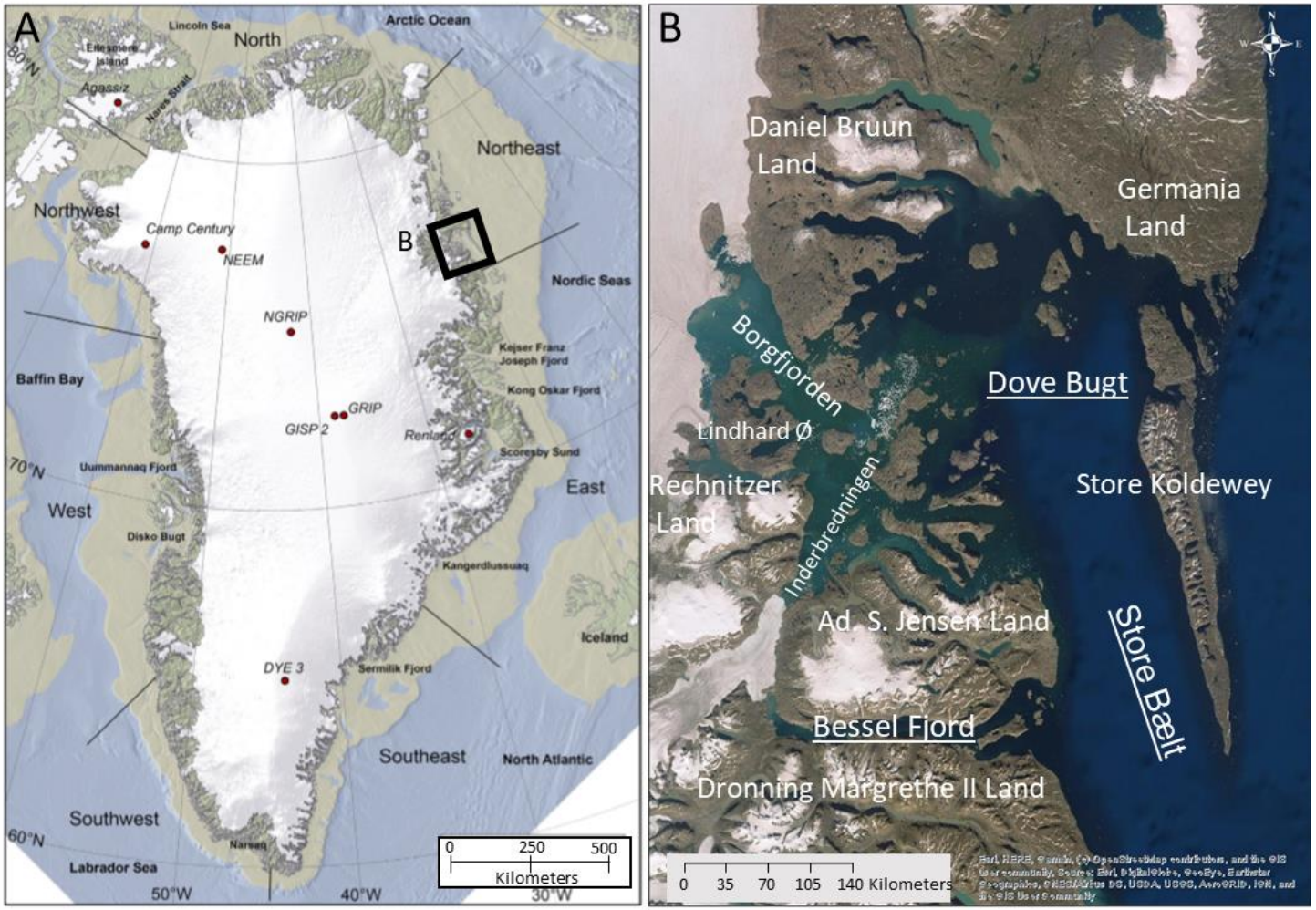

Figure 1.1. A: Map of Greenland, with a light brown color representing shelf regions that are above 500 m depth, black lines drawn separating different geographical regions of the island, red dots on drilling sites and black box around the study area. Taken and modified from Vasskog et al. (2015). B: Satellite image of the study areas and surrounding landscape.

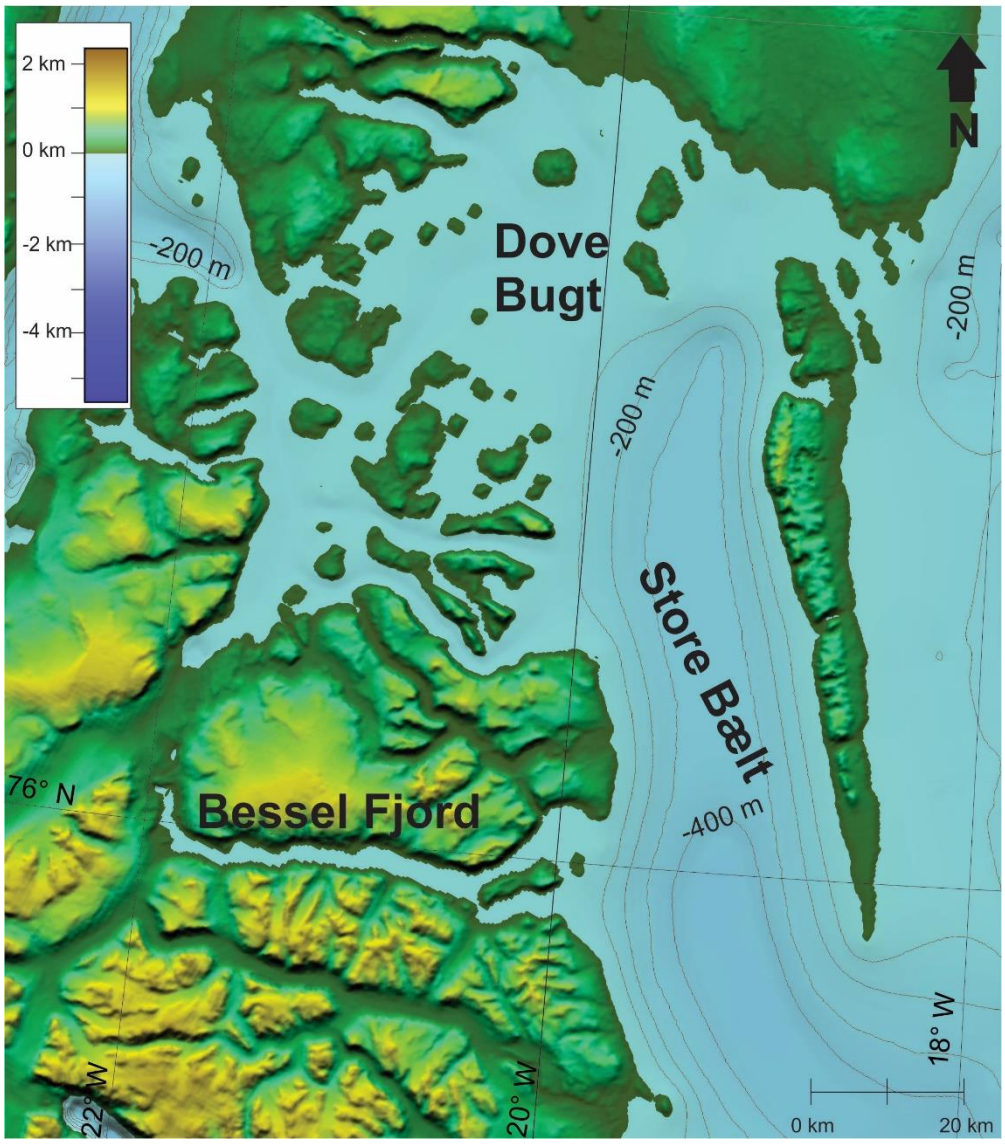

Figure 1.2. Bathymetric map of the Bessel Fjord and Dove Bugt areas displaying the previously collected IBCAO data. Note the lack of data within Bessel Fjord.

2 Study Area

2.1 Physiographic setting

Greenland, located between 59.8 to 83.6° N, is the largest island in the world, and contains a surface area of 2.2 million km^2 (Fig. 1.1A; Dahl-Jensen et al., 2009). It is geographically unique, with a large ice sheet that covers 80% of the island (Dahl-Jensen et al., 2009) and some of the largest fjord systems in the northern hemisphere (in some instances stretching hundreds of kilometers inland) (Funder et al., 1998). This study area is within Northeast Greenland (Fig. 1.1B), a region that is characterized by almost constant sea ice cover throughout the year (Laberg et al., 2017). The drainage basin of modern day Northeast Greenland encompasses 16% of the GrIS, which can largely be attributed to transportation of material through the NGIS (Khan et al., 2014).

The southernmost outlet of the NGIS, Storstrømmen, drains into Dove Bugt (~76° 54' 30.5568" N 20° 20' 41.9316" W), a large embayment that is sheltered from the East Greenland Current (EGC) by an elongated island referred to as Store Koldewey (Fig 1.1B). The bay is also surrounded by Germania Land and Daniel Bruun Land to the north and Adolf S. Jensen Land and Rechnitzer Land to the southwest. Western Dove Bugt contains numerous islands and fjords as well as outlets of the ice stream, local glaciers and ice caps. Between Adolf S. Jensen Land and Rechnitzer Land, the northern branch of the glacier Soranerbræen enters Dove Bugt through the bay Inderbredningen (Fig. 1.1B). The southern outlet of Dove Bugt connects to the Greenland Sea through a sound referred to as Store Bælt (Fig. 1.1B).

Along the seafloor of the southern outlet of Store Bælt one can find the Dove Bugt Trough (Fig. 2.1A). This trough is one of many transverse cross-shelf troughs that have been identified across Northeast Greenland (Laberg et al., 2017). It trends in a southeastward's direction for 120 km until it merges with the Hochstetterbugten Trough (Arndt et al., 2015). The northern reaches of this trough have been referred to as the Store Bælt cross-shelf trough by some authors (Evans et al., 2009). Store Koldewey Trough, identified just north of Dove Bugt Trough (Fig. 2.1A), is the only trough in the region that does not connect to a major fjord system, and terminates near Germania Land (Arndt et al., 2015; Laberg et al., 2017). North of 77°N the shelf morphology

appears as a large coast-parallel inner trough, which turns into the shelf-transverse Westwind Trough in the northeast and the Norske Trough in the southeast (Laberg et al., 2017).

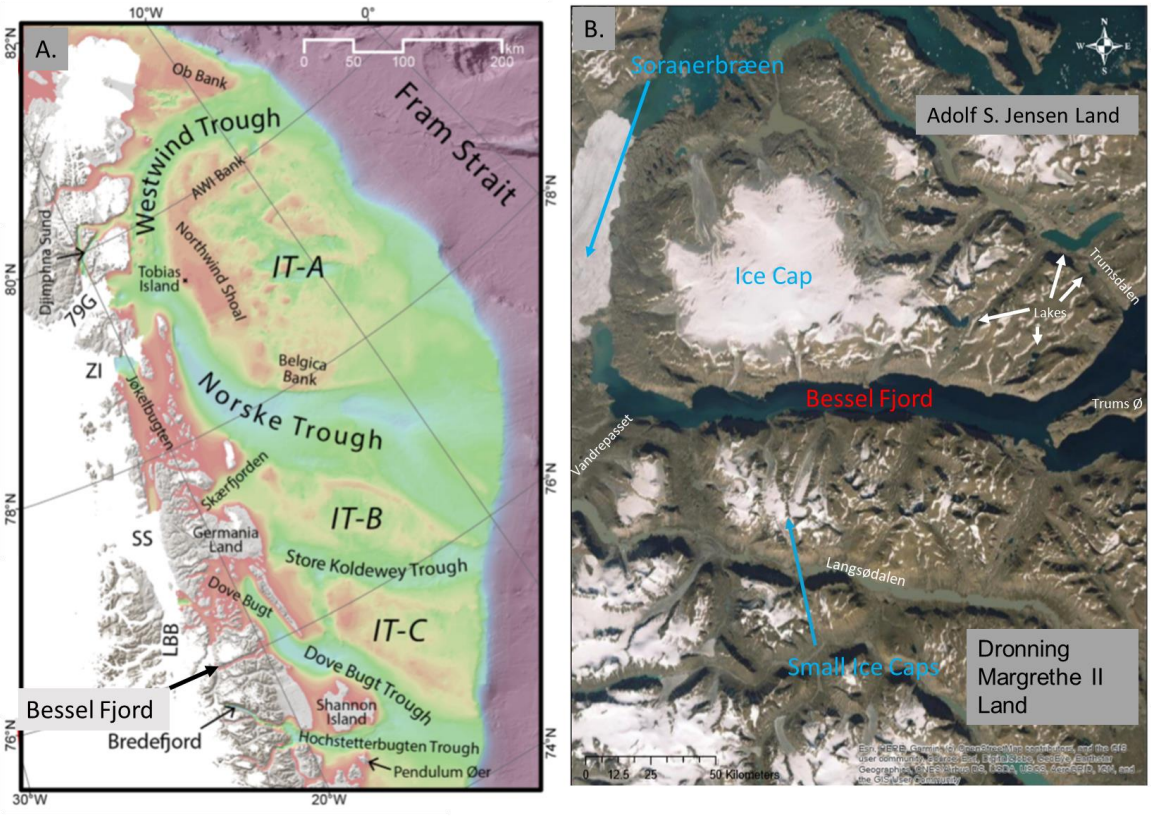

Figure 2.1. A: Bathymetric map of the continental shelf of NE Greenland. Taken and modified from Arndt et al., (2015). B: Map of Bessel Fjord and the surrounding area.

In southern Dove Bugt, west of Store Bælt and the termination of Store Koldewey, one can find Bessel Fjord (75° 58' 49.962" N 21° 11' 7.6848" W; Fig. 2.1B). This fjord runs in a roughly west-east direction and contains islands to the east that split the entrance to the fjord into southern and northern passages (Fig. 2.2). The back of the fjord contains a second outlet for the glacier Soranerbræen and numerous additional outlets for ice caps that can be found along the length of the fjord. The fjord measures approximately 47 km in length when measured from the termination of Soranerbræen to the island of Trums Ø (Fig. 2.2). The width is relatively uniform throughout the fjord, ranging from 1.8 to 3.7 km. No bathometric study of the fjord has been published to date.

South of Bessel Fjord, Dronnings Margrethe II Land has been divided into two regions: the mountainous Nørlund Land to the north and the flatter Hochstetter Forland to the south/southeast. Nørlund Land contains small ice caps and numerous fluvial outlets that are sourced from mountainous areas. Additionally, the valley Langsødalen lies south of Bessel Fjord (Fig. 2.1B) which contains the ice cap fed river Langelv and the lake Langsø. An additional small lake referred to as Skyggesø can be found southwest of the fjord. Adolf S. Jensen Land to the north contains a large ice cap with ice cap lobes that enter the fjord and fluvial input from the ice cap as well as multiple lakes.

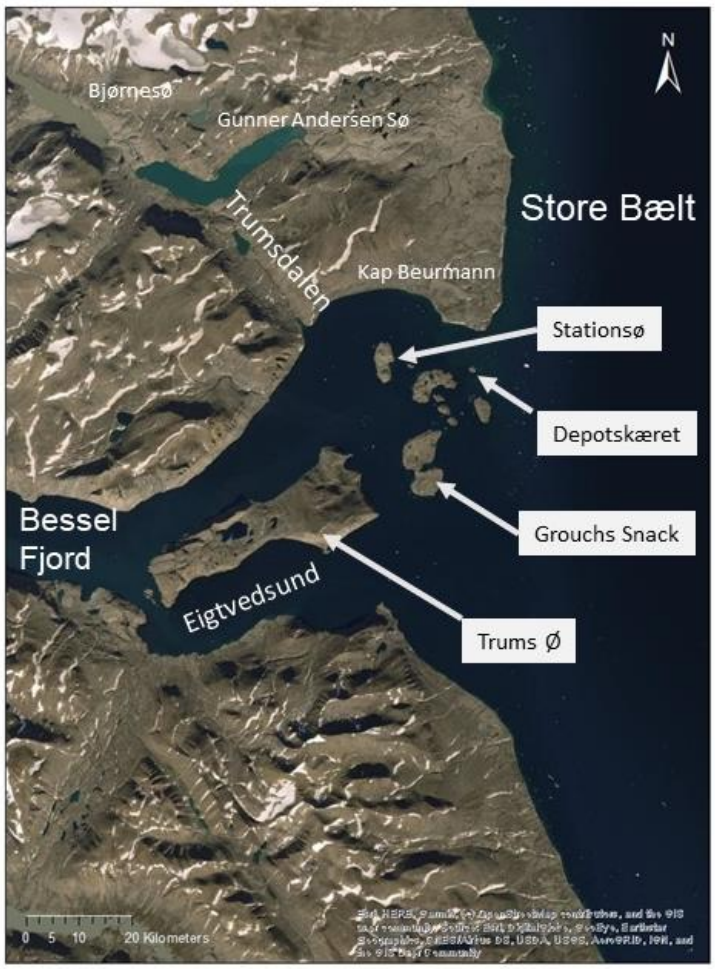

Figure 2.2. Satellite image of outer Bessel Fjord.

2.2 Bedrock geology

The bedrock geology of the Dove Bugt area primarily consists of Proterozoic and early to mid-Paleozoic sequences that have undergone varying degrees of metamorphism. Lithological zones relevant to this study include the Nørreland thrust sheet, Hagar Bjerg thrust sheet, the Foreland, Imbricate thrust zone, western thrust belt and post-Caledonia deposition (Table 2.1; Fig. 2.3). Several major shear zones cross the region, including the NNE–SSW-trending Storstrømmen shear zone (SSZ), the E–W-trending Bessel Fjord shear zone (BFSZ) and the NNW–SSE-trending Germania Land shear zone (GLSZ). For a detailed view of the bedrock of the study areas see Fig. 2.4.

The complexes of Caledonian thrust sheets extending north from Bessel Fjord, and encompassing Dove Bugt, Germania Land and Skærfjorden, consist of complexes of gneiss that make up the Nørreland thrust sheet (Fig. 2.3). The allochthonous crystalline gneiss complexes of this region have yielded protolith ages of 2 Ga and are believed to have developed during a period of crust formation in the Palaeoproterozoic (Kalsbeek et al., 1993) and have since been reworked during the Caledonian orogenesis. North of Danmarkshavn on Germania Land, the gneisses contain Caledonian eclogites, where south of this, in the region spanning northern Dove Bugt to the BFSZ in the south, the gneisses typically appear to be of amphibolite facies (Gilotti, 1993; Gilotti et al., 2008). The southern section of this region has been referred to as an "undefined unit" by Henricksen & Higgins (2009). Gilotti & McClelland (2008) suggest that it is not likely that the gneisses of the Nørreland thrust sheet represent a single crustal slab, however, no internal thrust contacts have recognized to date. It has been suggested that the existence of a non-migmatitic equivalent to the Smallefjord sequence west of the head of Bessel Fjord could indicate that this region is a part of a separate thrust unit or a higher level of the Nørreland thrust sheet (Henricksen & Higgins, 2009).

The most widespread gneiss units are grey orthogneisses that range in composition and structure. In numerous places, gnesisses are cut by younger, foliated metagranitoid sheets, which frequently contain feldspar augen. Scattered layers and lenses of metasedimentary lithologies (possible of Paleoproterozoic age) can be found within the gneiss complexes and are often

Table 2.1. The orogenic events and lithostratigraphic divisions of the Dove Bugt region. Taken from Henricksen & Higgins (2009).

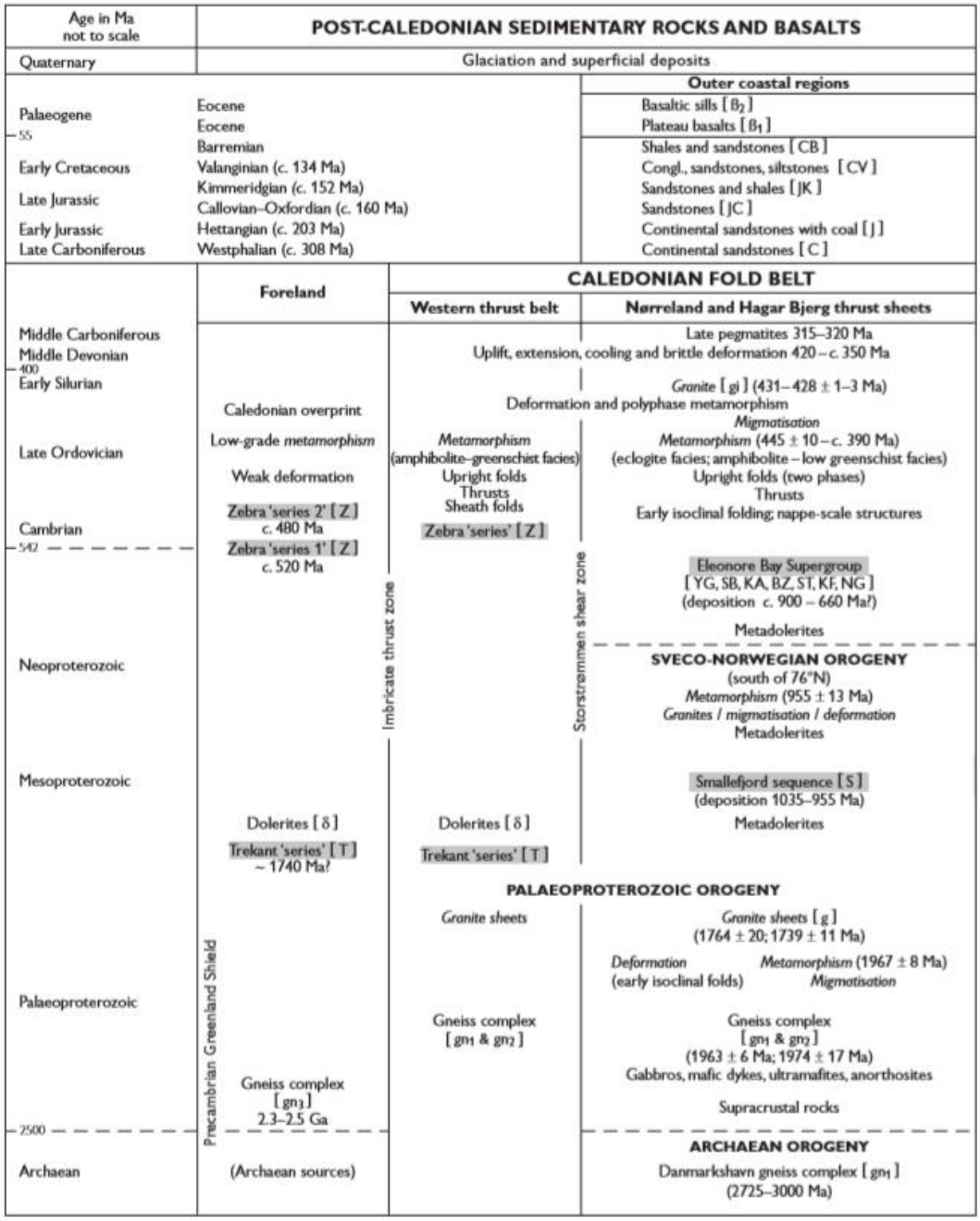

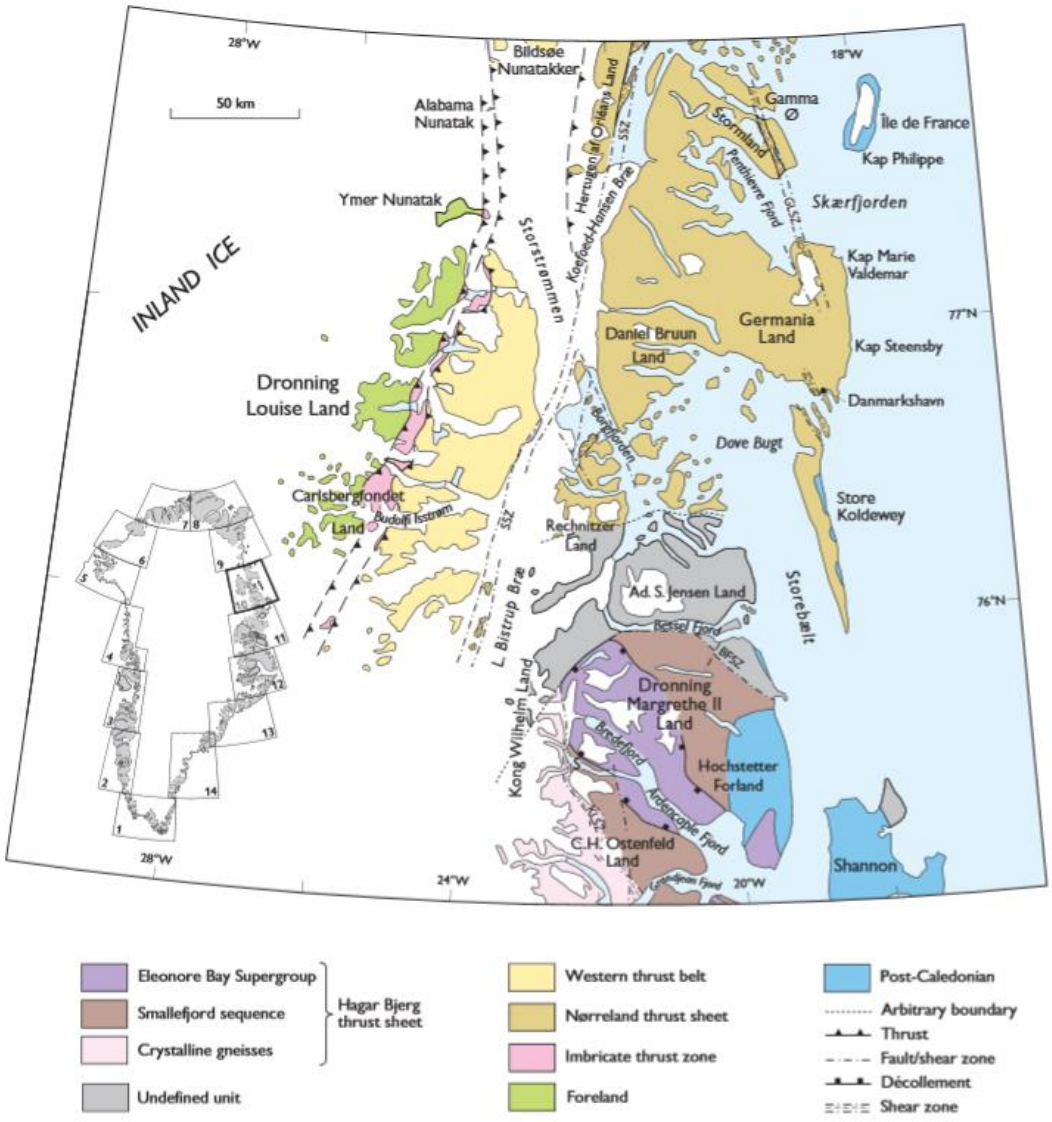

Figure 2.3. Simplified geologic map of Dove Bugt and adjacent areas with structural domains. SSZ- Storstrømmen shear zone; BFSZ- Bessel Fjord Shear Zone; GLSZ- Germania Land Shear Zone; KLSZ- Kildedalen shear zone. Taken from Henricksen & Higgins (2009).

associated with basic pods and amphibolites. Supracrustal rock units within the Nørreland thrust sheet consist of marbles and calc-silicate rocks, cordierite- and sillimanite-bearing paragneisses and mica schists, and semipelitic and siliceous metasedimentary rocks. Layers and lenses of gabbro-anorthositic, megacrystic anorthositic and ultramafic igneous rocks have also been identified within the grey gneisses (Henricksen & Higgins, 2009). South of the BFSZ, the region contains extensive outcrops of Palaeproterozoic basement gneisses as well as the

Mesoproterozoic Smallefjord metasedimentary sequence and Neoproterozoic Eleonore Bay Supergroup succession. The gneisses are similar to the gneisses of the Nørreland thrust sheet and are mostly amphibolite facies grey gneisses with occasional foliated metagranitoid units (Henricksen & Higgins, 2009).

The Smallefjord sequence, located between Grandjean Fjord (75°N) and Bessel Fjord (76°N), mostly consists of medium- to coarse-grained semipelitic schists and gneisses, interlayered with psammitic schists and is structurally bound by the BFSZ to the north and southwest. The sequence is believed to have been deposited later than c. 1035 Ma and prior to a regional metamorphic event at c. 995 Ma and subjected to renewed deformation and metamorphism during the Caledonian orogeny (Strachan et al., 1995; Henricksen & Higgins, 2009). The northwestern segment of the Smallefjord sequence is present as strips in the gneisses. Mineral assemblages in the semipelitic rock units are quartz + plagioclase + biotite + muscovite ± garnet ± sillimanite ± kyanite, which are common feature of amphibolite facies metamorphism. The sequence's metasedimentary rocks are frequently strongly migmatised with abundant discontinuous, concordant layers and lenses of quartzo-feldspathic material. This material can form up to 30-50% of the total rock volume, and is composed of roughly equal proportions quartz, plagioclase and potassium feldspar, with minor quantities of biotite and muscovite. Subconcordant sheets and pods of foliated amphibolite as well as irregular sheets and lenses of deformed granites and augen granites have also been found within this sequence. Near the glacier Soranerbræen, in the northernmost section of the sequence, are strips of metasedimentary rocks. In contrast to the migmatitic sedimentary rocks to the south, these are non-migmatitic and are potentially, structurally apart of a higher level of the thrust complex (or possibly a different thrust sheet). This uncertain structural position of the region around Ad. S. Jensen Land is referred to as "undefined" on Fig. 2.3 (Henricksen & Higgins, 2009).

The Elenore Bay Supergroup consists of three groups with numerous subdivisions. This includes the Nathorst Land Group (alternating units of quartz arenite, interbedded sand stone and mudstone, and black silty mudstone), the Lyell Land Group (six units composed of white, brown and purple weathering quartz arenites and dark green, brown and deep red silty mudstones) and the Ymer Ø Group (isolated outcrops of limestone and dolomite (Sønderholm et al., 1989;

Sønderholm & Tirsgaard, 1993; Tirsgaard & Sønderholm, 1997; Henricksen & Higgins, 2009). Caledonian granitic intrusions can be found between the Grandjean Fjord – Bessel Fjord region in the Eleonore Bay Supergroup and Smallefjord sequence (Hansen et al., 1994; Strachan et al., 2001) but are unknown north of Bessel Fjord or in the Nørreland thrust sheet (Henricksen & Higgins, 2009).

West of the field sites, in the regions of western Dronning Louise Land and the Ymer Nunatak to its north, have been interpreted as being a Caledonian foreland (Fig 2.3). These areas fall within the Precambrian Greenland Craton, which is a section of the eastern margin of the North American continent of Laurentia. The western foreland of Dronning Louise Land consists of Palaeoproterozoic crystalline gneiss complexes that are unconformably overlain by the two sedimentary sequences: the Trekant 'series' and the Zebria 'series' (which are separated by a major hiatus of over 1 Ga). The crystalline complexes, which are for the most part homogeneous granitoid orthogneisses, as well as the Palaeoproterozoic Trekant 'series' are intruded by a dense swarm of doleritic sheets and dykes that are believe to be of Mesoproterozoic age. The Trekant 'series' has been correlated to the Independence Fjord Group in Northern Greenland and is a 510 m thick sequence. The bottom parts of the sequence consist of crudely stratified conglomerates with angular fragments of gneiss, which pass upwards into cross-bedded, grey-green and purple-red akosic and quartzitic sandstones that are interbedded with siltstones and quartz pebble conglomerates. The Zebra 'series', which has been dated to the Lower Cambrian and Lower Ordovician, are not cut by dykes and rest unconformably on either the crystalline gneisses or the Trekant 'series' sediments (Strachan, 1994). The Zebra 'series' is a thin sequence of shallow marine quartzite, mudstones, magnetite-hematite-bearing sandstones and limestones (Henricksen & Higgins, 2009).

The Imbricate thrust zone is a 5-15 km wide, NNE–SSW-trending thrust zone, that that traverses Dronning Louise Land and lies between the Foreland and thrust sheets to the east. Its geologic units, comprising intensely deformed sedimentary sequences and associated basic rocks, have been correlated with rock units in the Foreland (Strachan et al., 1992; Strachan, 1994). The Western thrust belt consists of gneisses that are acid to intermediate grey orthogneisses with

local mafic enclaves (Strachan et al., 1992) and are overlain by metasedimentary sequences (Fig. 2.3; Henricksen & Higgins, 2009).

Sedimentary rocks of Jurassic-Cretaceous age have been identified along a 40 km long, north-south trending region on the eastern side of Store Koldewey. Glacial erratics of Jurassic coal have been identified in Germania Land and suggest that deposits of Jurassic age were once more extensive and may be present beneath the Inland Ice to the west. Through geophysical studies, large Mesozoic sedimentary basins have also been identified beneath the waters of Dove Bugt and on the shelf offshore (Hamann et al., 2005). The Mesozoic rocks on Store Koldewey (Stemmerik & Piasecki, 1990) consist of four lithological distinct units: the Vardekløft Formation/Group (Middle Jurassic sandstones and siltstones), the Bernbjerg Formation which is now a part of the Hall Bredning Group (Upper Jurassic sandstones that's succeeded by shale), the Palnatokes Bjerg Formation (Lower Cretaceous conglomerates, sandstones and siltstones) and the silty shales and sandstones of Barremain age or younger (Surlyk, 2003; Henricksen & Higgins, 2009). Scattered outcrops of Mesozoic rocks have also been identified on Hochstetter Forland and on the island of Shannon, both of which correspond to units found on eastern Store Koldewey. The island of Shannon also contains Palaeogene basalts and sills (Henricksen & Higgins, 2009) and blockfields of Scolithos-quarzites, red granites and red, bluish-grey to multicolored Precambrian quarzite (Hjort, 1981). Post-Caledonian bedrock has also been identified across multiple coastal regions south of Hochstetter Forland and Shannon (Surlyk, 2003).

2.3 Shelf lithostratigraphy

The formation of Northeast Greenland's shelf is largely associated with prolonged rifting events and basin formation between the Norwegian and Greenland margins. Events ranging from post-Caledonian orogenic backsliding and collapse during the Devonian (Andersen et al., 1999; Doré et al., 1999) to post-early Eocene passive margin development controlled by the broadening and deepening of the Norwegian-Greenland Sea (e.g. Myhre et al., 1992; Eldholm et al., 2002) occurred between the margins (Tsikalas et al., 2005). Rifting events have been identified

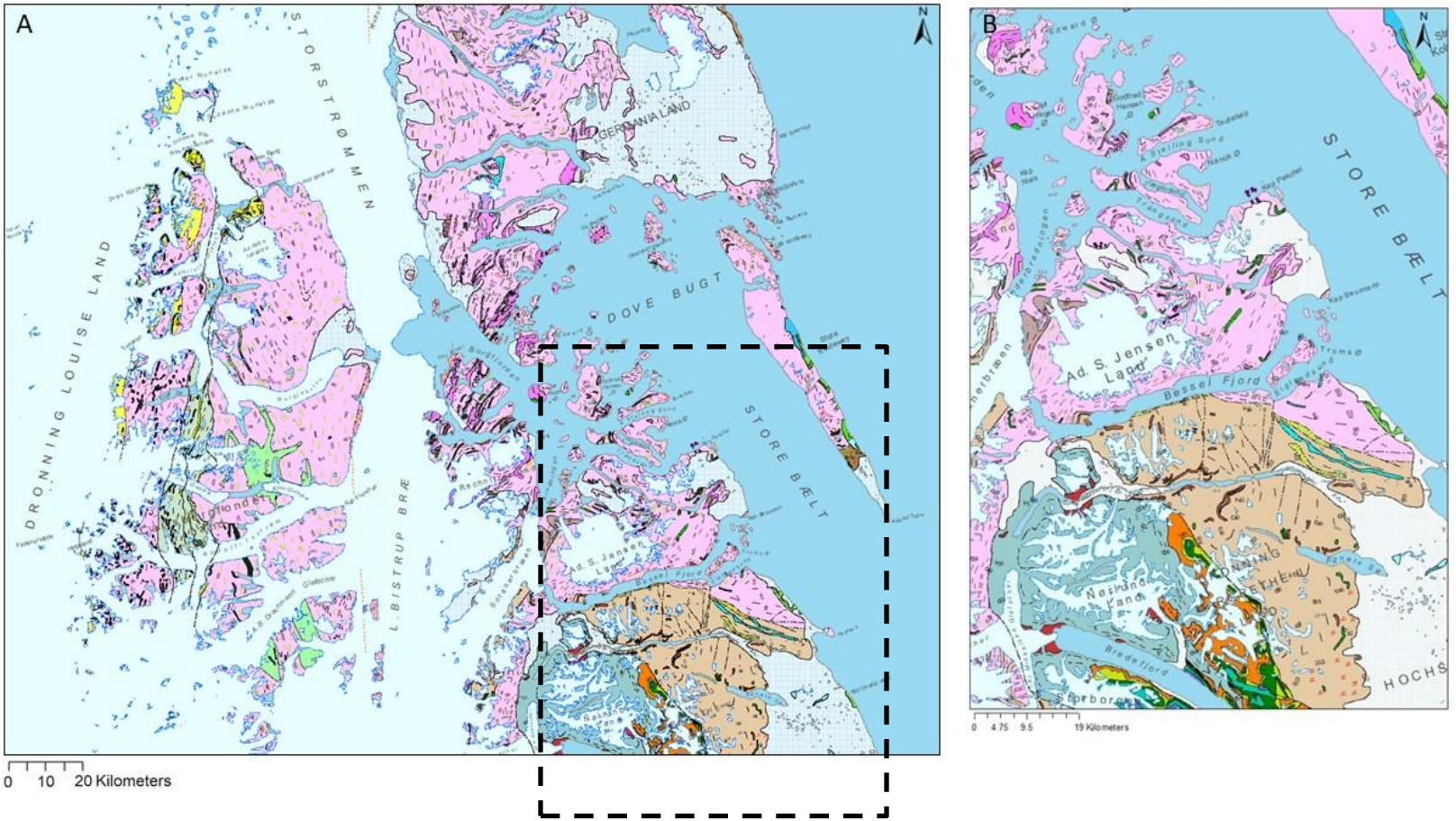

Figure 2.4. A: Detailed bedrock map of Dove Bugt and the surrounding area. Dashed line represents the approximate location of Fig. 2.4B, although Fig. 2.4B also includes geographical regions not featured on Fig. 2.4A. B: Detailed bedrock map of Bessel Fjord and the surrounding area. Taken and modified from The National Geological Survey of Denmark and Greenland: http://maps.greenmin.gl/geusmap/?mapname=greenland_portal&lang=en#baslay=baseMapGl&optlay=&extent=-4251735.740740741,5795667.781635802,5079745.740740741,10252422.218364198&layers=northpole_graticule,grl_geus_500k_geology_map

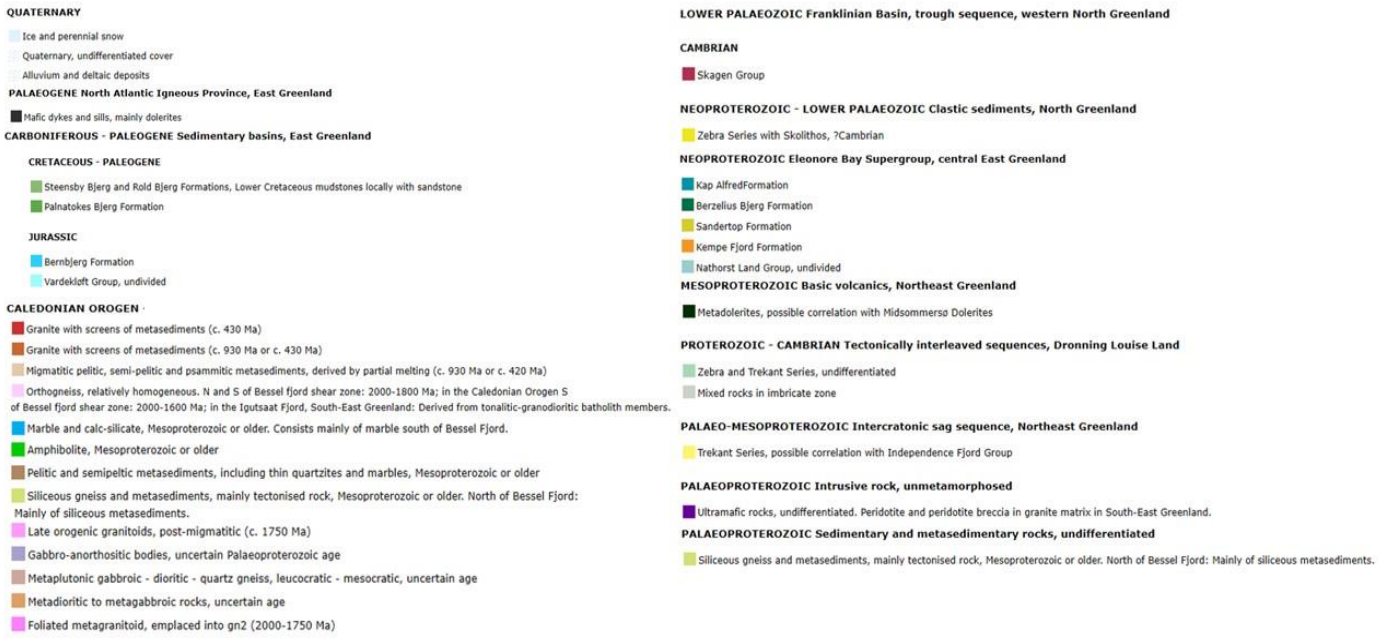

Figure 2.4. (cont.) Legend for detailed bedrock maps of Dove Bugt and Bessel Fjord (see previous page).

between the two regions during the Permian-Triassic, Middle-Late Jurassic, earliest Cretaceous, mid-Cretaceous and Late Cretaceous-Paleocene (Blystad et al., 1995; Doré et al., 1999; Roberts et al., 1999; Brekke, 2000; Tsikalas et al., 2005).

The East Greenland Shelf contains a limited number of deep exploration wells therefore additional means have been used to investigate the subsurface lithostratigraphy (e.g. seismic and aeromagnetic methods) and date interpreted horizons (i.e. applying knowledge about tectonic events, eustatic sea level change, identify lithologic markers and using magnetic anomalies to obtain a maximum age of overlying sediments) (Hamann et al., 2005). The 400 km long and 150-300 km wide North-East Greenland Shelf is characterized by several NE-trending structural highs interpreted from aeromagnetic data (H. C. Larsen, 1984, 1990) and has been subdivided into six additional regions by Hamann et al. (2005) in an overview study of the area.

Dove Bugt partially occupies a region called the Koldewey Platform (Fig. 2.5). This platform is a 30-70 km wide structural high between Store Koldewey and 80° N that has been identified by seismic and gravity data. It is the most westwards portion of the shelf with a relatively shallow basement depth, typically between 2000-3000 m. The eastern margin is formed by a series of

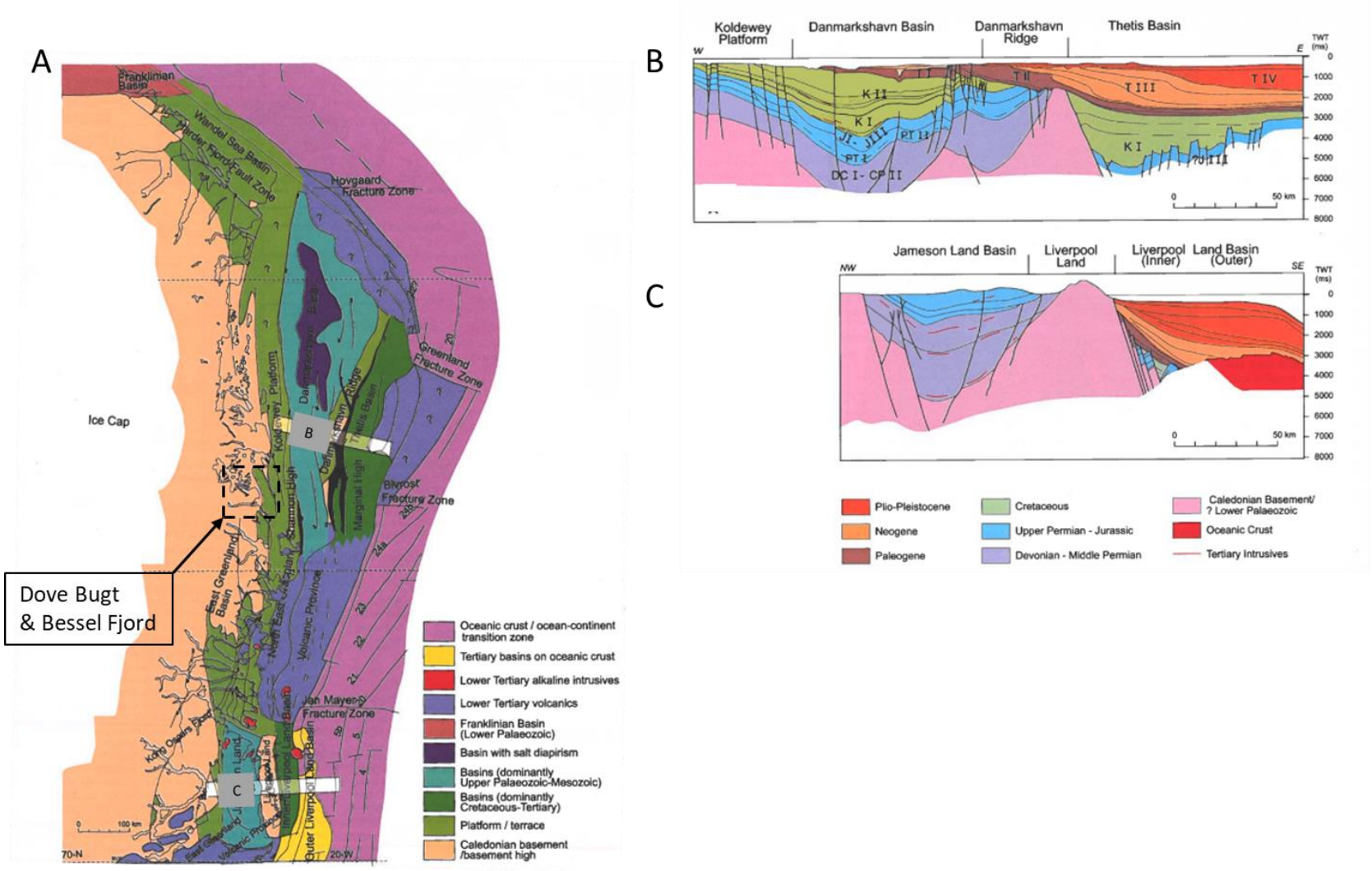

Figure 2.5. A: The interpreted offshore tectonic elements of the East Greenland shelf. B: Seismic cross section of the Northeast Greenland Shelf. C: Seismic cross section of the Jameson Land Basin- Liverpool Land Shelf. Taken and modified from Hamann et al. (2005).

north-south-trending, echelon faults which separate it from the Danmarkshavn Basin. This section of the platform contains punctuated successions of Upper Jurassic and Lower Cretaceous sediments that overlie basement and/or narrow down-faulted remnants of older, possibly Carboniferous strata. Seismic data has revealed a thin punctuated succession with numerous unconformities just east of Store Koldewey island (e.g. Stemmerik & Piasecki, 1990).

South of this, between 75° and 76° N, is a small, 100 km long and 20 km wide features referred to as the Shannon High (Fig. 2.5). This high is a steep-sided basement horst delineated by north-south oriented normal faults that were likely active during the Mesozoic. The northern extent of this high is believed to be controlled by a major fault zone that links a transfer zone at the continental margin to a linear feature near Bessel Fjord, and is marked by a Tertiary depositional basin. At the offshore areas north of Shannon, a thin succession of Tertiary sediments overlies the high, where tertiary volcanic material has been found directly above the basement on Shannon island (Hamann et al., 2005).

2.4 Geomorphology

A fjord is a glacially formed, over-deepened, semi-enclosed marine basin (e.g. Howe et al., 2010). They are primarily the result of glacial erosion carving into varying lithology and structural trends in the bedrock (Gjessing, 1956; Holtedahl, 1967; Nesje & Whillans, 1994; Howe et al., 2010). They typically occur in "fjord belts" that can be found along mid- to high latitudes in both hemispheres (Howe et al., 2010). Sills at the entrance of fjords separate their deep waters from the nearby coastal water, which restricts water circulation and oxygen renewal (Fig. 2.6; Howe et al., 2010). Water depths of ~500-700 m are common in fjords, and the basins themselves act as effective sediment traps during deglaciation and interglacial and interstadial phases (Aarseth, 1997).

Fjords are commonly classified by several parameters, including climatic regimes, glacier regimes and environmental factors. Domack & Mcclemen (1996) proposed a classification by climate, although Bessel Fjord meets the criteria for both *polar* and *subpolar* fjords. Polar fjords are common in eastern and northern Greenland and is characterized by almost permanent sea ice cover, which is a feature of Bessel Fjord. Summer mean air temperatures in Bessel Fjord do

exceed 0°C however, which is a common characteristic of subpolar fjords (Domack & Mcclemen, 1996). Hambrey (1994) classified fjords based on glacier types (temperature to cold), basal conditions (grounding or floating), sediment supply and glacier dynamics and categorized fjords as either *Alaskan, Svalbard, Greenland, Antarctic maritime* and *Antarctic arid regime* (Howe et al., 2010). It is likely that Bessel Fjord would fall under the Greenland regime, which includes dynamic and floating outlets of ice into deeper fjords, although, due to the lack of research on Soranerbræen (a tide-glacier found at the interior of Bessel Fjord) it is difficult to neatly place it into a regime. Syvitski & Shaw (1995) also developed a classification based on physical regimes, which would likely classify Bessel Fjord as an *ice-influenced fjord* (Howe et al., 2010).

Dove Bugt has been identified as a glaciated inner continental shelf region that has semi-restricted access to the Greenland Sea due to an elongated island on its eastern side. The shelfs proximity to the NGIS likely had a large role in shaping its subsurface morphology. On glaciated shelves, first-order morphological elements consist of banks and depressions (i.e. troughs and channels). Banks typically reflect the bedrock morphology; however, some are impacted by the deposition of diamicts on the shelf. Depressions typically take two general forms: transverse troughs and longitudinal channels. Transverse troughs are generally over-deepened in their inner region, may contain depths of over 1000 m and vary in width from 20 km in narrow continental shelves to 170 km in wide continental shelves (e.g. Bear Island Trough). Typically, these features represent a seawards extension of a fjord or glacial valley and are often a drainage route for ice streams (Vorren, 2003). As it was previously mentioned, Northeast Greenland contains numerous transverse cross-shelf troughs, one of which is adjacent to the study area (i.e. Dove Bugt Trough). Longitudinal channels frequently follow boundaries between sedimentary rocks on the shelf and older crystalline troughs on coasts or zones of structural weakness (e.g. faults) (Vorren, 2003). Examples of secondary features super imposed on these first order features include moraine ridges, linear features (e.g. drumlins, crag and tails, flutes, mega scale glacial lineations (MSGL)), plough marks and subglacial channels (Fig. 2.7; Vorren, 2003).

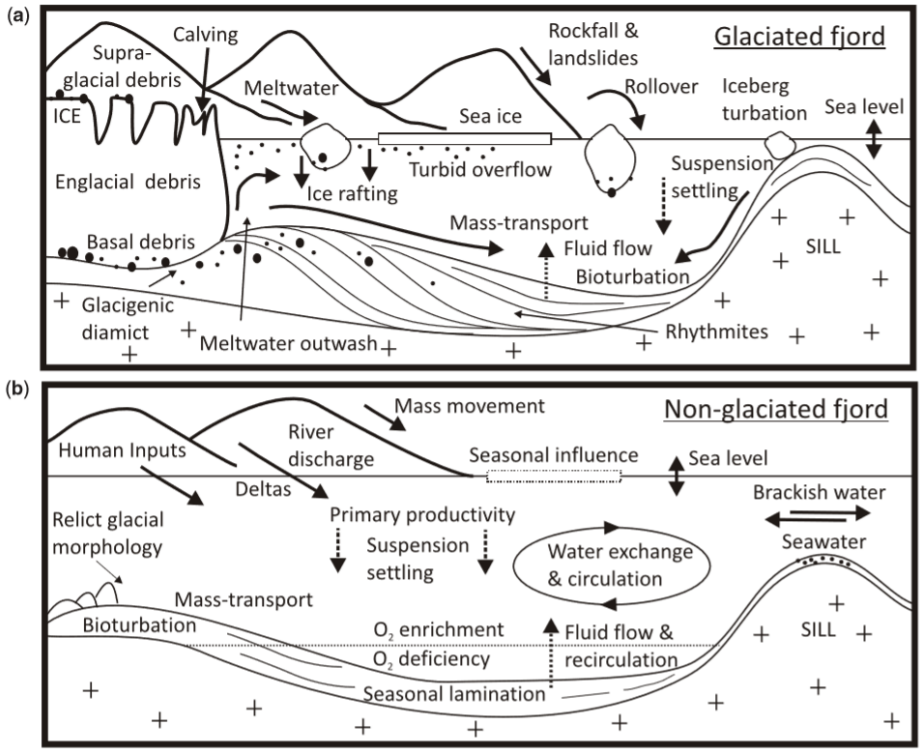

Figure 2.6. The main fjord processes and deposits in (a) glaciated fjords and (b) non-glaciated fjords. According to this classification, Bessel fjord is expected to have characteristics of both models. Figure taken from Howe et al. (2010) and (a) originally adapted from Hambrey (1994).

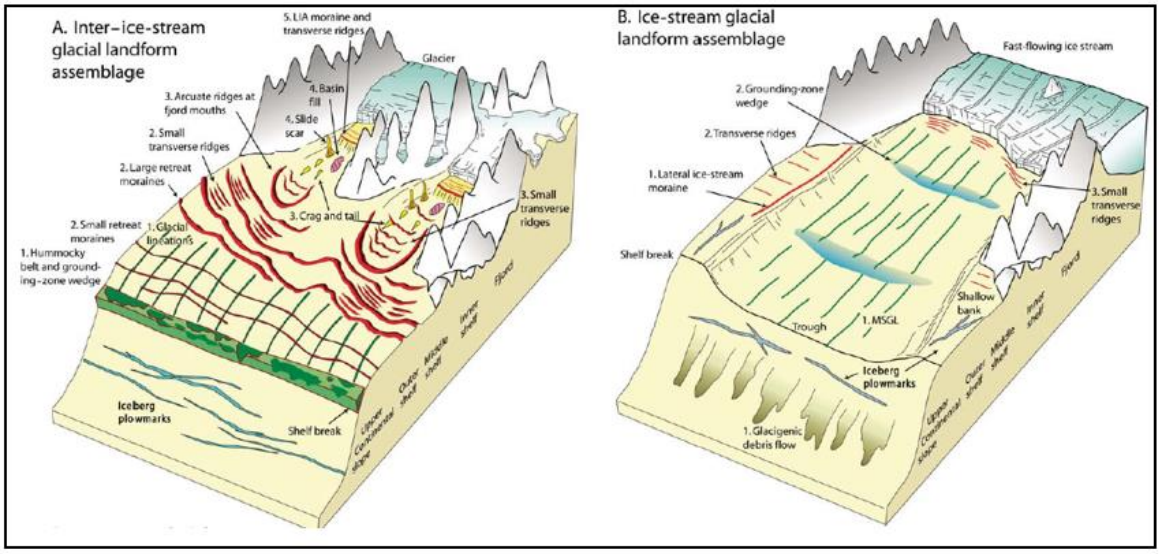

Figure 2.7. Models of submarine landforms produced on glaciated continental margins. A: An inter–ice-stream glacial landform assemblages found between fast-flowing ice streams in northwesternmost, Svalbard. B. An ice-stream–glacial landform assemblage from major Svalbard fjord systems. Figure modified from Ottesen & Dowdeswell (2009).

2.5 Glaciology

The GrIS covers over 80% of the Greenland's surface and is 3000 m thick in some sections (Dahl-Jensen et al. 2009). It is the second largest body of ice on the planet, covering 1.71 km^2, and contains an ice volume of 2.85 million km^3 (Weidick, 1995; Rignot & Mouginot, 2012). The ice mass is large enough to cause the global mean sea level to rise by ~7.5 m if fully melted (Dahl-Jensen et al., 2009). Although the GrIS drains through a number of rapidly flowing outlet glaciers, Northeast Greenland's drainage largely occurs through the NGIS (Fig. 2.8A; Khan et al., 2014). This NGIS extends over 600 km into the interior of the ice sheet and is currently experiencing sustained dynamic thinning (Khan et al., 2014). As ice from the NGIS reaches the coast, it splits into two branches and then discharge into the Fram Strait (Fig. 2.8A; Fahnestock et al., 2001). The northern branch consists of two outlets, Nioghalvfjerds isstrømmen and Zachariae isbræ (Vallelonga et al., 2014). The southern outlet, Storstrømmen, partially flows directly into the ocean but also merges with L. Bistrup Bræ (Khan et al., 2014).

Storstrømmen and L. Bistrup Bræ lie adjacent to the study area and are reported to be two of the largest surge-type glaciers in the world (Fig. 2.8B & D; Higgins, 1991). Both glaciers flow around Dronning Louise Land, a nunatak complex, and then merge in Borgfjorden (Mouginot et al., 2018). Here, remote sensing data and historical photography show that the terminus position has been fluctuating during the past century, with a suggested surge periodicity on the order of 70 years (Mouginot et al., 2018).

Directly west of Bessel Fjord lies Soranerbræen, a tidal outlet glacier that has receded by 3 to 5 km between 1906 and 1972 (Fig. 2.8B & 12C; Weidick, 1995). Likely due to the remote location, and historically inaccessible waterways caused by the heavy presence of sea ice, there have been very few studies on Soranerbræen. It is understood that tide-water glacier retreat can largely be attributed to calving and submarine melting (Motyka et al., 2003; Bartholomaus et al., 2013), and findings suggest that oceanic temperatures play a critical role in their frontal position (Luckman et al., 2015). The glacier's frontal position would have fluctuated as climatic conditions changed over many millennia, aiding in the development of Bessel Fjord and its present-day seafloor morphology.

Satellite imagery of the region has uncovered unnamed ice caps (Figs. 2.8B & 3.8C) with multiple outlets north and south of Bessel Fjord (Fig. 2.9). The geologic record from Greenland indicates that local glaciers and ice caps have advanced and retreated partially out of tune with GrIS during the last glacial/interglacial cycle (Adrielsson & Alexanderson, 2005; Kelly & Lowell, 2009; Alexanderson & Håkansson, 2014). They are theorized to be more sensitive recorders of climatic changes when compared to ice sheets and ice sheet margins, which have a longer response time (Alexanderson & Håkansson, 2014). South of the Bessel Fjord, in Dronning Margrethe II Land, satellite images reveal the presence of Ejner Mikkelsen Gletscher, which appears to have three outlets: to the south, east and north (Fig. 2.8B). Its northern outlet lies behind a valley that oriented east northeast, roughly parallel to Bessel Fjord (Fig. 2.8C). It is probable that during periods of increased glaciation that this outlet has expanded into this valley. Due to its proximity to Bessel Fjord, and its potential for encroaching on the fjord during colder events, it's worth taking note of its presence. See Table 2.2 for annual advancement and retreat positions of glaciers near the study area between 2000-2010. Data from this time interval suggest that all these glaciers are currently in retreat.

2.6 Climate

The enormous size of Greenland, spanning more than 2600 km from north to south, allows for a wide range of climatic variability, although collectively the climate has been described as "Arctic" (Cappelen et al., 2001). In northern Greenland, winters can exceed -70 °C, where summers in the south can reach above 25 °C near the coast (Cappelen et al., 2001). Prolonged fluctuations in the Canadian cold vortex, as its shift eastwards towards Greenland or southwest towards Hudson Bay, can have a significant impact on Greenland's climate (Cappelen et al., 2001). Regional differences can also be responsible for climatic differences. For example, drifting sea ice and cold waters in coastal regions causes the air to become cold and humid, compared to ice free, inland regions that have warmer air (Cappelen et al., 2001).

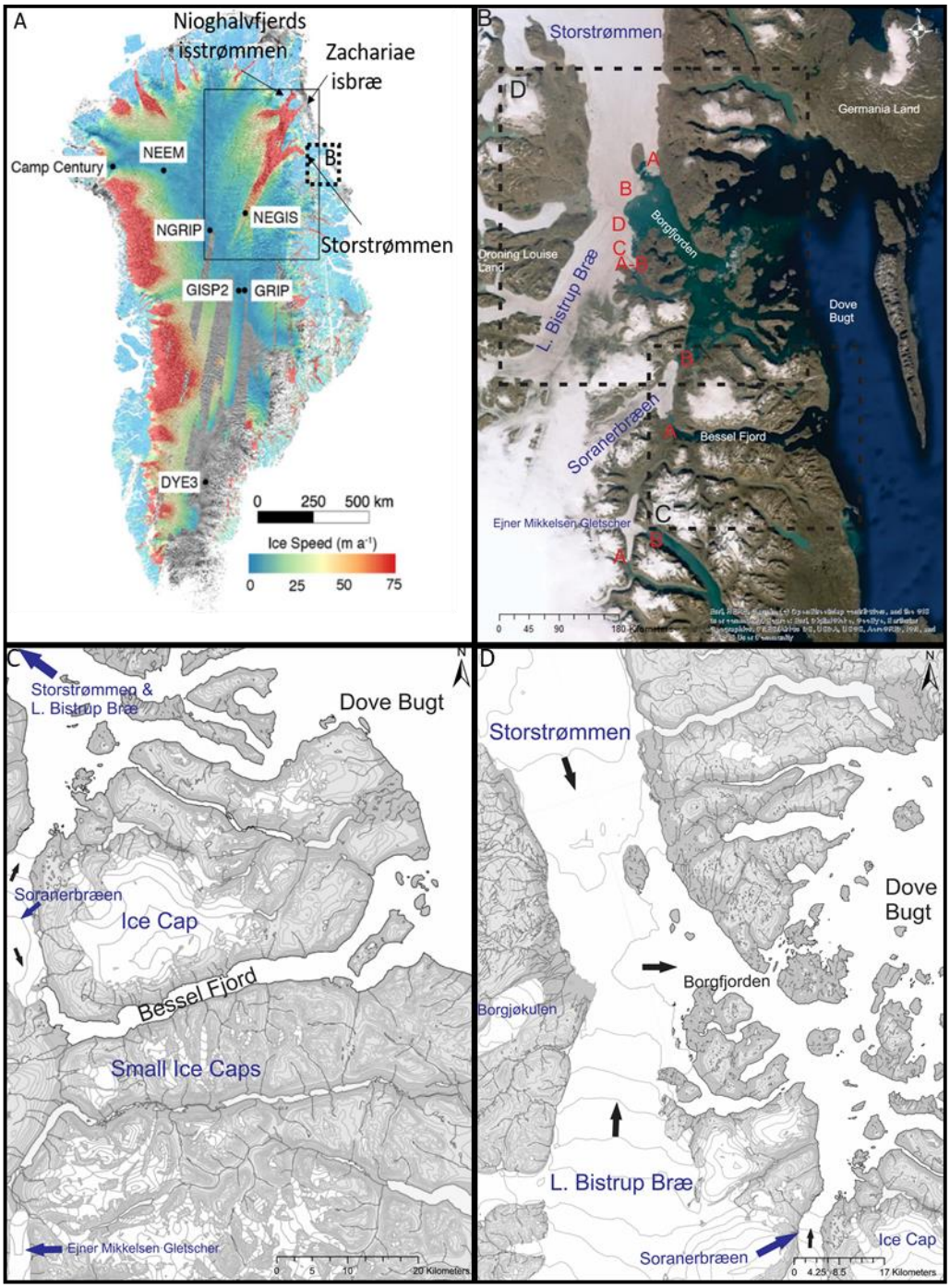

Figure 2.8. A: Map of ice flow velocities across Greenland, with a box around the NGIS. The three main outlets (Nioghalvfjerds isstrømmen, Zachariae isbræ and Storstrømmen) are labelled and a dashed box is around the location of Fig. 2.8B. Image taken and modified from Christianson et al. (2014). B: Map of the study area and surrounding glaciers (in blue). Red letters correspond to the location of glaciological data in Table 2.2, which quantifies the annual and total frontal change of glaciers near the study site from 2000 to 2010. Dash Boxes indicate the location of Figs. C and D. C: Image of local glaciers and ice caps around Bessel Fjord. D: Image of glaciers in western Dove Bugt. Black arrows in C and D indicate the direction for glacier movement.

Figure 2.9. Image of an outlet from an ice cap in Bessel Fjord. Photo taken by Torger Grytå.

Table 2.2. The annual and total frontal change of glaciers near the study site from 2000 to 2010 in meters. Letters after the names correspond to the positions in Figure 2.8B. Data taken from Murray et al. (2015).

Name	Latitude	Longitude	Width (km)	2000-01	2001-02	2002-03	2003-04	2004-05	2005-06	2006-07	2007-08	2008-09	2009-10	SUM
Soranerbræen a	76.035	–21.922	1.6	–24	–13	–5	–12	3	49	–85	–8	–42	–53	–190
Soranerbræen b	76.243	–21.691	3.6	–70	46	21	–63	18	70	–129	87	–29	–40	–89
Storstrømmen a	76.744	–22.450	20.1	13	100	–397	122	–167	65	127	103	–48	–622	–705
Storstrømmen b	76.842	–22.167	4.9	-	-	-	-	–837	67	–101	32	42	10	–788
L.Bistrup Bræ a	76.513	–22.332	2.5	–6	–96	105	–21	–103	5	15	–27	–209	–494	–832
L.Bistrup Bræ b	76.539	–22.385	2.7	–158	–46	48	7	122	91	–507	–79	–27	–30	–578
L.Bistrup Bræ c	76.565	–22.438	1.2	-	-	-	-	–130	-	-	–34	–26	–178	–367
L.Bistrup Bræ d	76.615	–22.495	4	-	-	-	-	–13	112	–194	–184	–432	–531	–1241
Ejnar Mikkelsen Gletscher a	75.552	–22.490	1.2	–27	–82	–64	–23	–52	7	–1	–34	–171	–38	–485
Ejnar Mikkelsen Gletscher b	75.657	–22.259	1.2	46	–120	–92	1	81	44	–30	–21	–26	–17	–134

Wind systems across Greenland vary between winter and summer and are dominated by the presence of two cyclones: the Baffin Bay low to the west and the larger Icelandic low to the southeast. During the winter southeastern Greenland is hit by the northwestern section of the Icelandic low, which results in heavy precipitation. North of 65° N dry onshore wind from the southwest reaches the west coast, causing low precipitation. Circulation during the summer is dominated by a pressure ridge extending from the northeast towards the center of the ice sheet, as well as the introduction of an additional low in the Polar basin. Precipitation decreases in the southwest and increases on the west coast. In respect to the south-westerlies and westerlies the

northeastern section of the ice sheet remains in the precipitations shadow and receives the lowest precipitation on the ice sheet (Ohmura & Reeh, 1991).

The geographical distribution of precipitation across Greenland is also quite varied. The rate of precipitation is typically highest along Greenland's coasts (Cappelen et al., 2001). Southern Greenland, and its eastern coast, experience a particularly high amounts of annual precipitation (Cappelen et al., 2001). Northern Greenland contains numerous "Arctic deserts", with are regions that are nearly snow free in the winter and evaporation can exceed precipitation in the summer (Cappelen et al., 2001). At sea level, southern Greenland experiences rain during the summer, and mostly snow in the winter, where rain is rare in the north, and snow can occasionally occur during the summer (Cappelen et al., 2001). Additionally, sea fog can become particularly prominent in regions of Greenland as well, especially between May and September (Cappelen et al., 2001).

In Northeast Greenland, winters are very cold due to the lack of open sea. Northerly wind directions are dominant, and winds and precipitation are frequently connected to cyclonic activity in the Greenland Sea (Cappelen et al., 2001). The strongest winds can be found in coastal areas, although it is possible for wind for to travel to certain fjords from the ice cap, taking the appearance of northwesterly and westerly Foehn or fall winds (Cappelen et al., 2001). This is a notable feature of Dove Bugt, where the wind transports large quantities of snow (Cappelen et al., 2001). In the summer, the fjords of Northeast Greenland are largely warm and sunny with the occasional periods of colder weather (Cappelen et al., 2001). Both Bessel Fjord and Dove Bugt's climate are impacted by the EGC, which brings on average 150,000 m^3 of ice per second from the Arctic Ocean (Cappelen et al., 2001). This current brings in fresh and cold water south along Greenland's eastern coast.

Throughout the year, the southernmost section of Northeast Greenland experiences the most precipitation (Cappelen et al., 2001). Inside fjords in the south, there is substantially less precipitation, which allows for the development of ice-free land (Cappelen et al., 2001). Ice in southern fjords may break in July, where fjords in the north may be filled with ice throughout the summer. Snow cover is typical between September and May (or possibly as late as July)

(Cappelen et al., 2001). Danmarkshavn, a weather station positioned on the southern shore of Germania Land in Dove Bugt, regularly collects temperature, humidity, wind, air pressure, precipitation, cloud cover, weather, snow cover and visibility data (Fig. 2.10; Cappelen et al., 2001). This station contains the most consistent modern climatic data for the area (e.g. Table 2.3).

2.7 Oceanography

Oceanic circulation around Greenland flows mostly in a clockwise direction (Fig. 2.11; Alley et al., 2010). Cold, fresh water leaves the Arctic Ocean through the Fram Strait and flows along the margins of east Greenland as the EGC (Hopkins, 1991; Alley et al., 2010). The EGC is restricted to the continental margin due to its low density and geostrophic currents and is characterized by cold Polar Water (PW) in the upper 150 meters, warm Atlantic Intermediate Water (AIW) between 150-800 meters and Greenland Deep Water (GDW) beneath 800 meters (Hopkins, 1991; Olsen, 2015). The source of the AIW is from recirculating Atlantic Water from the Arctic Ocean and a branch of the West Spitsbergen Current (Jennings & Weiner, 1996). Near the Denmark Strait, warmer Atlantic Water, that has been modified by the Irminger Current, turns and runs parallel to the EGC, (Alley et al., 2010). This flows at an intermediate depth on the East Greenland shelf, and moves along deep topographic troughs on the continental shelf and the margins of the Kangerdlugssuaq ice stream (Jennings & Weiner, 1996; Syvitski et al., 1996; Alley et al., 2010). The EGC moves further down the coast, around Cape Farewell, and northwards on Greenland's western coast. Here, it encounters a counterclockwise moving gyre that brings warm water to meet cold polar waters flowing through the Kennedy Channel, which allows for the southward movement of cold currents along northeastern Canada (Dahl-Jensen et al., 2009).

Fjords with a sill classically consist of three stratified water masses (Farmer & Freeland, 1983; Cottier et al., 2010). This includes a fresh water surface layer, an intermediate layer at sill depth, and a deep layer below (Cottier et al., 2010), which has also been found in some Greenlandic fjords (e.g. Azetsu-Scott & Syvitski, 1999; Cofaigh et al., 2001). The upper layer is typically composed of glacial meltwater, basal melting or other terrestrial runoff, such as rivers and

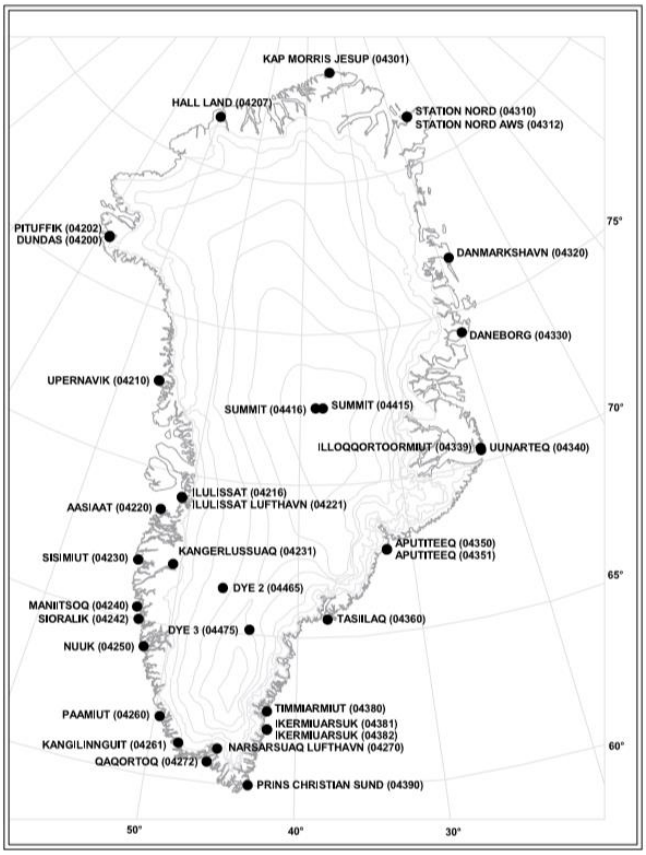

Figure 2.10. The location of weather stations across Greenland. Note the position of Danmarkshavn on Germania Land in Northeast Greenland. Taken from Cappelen et al. (2001).

Table 2.3. Climatological standard normal mean temperature (°C) and precipitation (mm) at the Danmarkshavn weather station between 1961-90. Data taken from Cappelen et al. (2001). Please note: the author mentions the absence of some monthly values.

	Jan	Feb	Mar	Apr	May	Jun	Jul	Aug	Sep	Oct	Nov	Dec	Year
Temperature (°C)	-23.1	-24.1	-23.4	-17	-7	0.8	3.7	2.3	-4.3	-13.7	-19.9	-21.9	-12.3
Precipitation (mm)	11	12	16	9	5	6	15	15	11	12	12	15	141

snowmelt (Cottier et al., 2010). The intermediate layer is frequently composed of advected water masses that are external to the fjord (Cottier et al., 2010). In East Greenland, the intermediate water is referred to as Polar Water and comes from the EGC (Azetsu-Scott & Tan, 1997; Azetsu-Scott & Syvitski, 1999; Colm Ó Cofaigh et al., 2001; Cottier et al., 2010; Straneo et al., 2010). As this layer is relatively warm, bottom melting allows ice-rafted debris to become released,

which may form layers within sediment (Azetsu-Scott & Syvitski, 1999; Cottier et al., 2010). The highly saline deep-water masses in Greenlandic fjords are believed to have a similar character to the cold halocline of the Arctic Ocean (Rudels et al., 1996; Kikuchi et al., 2004), rather than that of Svalbard (Nilsen et al., 2008), due to the regions large influx of freshwater, and the subsequent formation of winter sea-ice that only impacts the upper water layers (Cottier et al., 2010).

Seasonal hydrographic variations have been observed in fjords in Svalbard (Fig. 2.12; Cottier et al., 2010) and similar cycles are presumed to be present in the fjords of NE Greenland- although with a significantly shorter "warm" season. Cottier et al. (2010) observed a fully stratified fjord system in summer, with wind mixing being the dominant force. Through autumn, as air temperatures dropped and winds become stronger, heat becomes extracted from the fjord, while water temperatures drop, and the surface mixing layer deepens. During this period of mixing and cooling, cold, fresher water overlies more saline water and full convection throughout the entire water column may not be possible. Once water reaches a freezing point, continued surface cooling leads to the formation of sea ice and the release of brine (Haarpaintner et al., 2001). The increased salinity and density at the surface allowing for haline convection. Towards the end of winter there is also a small additional contribution of salt from the desalination of sea-ice over which has been attributed to an increase in oceanic heat fluxes (Widell et al., 2006). Depending on the fjord depth and salt flux, convection may extend over the entirety of the water column, allowing for the rejuvenation and re-oxygenation of bottom water (Nilsen et al., 2008). After sea ice break-up, there is a gradual increase in temperature through the surface water layer via mixing and reduction of salinity due to the renewed freshwater input during melt season. The dominant pycnocline of the summer eventually becomes reestablished, and the cycle begins anew.

External forces impacting fjords also have the potential to cause water masses to become modified, mixed or exchanged (Inall & Gillibrand, 2010). Local wind direction is controlled by the topography of the fjord, causing air movement in a bi-modal direction (i.e. down-fjord and up-fjord) (Nilsen et al., 2008). The result of this is modifying the outflow of surface water, either by intensifying it or reducing it depending on the wind movements orientation (Skogseth et al.,

2007), and inducing an upwelling effect. Wind also has an impact on vertical mixing, although it becomes suppressed during the winter due to sea-ice cover. The presence of sea ice allows for other mixing mechanisms become dominant, such as tidal and estuarine circulation. In contrast to seasonal convection related to brine released beneath ice cover, localized injections of freshwater can occur at depth due to the melting of icebergs or glaciers. This may result in local upwellings and vertical mixing.

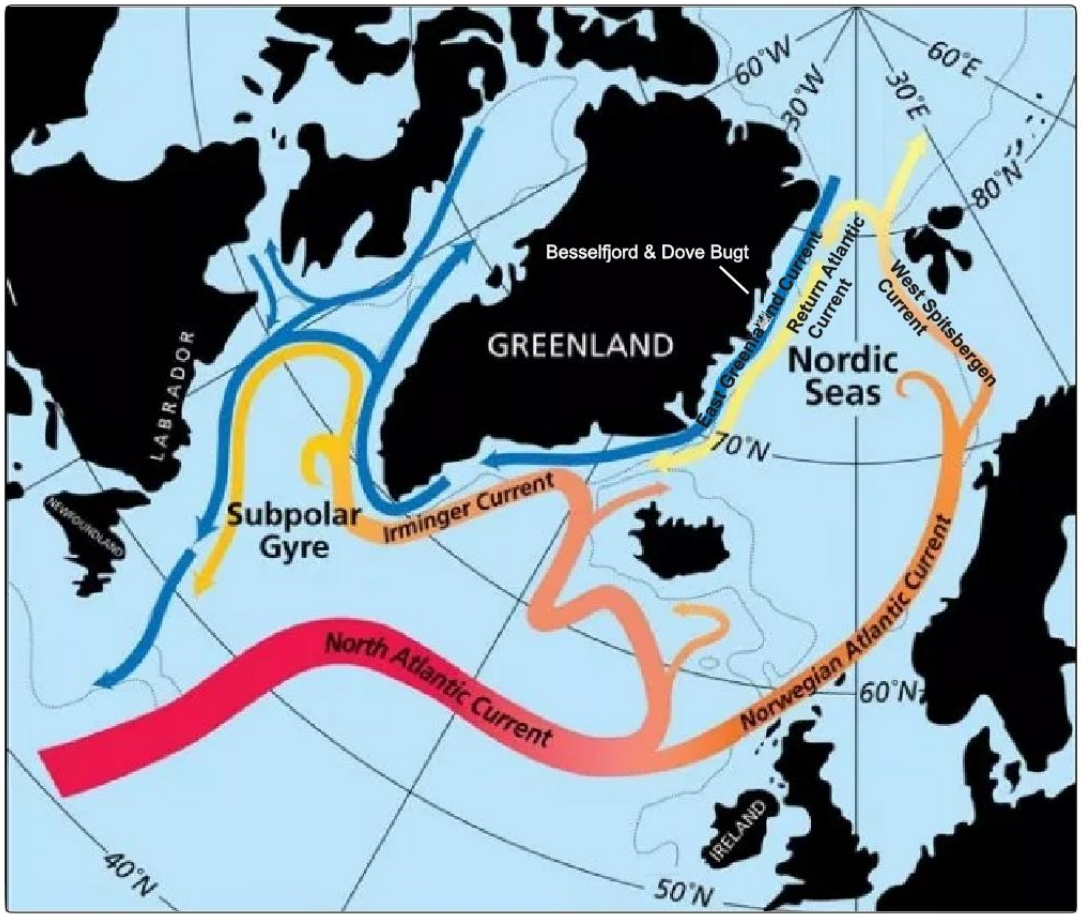

Figure 2.11. Ocean circulation around Greenland and throughout the Nordic Seas. Image originally taken and adapted from Watts (2010), but also adapted from Olsen (2015).

The Earth's rotation also effects fjords, which causes the distribution of freshwater to not be uniform across fjords. Surface meltwater entering a fjord at the head is deflected and the freshest and coolest water are found to the right in the direction of outflow. Similarly, in-following water masses will tend to move towards the right-hand shore. Archeological publications had noted the presence of a polynya just south of Store Koldewey (Sørensen, 2012; Sørensen & Gulløv, 2012). Polynyas have been identified across Northeast Greenland (e.g. Budéus et al., 1997; Schneider & Budéus, 1997; Pedersen et al., 2010) and a study of Young Sound Fjord (~74.4 °N 20.5 °W) by Dmitrenko et al. (2015) has found evidence that these features have the potential to impact the water chemistry of adjacent fjords

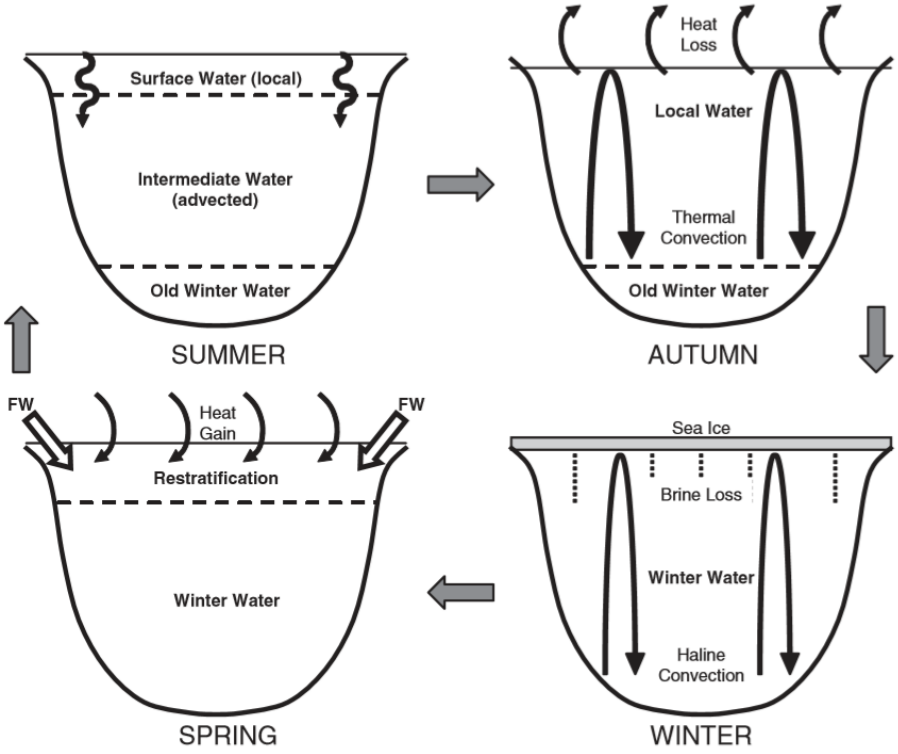

Figure 2.12. Images of seasonal cycles within shallow (300m) Arctic Fjords in Svalbard. Taken from Cottier et al. (2010).

3 Background

3.1 Glacial history of Northeast Greenland: LGM and deglaciation

Northeast Greenland's glacial history remains relatively obscure compared to other regions of the Greenland. It has been addressed by multiple authors, including Funder et al. (2011), who compiled some of the most up-to-date publications on Greenland's glacial history over the past 300 ka BP and Vasskog et al. (2015), which contributed additional findings from the last glacial cycle. Data concerning Late Weichselian deglaciation history and Holocene palaeoenvironment of the Northeast Greenland shelf and fjords are particularly scarce, therefore, the maximum position of the ice, timing of deglaciation, and dynamics of the East Greenland Ice Sheet during the Last Glacial Maximum (LGM) has yet to be firmly established (Funder et al., 2011).

The Weichselian glaciation (MIS 5d-1, ca. 115–11.7 ka BP) was the last glacial period in geologic history. During the Early and Middle Weichselian (MIS 5d and 3, ~116-27 ka BP) ice cores from Greenland provide evidence for more than twenty rapid warming events, referred to as Dansgaard-Oeschger (D-O) events or Greenland Interstadials (Dansgaard et al., 1993; Vasskog et al., 2015). The most detailed record of glaciations dating to the Early Weichselian can be found at Scoresby Sund (Fig. 3.1), where terrestrial studies suggest that a warm-based glacier advanced several hundred kilometers to the inner shelf (Funder et al., 2011). A glacial retreat followed, as well as a marine transgression, and subsequent readvance and retreat (referred to as the Aucellaelv and Jyllandselv stades) (Funder et al., 1998, 2011).

Early studies of coastal Northeast Greenland between 75-76°N suggested that the regional Weichselian sequences, in chronological order, consists of a Kap Mackenzie stadial, a Hochstetter Forland interstadial, Muschelbjerg stadial, Peters Bugt interstadial and the Nanok stadial (Hjort, 1981). Later, Hjort & Björck (1983) concluded that the two older glaciations, Kap Mackenzie and the Muschelbjerg stadials, are of Saalian age or older. The Nanok stadial has been further divided into the Nanok I and Nanok II stadials, which have been interpreted as occurring during the LGM and Preboreal Oscilllation, respectively (Hjort, 1979; Hjort & Björck,

1983; Funder, 1989; Johnsen et al., 1992; Larsen et al., 1995; Björck et al., 1997; Funder et al., 1998; Wagner et al., 2008).

Geomorphological features (e.g. mega-scale glacial lineations, drumlins, moraines, iceberg scour marks, debris flows) identified through geophysical surveys in Greenland suggest that the ice sheet reached the continental shelf during the LGM (~24-16 ka BP) (Funder et al., 2011; Vasskog et al., 2015). Funder et al. (2011) mapped the perceived position of the ice sheet during the LGM based on data that was available at the time and presented the furthest extent of Northeast Greenland as a "conceptual" minimum position (Fig. 3.1A). South of Dove Bugt, seafloor geomorphological evidence suggests that the GrIS reached the continental shelf edge off Kejser Franz-Joseph Fjord and Kong Oscar Fjord during the LGM (Fig. 3.2; Arndt, 2018). It has been suggested that the ice sheet reached the shelf edge at Scoresby Sund, however a grounding zone wedge (GZW) found 65 km inshore of the shelf edge is believed to possibly be the actual LGM ice extent (Arndt, 2018).

Further north, Arndt et al. (2015) created digital bathymetric model (DBM) for Northeast Greenland which incorporated bathymetric data from 30 multibeam cruises, over 20 single-beam cruises and reflector depths from industrial seismic lines (Fig. 3.2). This study, as well as a follow up study (i.e. Arndt et al., 2017), uncovered numerous geomorphological features, some of which were interpreted as glacial lineations, GZWs in the mid-shelf position on cross shelf troughs, a marine ice dome between Westwind Trough and Norske Trough, moraines and iceberg ploughmarks (Arndt et al., 2015). Arndt et al. (2017) concluded that this geomorphological evidence supports the theory that that large ice streams had reached the shelf edge via the Westwind Trough and Norske Trough during the LGM.

Bathymetric and high-resolution seismic findings on the outermost section of Store Koldewey Trough (at ~76°N) provides further evidence that grounded ice was on the shelf break during the LGM (Laberg et al., 2017; Olsen et al., in review). Despite this being the only cross-shelf trough in the region not being fed by a fjord, landform interpretations include GZWs, recessional moraines, MSGL and iceberg ploughmarks (Laberg et al., 2017). Since the continental shelf around Northeast Greenland is the broadest shelf along Greenland's margin, an ice sheet

expanding to the shelf break may represent the largest possible oscillation of the GrIS (Arndt et al., 2015). Studies from East Greenland's continental slope and basin further support bathymetric findings on the shelf and the expansion of the GrIS to an outer shelf position (e.g. Wilken & Mienert, 2006; García et al., 2012).

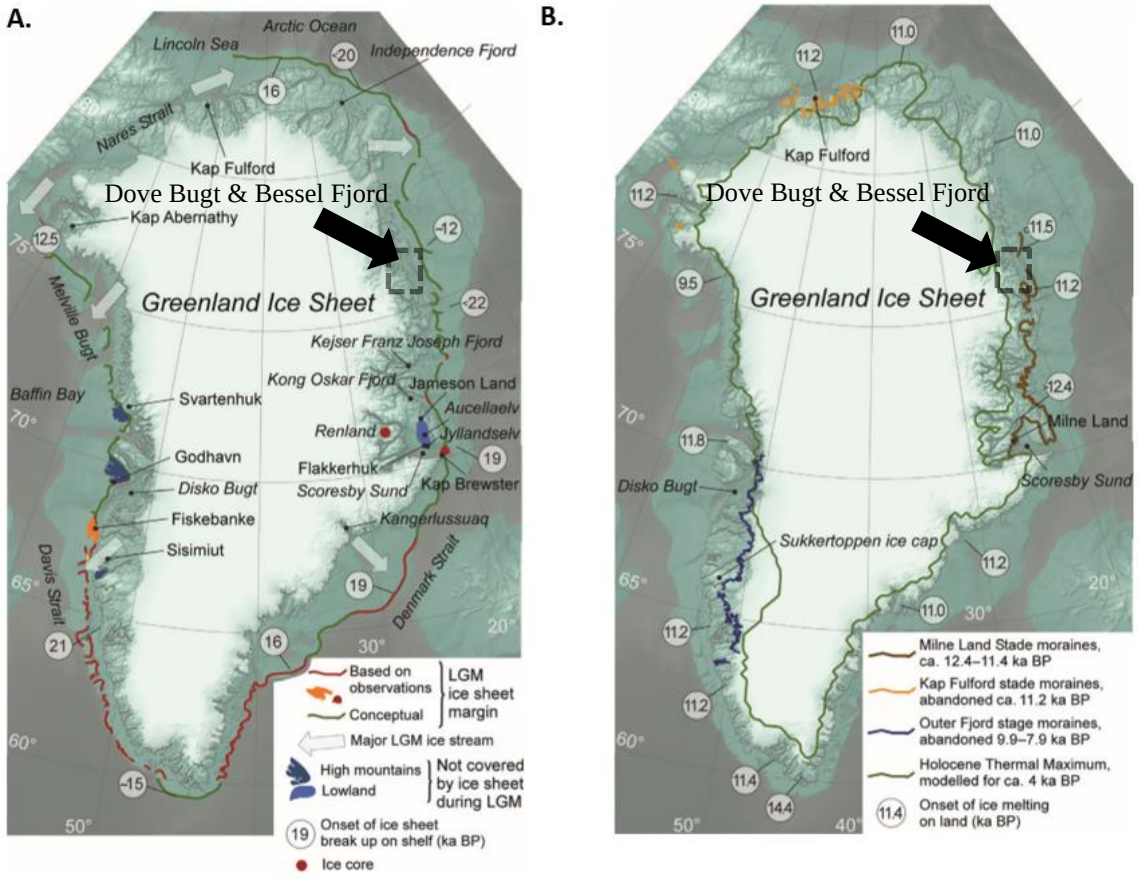

Figure 3.1. Modified maps of Greenland from Funder et al. (2011). A: Reconstruction of the LGM ice sheet extent and timing. B: The position of the ice sheet during the deglaciation which followed the LGM.

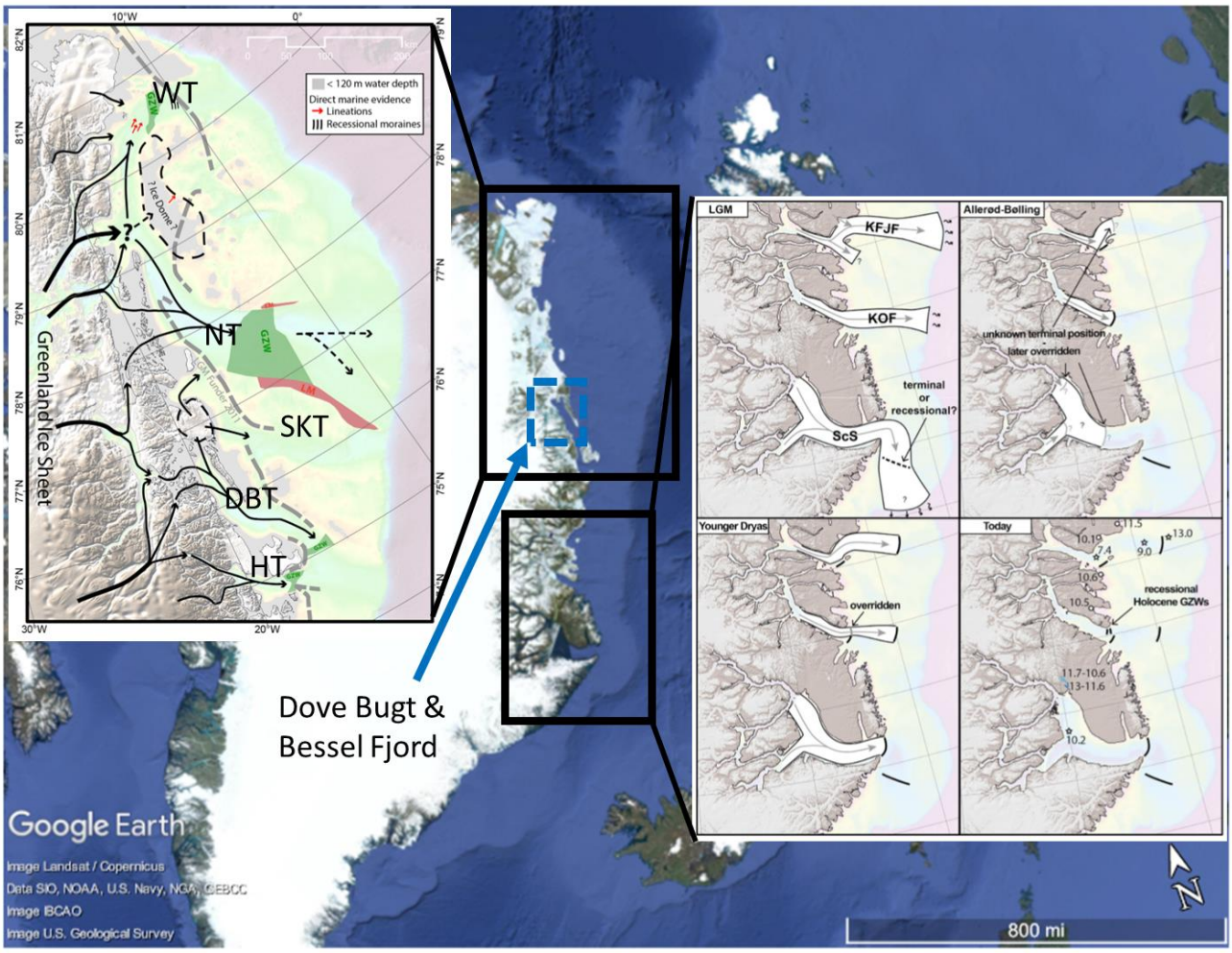

Figure 3.2 GoogleEarth image of Greenland with the study area indicated with a blue dashed box. Two regions of Greenland whose seafloor morphology have been analyzed and interpreted are represented by two black boxes. The figure on the left, which encompasses Northeast Greenland's coast, shows Arndt et al. (2015) interpretation of paleo-ice flow on the shelf based on morphological features in their digital bathymetric model. This includes (from north to south) Westwind Trough (WT), Norske Trough (NT), Store Koldewey Trough (SKT), Dove Bugt Trough (DBT) and Hochstetterbugten Trough (HT). Cross-trough shelfs (light green), GZW (dark green), lateral moraine (red) and Funder et al. (2011) minimum LGM extent (dashed grey lines). Taken and modified from Arndt et al., (2015). The figure on the right shows Arndt et al. (2018) interpretation of east Greenland's ice-stream flow directions and extent at Kejser Franz Joseph Fjord (KFJF), Kong Oscar Fjord (KOF), and Scoresby Sund (ScS) during the LGM (21–16 14C ka BP), the Allerød–Bølling interstadial (14.45–12.7 ka BP) and the Younger Dryas (12.7–11.55 ka BP). Arndt et al., (2018) indicate the location of moraines and grounding-zone wedges mapped in this study with black lines and deglaciation ages from marine sediment cores (stars) in cor ka BP (Marienfeld, 1991; Dowdeswell et al., 1994; Evans et al., 2002)*, from onshore radiocarbon dating (circles) in cal ka BP* (Bennike & Wagner, 2012) *and formation age of terrestrial moraines in Kjove Land (light and dark blue) in ka BP* (Kelly et al., 2008)*.*

A period of deglaciation (17-11.5 ka BP) followed the LGM, which also encompasses the Allerød– Bølling interstadial (~14.7-12.7 ka BP) (Fig. 3.2B). Ice streams along the northeast coast of Greenland (ca. 81-71°N) became less vigorous, possibly as a response to decreased cyclone passages and precipitation, caused by the restriction of the Denmark Strait (Funder et al., 2011). Timing of the deglaciation varied throughout Greenland, and its break-up along the continental shelf was not only driven by temperature changes, but also by factors like sea-level change and ocean warming, shelf bathymetry and drainage and sea ice conditions (Funder et al., 2011). Finding along the Store Koldewey Trough reveal a complex pattern of retreat moraines, which point to a stepwise early deglaciation after the LGM rather than a deglaciation brought on by an abrupt sea level rise (Laberg et al., 2017).

During the Younger Dryas (12.8-11.7 ka BP), which is represented in ice records with lower temperatures and a particularly strong warming at its conclusion (Steffensen et al., 2008), there is no uniform ice-marginal response across Greenland (Funder et al., 2011). In Scoresby Sund, fjord and valley glaciers advanced during the Milne Land Stage, but these advances were already occurring during the Allerød interstadial and retreated prior to the end of the Younger Dryas (Hall et al., 2008, 2010; Kelly et al., 2008; Funder et al., 2011). GZW found in the mid-shelf position of Westwind Trough, Norske Trough, Kejser Franz Joseph Fjord and Kong Oscar Fjord have been interpreted as a readvancement of the GrIS during the Younger Dryas (Arndt et al., 2017; Arndt, 2018). This readvance is theorized to have erased sections of the Allerød–Bølling terminal moraines (Arndt, 2018). Terrestrial and nearshore shelf data from the subsequent Preboreal Oscillation (PBO; 11.5–11.4 ka BP) show that there was not a uniform ice sheet response to the periods initial cooling or the abrupt warming at its conclusion (Funder et al., 2011).

Recently published terrestrial cosmogenic nuclide dates from the Dove Bugt region suggest that Store Koldewey was deglaciated by 12.7 ka BP (Skov et al., 2020). Findings from lacustrine sedimentary records (Cremer et al., 2008) and macrofossil remains (Bennike & Björck, 2002) also suggest that most areas at the outer coast of Northeast Greenland were deglaciated in a period spanning roughly 1500 years after the start of the Holocene (Klug et al., 2016). A minimum date of 11.2 ka BP has been proposed for the deglaciation of Hochstetter Forland,

south of Bessel Fjord in southern Dronning Margrethe II Land and 9.5 ka BP in Germania Land in northern Dove Bugt (Bennike & Weidick, 2001). These dates coincide well with the deglaciation of Scoresby Sund, which is believed to have become ice free around 12.4 ka yr. BP (Hall et al., 2008, 2010; Kelly et al., 2008; Funder et al., 2011).

3.2 Holocene paleoclimate of East Greenland

The Holocene epoch, marked by largely warmer temperatures than the Pleistocene epoch that preceded it, began at 11.7 ka BP and continues until present day. In the Early Holocene, summer insolation in the Northern Hemisphere peaked at approximately 11 ka BP (Berger & Loutre, 1991; Laskar et al., 2004), although warming was delayed due to negative feedback mechanisms (Kaufman et al., 2004; Carlson et al., 2008; Renssen et al., 2009, 2012; Vasskog et al., 2015). This caused a gradual warming trend in the north, although the Greenland ice core record indicates there were multiple quick, short cold reversals termed the PBO (~11.4 ka BP), the 9.3 ka BP event, and the 8.2 ka BP event (Rasmussen et al., 2007; Vasskog et al., 2015). During the Early Holocene, the GrIS retreated onto land and in some locations retreated to its current position or beyond (Hughes et al., 2012; Carlson et al., 2014; Dyke et al., 2014; Larsen et al., 2014; Winsor, 2014; Vasskog et al., 2015; Winsor et al., 2015). Using a variety of dating techniques (e.g. Briner et al., 2013; Carlson et al., 2014) and biostratigraphy (e.g. Weidick et al., 2012) it was determined that the ice sheet retreated close to, or in some cases past, its Late Holocene maximum extent across Greenland (Vasskog et al., 2015). North of Dove Bugt, the deglaciation of Germania Land is believed to have been initiated at 10.5 ka B.P. (Landvik, 1994), and a general recession of 40 m a^{-1} continued until the Storstrømmen Sound began to open, separating Germania Land from mainland Greenland (Weidick et al., 1996).

The Holocene Thermal Maximum (HTM) marked a period of higher temperatures that are commonly associated with an increase in insolation and related positive feedback (i.e. a decrease in surface albedo from the loss of ice and snow) which created a polar amplification effect (e.g. Holland & Bitz, 2003; Serreze & Francis, 2006; Masson-Delmotte et al., 2006; M. Serreze et al., 2009; Miller et al., 2010; Vasskog et al., 2015). Near the study area, lake studies on aquatic organisms (chironomids) at Duck Lake and Hjort Lake on Store Koldewey indicate that this

region was at its warmest between ~8 and 4 ka, (Wagner et al., 2008; Klug et al., 2009; Schmidt et al., 2011). Sediments collected from Melles Lake on Store Koldewey show an increase in organic-matter accumulation as early as ~10 ka, which might mark the earliest onset of warmth during the Holocene (Klug et al., 2009; Briner et al., 2016). The highest concentrations of organic matter and aquatic mosses are found within the early to mid-Holocene sediments, where the thermal maximum ended here at ~5.5 ka. From ~4.5 ka onwards, colder climates on Store Koldewey persisted, which coincides with an increase in sea-ice extent on southeastern Greenland's shelf (Jennings et al., 2002; Briner et al., 2016). South of Store Koldewey, pollen assemblages from Dødis Sø, Peters Bugt Sø and Ailsa Sø on Hochstetter Forland suggest that summer temperatures are higher than present between 8.8 and 5.6 (Björck & Persson, 1981; Björck et al., 1994). The timing of the HTM is not uniform across East Greenland (Fig. 3.3) and the early onset of warmth at Store Koldewey is attributed to local early deglaciation (Briner et al., 2016).

The start of the Late Holocene is marked with cooler temperatures, particularly in northern latitudes (Marcott et al., 2013; Vasskog et al., 2015). This 'Neoglacial period' is believed to have occurred between 6 to 3 ka BP (Davis et al., 2009; Vasskog et al., 2015). Dated marine material collected along the neoglacial moraines of Storstrømmen Sound (clustered around 6-5 and 4-3 ka B.P.) indicate that the sound may have closed multiple times throughout the Holocene (Weidick, 1996). Despite this cooling, available data suggests that the GrIS reached its minimum size between ~5 and 2 ka, although timing of its minimum configuration and later expansion varied regionally (Larsen et al., 2015; Young & Briner, 2015; Briner et al., 2016). The Little Ice Age (LIA) refers to the period in which glaciers in the North Atlantic region reached their maximum Neoglacial extent during the last few centuries (Grove, 2001; Vasskog et al., 2015). This period is less straightforward for Greenland, however, as proxy reconstructions point towards a warmer than present LIA temperatures at the sub-polar gyre and southern Greenland (Mann et al., 2009), and a not so well understood ice sheet extent (albeit, there is data for a few regions) (Vasskog et al., 2015). At Storstrømmen Sound, a single young date of 1.2 ka B.P. of marine material indicates that the sound was open near to the present day and was likely filled with glacial ice during the LIA (Weidick et al., 1996).

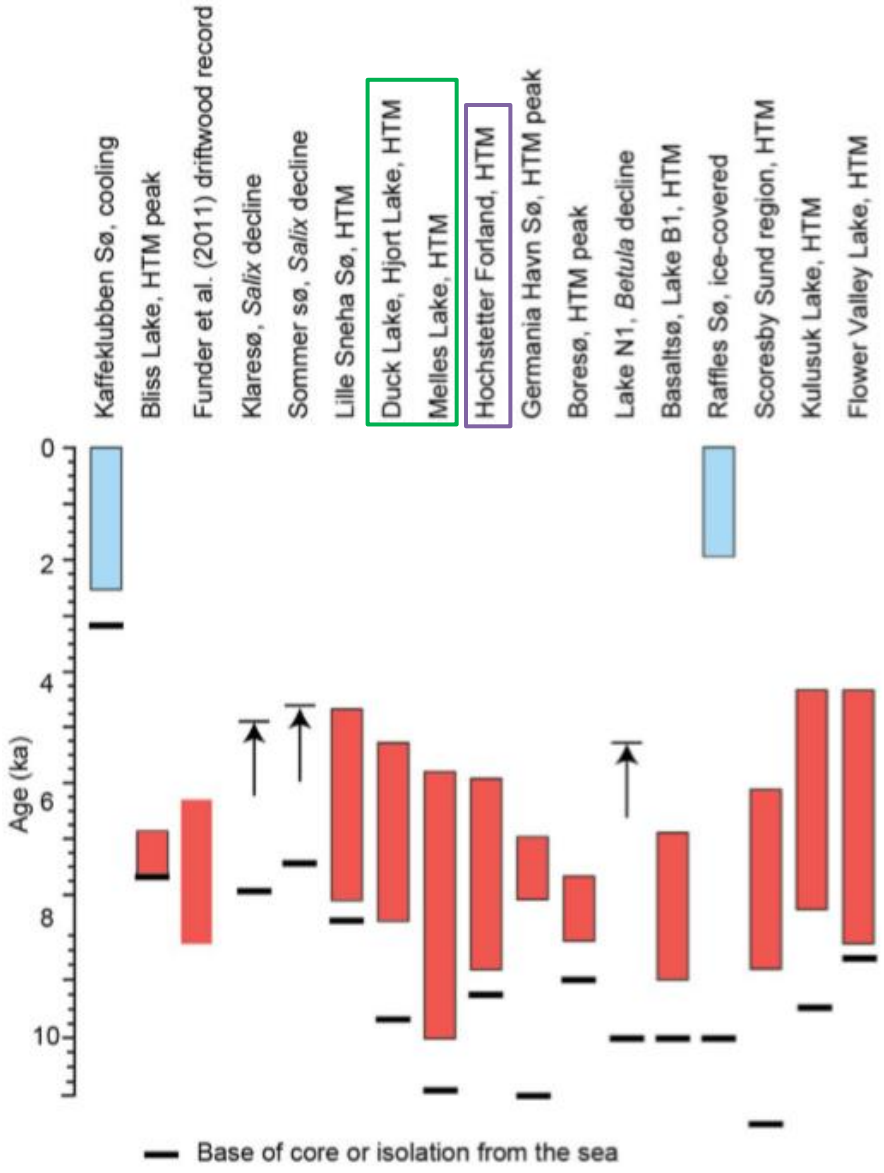

Figure 3.3. The timing of the Holocene thermal maximum (HTM) (red bars), the peak of the HTM, decline of pollen records and beginning on late Holocene cooling (blue bars) from select records in east Greenland. The green box surrounds records that are to the east of the study area and the purple box surrounds records to the south of the field site. Figure taken and modified from Briner et al., (2016).

4 Material and Methods

The datasets in this master's thesis were acquired in 2017 by The University of Tromso's Research Vessel, Helmer Hanssen, as a part of the TUNU project (Christiansen, 2012). This project is largely associated biological studies; however, the R/V was able to collect sediment cores, swath bathymetry data and chirp profiles across Dove Bugt and Bessel Fjord in Northeast Greenland. Due to complexity of these two regions it was determined that the analysis of chirp data would be excluded from this master's thesis. Below you can find a detailed description of the instrumentation and lab procedures used in this study.

4.1 Swath Bathymetry

A swath bathymetry sonar system is a high-resolution imaging system in which the seafloor is scanned by fans of beams that are emitted from a set of echo sounders. The echo sounders are facing sideways towards the acquisition direction at a specified angle relative to the vertical (Denbigh, 1989). This geophysical technique allows one to acquire information about the seabed morphology, which can have numerous applications in relation to seafloor analysis (e.g. Rutledge & Leonard, 2001; Laberg et al., 2009; Ramana et al., 2009). Aboard the Helmer Hanssen, a Kongsberg Maritime Simrad EM 302 multibeam echo sounder was used to collect bathymetric data for this study (Fig. 4.1). This system has a depth range of 10 to 7000 m and 432 soundings per swath (Kongsberg Maritime, 2017). Prior to receiving the data, it was gridded using Petrel software and interpretations were made using Global Mapper 18 once the data was received. The surfaces were created using a 5x5m grid cell size, and a surface made from an International Bathymetric Chart of the Arctic Ocean (IBCAO) dataset was gridded using a 500x500m grid cell. Images from GoogleEarth and the Geological Survey of Denmark and Greenland (GEUS) were also overlaid on the surfaces using an Image Rectifier tool. The data covered sections of Bessel Fjord and southern Dove Bugt (Fig. 4.1).

During data analysis, potential artifacts have been observed throughout the dataset (Fig. 4.2). This includes gaps in the data (Fig. 4.2A, B, D), positive relief features (possibly "mismatched" data) (Fig. 4.2B), circular impression from turning of the ship (Fig. 4.2C) and linear features that appear due to a "mismatch" between individual swaths (e.g. due to unsuccessful tide corrections)

(Fig. 4.3). It was suspected that the linear features may be geomorphic features that appear 42 to 50 m wide and 0.5 to 1 m high, however after further inspection it has been determined that they are likely artifacts.

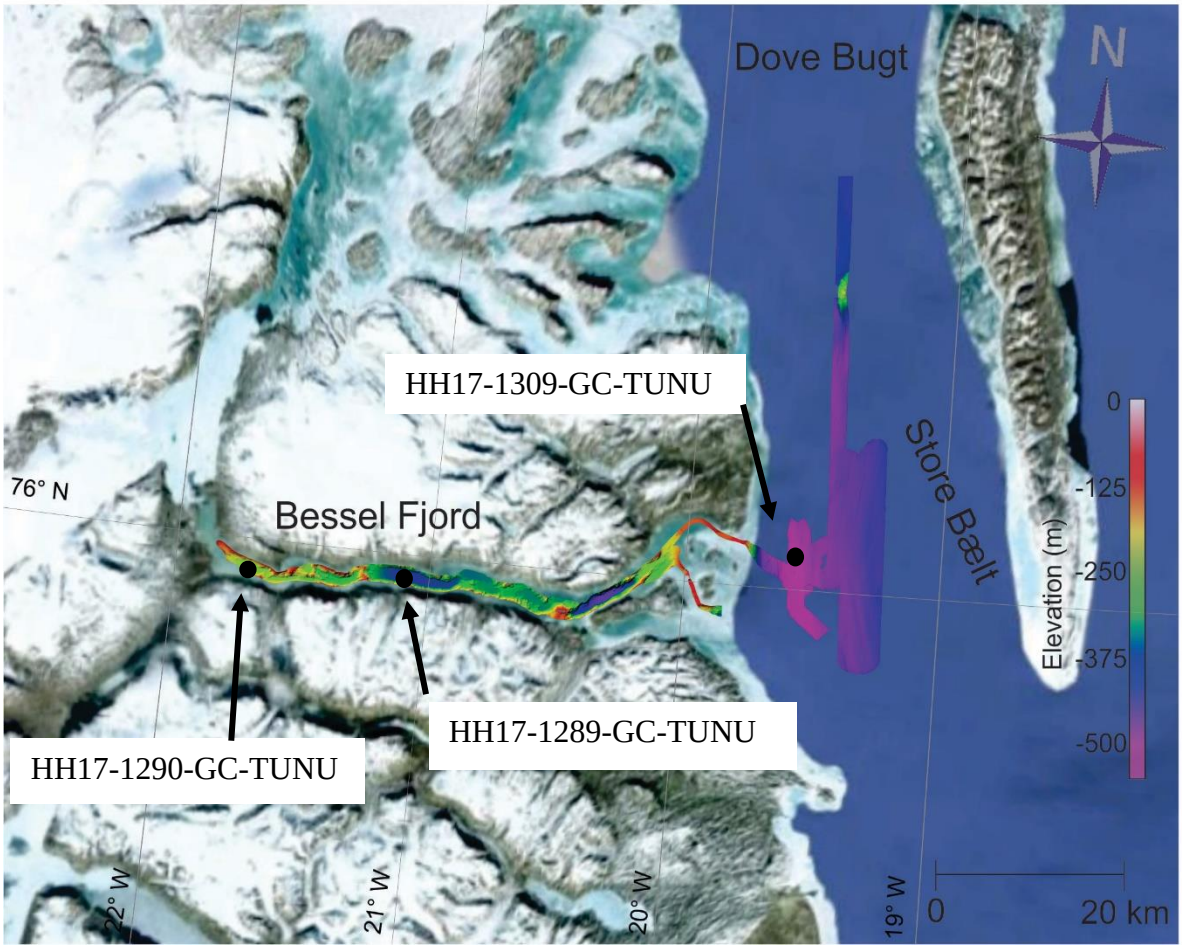

Figure 4.1. Image of recovered bathymetric dataset from the 2017 TUNU cruise. The location of the three gravity cores collected in the area are represented by black circles.

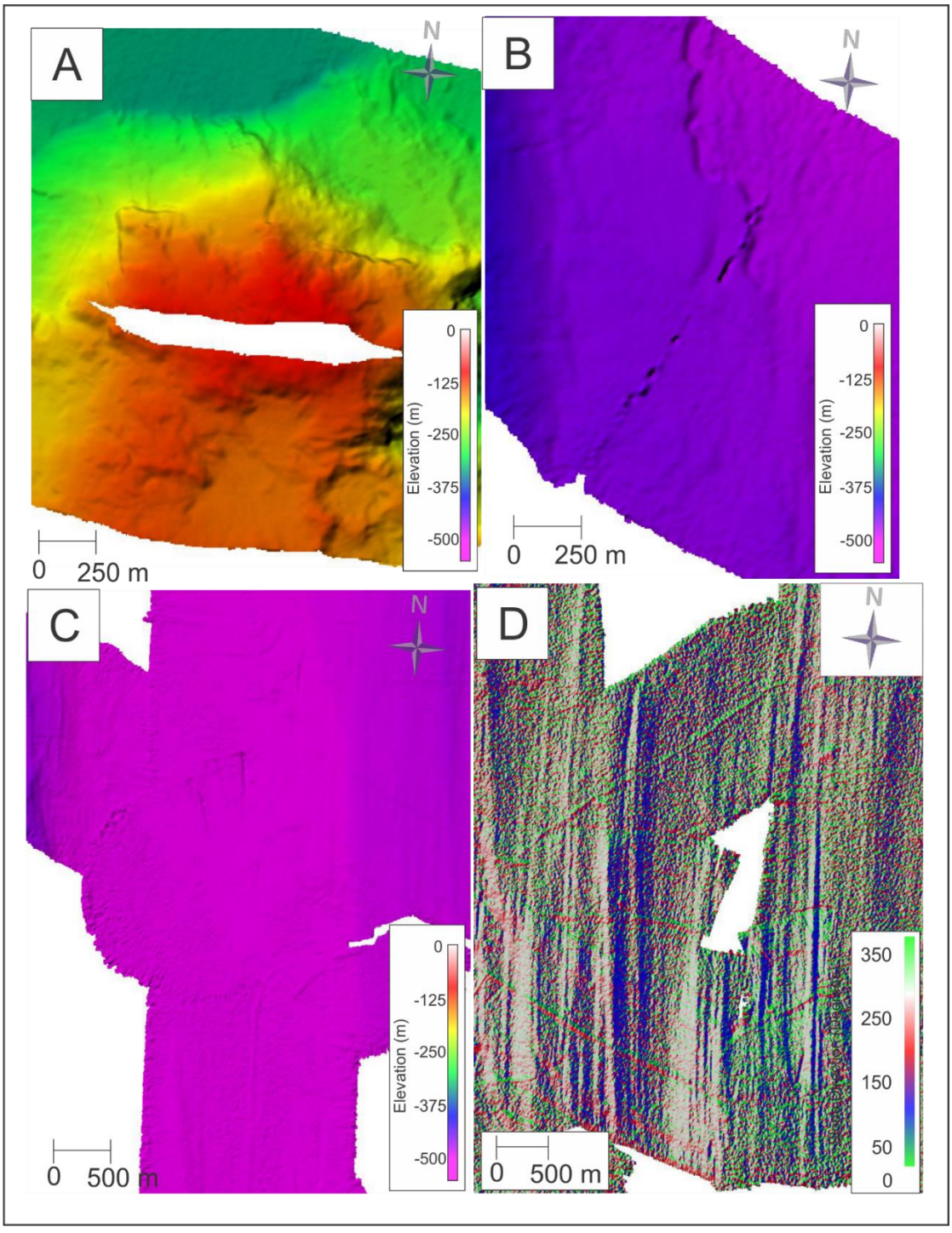

Figure 4.2. Examples of the different types of artifacts identified in the bathymetry dataset of Bessel Fjord and Dove Bugt. A: A gap in the dataset in Bessel Fjord. B: Positive relief feature that may be "mismatched" data in southwestern Dove Bugt. C: Circular artifact from a ship turning in southwestern Dove Bugt. D: Linear artifacts in western Dove Bugt, projecting out from near the mouth of Bessel Fjord in an east-west direction. This image also contains a gap in the dataset.

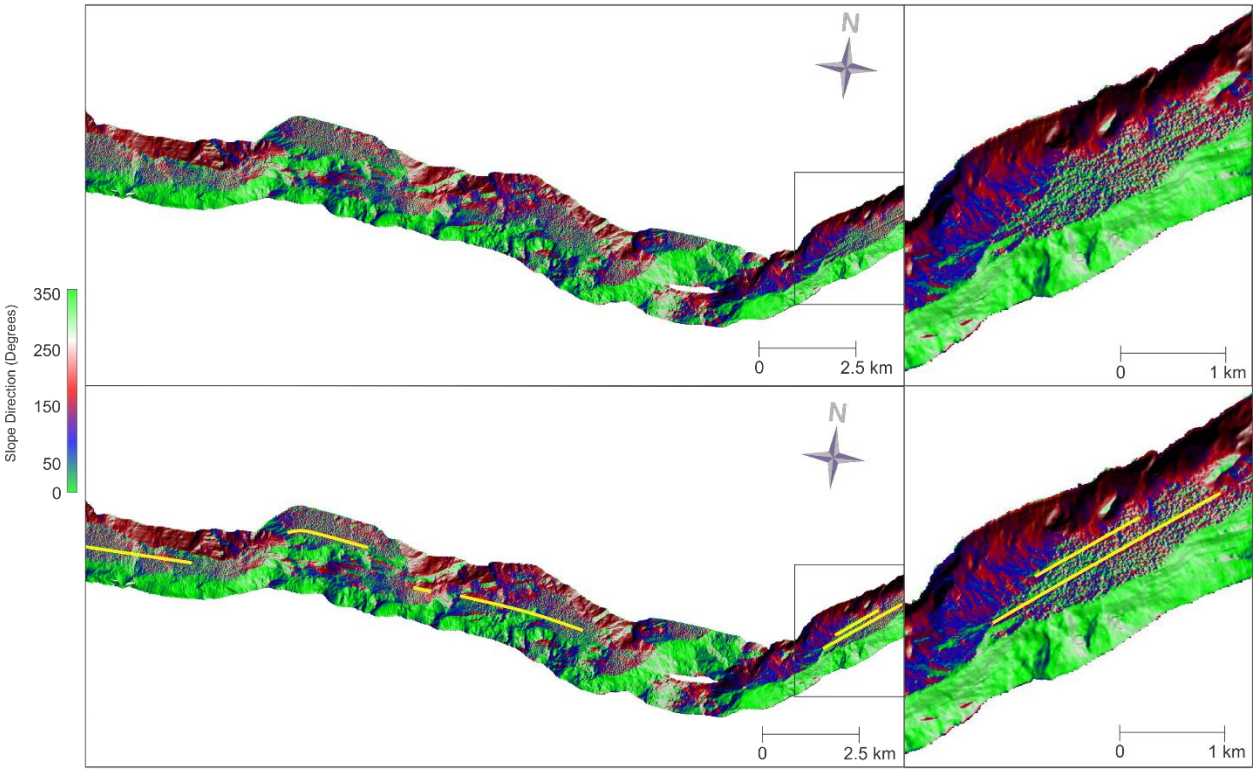

Figure 4.3. Linear artifacts identified in the bathymetry of Bessel Fjord.

4.2 Sediment Cores

Three sediment cores were obtained using a gravity corer installed onboard *the R/V Helmer Hanssen*. Two sediment cores were collected within Bessel Fjord (HH17-1289-GC-TUNU & HH17-1290-GC-TUNU) and one was collected immediately outside of Bessel Fjord, in Dove Bugt/Store Bælt (HH17-1309-GC-TUNU) (Fig. 4.1). The gravity corer itself contains a 6 m long steel barrel with plastic linear covering the interior. A 1600kg weight is attached to the steel barrel to assure the corer penetrates the subsurface sediments. After cores had been retrieved at the surface, they were split into ~1m sections, labeled, capped with plastic caps, and stored at 4˚C. Laboratory work was performed on these three cores at the Department of Geosciences at UiT The Arctic University of Norway between August 2019 and January 2020. Below is a description of each of the lab instrumentation and procedures used in this study.

4.2.1 Laboratory Work

4.2.1.1 Multi Sensor Core Logger (MSCL)

Prior to splitting the cores, physical measurements were first obtained using a GEOTEK Multi Sensor Core Logger (MSCL-S). These measurements included the core diameter, temperature, gamma-ray attenuation, P-wave velocity, P-amplitude and magnetic susceptibility. The resulting wet bulk density, p-wave velocity, magnetic susceptibility and (later calculated) acoustic impedance were later used in sediment core analysis. The cores were placed at room temperature 24 hrs prior to analysis and the machine was calibrated prior to use.

Wet Bulk Density

The bulk density of a material is the mass of any particle of the material divided by the total volume that the mass occupies. Within sediments, variations will occur based in mineral composition and compaction (GEOTEK, 2016). This is measured as a gamma ray source and detector are positioned across from the core on a sensor that is aligned with the middle of the core. A beam of collimated gamma rays is released from a 137-Caesium source with energies principally at 0.662 MeV, which passthrough the core as photons and is detected on the other side. Attenuation of gamma rays occurs by Compton scattering, which is directly related to the number of electrons in the gamma ray beam (i.e. the core thickness and electronic density). Therefore, the measurement of gamma photos that pass through the core unattenuated can determine the density of the material (GEOTEK, 2016).

P-wave

P-wave (primary-waves) are compressional waves that propagate by means of compressional and dilational uniaxial strains in the direction of wave travel (Kearey et al., 2002). Unlike s-waves, p-waves can travel through any type of material. Particle motion in p-waves involves oscillation about a fixed point in the wave propagation direction (Kearey et al., 2002). In marine sediments, the p-wave velocity is influenced by changes in lithology, bulk density, porosity, lithostatic pressure, degrees of fracturing, degree of consolidation and/or presence of solid gas hydrates or gas (among other thing) (St-Onge et al., 2007). In the MSCL system, a short p-wave

pulse is produced at the transmitter, which propagates through the core and is detected by a receiver on the other end. Pulse timing software is used to measure the travel time of the pulse (GEOTEK, 2016). Typical p-wave velocities are 330 m/s in air, 1480 m/s in seawater and about 5000 m/s in granite (GEOTEK, 2016).

Magnetic Susceptibility

The magnetic susceptibility of a substance is the degree of magnetization of a material in response to an applied magnetic field (GEOTEK, 2016). Paramagnetic, ferromagnetic, ferrimagnetic or antiferromagnetic material will register as having a positive magnetic susceptibility, where diamagnetic material (e.g. silica) will have a negative magnetic susceptibility reading (GEOTEK, 2016). Ferrimagnetic minerals, such as magnetite, can produce magnetic susceptibility values that are 3 to 4 times larger than those of antiferromagnetic minerals, such as hematite (Stoner et al., 1996). In this instrumentation a Bartington loop sensor was used to obtain magnetic susceptibly measurements.

Acoustic Impedance

The acoustic impedance, Z, of a material is the product of its density, ρ, and wave velocity, v. That is:

$$Z = \rho v$$

This parameter is not easily related to a tangible rock property, however, frequently the harder the rock the higher its acoustic impedance (Kearey et al., 2002). The smaller the contrast in Z across an interface the greater the proportion of energy transmitted through the interface (Kearey et al., 2002). Knowing the acoustic impedance of a material can be a useful tool when it is used in conjunction with chirp data. Here, the acoustic impedance was calculated prior to the decision to exclude the chirp dataset, however it was decided that this calculated parameter would remain in this master's thesis.

MSCL Plots

In Chapter 5: Lithostratigraphy, magnetic susceptibility, P-wave, bulk density and acoustic impedance plots have been plotted next to x-ray images and core photos taken with the Avaatech XRF core scanner. Plots for these four parameters at times did not have total lengths that matched the measured lengths of the cores. Additionally, they were found at times to have outlier datapoints at the very beginning and end of the cores. Therefore, through detailed inspection of the dataset, certain values at the beginning and end of core sections were excluded from the plots. Additionally, all values beneath 1480 m/s were excluded from the p-wave plots. This was done because it is possible that velocities beneath 1480 m/s represent air pockets (GEOTEK, 2016), possibly a product the core linear not being coming filled with sediment.

4.2.2 X-Ray Photography

A GEOTEK MSCL X-ray Computed Tomographic imaging machine was used to create X-ray radiographic scans of full core sections prior to being split into halved sections. This methodology is particularly useful as a non-invasive way to analyze the content of geologic material (e.g. Orsi et al., 1994; Mees et al., 2003; Tonai et al., 2019; Zhang et al., 2019). X-rays are produced as a result of the transformation of the kinetic energy attained by electrons accelerated under a potential difference into electromagnetic radiation, as a product of collisional and radiative interactions (Seibert, 2004). Sediment density is largely responsible for affecting x-ray attenuation (Tanaka et al., 2011), however it may also be impacted by water content, compaction and porosity (St-Onge et al., 2007). Here, images were taken every 20 mm with the transmission of 120kV and 225 µA X-rays. Images were also collected using laminography but were not used in this master's thesis.

4.2.3 Sediment Core Splitting and Logging

The three gravity cores were split using a Marinetechnik Kawohol core liner saw. Cores were opened from top to bottom and were completely split in half using different instrumentation, including an electro-osmotic knife. After being properly labeled and packed in plastic each half was placed in refrigeration at 4 °C.

After the working half of the cores were cleaned, a systematic visual description of the surface was performed. Detailed logs were developed noting details in sediment grain size and sorting, sedimentary structures, fossils, etc. Colors were determined using the Munsell Soil Color Chart. Large clasts were documented, removed, measured and photographed. The lithofacies classification system assigned to varying sedimentological sections within each unit was taken from Eyles et al. (1983). See Table 4.1 for a list of each of the lithofacies codes used in this study.

4.2.4 **XRF Scan**

XRF data was collected on an Avaatech XRF core scanner, which contains an arrangement with an X-ray source, helium chamber/measuring triangle and a detector. X-ray fluorescence (XRF) scanning is a non-invasive scanning technique that analyzes secondary radiation (i.e. fluorescence) that is produced from the collision of X-rays with matter (Forwick, 2013). This occurs when x-rays collide with an atom and eject electrons from their orbits. Due to electrostatic forces, vacancies created in these orbits become filled with electrons from a higher shell, which creates and releases excess energy/radiation. Each element has a characteristic fluorescing energy, hence allowing for identification of the elements in the sample (Forwick, 2013).

Table 4.1. Lithofacies codes and how the corresponding facies is defined. Facies cores are taken from Eyles et al. (1983).

Facies Code	Facies
Diamict, D	
Dc	Clast supported
D-m	Massive
Dms(r)	Matrix-supported, stratified diamict with evidence of resedimentation
Sand, S	
Sh	Horizontal laminations
Sm	Massive
Sd	Soft sediment deformation
Sg	Graded
Fine-grained (mud), F	
Fl	Laminated
Fm	Massive
F-d	with dropstone

Measurements on the Avaatech XRF core scanner are performed on multiple runs, with varying currents, voltages and filters, due to the wide spectrum of energies required to excite the various elements. Here, XRF data was collected at 10 kV, (1000 μA) with no filter to measure light elements from Mg to Co and at 30 kV (2000 μA) with a Pd-thick filter, to measure medium-heavy elements from Ni to "ca." Mo (Forwick, 2013). Measurements were collected in 1 cm intervals across the entirety of each core. Large clasts that were visible from the surface of each half core were removed to prevent interference with the core scanner. Additionally, prior to core analysis photographs were also obtained using the core scanner.

4.2.4.1 XRF Dataset and Plots

Like the dataset obtained with the MSCL, core section lengths in XRF datasheets did not match the true length of each core at times and some elemental concentrations were abnormal at the beginning and ends of some core sections. To remove any distortion that the core liner and/or caps may be causing, datapoints at the top and bottom of certain sections were removed from plots presented in Chapter 5: Lithostratigraphy. As the use of XRF is a relatively new methodology applied to glaciated fjord systems (as well as marine studies as a whole), plots produced in Chapter 5 resemble those produced in Olsen (2015) in an effort to see similarities between fjords in East Greenland. SUM quantity used in elemental ratios consist of the 10 most abundant elements in the dataset (i.e. Al, Si, S, K, Ca, Ti, Mn, Fe, Br and Rb).

4.2.5 Radiocarbon Dating

In order to establish a chronology for the gravity cores, radiocarbon dating was performed on identified shell and foraminifera material from the cores. This methodology measures the decay of ^{14}C and can be used on material younger than 50,000 years old. In the upper atmosphere ^{14}C in generated with cosmic rays collide with nitrogen atoms. After ^{14}C forms it rapidly combines with oxygen to form carbon dioxide. This carbon dioxide then mixes through the atmosphere and oceans and is eventually enters the biosphere. After an organism dies and doesn't take in anymore ^{14}C, this isotope begins to decay. Radiocarbon dating uses the known half-life of the isotope to establish an age (Bowman, 1990).

4.2.5.1 Lab Procedure

While creating a sedimentary log of for core HH17-1289-GC-TUNU several shells and shell fragments were identified (Fig. 4.4). At 34 cm a semi-spherical organic patch was identified containing two intact *Yoldiella lenticula*, a shell fragment and plant material. One of the two *Yoldiella lenticula* were collected for dating (Fig. 4.4A) and the remaining material was placed in a refrigeration unit. At 71 cm a large 3cm half of a *Hiatella arctica* shell was collected for dating from the archive half of the core. At 125 cm a bivalve shell fragment was also collected for dating.

Subsampling of cores HH17-1290-GC-TUNU and HH17-1309-GC-TUNU was performed at four positions across the two cores (two per core) to obtain datable foraminifera material. Two centimeters of material was extracted from each location and each centimeter was kept separate from one another to inspect separately. This material was sieved in 1 mm, 100 μm and 63 μm meshes and sediments recovered from the 100 μm sieve was inspected for foraminifera.

Benthic foraminifera were exclusively collected for dating purposes (Fig. 4.5). Within HH17-1309-GC-TUNU Section 4 74-76 cm (core depth 377 cm) *islandiella norcrossi* (rare to common) & *stainforthia feylingi* (rare) and a plantonic species were identified (Fig. 4.5B). A sample collected from HH17-1309-GC-TUNU from section 2 at 74-76 cm (176-178 cm down core) did not yield enough foraminifera material for dating, however an ostracod was identified in the sediment (see Appendix A). Within gravity core HH17-1290-GC-TUNU a large quantity of agglutinated samples were identified through the sediments in Section 1 96-98 (97 cm) (Appendix A). Calcareous benthic species were far fewer in number but included predominantly *Melonis barleeanus* (Fig. 4.5A) as well as a few *islandiella norcrossi*, but in much smaller quantities. A sample collected from section 4 6-8 cm (311-313 cm down core) yielded a small quantity of *cassidulina reniforme* and *islandiella norcrossi* foraminifera. The agglutinated samples found within section 1 did not seem to appear within this sample. A summary of the materials used for dating can be found below in Chapter 5: Results.

4.2.5.2 **MICADAS and Calibration**

Six samples were sent to the Mini-Carbon-Dating-System (MICADAS; Alfred-Wegener-Institut, 2019) at the Alfred Wegener Institut in Bremerhaven, Germany. As the name suggests, MICADAS is a particularly small accelerator mass spectrometer (AMS) system, using an acceleration voltage of only 200 kV (Synal et al., 2007). When using an AMS for dating, individual ions of ^{12}C, ^{13}C and ^{14}C are measured directly. These ions are accelerated in an electrostatic accelerator to a very high velocity and then pass through a magnetic field that separates the different ions, allowing them to be individually distinguished (Stuiver, 1978; Elmore & Phillips, 1987; Bradley, 2015). Five of the six submitted samples were successfully dated (the sixth did not have enough dateable material). The results were then calibrated using Calib 7.1. An estimated marine reservoir age of $\Delta R = 162$, and standard deviation of 27, was derived from choosing the four closest reference points in the Marine Reservoir Database (Håkansson, 1973; Funder, 1982).

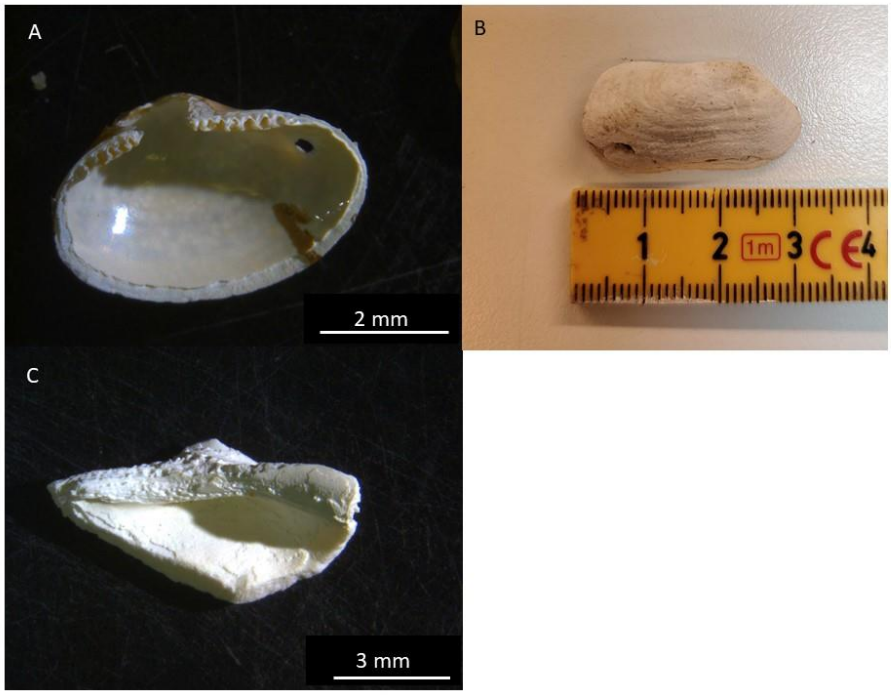

Figure 4.4 Images of shells extracted from core HH17-1289-GC-TUNU for Carbon-14 dating. A: Image of one side of the two shells from HH17- 1289-GC-TUNU at 34cm. B: Image of half of a bivalve shell collected from HH17-1289-GC-TUNU at 71 cm. C: Image of the shell fragment collected from HH17- 1289-GC-TUNU at 125 cm.

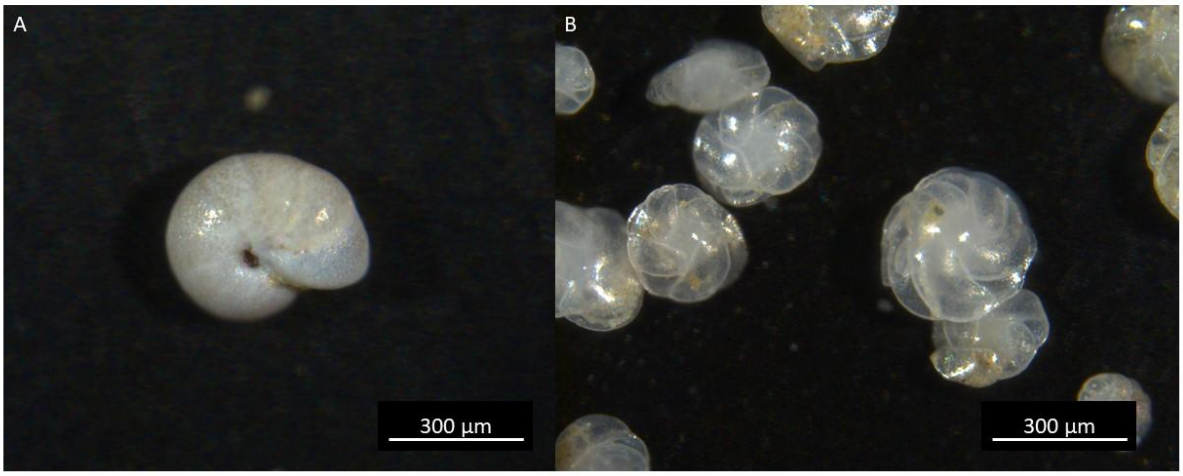

Figure 4.5 Images of foraminifera used in carbon-14 dating. A: Melonis barleanus taken from HH17-1290-section-1-96-97-GC-TUNU. B: Islandiella norcrossi collected HH17-1309-section-4-74-75cm-GC-TUNU.

4.2.6 **Sediment Grain Size Analysis**

Sediment grain size analysis was performed on 49 samples across all three cores using the Beckman Coulter LS 13 320 Multi-Wavelength Laser Diffraction Particle Size Analyzer. During analysis preparation, 4-gram sediments were sampled at a variety of localities deemed of interest for this study. The highest concentration of samples was collected from sample HH17-1309, largely in 10 cm intervals. Sample were treated in HCl (for $CaCO_3$ removal), H_2O_2 (for organic content removal) and pre-heated VWB 18 Thermal Bath. Almost every sample appeared to boil over slightly during this process, therefore it is possible that small quantities fine grained sediment was lost during this process. Following each treatment, samples were cleaned using distilled water and multiples runs through a centrifuge. Sample were then place in an oven at 26°C to remove water content. 0.2 grams of sediment were separated and placed into separate containers with 20 ml of water for later analysis. These mixtures were then placed on a shaking table for over 48 hrs.

Immediately before each sample was placed into the Beckman Coulter LS 13 320 Multi-Wavelength Laser Diffraction Particle Size Analyzer, a few drops of Calgon were added to the sample, which was placed into a Branson 200 ultrasonic cleaner for ~7 minutes. Samples were

shaken briefly prior to pouring into the particle analyzer, and then were poured over a >2 mm mesh to catch grains that were too large for the machine (i.e. a single grain was captured for core HH17-1309-GC-TUNU at 41.5 cm and 74 cm). The samples were placed into a rotating tub of water where a laser counted and measured the size of grains between 0.4µm and 2000µm. Each sample underwent three separate runs within the instrumentation. A mean of these three runs were calculated and analyzed using the GRADISTAT Excel-software. Sediment names used in this thesis are based on Folk (1954) and mean grain size from the methodology published by Folk & Ward (1957). Grain size distribution plot have been developed for samples taken from HH17-1309-GC-TUNU and can be found in Appendix B.

5 Results

5.1 Swath Bathymetry

Swath Bathymetry data from Bessel Fjord and lower Dove Bugt was used to interpret submarine geomorphological landforms (Fig. 5.1). The dataset for Bessel Fjord contains most of the fjord, excluding some areas close to Soranerbræen, near fjord walls, and the southern section of the fjord's entrance. Dove Bugt's dataset consists of bathymetric data from the western and central Store Bælt. The Dove Bugt dataset also contains an elongated strip of data, north of 76° 09' N, that will not be included in this study.

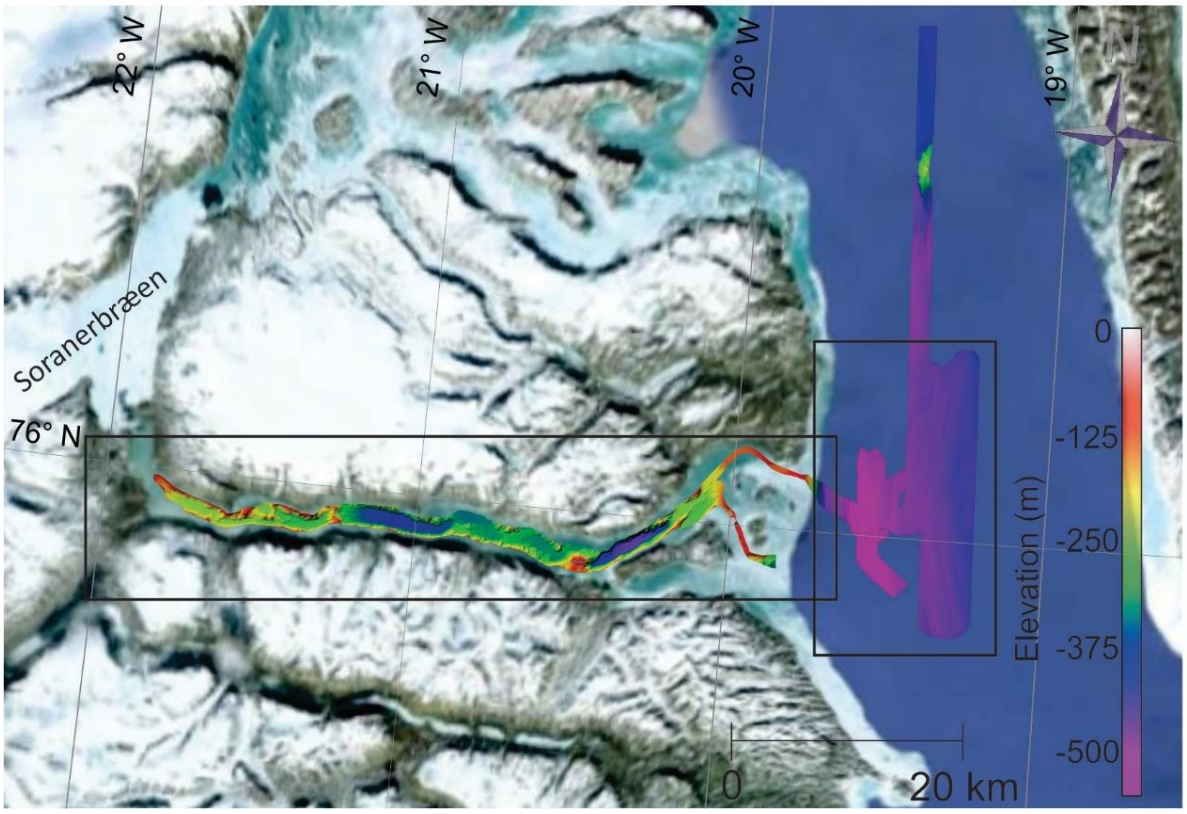

Figure 5.1. Map of Bessel Fjord and lower Dove Bugt with black boxes around bathymetric data acquired and analyzed his study.

5.1.1 Bessel Fjord

The bathymetric data collected from Bessel Fjord contains ~53 km of the fjord's seabed from west to east (Fig. 5.2; A-A') and covers two smaller areas at the fjord's mouth (Fig. 5.2; B-B' &C-C'). The width of the bathymetry data on average ranges from 1-2 km and varies as to how close the data limits gets to the flanks of the fjord. The fjord has been divided into three broad geographical regions referred to as the Inner Fjord, Mid-Fjord and Outer Fjord (Fig. 5.2C). These geographical divisions have been placed near large thresholds that transect the fjord. Below is a brief description of the fjord geometry and large-scale landforms in these regions (5.1.1.1-5.1.1.3). Smaller scale features are described in the subsequent section (5.1.1.4).

5.1.1.1 Inner Fjord

Overview

The Inner Fjord bathymetric area of Bessel Fjord comprises a region that is ~18 km long and on average 1200 to 1400 m wide (with a maximum width of ~1900 m) (Fig. 5.2). The bathymetry tends to deepen to the east, with a depth exceeding 300 m near the far eastern end of the Inner Fjord region. This area of the fjord contains numerous basins and sub-basins with a variety of styles of thresholds between them. The presence of these basins can allow the further division of the fjord into additional sections, referred to here as Section 1 and Section 2.

Section 1 (Inner Fjord)

Section 1 of the Inner Fjord region is ~11.7 km long and contains a fluctuating width (Fig. 5.3). The western most portion of this section contains a ~2 km long raised seabed that is gently dipping (average ~<1 to 6°) to the southeast. The gently dipping slope is punctuated by steep escarpment. The next ~4 km, the slope tends to decrease slightly (~<1 to 2°) in a region that remains at approximately 230 to 238 m depth. Gravity core HH17-1290-GC-TUNU has collected near the middle of this relatively flat lying area (Fig. 5.3). The eastern side of Section 1 contains >2 km long region of raised topography to the north and two small, <10 m deep sub-basins (SB1 & SB2) that are separated by a <5 m high, 600 m long section of irregular topography

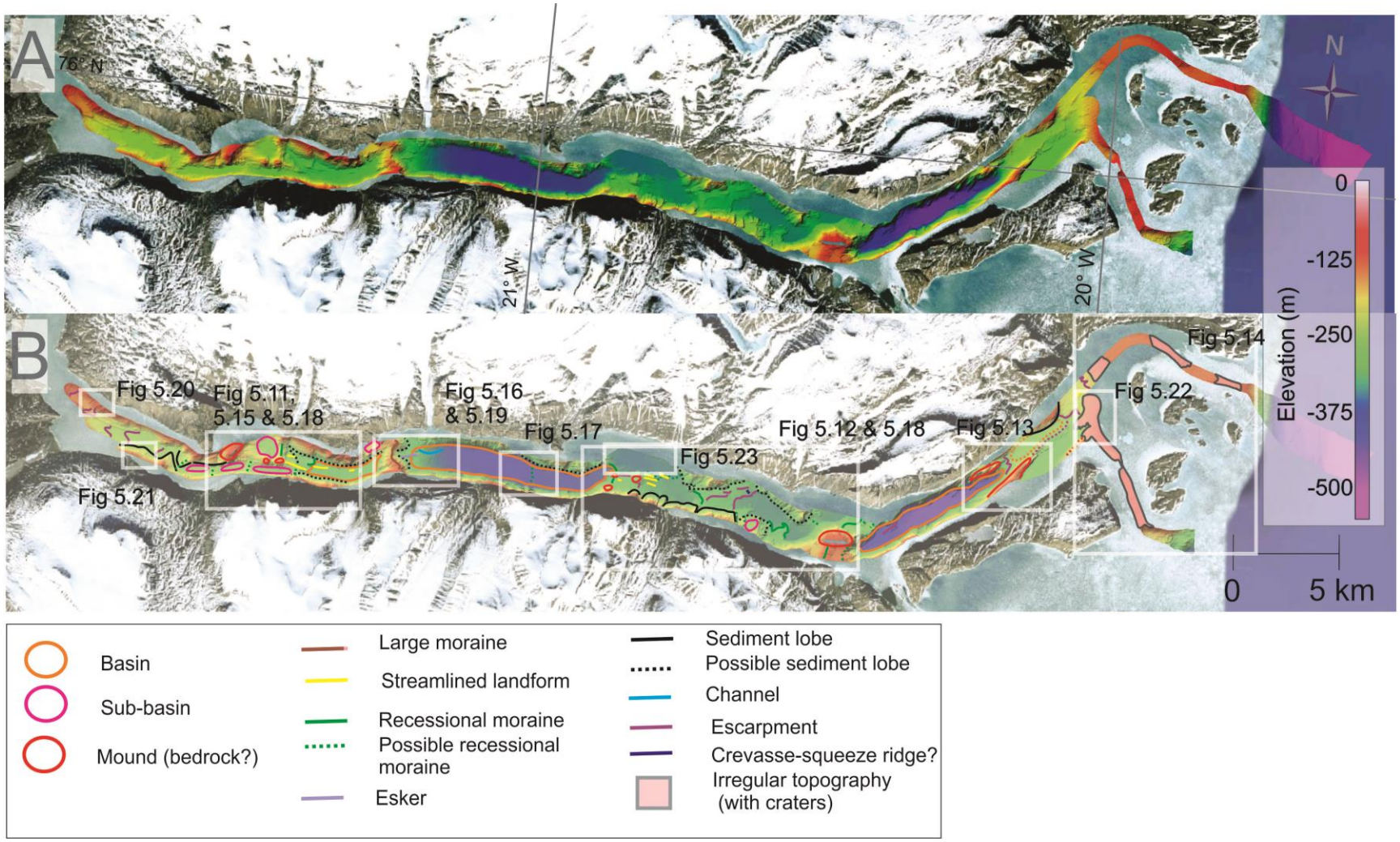

Figure 5.2. A: Bathymetric map of Bessel Fjord. B: Bathymetric map of Bessel Fjord with mapped features and boxes around figures featured later in this section.

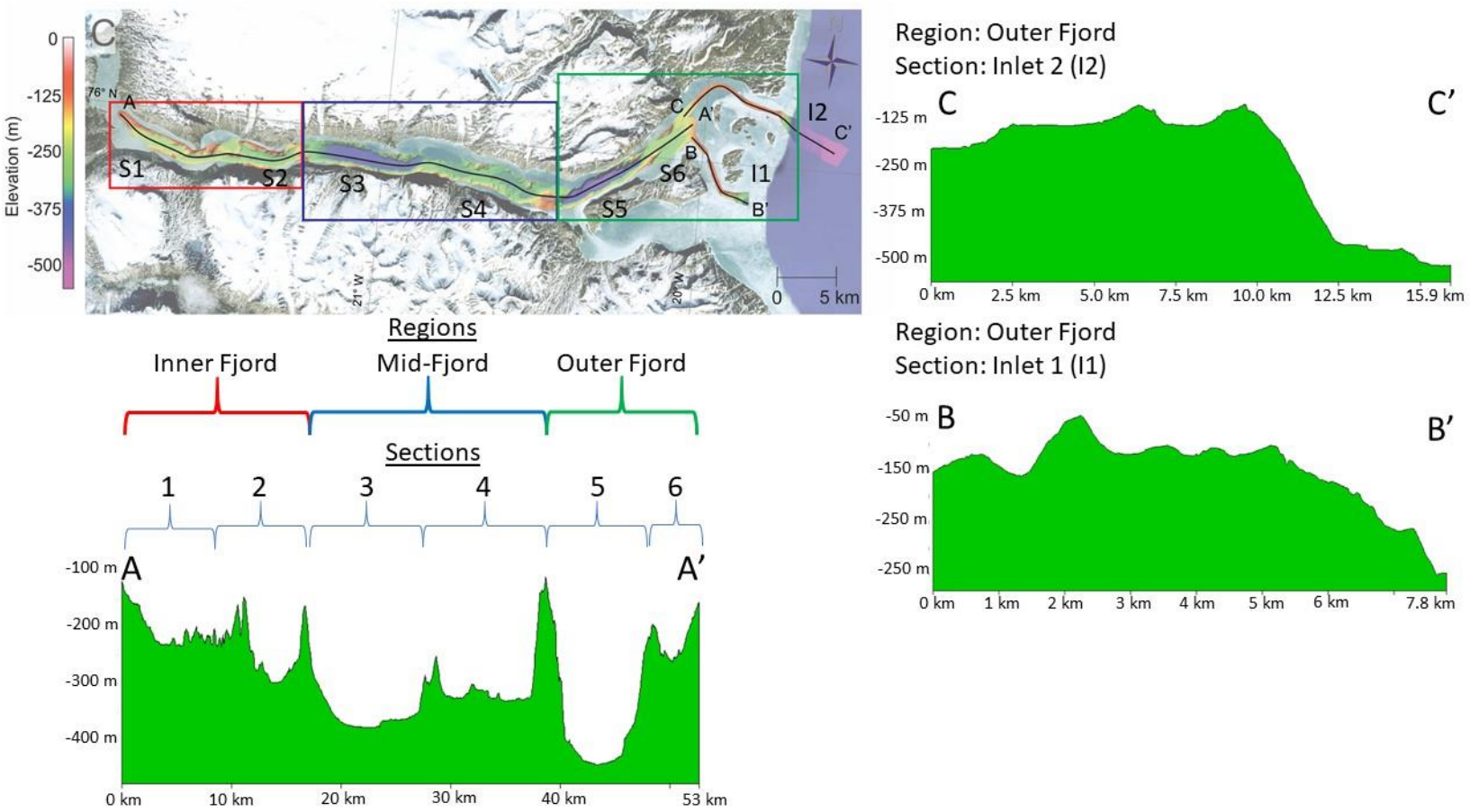

Figure 5.2 (cont.). *Bathymetric map of Bessel Fjord with geographical divisions and cross sections. A-A' is a cross section of the fjord out to the northern most point of Trums Ø, B-B' is a cross section of Inlet 1 (I1) and C-C' is a cross section of Inlet 2 (I2).*

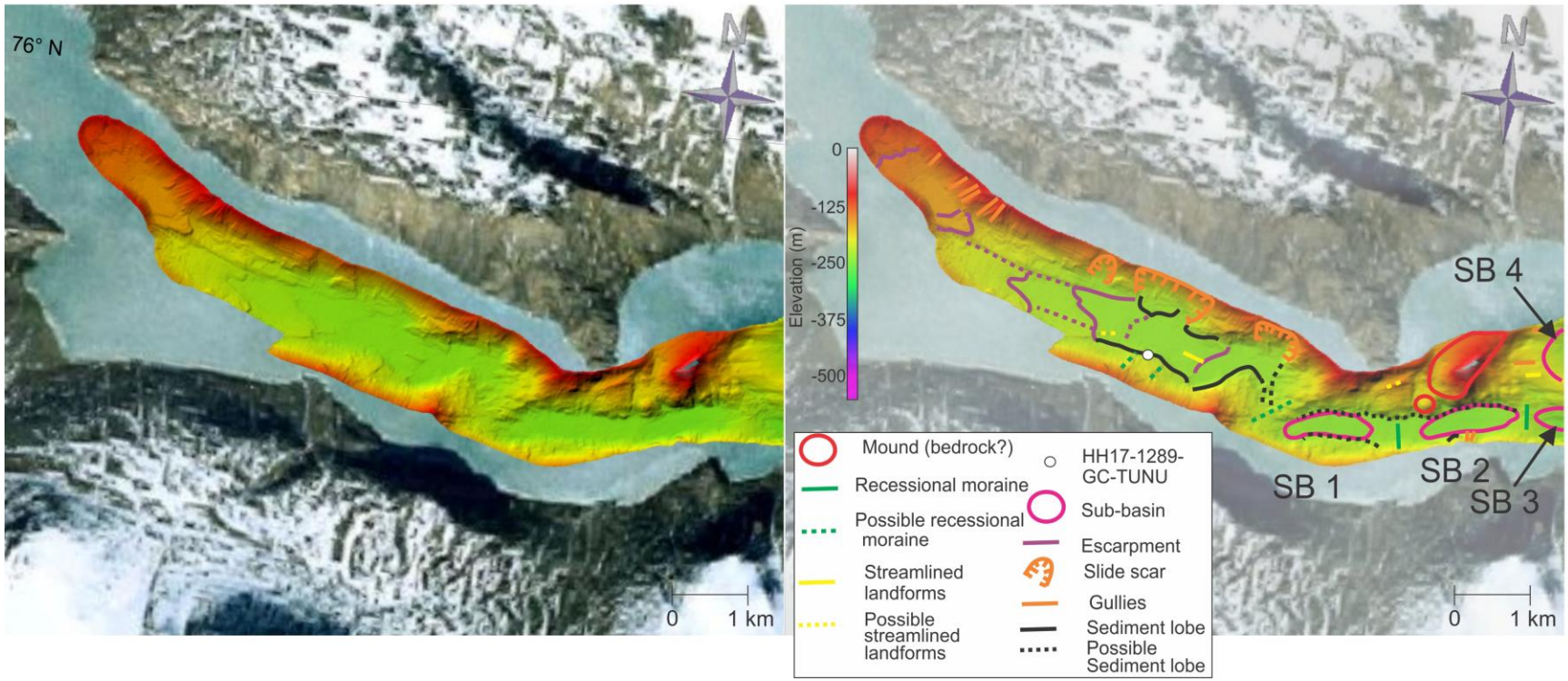

Figure 5.3 Image of the bathymetry of Section 1 of the Inner Fjord Region of Bessel Fjord. SB- Sub-basin.

Section 2 (Inner Fjord)

Section 2 of the Inner Fjord region is ~7 km long and contains two sub-basins to the west (Fig. 5.4). The southernmost sub-basin (SB3) is 320 by 1000 m and has a depth of 158 to 161 m. This sub-basin is separated from the northern most sub-basin (SB4) by a topographic barrier. SB4 is ~500 by 500 m and slightly raised relative to the southern basin (at 145-148 m depth). An ice lobe has been observed north of this sub-basin. To the east of these sub-basins is a 4.5 km long larger basin (B1) that becomes narrower to the east. Depth in this basin range between 280 to 300 m below sea level. Another smaller sub-basin (SB5) has also been identified northeast of this larger basin, sitting at a depth of 193 m below sea level

5.1.1.2 Mid-Fjord

Overview

The Mid-Fjord region of Bessel Fjord is 21.75 km long and a width that ranges from 1400 to 2000 m. Like the Inner Fjord Region, this region can be divided into two sections termed Section 3 and Section 4. The elevation tends to increase to the east in this region.

Section 3

Most of Section 3 consists of a 10.5 km long basin (B2) that is deeper than the basin to the east (~380 m in the west, increasing to 370 m ~6.5 km into the basin) (Fig. 5.5). Its width tends to get narrower in the eastern. Gravity core HH17-1289-GC-TUNU was collected within the basin, near the fjord's southern sidewall (Fig. 5.5). An ice cap lobe has also been observed to the northwest of the basin.

Section 4

Section 4 consists of an area ~11 km in length and 1.8 to 2 km in width (Fig. 5.6). In contrast to the preceding section, this region occupied a flat lying region separated by different layers of escarpment and protruding smaller bathymetric features (discussed below). The seabed is at a ~283 to 346 m depth, which is elevated compared to the previous section. To the west, the

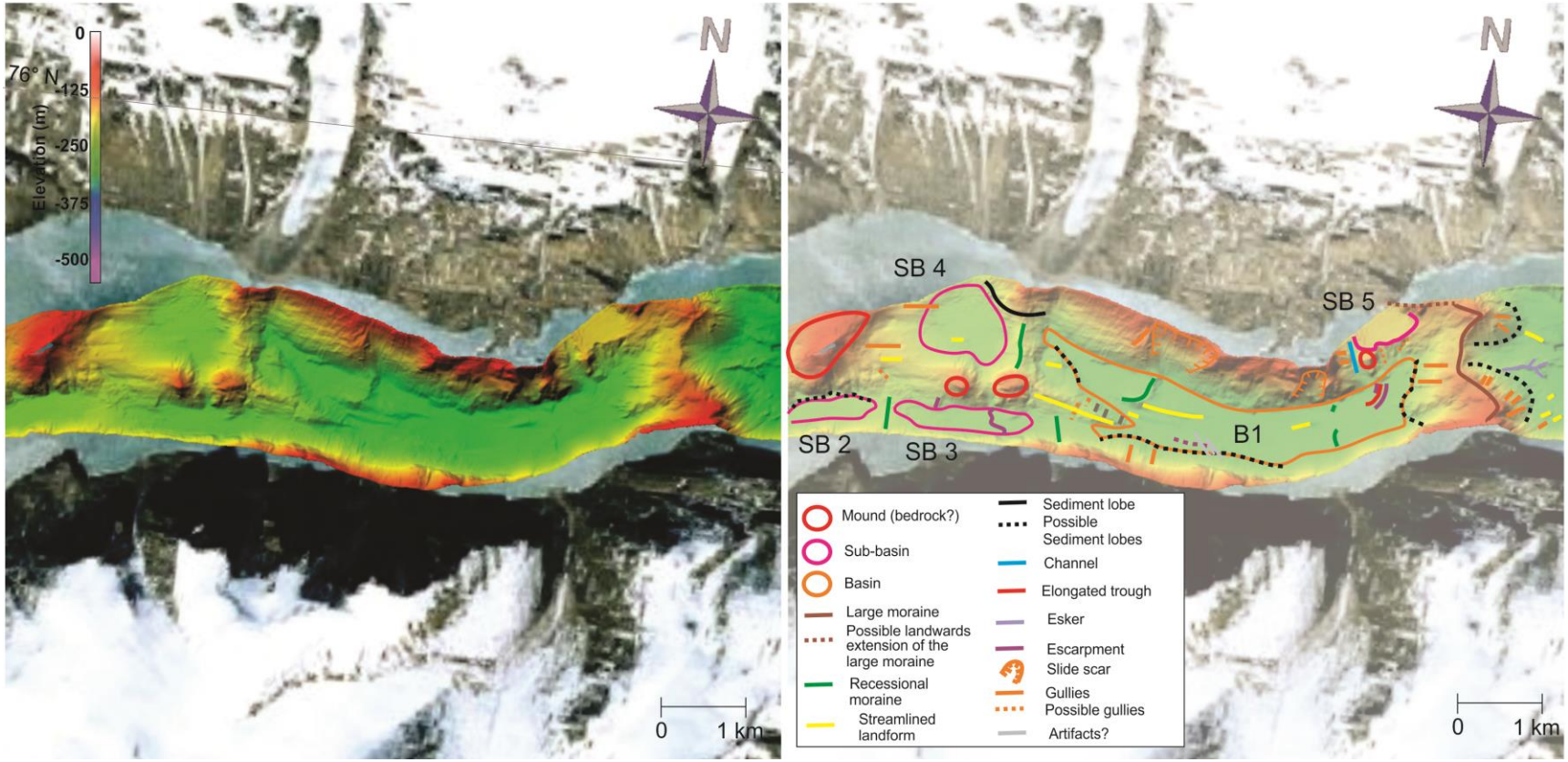

Figure 5.4. Image of the bathymetry of Section 2 of the Inner Fjord Region of Bessel Fjord. SB- Sub-basin; B- Basin.

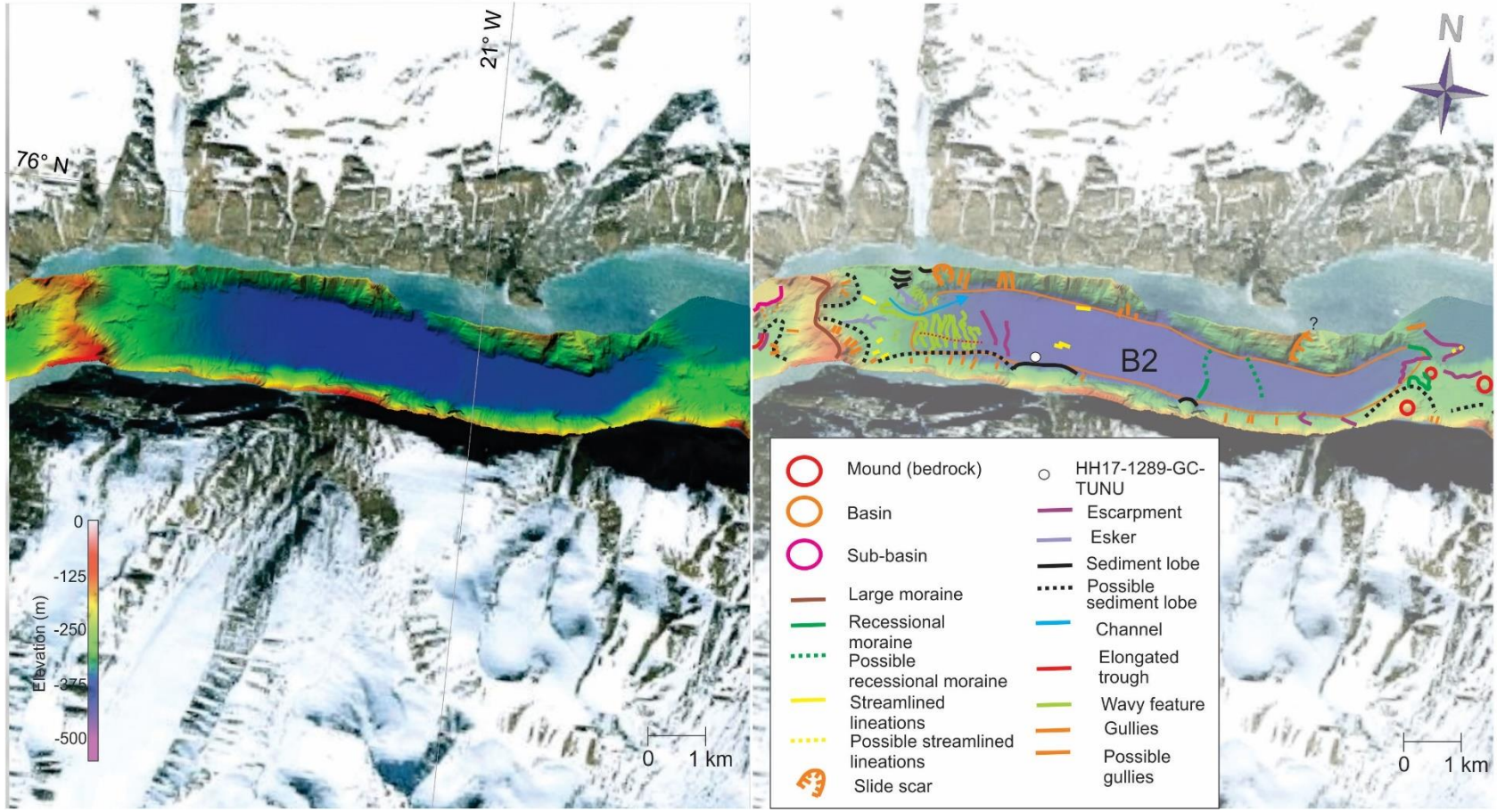

Figure 5.5. Image of the bathymetry of Section 3 of the Mid-Fjord Region of Bessel Fjord. B-Basin.

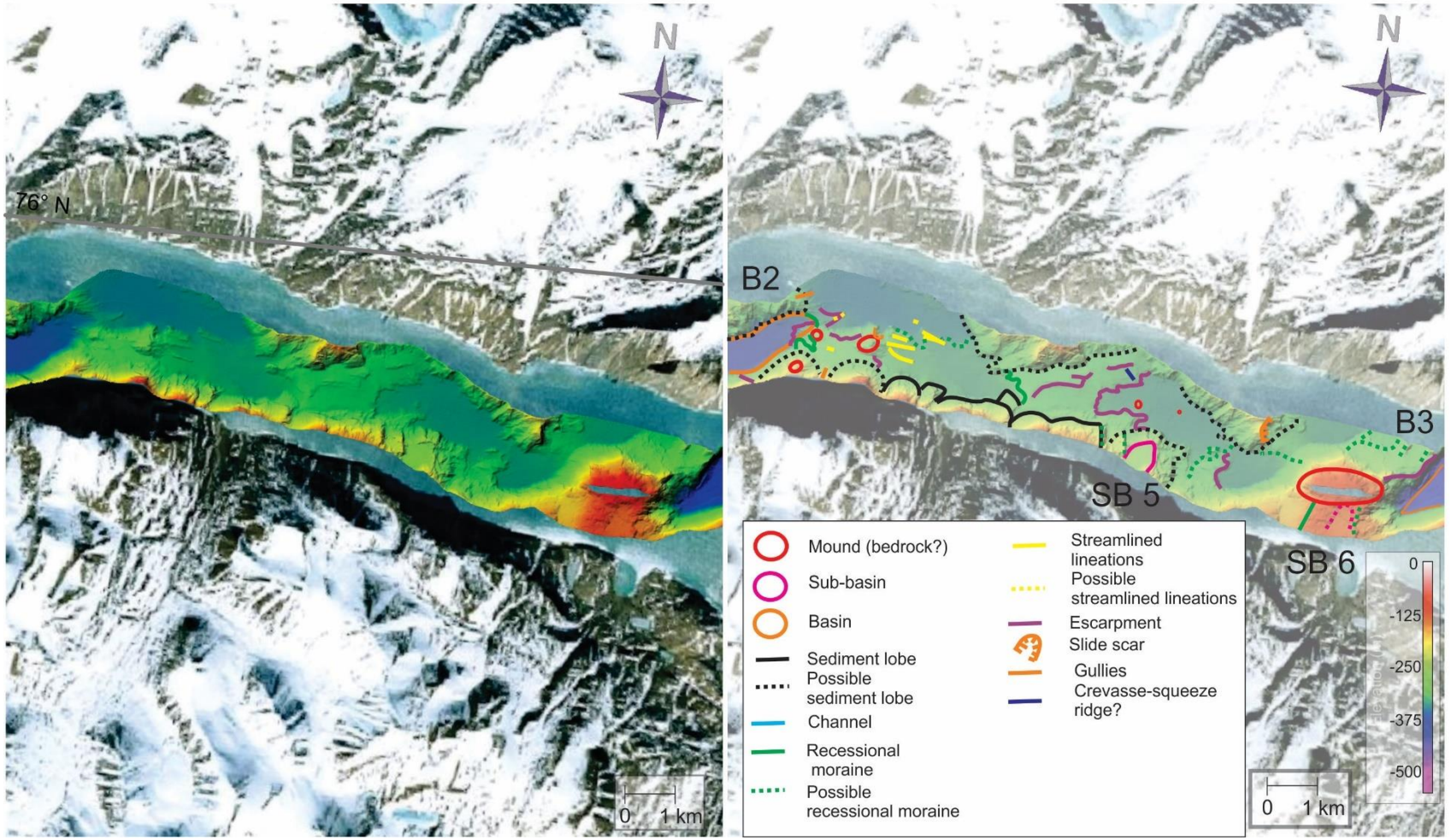

Figure 5.6. Image of the bathymetry of Section 4 of the Mid-Fjord Region of Bessel Fjord. SB- Sub-basin; B-Basin.

seafloor is raised in the south relative the surrounding regions and is dipping to the east 1 to 4°. A small, 500 by 500 m sub-basin (SB5) that is similar to SB4 has been identified along the southern wall of the fjord, on the eastern side of the section. Like the other sub-basin, it appears raised above the main seafloor, at a depth of 245 m. Unlike the other sub-basins, the surface appears to be dipping at 0.5 to 2.5° in a northerly direction. The sub-basin is surrounded by a 38 m wall to the northwest, 22 m wall to the northeast and 15 m wall to the southeast. A separate sub-basin may also present between Section 4 and Section 5 (SB6) south of a large topographic barrier, although it is difficult to determine if this should be described as a sub-basin.

5.1.1.3 Outer Fjord

Overview

The Outer Fjord region consists of a ~14 km long, 1.2 to 2 km wide segment of bathymetric data with two branching inlets to the east leading to Store Bælt. These are referred to as Inlet 1 (I1) and Inlet (I2). Like the other two regions, the western Outer Fjord region can be split into two sections referred to as Section 5 and Section 6. These sections run in a northeast direction between the fjord's wall and the island Trums Ø. Bathymetric data has also been collected between two inlets. To the southeast, Inlet 1 includes the region between Trums Ø and Grouchs Snack as well as the southern side of Grouchs Snack. This continues past the island of Stationsø and Kap Beurmann into Store Bælt.

Section 5

Section 5 contains a large basin (B3) that is ~8.3 km long and 475-1000 m wide, with the longer side oriented to the northeastern (Fig. 5.7). Depths in the basin are 440-445 m in the center of the basin, with the maximum depth reaching 449 m. The southern side of the basin is separated from the previous section by a large mound dipping at 26° into the basin. The previous section is separated by escarpment sloping at 50° eastwards into the basin.

Section 6

The area which encompasses Section 6 is a 5.5 km by ~2 km area (Fig. 5.8). The seafloor mostly consists of two relatively flat areas sitting at different elevations and separated by a topographic barrier. The northern most flat area sits at a depth of ~245 m and is surrounded by raised ridges. The ridges make this region a potential sub-basin (SB7), however since these ridges are not found in the western portion of the section, and the seafloor doesn't appear to have a "bowl" shape typical of a basin, it is difficult to determine if it should be defined in this way. The lower flat area is at 260-265 m depth and is surrounded ridges and/or escarpment. Across the entire section, the seafloor increases in elevation to the northeast where the seafloor becomes "irregular".

Inlets: I1 & I2

The bottom most inlet (Inlet 1) covers a length of ~7.8 km (Fig. 5.9). Its northern most extent reaches an elevation of ~97 m, dips down slightly to the southeast and then increases to 50 m depth at a narrow strip in the dataset. In this region of the inlet, the seafloor takes on an irregular character, similar to eastern Section 6. The seafloors elevation then decreases and increases multiple times before decreasing and sloping to the southeast into Store Bælt. Downslope numerous escarpments have been identified. The inlet to the north (Inlet 2) contains similar characteristics to Inlet 1 (Fig. 5.10). The topography tends to alternate between raised areas with irregular topography and flatter areas with less distinct geomorphological features. The slope leading into Store Bælt slopes to the east at 6° and gradually increases to a 12° slope further into Dove Bugt. The slope is highly irregular and has multiple sections that tend to slope at 10 to 22° to the northeast.

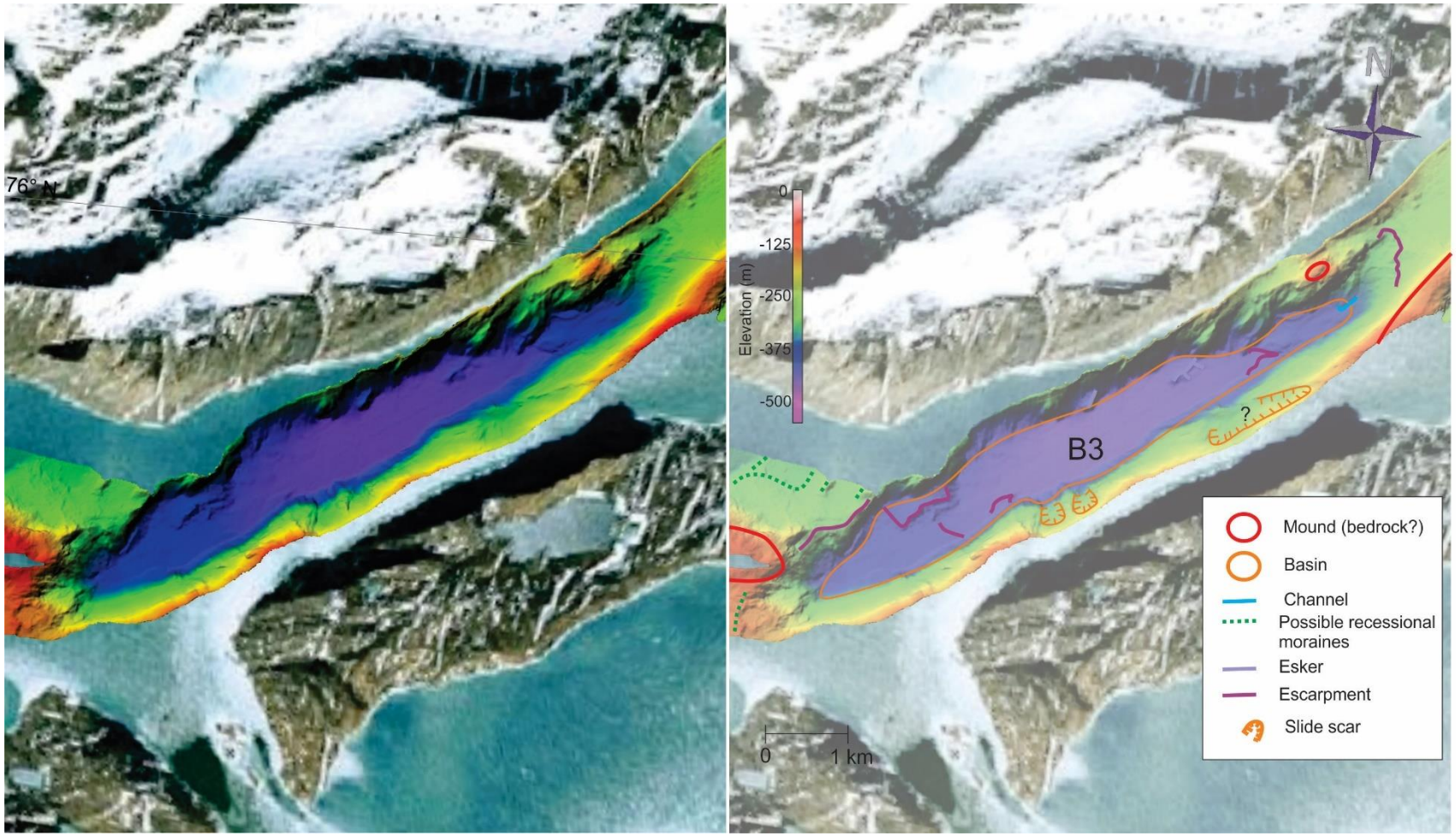

Figure 5.7. Image of the bathymetry of Section 5 of the Outer Fjord Region of Bessel Fjord. B-Basin.

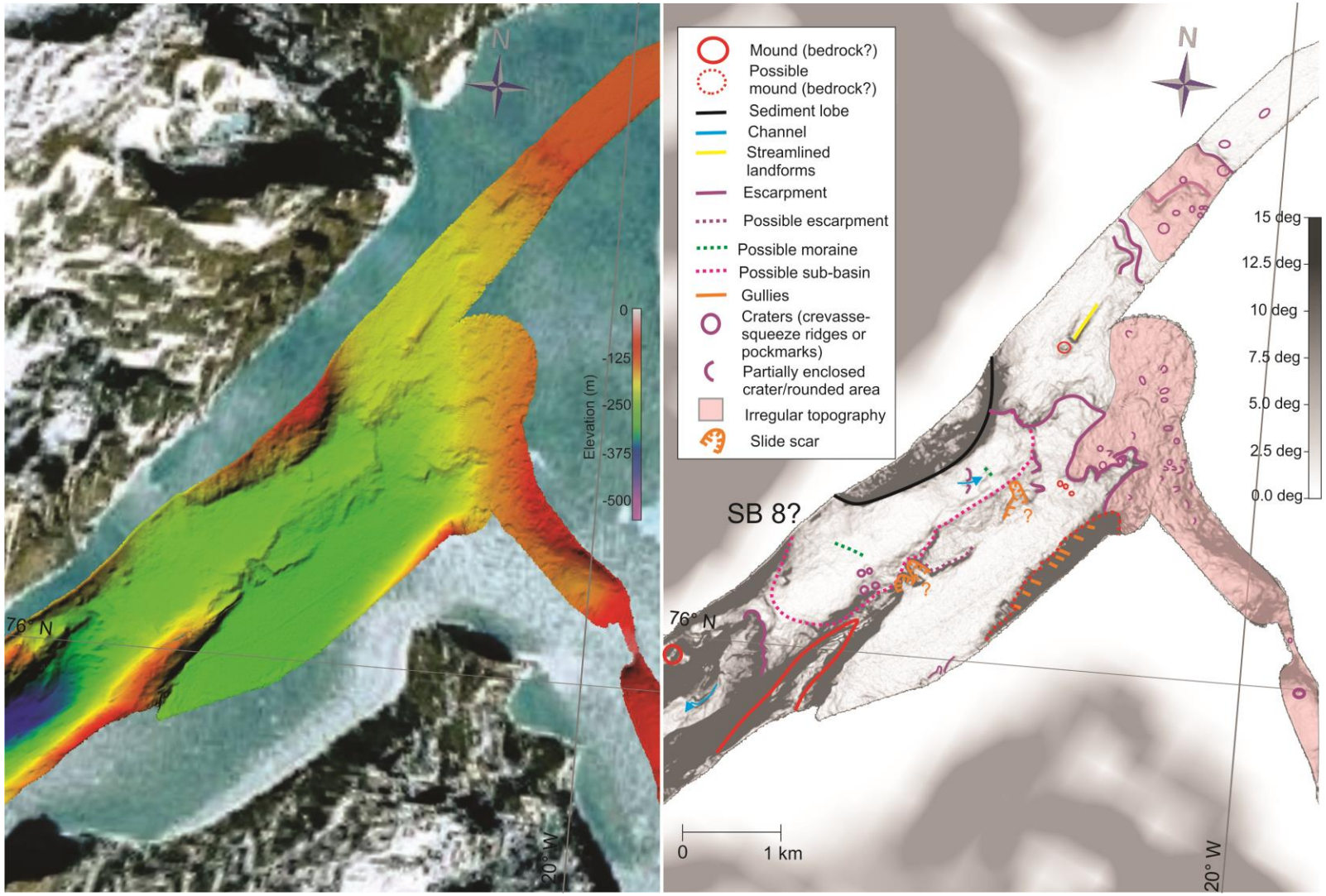

Figure 5.8. Image of the bathymetry of Section 6 of the Outer Fjord Region of Bessel Fjord. SB- Sub-basin.

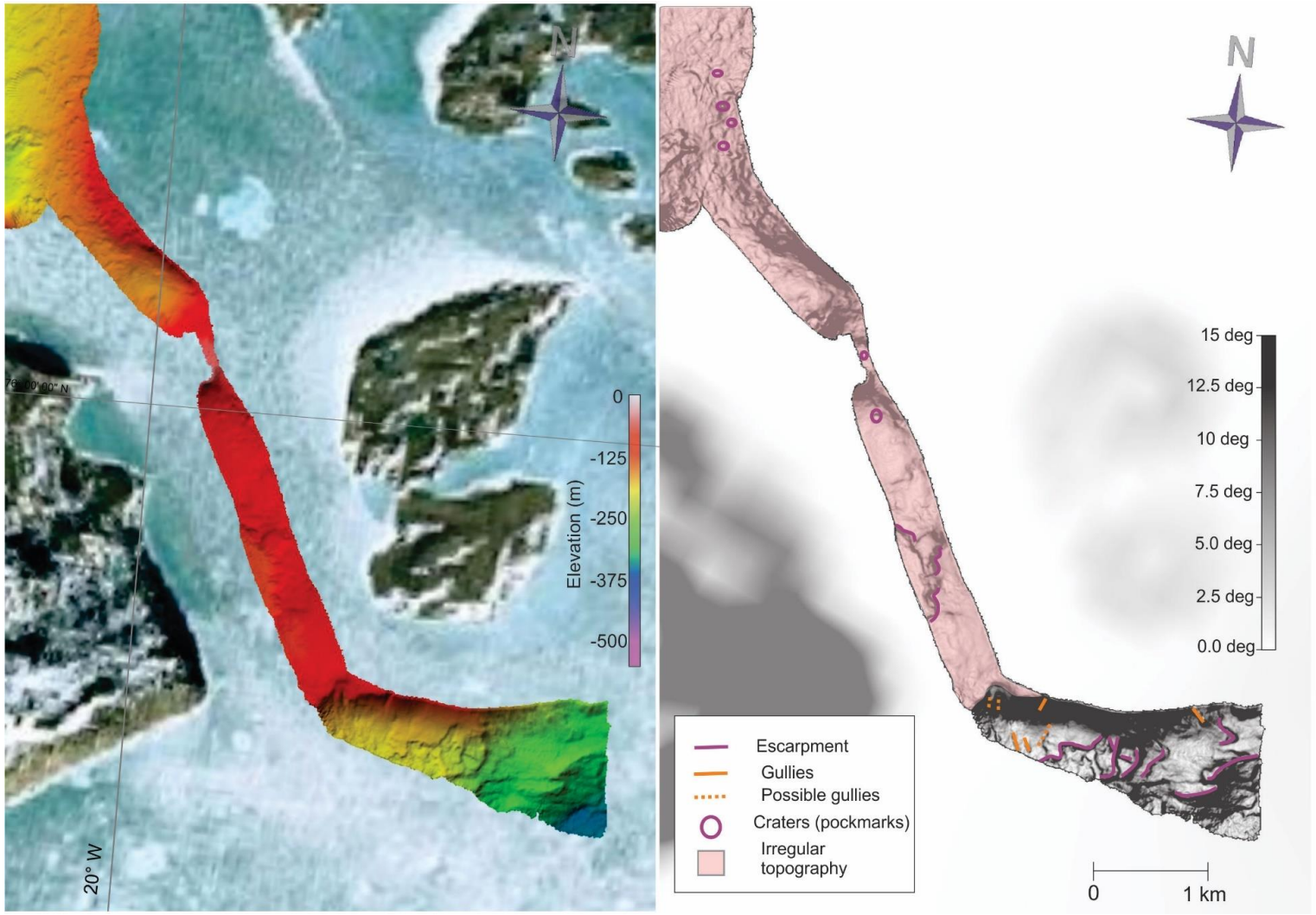

Figure 5.9. Image of the bathymetry of Inlet 1 of the Outer Fjord Region of Bessel Fjord.

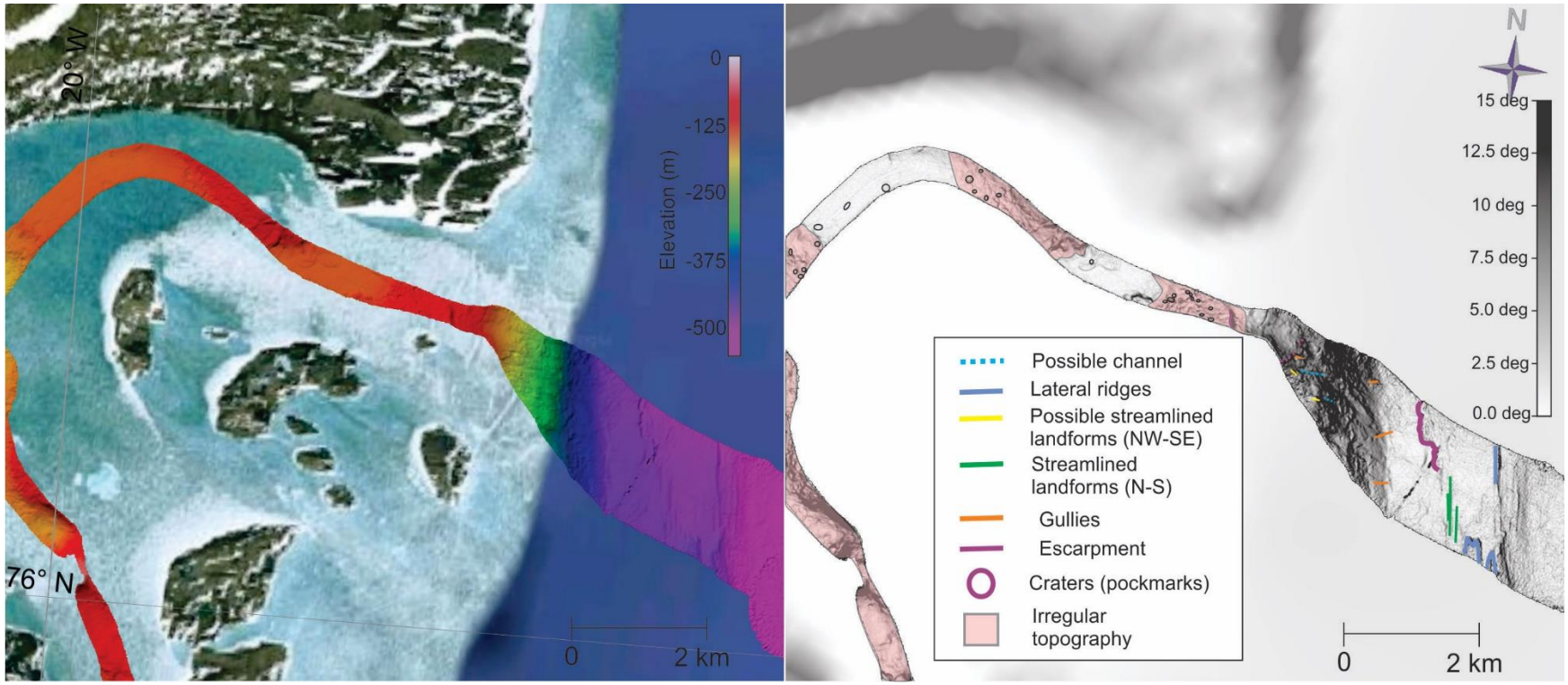

Figure 5.10. Image of the bathymetry of Inlet 2 of the Outer Fjord Region of Bessel Fjord.

5.1.1.4 Landform Description and Interpretation: Bessel Fjord

The following is a description of each observed landform in Bessel Fjord and southern Dove Bugt. Please see Table 5.1 for a full list of all the observed and discussed landforms.

Mounds- Bedrock

Mounds of varying sizes have been identified within the Inner Fjord, Mid-Fjord and Outer Fjord regions of Bessel Fjord. These features are frequently observed near other mounds and are, at time, near thresholds between basins. In western Section 2, three mounds have been identified near the two previously discussed sub-basins (SB3 & SB4) (Fig. 5.11). The western most mound (M1) is the largest of the three, measuring ~750 by 1175 m, with the elongated side oriented in a NE-SW direction. Viewed along the fjord's axis, the mound appears relatively symmetrical, although the NW side of the peak has the steepest slope. The two smaller mounds (M2 & M3) measure roughly 500 by 500 m in length and have a symmetrical slope viewed along the fjord's axis and slopes that range from ~13 to 20° on both sides.

In southwestern Section 4, several mounds which surround a section of raised topography (M4; Fig. 5.12). A significantly larger mound, > 215 m in height, has been identified in the eastern side of the section, acting as a threshold between Section 4 & 5 (M5; Fig. 5.12). The width of this larger mound near its base is ~1 by 1.8 km and contains a sub-basin like feature to the south (SB6). Within the Outer Fjord region, at the end of Section 5 and leading halfway through Section 6 are two elongated mounds orientated in a roughly parallel direction (M6 & M7; Fig. 5.13). M6 is on the northern sidewall of Section 5, with a height of ~200 m and a width of ~0.5 by 2 km. M7 is partially outside of the bathymetric dataset, but the sections that are within it have a maximum height of 250 m and are 0.5 by 2.8 km. This mound is to the southeast of M6 and protrudes into Section 6. A third mound was identified in Section 6 (M8), however given its orientation and position near a stream it was theorized as being a different geomorphic feature (Fig. 5.8).

Additionally, between the two inlets various mounds have been identified on top of a region of raised topography (Fig. 5.14). In Inlet 2, a nearly 2 km wide, >60 m high mound sits apart from a

Table 5.1. List of the landforms observed in Bessel Fjord and southern Dove Bugt.

Region	Description	Width	Length	Height	Notable Feature	Interpretation
Bessel Fjord	Mounds	1.5-2 km	500->750 m	60 m	Diverse morphology	Multiple possible origins: bedrock, medial moraine, etc
	Transverse ridges	150-600 m	120- 500 m	<5-58 m	Perpendicular to the fjords axis	Recessional moraines
	**large ridge*	1485 m	600-1600 m	72 to 162 m		Large recessional moraine
	**Oblique ridge*	83 m	200 m	7 m	Not parallel or perpendicular to the fjord axis	Crevasse-fill ridge
	Linear ridge	45-350 m	100-1000 m	3-9, 80 m	Parallel to the fjords axis	Streamlined landforms
	Sinuous ridges	50-120 m	350-800 m	10-15 m		Esker
	Wavy transverse ridges	400-700 m	~45-100 m	2-5 m	Perpendicular to the fjords axis	Sediment wave
	Elongated depression	~200 m	~1 km	6-8 m		Channels
	Chute	~20-100 m	60-400 m	1-15 m		Gullies
	Lobes	~ 1km	~500 m	~100-240 m	Diverse morphology	Sediment lobes
	Rounded depressions	55 m	50 m	2 m		Crevasse squeeze ridges or pockmarks
Dove Bugt	Elongated lineations	35-50 m	~1->10 km	<1-3 m	Roughly N-S	Large streamlined landforms
	**Wide*	200-650 m	3.8 to 8.8. km	4.5-15 m		
	Furrows (scour marks)	~40-100 m	<100-200	3-5 m	Irregular	Iceberg plough marks
	Depression and mound	200 m	450 m	3-4 m	Mound to the south of the depression	Hill-hole pair
	Transverse ridges (?)	150-400 m	~30-100 m	0.5-1 m	Possible artifact?	Recessional moraines
	Ridges near fjord enterance	30-50 m	>500 m	~3-10 m	Mostly outside of the dataset	Lateral moraines
	Large transverse ridge	~900 m	>2.5 km	7 m		Raised bedrock

1500 wide mound that also stands at >60 m. Although both features appear to be fanning outwards, the western most mound happens to be sloping 7-9 ° to the southeast where the eastern most mound is sloping 5-6 ° to the north, northeast. Further south. the mounds in Inlet 1 appear to be sloping in a southwestern direction, other than a single region of raised topography that sits above 50 m water depth. This section of the sea floor happens to be dipping towards the northeast.

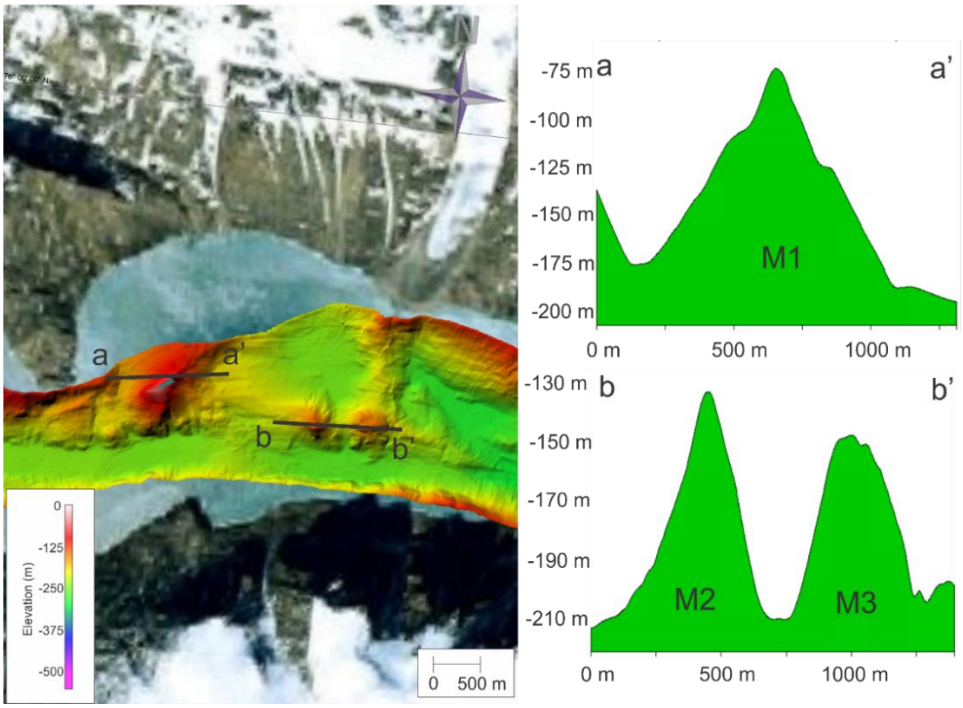

Figure 5.11. Bathymetric image and cross sections of mounds in Section 2 of the Inner Fjord. M- mound.

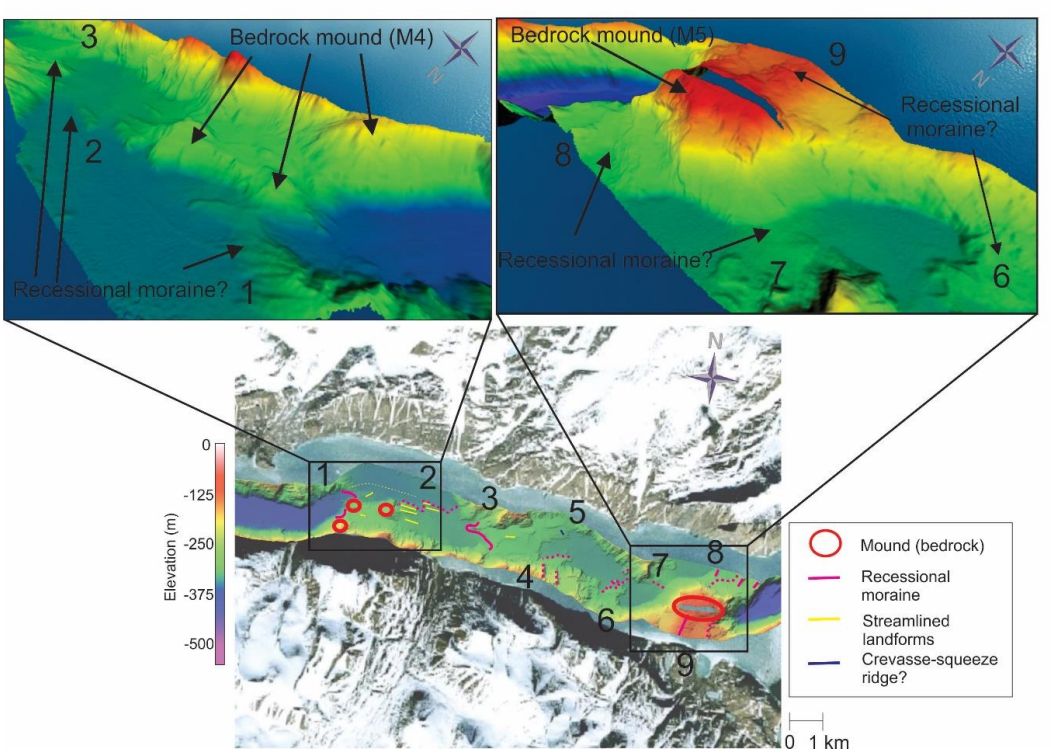

Figure 5.12. 2D and 3D bathymetric images of mounds and transverse ridges in Section 4. Recessional moraines are numbered 1-9. M- mound.

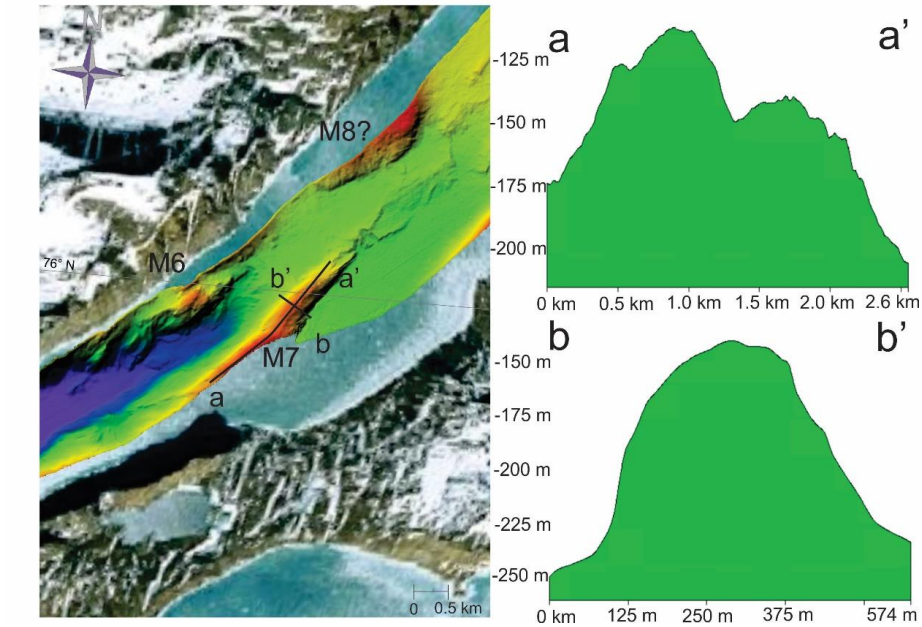

Figure 5.13. 2D and 3D bathymetric images of an elongated mound between Section 5 and 6 in the Outer Fjord Region. M- mound.

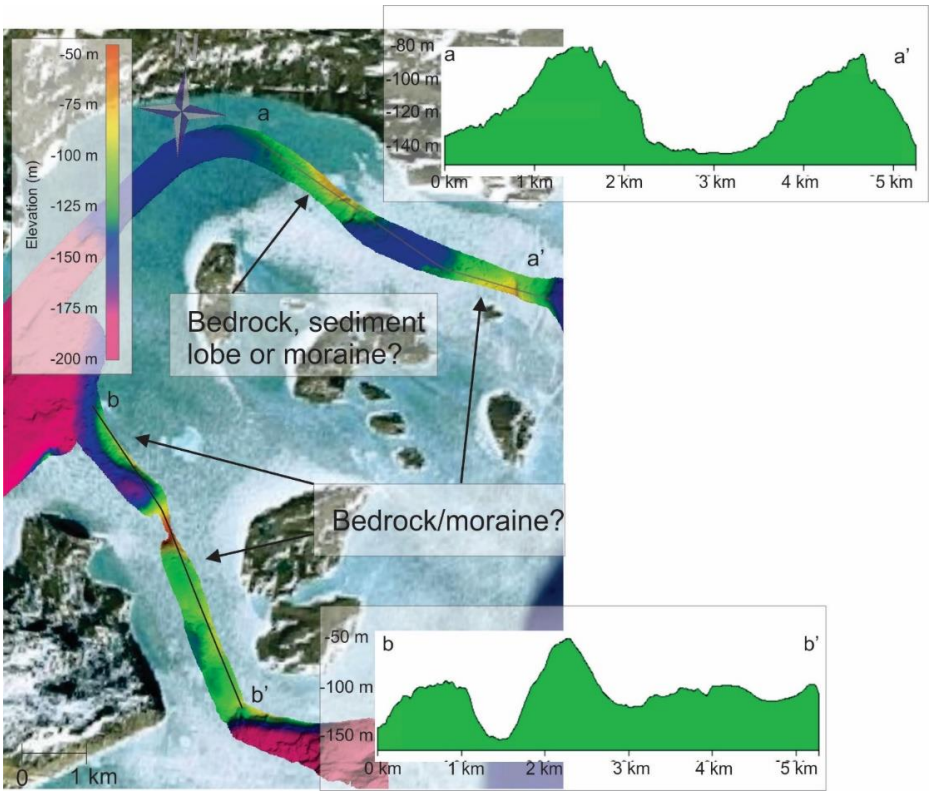

Figure 5.14. Bathymetric image and cross sections of Inlet 1 and Inlet 2.

Interpretation: Large mounds have been interpreted as being (mostly) bedrock material. This interpretation has been proposed based on their geometry, irregular topography and their positions near sub-basins and flat lying areas of different elevations. This suggests that glacial ice may have moved around these features as topographic barriers. Alternatively, given the position of M2 and M3 in Section 2 near the outlet of an ice cap, it is possible that these features represent ice proximal deposits (IPD) as outlined in Dowdeswell et al. (2015). This seems less likely, however, given the geometry of these features and surrounding seafloor topography. The elongated mounds in the Outer Fjord have been interpreted as bedrock that may have been impacted more heavily by glacial erosion. However, given the position of the southernmost mound (OFM2) between two flat regions of seafloor of different elevations, this feature may have also acted as a topographic barrier for grounded ice. Conversely, this southernmost

elongated mound could be a medial moraine separating two different ice bodies (see Discussion) (Dowdeswell et al., 2016c; Ottesen et al., 2017).

The raised topography between the inlets is interpreted as a sill, which is a common feature in fjords. The mounds sitting on top of the sill are interpreted as either being bedrock, sediment lobes or moraines (see below). The SW dipping mounds in Inlet 1 and the NNE dipping mounds in Inlet 2 suggest that there is a larger feature between these two inlets. Without the analysis of chirp data, it is hard to say if it's bedrock and/or a moraine, however the appearance of irregular topography on these mounds may suggest that there is soft sediment on these features (see below). The higher mound sloping to the NE in Inlet 1 is likely a separate feature but could be connected to this feature in the middle of these islands. The northern most feature, sloping to the southwest is interpreted as being a sediment lobe, but may also be bedrock or moraine material. With limited visibility in the area it is difficult to say anything about these features conclusively.

Transverse Ridges- Recessional Moraines

Description: Between Sections 2 and 4, transverse ridges have been observed oriented perpendicular to the fjord's axis. In Section 2 smaller ridges often conform to the topography (i.e. between bedrock mounds and the fjord's sidewall; S2TR1, S2TR2, S2TR4; Fig. 5.15). The ridge denoted as "S2TR4" in Fig. 5.15 is the largest of these, with a width of 600 m and a height of ~58 m. In Basin 1, substantially smaller ridges have also been identified (Fig. 5.15). Between Section 2 and 3 is a much larger transverse ridge that occupies nearly the entire width of the fjord, at 1485 m across (S2TR7; Figs. 5.15 & 5.16). An aerial view of this feature shows that the ridge is crescent shaped, concave towards the mouth of the fjord, and has raised topography on the northern and southern ends of the ridge. Because of these uneven ridges, and differences in seafloor elevation on either side, the height of the ridge varies, ranging from 72 to 162 m. The width of the ridge ranges from 600 m in the center to a 1 to 1.6 km on the flanks. The ridge slopes to the east at 10 to 19° in the north, 7 to 18° in the center and 23 to 30° in the south, as well as 6 to 12°, 3 to 18° and 5 to 9° to the west, respectively. The ridge is also largely asymmetrical and nearly 22.5 km from the present-day ice margin. Mid-Section 3 a substantially

smaller transverse ridge occupies the width of the basin (Fig. 5.17). This 200-250 m wide ridge has a height of 7 to 13 m and a steeper ice-proximal side.

Some transverse ridges in Section 4 appear to have a slightly different geometry than those identified in Section 2 (Fig. 5.12). Here, they range in height from 10 to 35 m, and the topography is raised to the east (Fig. 5.15; 1, 3, 4, 8 & 9). An example of one of these ridges is "1" in Fig. 5.12, which is 10-15 m in height, 350 to 650 m wide, and separates Basin 2 from an area of raised topography. The slope of this feature appears to be steeper on the ice proximal size. Some ridges here are similar to those identified in Section 2 (Fig. 5.12; 6 & 7). A single obliquely oriented ridge has also been identified in this section (Fig. 5.12; 5).

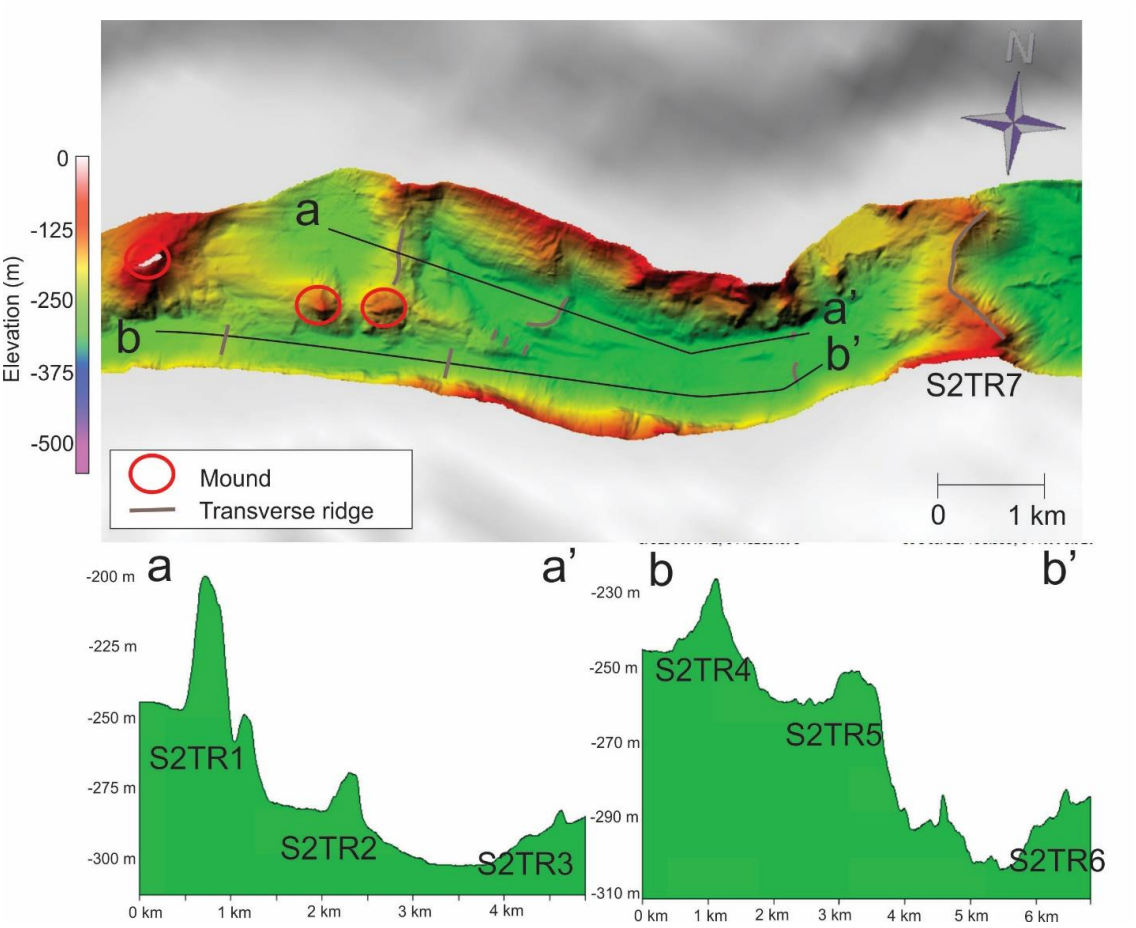

Figure 5.15. Bathymetric image and cross section across multiple transverse ridges in Section 2. S2TR- section 2 transverse ridge.

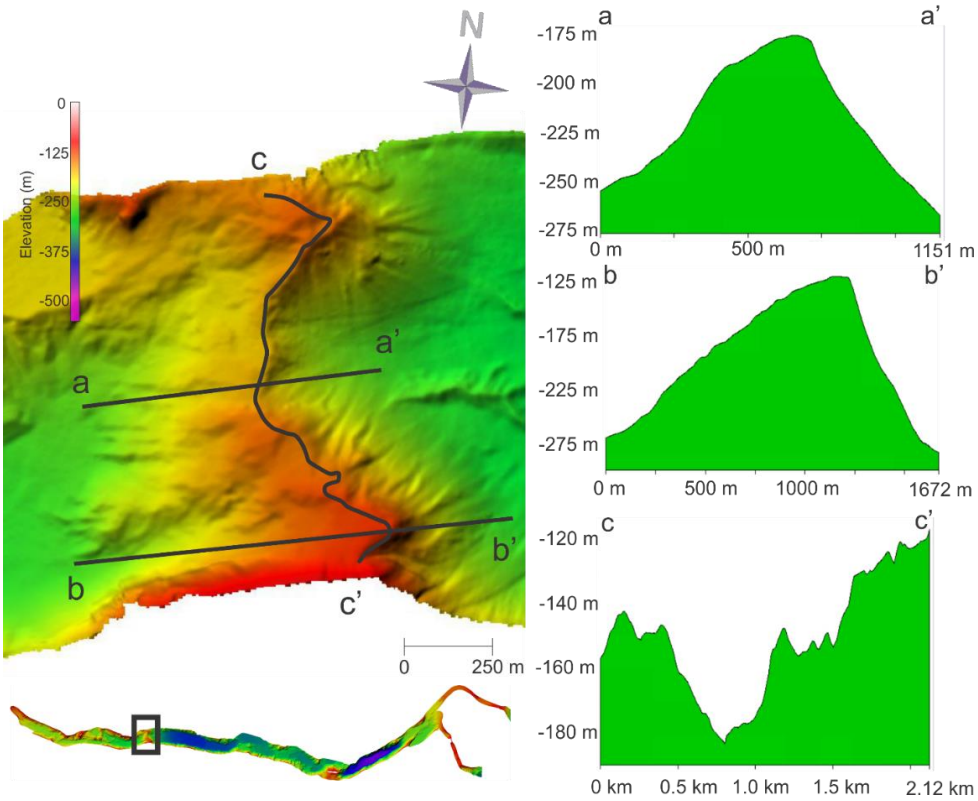

Figure 5.16. Bathymetric image and cross sections of the transverse ridge between Section 2 and Section 3.

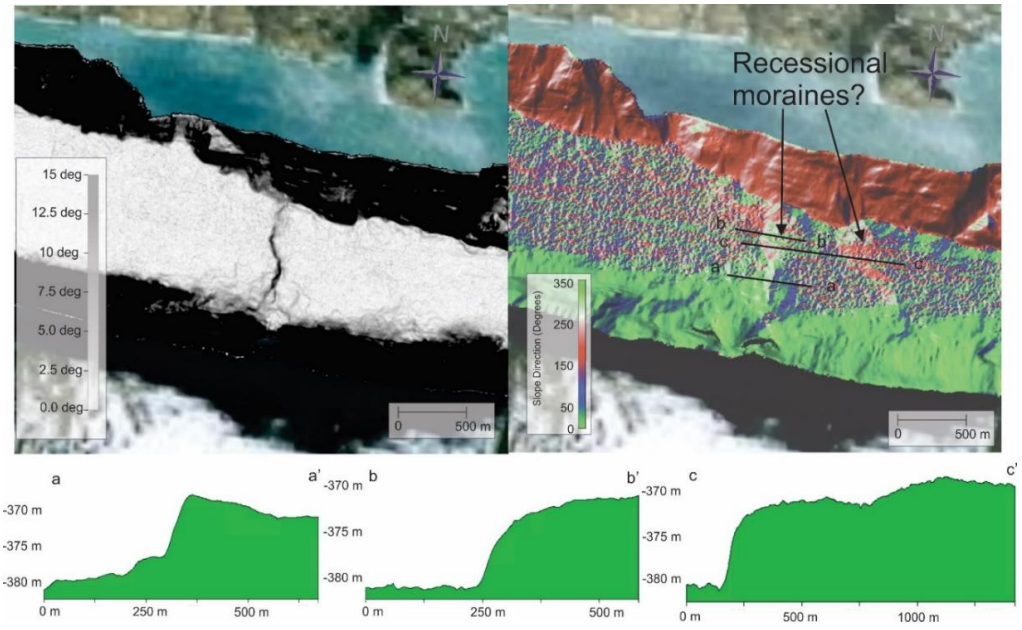

Figure 5.17.2D bathymetric image and cross section of escarpment and a transverse ridge in Section 3. See Figure 5.2 for images position in Bessel Fjord.

Interpretation: Transverse ridges have been interpreted as recessional moraines. Recessional moraines form during glacial stillstands or readvancements during the retreat of a grounded tidewater glaciers margin. These features cannot be built with a floating ice shelf beyond the grounding zone and are heavily influenced by topographic variations (e.g. topographic shallow areas have reduced water depth and buoyancy at the glacial margin, where lateral topographic variations can cause constrictions and back-stress which slows down ice recession). Small transverse ridges can often form at ice margins, sometimes annually, and have the potential to have minor readvancements in the winter (Dowdeswell et al., 2016). Submarine transverse ridges have been observed around the world and have been identified in a variety of sizes and morphologies (e.g. Winkelmann et al., 2010). The particularly large transverse ridge identified between Section 2 and 3 is also interpreted as a recessional moraine, although, it is interpreted as formed during a major ice readvancement. Large moraine ridges have been identified in other Greenlandic fjords (e.g. Dowdeswell et al., 2014; Batchelor, et al. 2018) as well as large Greenlandic moraines with steeper ice distal sides (Batchelor et al., 2019). Based on bathymetric data alone, it is difficult to determine if this moraine is entirely composed of glacimarine deposits (from over- and underflows) (Hambrey, 1994) and/or bedrock material.

Less likely, but alternatively, some of these features may be crevasse-squeeze ridge (Evans & Rea, 1999; Rea & Evans, 2011; Klages et al., 2013). These features are typically aligned perpendicular to ice flow (or an oblique angle) and are believed to result from the squeezing of basal till into subglacial crevasses during stagnation of the overlying ice (Rea & Evans, 2011; Klages et al., 2013). Heights range from 1-3 m, crevasse-squeeze ridges as tall as 12 m have been seen in marine environments (Rea & Evans, 2011). They have also been seen in/nearby fjord environments with varied geometries (e.g. Ottesen & Dowdeswell, 2006; Ottesen et al., 2008). In Bessel Fjord, the oblique transverse ridge labelled “5” (Fig. 5.2) in Section 4 appears to resemble a crevasse-squeeze ridge more than the other features.

Linear Ridges Oriented Along Fjord Axis- Streamlined landforms

Description: Linear features, oriented along the fjord’s axis (or slightly oblique to it) have been identified across the entirety of Bessel Fjord (Fig. 5.18). Their sizes range from 100 to 1000 m in

length and ~3 to 9 m in height, although some identified in Section 2 are as high are 80 m. Length to width ratios range from 2:1 to 5:1 and their morphology tends to vary (e.g. the profiles in Fig. 5.18). Most tend to be sloping towards the Outer Fjord, although they appear to also slope in the opposite direction or have an irregular/flat top. Their morphology in horizontal profile can range from highly irregular to a semi-smooth, rounded ridge. They have been identified both independently and in clusters and are frequently found in basins and flat lying areas.

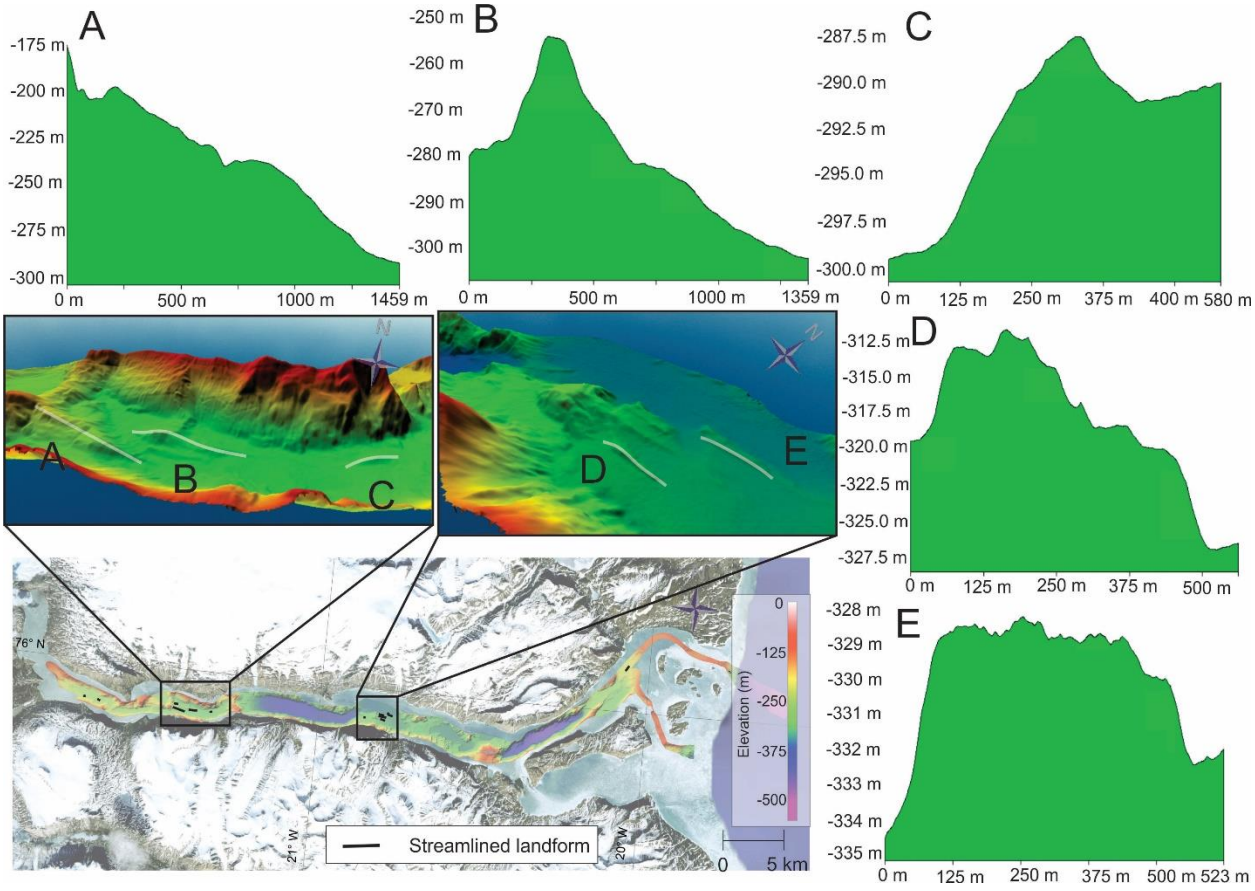

Figure 5.18. 2D and 3D bathymetric images, and corresponding cross sections, of linear ridges identified across Bessel Fjord. Note: all cross-sections were taken west to east.

Interpretation: These features have been interpreted as streamlined landforms. This is a collective term used to describe landforms that developed subglacially in deformable sediment substrate or glacially carved bedrock (Dowdeswell et al., 2004; Rydningen et al., 2013;

Krabbendam et al., 2016). The orientation of these bedforms is typically indicative of the direction of past glacial flow (Dowdeswell & Vásquez, 2013). Specifying what type of streamlined landforms are in Bessel Fjord is a bit more problematic due to the irregularity and diversity of their morphology. The development of a crag-and-tail feature requires a resistant crag and a tail composed of softer sediment (Dowdeswell et al., 2016a; Shaw & Potter, 2016). It is possible that crag-and-tail features are present (e.g. Fig. 5.18; lineation A and the lineation above D are both to the east of a resistant bedrock material) however they would be isolated landforms. The width to length ratio of these lineations are smaller than mega glacial lineations observed in fjords and other environments (e.g. Ottesen et al., 2008; Spagnolo et al., 2014) and these features also do not appear to fit the dimensions or morphology of typical drumlins (Clark et al., 2009; Spagnolo et al., 2010). Nonetheless, the do have implications as to the dynamics of ice flowing through Bessel Fjord.

Sinuous Ridges- Eskers

Description: Sinuous ridges have been identified in Section 3 and 5 (e.g. Fig. 5.19). They are generally oriented parallel (or oblique) to the fjord axis, dipping to the east, however a sinuous ridge has also been identified dipping to the west in Section 5. Two pronounced examples of these ridges can be found in Section 3, to the east of a large transverse ridge previously interpreted as a recessional moraine (Fig. 5.19). The most western ridge dips at 5 to 8° to the east and covers a length of approximately 800 m. Its branching ridges are approximately 10 to 15 m high and 50 to 100 m across. The most eastern ridge dips at 5 to 10° to the southeast and is approximately 10 m or less high and 50 to 120 m wide.

Interpretation: These sinuous rides have been interpreted as eskers. Eskers form by sediment infilling of subglacial and englacial conduits. They tend to appear in the direction of former ice flow and generally form during terminal stages of glaciations and are therefore commonly associated with moraines (Shreve, 1985). They vary in size based on the glacial systems drainage pattern, as well as a variety of other factors, however the eskers identified in Bessel Fjord appear substantially smaller than those identified in other studies (Shreve, 1985; Ottesen et al., 2008; Forwick et al., 2016; Storrar et al., 2020).

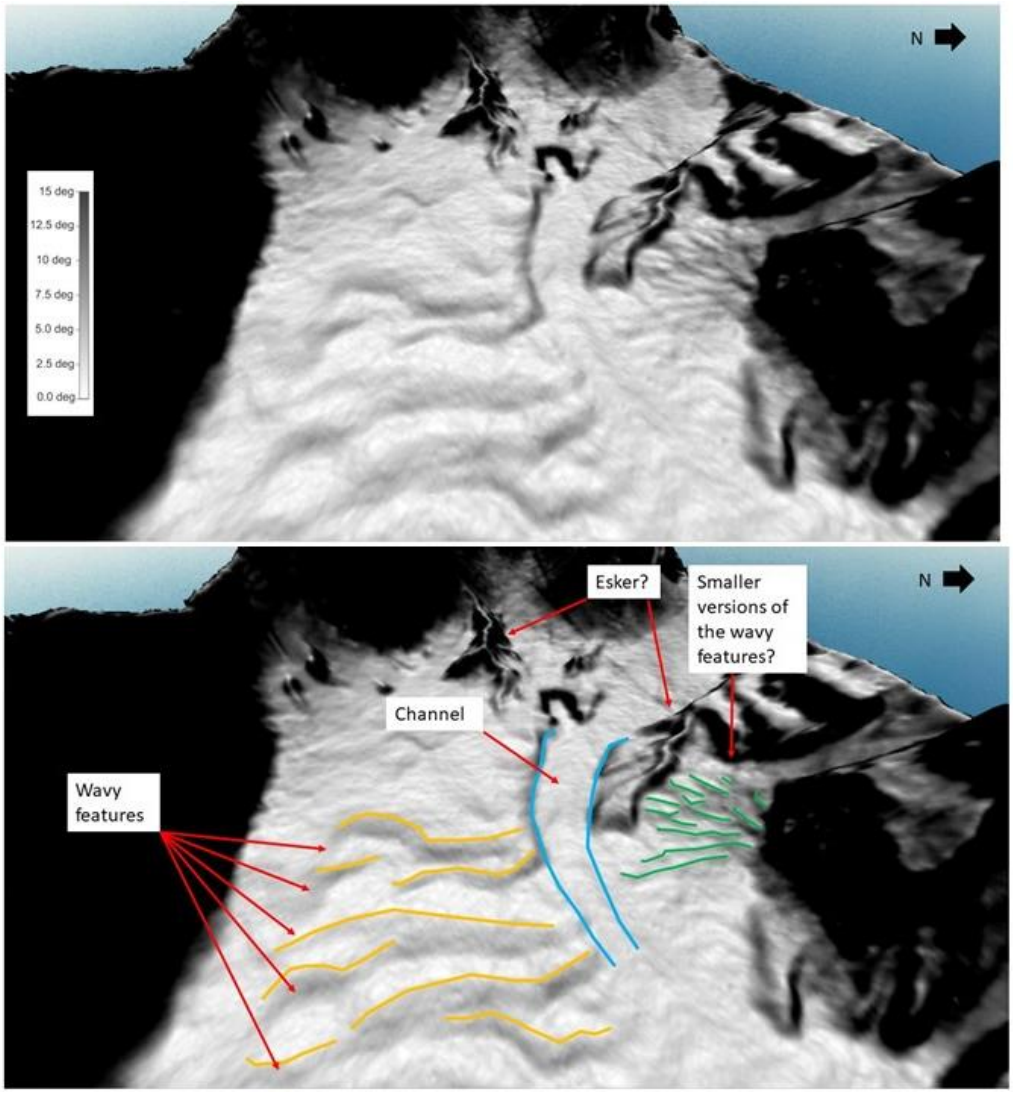

Figure 5.19. 3D bathymetric image of various features in Section 3 of the Mid-Fjord Region.

Wavy Transverse Ridges- Sediment Waves

Description: Adjacent to the two sinuous ridges describe in Section 3, and the "trough" described below, are a series of wavy transverse ridges to the east of a large recessional moraine (Fig. 5.19). These features occupy an area of ~500 by 1500 m and consists of a small ridge or flat area that then slopes at a 3 to 6° angle to the east. Each wave "crest" is ~50 to 100 m apart from the other, although some appear to begin only halfway through the width of the area, where

others occupy the entire width, north to south. These waves are possibly crosscut by a trough-like feature to their north (described below). To the north of this trough is a similar "step-like" feature that resembles these features in the south but are substantially smaller. They are initially oriented to the south, but curve towards the east further down slope. The general slope of the landscape in the southern ridges is ~1.7 °, where the slope on the northern ridges are 10° up slope and gradually change to 4.5°.

Interpretation: These features have been interpreted as sediment wave. Sediment waves have been identified on deltaic and glacifluvial deltaic systems and have been associated with retrogressive slope failures, gravity-induced sediment creep and the migration of sediment waves upslope (Cartigny et al., 2011; Hill, 2012; Eilertsen et al., 2016; Stacey & Hill, 2016). The mechanism behind the formation of these features will be discussed in the following chapter.

Elongated Depressions- Channels

Description: An elongated depression has been identified to the east of the large transverse ridge (interpreted as a large moraine) in Section 3 (Fig. 5.19). Following the axis of the landform, its length is ~1 km and width at ~200 m in the west and narrows to the east. It slopes eastwards at 1.8 to 2° with a slight meandering morphology although it may be curving around the existing topography. From its southern levee it appears to be 6 to 8 m deep in the west and decreases in depth to the east.

Interpretation: This feature has been interpreted as a channel. The development of channel morphology is controlled by the erosional and depositional properties of turbidity currents (Mulder, 2011). Its morphology is highly dependent on type of transported sediment (i.e. coarse-grained sediment transport typically results in wide, straight and shallow channels, where fine grained sediments produce narrow, deep meandering channels). Similar features have also been identified in Section 2 and Section 5 behind eastward rises in topography which have also been interpreted as channels, although they are less pronounced than the previously mentioned feature. Features classified as channels have also been identified on Bessel Fjords outer slope (on Inlet 2), although there is some uncertainty in this classification.

Chutes-Gullies

Description: Chutes have been identified on many of the sidewalls of the fjord, particularly in Sections 1-4 (Figs. 5.3-6). They are generally 20 to 100 m in width (occasionally over >150 m) and frequently cover the height of the fjord's walls (e.g. Fig. 5.20). Their depths range from 1 to 15 m and appear on material sloping at a minimum of ~ 5° but can more commonly be found on walls dipping at 10 to 30° (or more). They are commonly accompanied by steep sided gaps in the side walls, interpreted as slide scars (e.g. Fig. 5.20). The geomorphological difference between these features and "elongated depressions" is not extremely clear at times, however landforms classified as "chutes" are generally narrower, frequently found on steeper terrain (but not always) and are a much more common landform. Elongated troughs (depressions in the ground that don't appear on a sloping surface) have also been identified in Bessel Fjord (e.g. eastern portion of Section 2) but are not being interpreted in this thesis. Along with being found on the fjord's sidewalls, they have also been observed on the large recessional moraine between Section 2 and 3 (Fig. 5.16) as well as on the outer slope of Bessel Fjord, leading into Dove Bugt (Figs. 5.9 & 5.10).

Interpretation: These features have been interpreted as small gullies. This interpretation has been chosen based on their orientation, geometry and frequent position near other erosional features (e.g. slide scars). They are believed to form through retrogressive erosion or from density flow cascading (Mulder, 2011). They are distinguished from other seafloor erosional features (e.g. furrows and grooves) due to their small size, as well as straight and shallow channels that are tens of meters deep (Field et al., 1999; Surpless et al., 2007; Micallef & Mountjoy, 2011). Although these features are common on continental shelf settings (Micallef & Mountjoy, 2011) they have also been identified on the sides of fjords (Batchelor et al., 2018; Trottier et al., 2020).

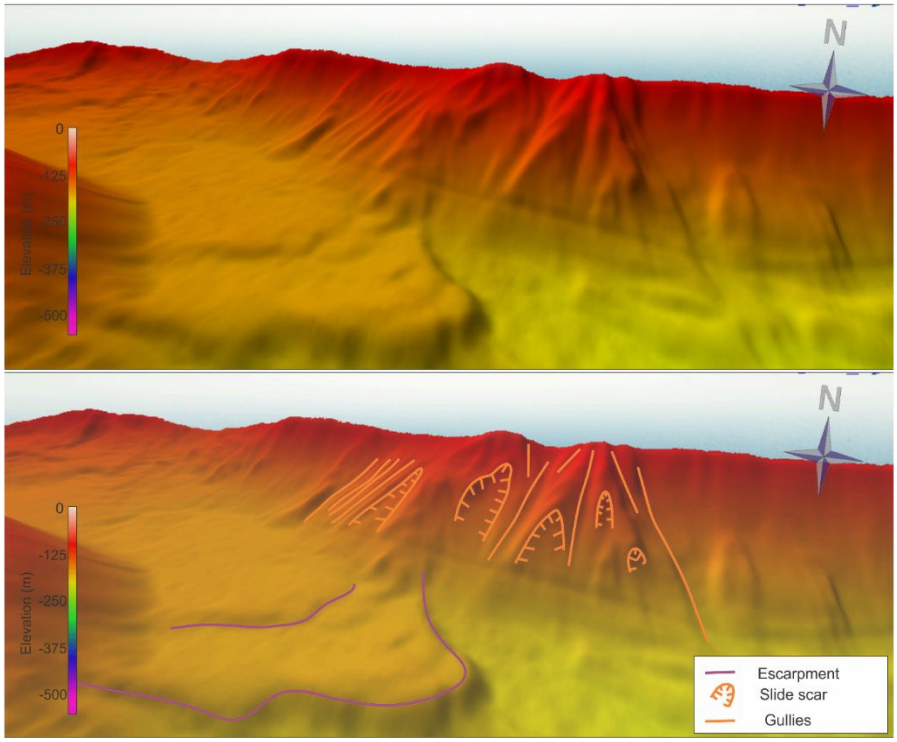

Figure 5.20. 3D images of chute, slide scars and escarpment in Section 1 of the Inner Fjord Region. See Fig. 5.2 for the exact location of these landforms.

Lobes- Sediment Lobes

Description: In Sections 1-4 and 6 lobe-like features have been identified, largely along the sidewalls of the fjord (e.g. Fig. 5.21). On average they are approximately 1 km wide and 0.5 km long (perpendicular to the fjords axis), although some are substantially larger (e.g. Fig. 5.8). They can be found near the outlets of rivers (e.g. Figs. 5.3 & 5.21), icecap lobes (e.g. Fig. 5.4) and sidewalls with no fluvial source (e.g. Fig. 5.4). Their morphology and slope vary, although they tend to fan out from a point of higher elevation. Many appear to have slopes >30°, where others contain slops that are <10°. The morphology includes (but is not limited to) relative homogenous masses (e.g. Section 6), feature that fans out and contain small gullies and/or small channels (e.g. Section 1; Fig. 5.21) and irregular ridges that branch outwards and are separated by small depressions (Section 1; Fig. 5.21). Gravity core HH17-1290-GC-TUNU was collected near the base of a sediment lobe (Fig. 5.21). This lobe is ~1300 m wide and 530 m long

perpendicular to the axis of the fjord. This width and length only include the submarine bathymetric data and when measured from the nearest terrestrial area (at a river's mouth) the length is closer to ~1200 m.

Interpretation: These features have been interpreted as sediment lobes. Sediment lobes, as they are defined here, include mass-transport deposits, terrestrial alluvial fans building out into the fjord, deltaic deposits and ice-proximal fans. Mass-transport deposits can develop when normal stresses exceed the rocks or sediments resisting shear strength (Løseth, 1999). Colluvial processes are typically attributed to their formation (e.g. rockfall, debris flow, snowflow) and dimensions are dependent on the landscape's topography, climate, and the materials supply and physical/chemical properties (Blikra & Nemec, 1998; Lønne & Nemec, 2004). When an alluvial fan builds into standing water it is referred to as a fan delta (Prior & Bornhold, 1990). These features typically contain coarse sand and gravel and are found near steep fjord walls (Prior & Bornhold, 1990). Ice-proximal fan can develop when sediment rich subglacial water loses energy as it leaves its subglacial channel and enters a fjord (Syvitski, 1989; Powell, 1990; Mugford & Dowdeswell, 2011). Coarser material (e.g. gravel and course sand) becomes deposited immediately outside of the terminus, where fine grained sediments are transported with the less dense fresh water (relative to the saline fjord water) and is deposited at a distance away from the subglacial channel's outlet (Syvitski, 1989; Dowdeswell et al., 2016b).

River deltas are deposits built by terrestrial feeder system into a water body, resulting in the irregular progradation of a shoreline that is typically modified through basinal processes and channel switching (Nemec, 1990b). Gilbert-type deltas (i.e. deltas with a steep foreset slope, tripartite structure and are associated with high course sediment supply and deep basins) have been identified glaciodeltaic and fjord settings (Corner et al., 1990). Within Section 1 and Section 3, gravity core HH17-1290-GC-TUNU and HH17-1289-GC-TUNU have been collected at the base of what have been interpreted to be deltas (Fig. 5.12).

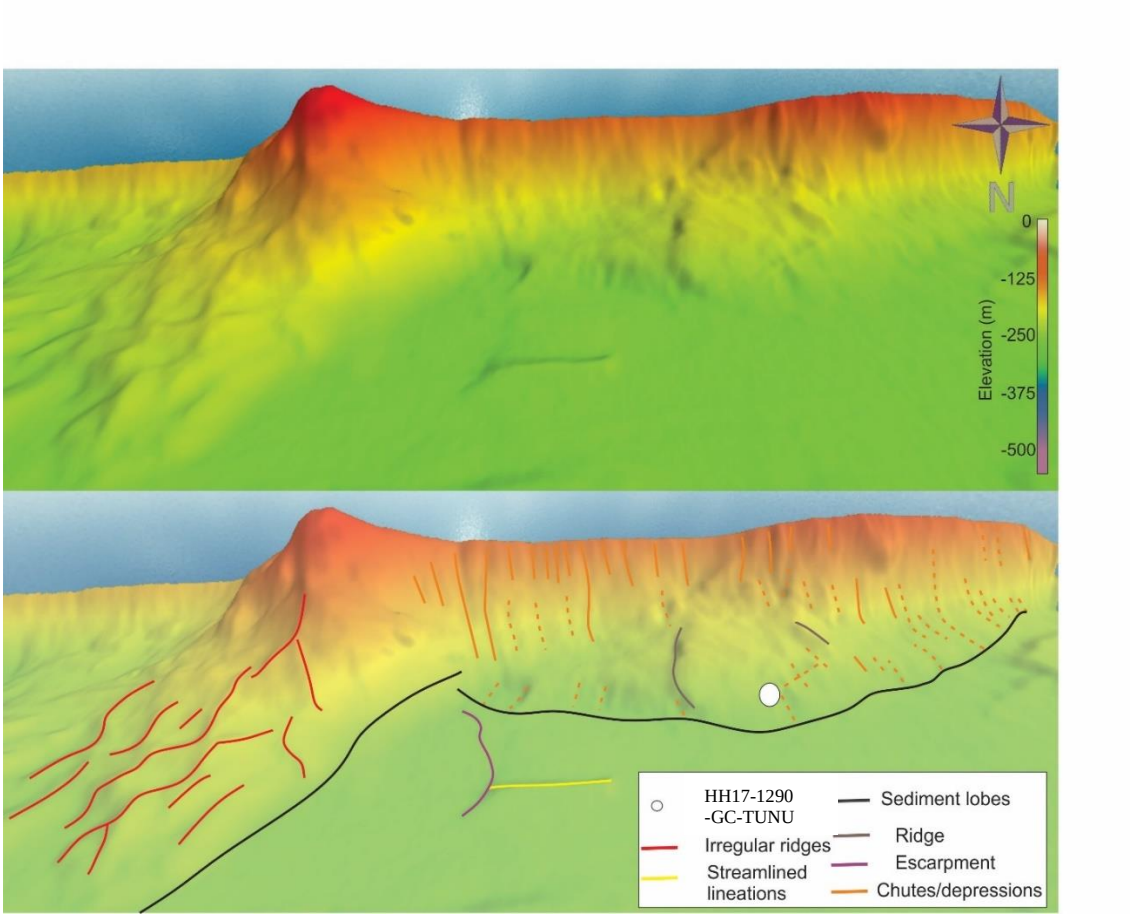

Figure 5.21. 3D bathymetric images of sediment lobes and other geomorpological features in Section 1 of the Inner Fjord Region. The sediment lobe to the right appears just below a river outlet. See Fig. 5.2 for the precise location of these features.

Rounded Depressions - Crevasse-Squeeze Ridges or Pockmarks

Description: Regions of irregular topography can be found at the mouth of Bessel fjord at elevations above ~200 m. This is frequently seen in the northeast portion of Section 6, Inlet 1 and sections of Inlet 2 (Fig. 5.8-10). These regions typically have varying amount of escarpment as well as circular to semi-circular depressions (e.g. Fig. 5.22). Circular depressions have been identified with raised ridges surrounding them, on sloping terrain or relatively flat seafloor, although most appear on a sloped surface. On average, their dimensions are 55 by 50 m wide and 2 m deep, although some larger circular depressions have been identified with widths as large as

100 by 100 m and others with depths as great as 3 m. Half enclosed circular depressions have also been spotted near fully intact depression and have been interpreted as being the same features but with collapsed side walls.

Interpretation: The appearance of these depressions at the outside of the fjord has led to more than one potential interpretation. The interpretation that seems the most likely is that these features are a rhombohedral network of crevasse-squeeze ridges. Within the context of an ice stream, these features were believed to form when soft sediment becomes squeezed into crevasses beneath an ice mass after a change in ice flow regime from fast flow to stagnation (Sharp, 1985; van der Veen, 1998; Andreassen et al., 2014). The development here would require the fracturing of a glacier's snout, which is normally seen during glacier surges (David J A Evans & Rea, 1999). It has been suggested that bottom crevassing can occur on grounded glaciers if there is sufficient basal water pressure that almost equates to the ice overburden pressure and when the glacier is close to floatation (Solheim & Pfirman, 1985; van der Veen, 1998; Ottesen & Dowdeswell, 2006; Andreasen et al., 2014). In the context of this fjord system, these may have formed when Soranerbræen met a branch of the NGIS and halt/changed its previous flow direction (as will be discussed below).

Alternatively, these landforms can be interpreted as pockmarks. These morphological features are commonly understood to be the result of the expulsion of gas and/or pore fluids from an underlying leaking petroleum system (Rise et al., 2014) and are frequently associated with prolonged periods of recurring fluid escape (Hovland et al., 2002). In some instances, the formation of pockmarks can be attributed to the melting of ice or gas hydrates (Solheim & Elverhøi, 1993; Judd et al., 1994; Long et al., 1998; Hovland et al., 2002). Although they are frequently associated with continental shelf settings (Rise et al., 2014), they have also been observed in fjords across the world (Plassen & Vorren, 2003; Forwick et al., 2009; Dowdeswell & Vásquez, 2013; Rise et al., 2014). Given the craters position at the end of the fjord, where the fjord's main tidewater glacier may be forced to react to a larger ice stream moving to the south, the former interpretation of these landforms is preferred although the presence of pockmarks isn't impossible.

Within the Mid- and Outer Fjord's basins and flat lying areas, sporadic small craters (<40 m wide, <1 m deep) have also been identified. The highest concentration of these smaller craters is on the western side of Section 4 (Fig. 5.6; a) and the southeastern side of Section 6 (Fig. 5.8). Shaw & Lintern (2016) has reported seeing scoured seafloor on the seafloor of Douglas Channel in British Columbia. These features could be of possibly similar origin, or perhaps also pockmarks. Because of their size there is significantly more uncertainty as to what their origin may be.

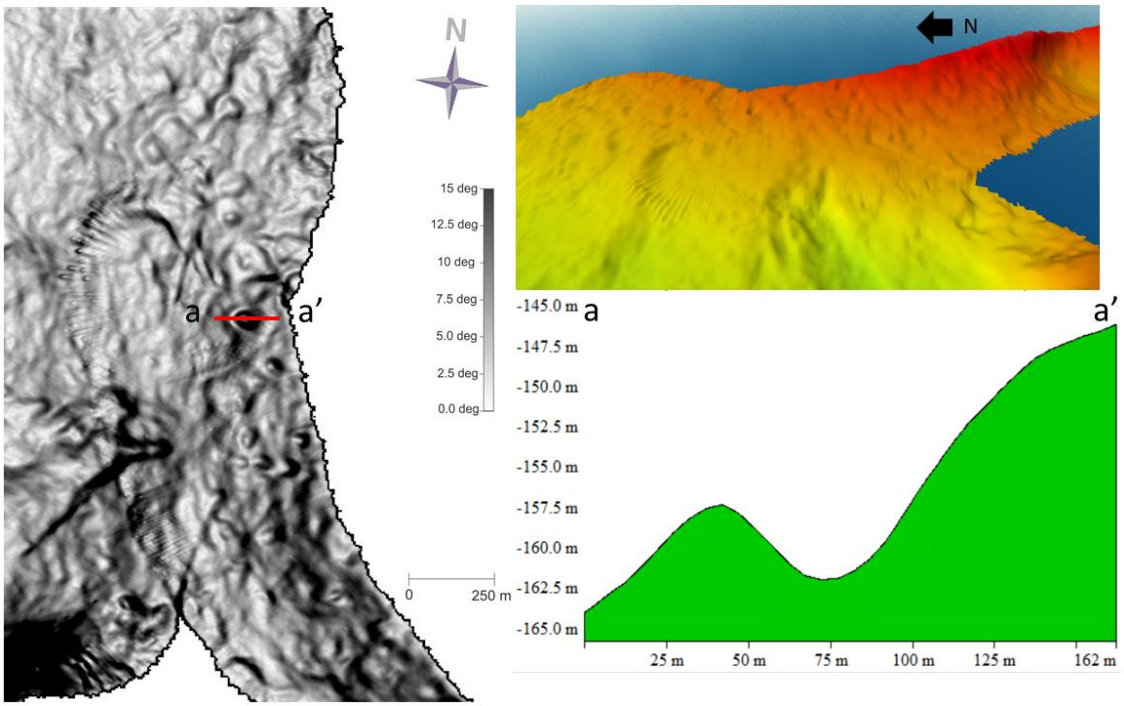

Figure 5.22. 2D and 3D images of crater like features identified in Section 6 of the Outer Fjord Region.

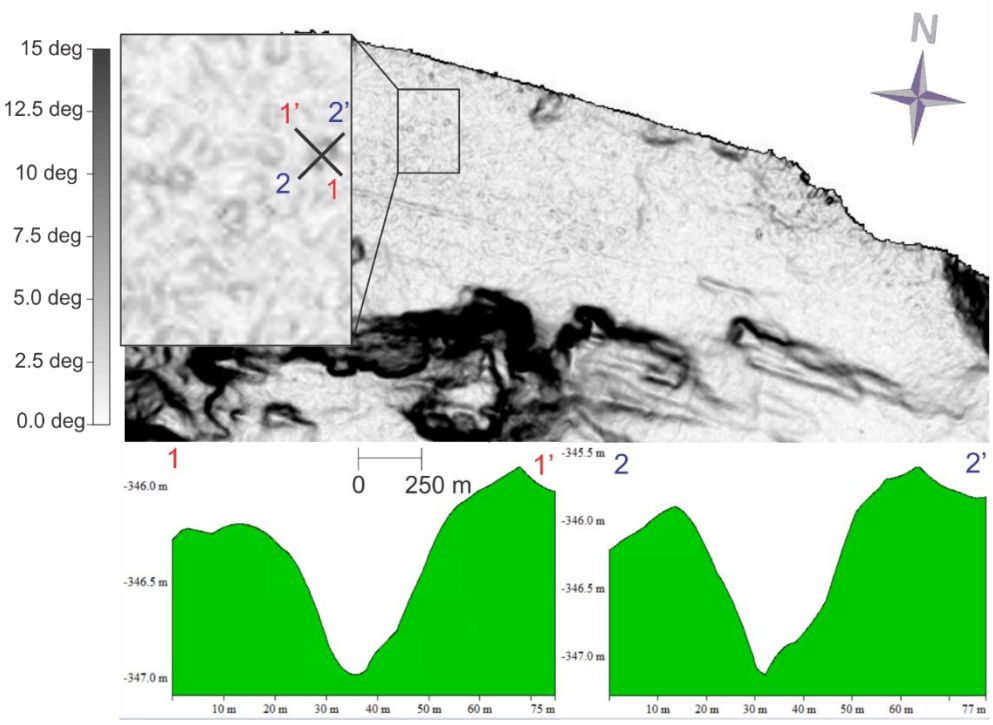

Figure 5.23. 2D bathymetric image of small craters observed in Section 4 of the Mid-Fjord Region.

5.1.2 **Dove Bugt**

5.1.2.1 **Overview**

The Dove Bugt bathymetric dataset covers a region approximately 24.5 km south to north outside of Bessel Fjord (Fig. 5.24). Just outside of the fjord's mouth the seabed slopes at 10° eastwards to a depth of 400 m. The topography gently slopes eastwards for 1.5 km before dropping at a steeper slope (5 to 15°) to form and irregularly shaped elongated channel with a maximum seafloor depth of 520 m (Fig. 5.25). This channel-like feature runs in a roughly south, southeast to north, northwest direction. The gravity core HH17-1309-GC-TUNU was collected along its northeastern wall near two scour marks (Fig. 5.25). Other than these two scour marks, and elongated ridge in the southern section of the study area, this channel-like feature does not contain any large-scale geomorphological features. To the east of this large channel feature, the seafloor continually rises to a relatively flat region of in of ~440 m depth (maximum depth of ~415 m in the northeast).

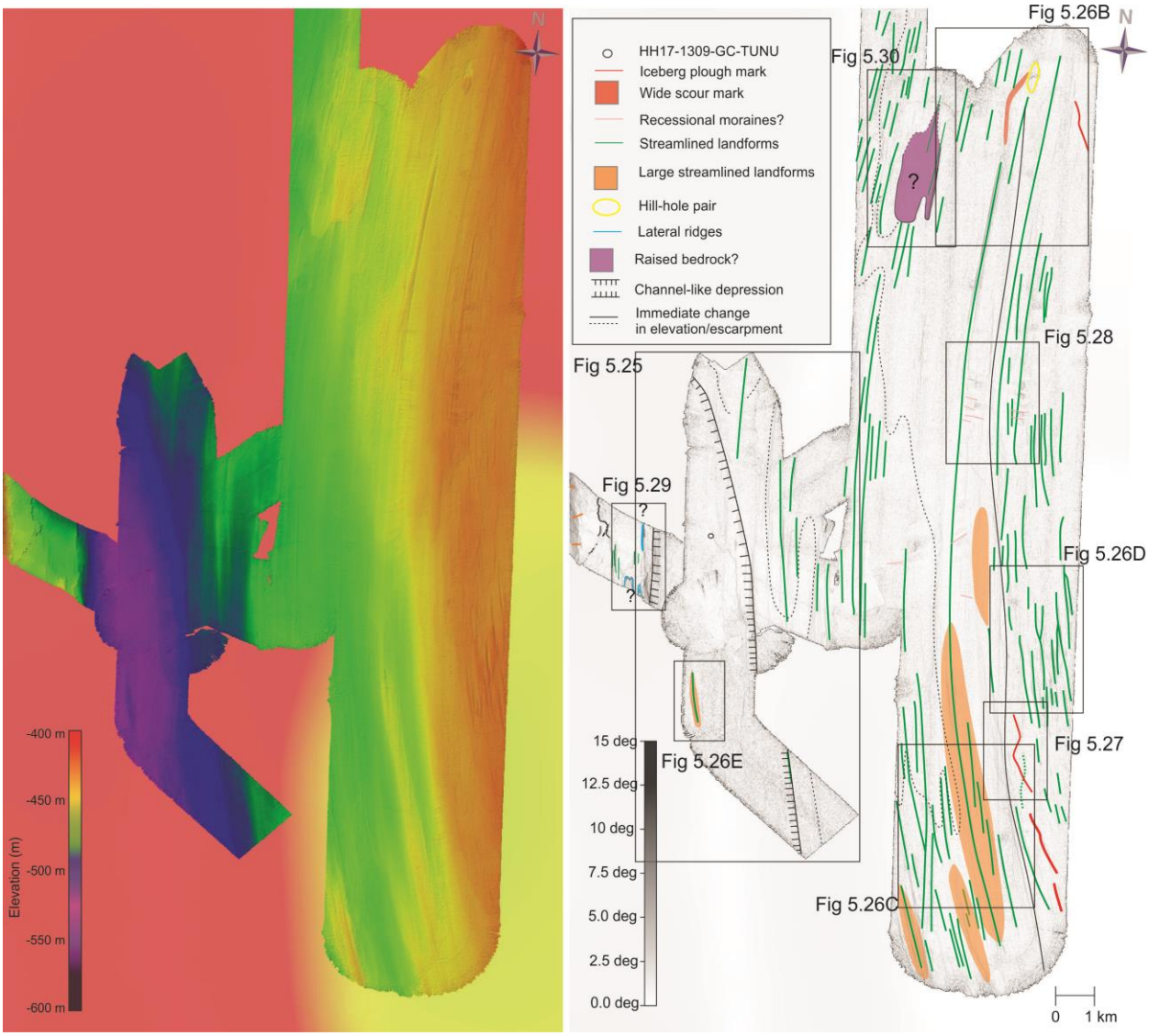

Figure 5.24. Bathymetric image of Dove Bugt. The image to the left includes the seafloor relative to water depth. The image to the right is of the intensity of the seabed's slope and includes landform interpretations and black boxes around images that are addressed below.

5.1.2.2 **Landform Description and Interpretation: Dove Bugt**

This section contains descriptions and interpretations for landforms identified in southwestern Dove Bugt. Please see Table 5.1 above for a full list of the landforms, their dimensions and interpretations.

Elongated Lineations- Large Streamlined Landforms

Description: The most dominant feature in the Dove Bugt bathymetric dataset is slightly curved lineations that run approximately N, NW in the south and turn N, NE in the north (Fig. 5.25). The most common lineations are 35 to 50 m wide, <1 to 3 m in height and often stretch for one to several kilometers (Fig. 5.26A). Larger variations of this features have been observed, some with widths of 150 m and heights of 5 to 6 m (Fig. 5.26B). Length to width ratios for these features are well above >10:1. Above an elevation of 435 m depth, near the center of the Dove Bugt, the lineations also appear to be wider than the typical lineations observed in the area (at 60 to 150 m wide) and take on a slightly more chaotic pattern where lineations appear to be either running into each other or overlapping each other (Fig. 5.26D). Significantly wider lineation's have also been observed in southwestern Dove Bugt, often in the southern section of the study area (Figs. 5.26C & E). These range from 200-650 m wide, 3-8 to 8.8. km long (height to width ratios 7:1 to >10:1) and contain heights ranging from 4.5 to 15 m. These larger features appear to have the smaller lineations mentioned above superimposed on their surface in some instances. One of these larger lineations has been identified within the deep SSE-NNW oriented channel (Fig. 5.25E) and appears to have a steeper ice-distal when measured along the perceived direction of flow.

Interpretation: These elongated features have been interpreted as large streamlined landforms. The thinner features with a length/width-ratio >10 have been interpreted MSGL where the other streamlined landforms are not as easily classifiable. MSGL lineations have been identified in palaeo-ice stream environments (e.g. Stokes & Clark, 2001) and may imply fast flowing ice if the landform has a length/width-ratio >10 (Stokes & Clark, 1999).It is difficult to determine whether these landforms developed through depositional or erosional means, although, the genesis of MSGL have been an ongoing discussion (e.g. Clark, 1993; Clark & Stokes, 2003; Ó Cofaigh, 2005; Rydningen et al., 2013). Both the smaller lineations and larger lineations are interpreted as being developed by subglacial erosional or depositional means.

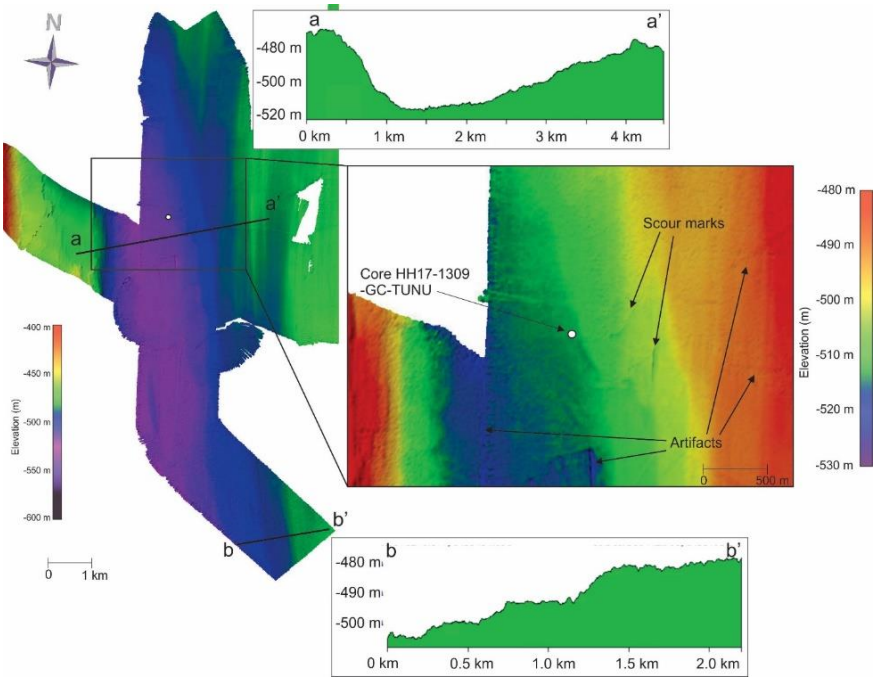

Figure 5.25. Bathymetric image of the deep channel feature and gravity core HH17-1309-GC-TUNU in western Dove Bugt.

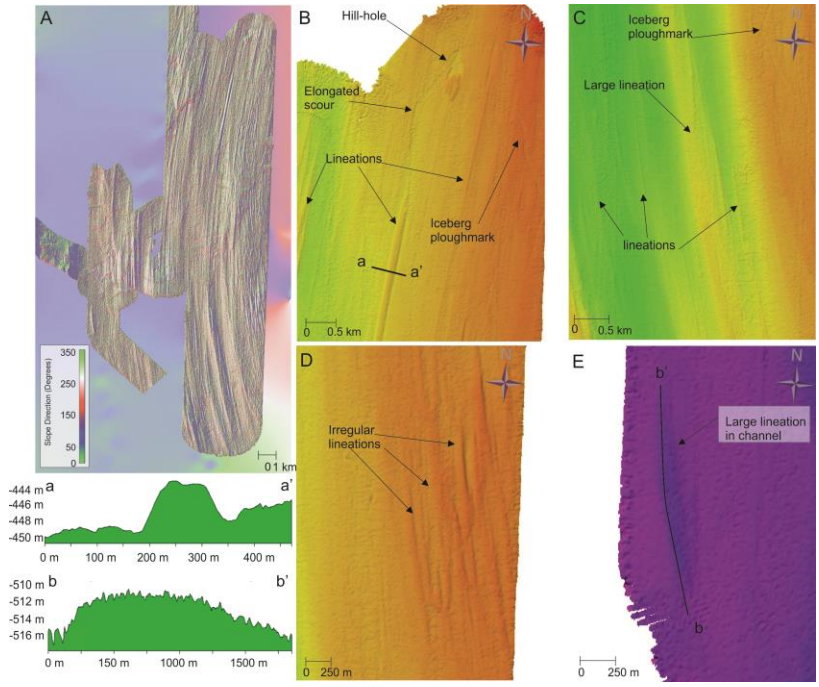

Figure 5.26. Bathymetric images of streamlined lineations across Dove Bugt. A: Image of Dove Bugt with a slope direction shader color schematic turned on. Note the orientation of the landforms. B: Image of large/small lineations, a hill-hole pair and iceberg plough mark. C: Image of large/small lineations and an iceberg plough mark. D: An image of irregular lineations in central Dove Bugt. E: Large lineation in the channel-like feature in southwestern Dove Bugt.

Furrows (Scour Marks)- Iceberg Plough Marks

Description: Irregular scour marks, ~40 to 100 m wide have been identified in regions of Dove Bugt, primarily in areas that are above 440 m depth (Figs. 5.26B & 5.27). These features are typically elongated in an NNW to SSE direction and 3 to 5 m deep. A wider scour mark has also been identified in the northern side of the study area (Fig. 5.27) and in rare circumstances at substantially lower depths (e.g. Fig. 5.25). The width of this feature is narrower in the south (<100 m) and gradually increases to the north (>200 m). Its depth is 3 to 5 m wide and is oriented generally in a N-S direction. The feature curves westwards in the north and leads to depression and mound feature (described below). Additionally, two scour marks have also been identified within the elongated channel-like feature in western Dove Bugt, near HH17-1309-GC-TUNU (Fig. 5.25).

Interpretation: The irregular scour marks have been interpreted as iceberg plough marks. Plough marks develop when the keels of icebergs exceed the water depth and cause the erosion of shelf sediments (Dowdeswell et al., 1993; Syvitski et al., 2001). The intensity of the erosion depends on the drift track, dimensions and rate of production of icebergs, water depth and the type of substrate (Dowdeswell et al., 1993). Approximately half of Greenland's continental shelf is believed to have been reworked by iceberg keels, especially at water depths less than ~400 m (Brett & Zarudzki, 1979; Dowdeswell et al., 1993, 2014, 2016; Syvitski et al., 2001). The scour marks identified in the channel-like feature may be of iceberg origin, but due to their depth of over >500 m it is more likely that they have formed through processes related to mass wasting or fluvial erosion.

Depression and Mound- Hill-Hole Pair

Description: A 200 by 450 m wide, 3-4 m deep depression has been identified in northern Dove Bugt (Fig. 5.26B). This feature overprints elongated, N-S lineations and is next to a large mound that has a width of approximately 235 by 450 m and is 3 to 4 m tall. It appears that this mound may also contain elongated lineations on its surface.

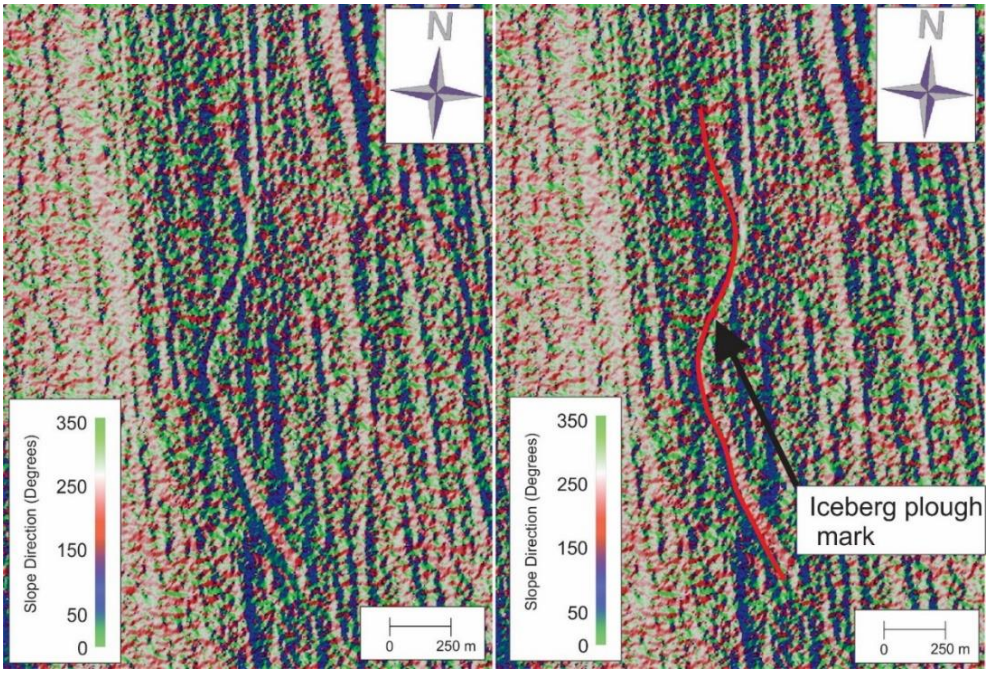

Figure 5.27. Bathymetric image of scouring interpreted as iceberg plough mark.

Interpretation: These features have been interpreted as hill-hole pairs. These features form when ice-thrust rafts of sediment are removed from the bed by cold-based, slow-flowing ice that relocates the sediment in the depression (Klages et al., 2013, 2015). In this instance, a south bound (offshore) ice stream would have ripped frozen sedimentary material from the seabed and deposited it to the south.

Transverse Ridges- Recessional Moraines

Description: On northeastern side of the Dove Bugt dataset, roughly west to east oriented lineations have been identified on top of large, distinct, roughly north to south oriented lineations (Fig. 5.28). It has been established above that these north-south running lineations have been interpreted as MSGL, however the origin of these superimposed ridges is less clear. They appear to override the N-S oriented lineations and are positive and negative relief features. The positive relief features (Fig. 5.28, orange, 1-1’ in cross section) generally measure 0.5 to 1 m in height and in many occasions have a depression immediately to their north or south. Where they are

clustered, they spaced ~45 to 250 m apart. Negative relief features (Fig. 5.28, yellow, 2-2’ in cross section), approximately 1 to 2 m deep, have also been found cross cutting the N-S oriented lineations to the north of these positive relief features. Fig. 5.28 shows the most prominent of these ridges and depressions, however it should be noted that smaller versions of these features have been identified across most of the Dove Bugt dataset, also cutting into the large MSGL.

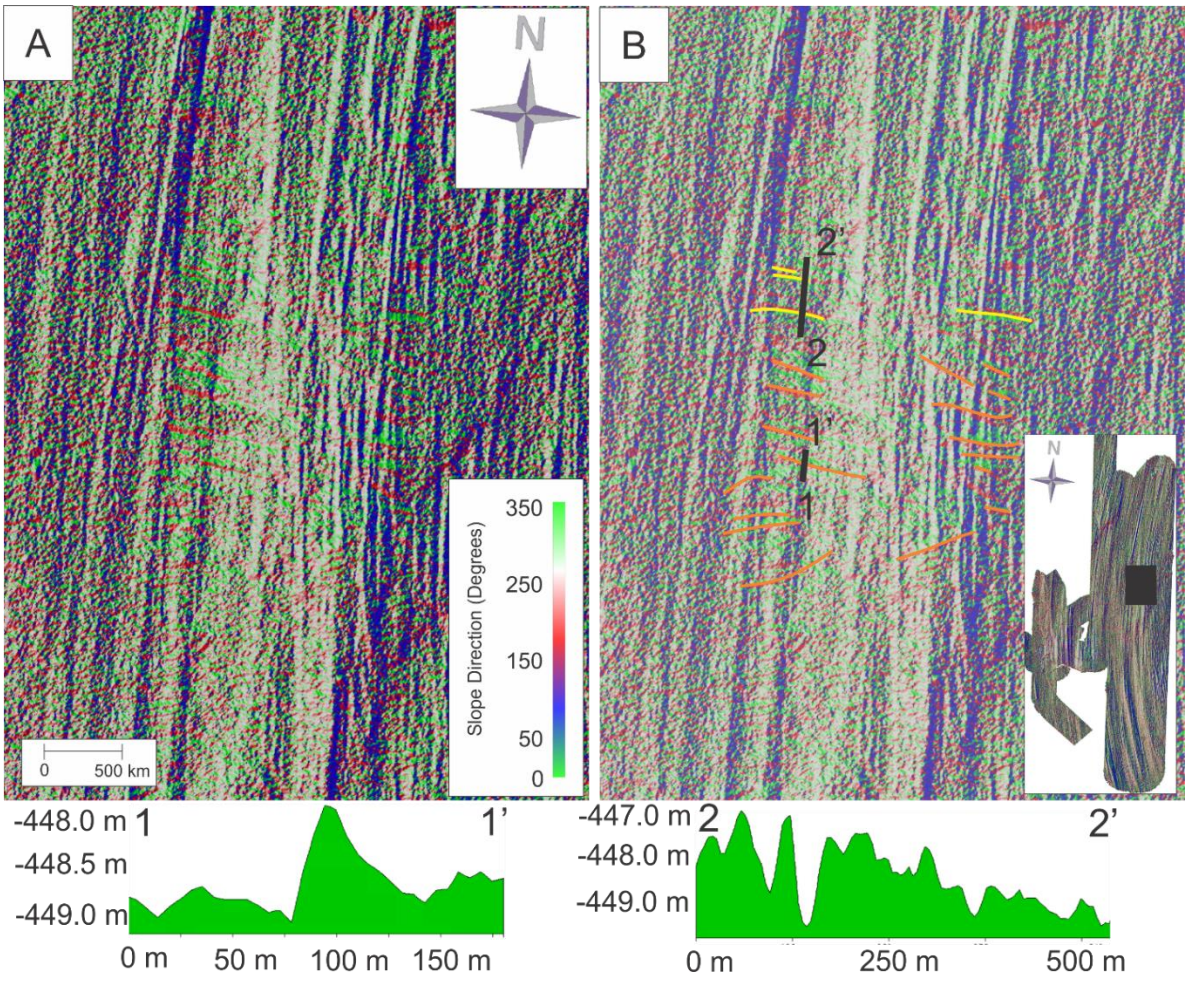

Figure 5.28. Bathymetric image of positive and negative relief features that are superimposed on streamlined lineations. They have been interpreted as recessional moraines, but it is possible that they are artifacts.

Interpretation: Based on the orientation and geometry of these features, they have been interpreted as recessional moraines. Other authors have witnessed perpendicular transverse ridges on MSGL and have also interpreted them as recessional moraines (e.g. Dowdeswell et al., 2008; Ó Cofaigh et al., 2008). The presence of recessional moraines would indicate a step wise deglaciation. Transverse ridges are commonly developed from an annual ice push, where winter sea ice suppresses iceberg calving and promotes a minor readvancement (Boulton, 1986; Ottesen & Dowdeswell, 2006; Dowdeswell et al., 2008). Alternatively, these features may also be an artifact, due to their similar appearance to artifacts outlined in the Material & Methods Chapter (Fig. 4.2D).

Ridges Near the Fjord's Entrance- Lateral Moraines

Description: On the western side of Dove Bugt, elongated ridges have been identified just downslope and east of the large sill sitting just outside of Bessel Fjord (Fig. 5.29). These ridges are also just west of the large, elongated N-S trending channel in Dove Bugt. The ridge to the northwest slopes at a 12-26° to the southeast, where the ridge to the northeast (just above the deepened channel) slopes 13-16°.

Interpretation: Because these features are only partially within the dataset they cannot be fully interpreted with confidence. It is suspected that the northern two ridges may be lateral moraines from at least two different glaciations, where the bottom two ridges might be streamlined landforms or transverse ridges. Across this region the elevation tends to increase to the south, therefore, it is also possible that there is a larger landform that is connected to these two southern ridges that is just out of the bounds of the dataset. Alternatively, the northern most feature may be a slide scar, but it is difficult to say this with confidence. These features are noteworthy but few large interpretations about the region will be based on these findings.

Large Transverse Ridge- Raised Bedrock

Description: In the northwestern portion of the dataset lies an irregular mound that rises ~7 m above the surrounding seabed (Fig. 5.30). The shape of the feature is not well defined. From west to east the feature appears to be ~900 m wide with 3.5-5° slopes to the west and east. The front

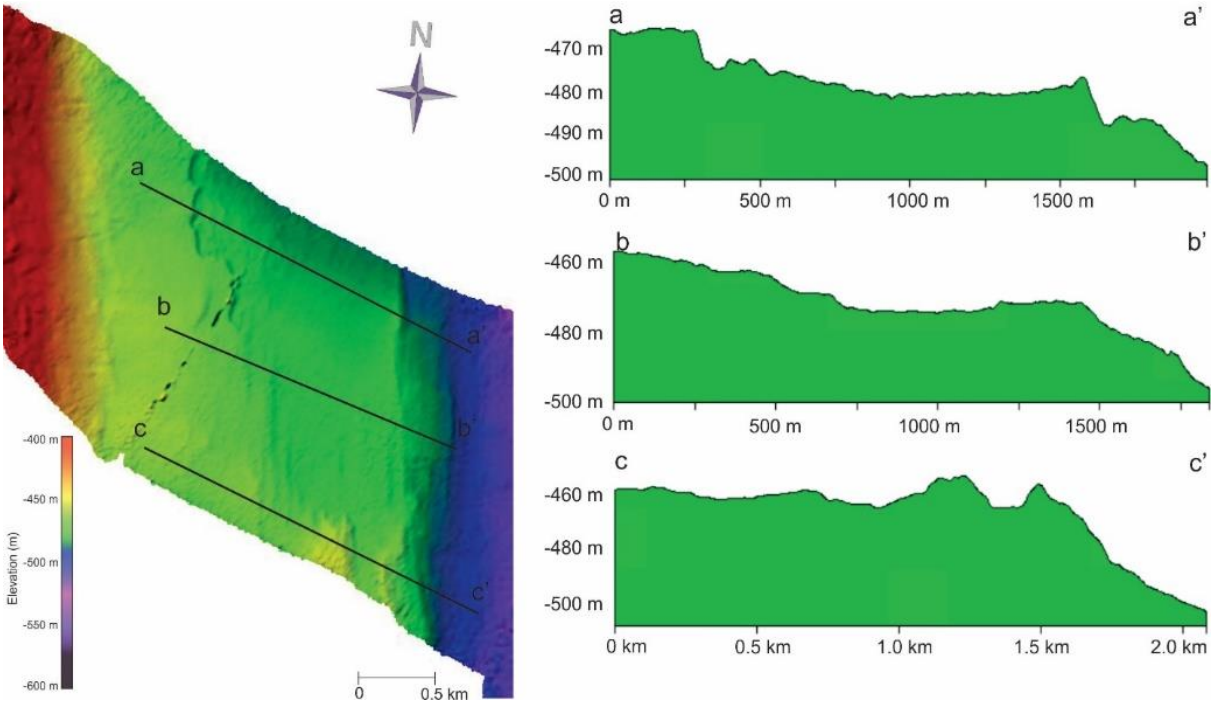

Figure 5.29. Bathymetric image and cross sections of ridges identified immediately east of Bessel Fjord. Note that two ridges can be observed in the northern portion of the image (a-a') but appear to disappear halfway through the slope (b-b'). Two additional ridges that continue southwards can be seen in the southern portion of the slope (c-c').

of the feature in the south can be prominently seen, however, it appears to trail off in a northward's direction. Elongated, N-S trending, lineations appear to terminate on the south side of the feature, however well-defined lineations of a similar style appear to surround the feature to the west, north and east. Lineations appear on top of these features surface to the east and north as well. On the western side of this elevated region, smaller transverse ridges, separated 70 to 120 m apart have also been identified.

Interpretation: Based on the geometry and isolated position in Dove Bugt this feature has been interpreted as eroded raised bedrock. This would have likely formed as the result of resistant bedrock becoming eroded by the overlying ice stream. Based on the asymmetrical profile and steep ice-distal slope an alternative interpretation of this feature is that it is a GZW (Batchelor & Dowdeswell, 2015), although this is not favored here due to its isolated position in Dove Bugt (see Discussion).

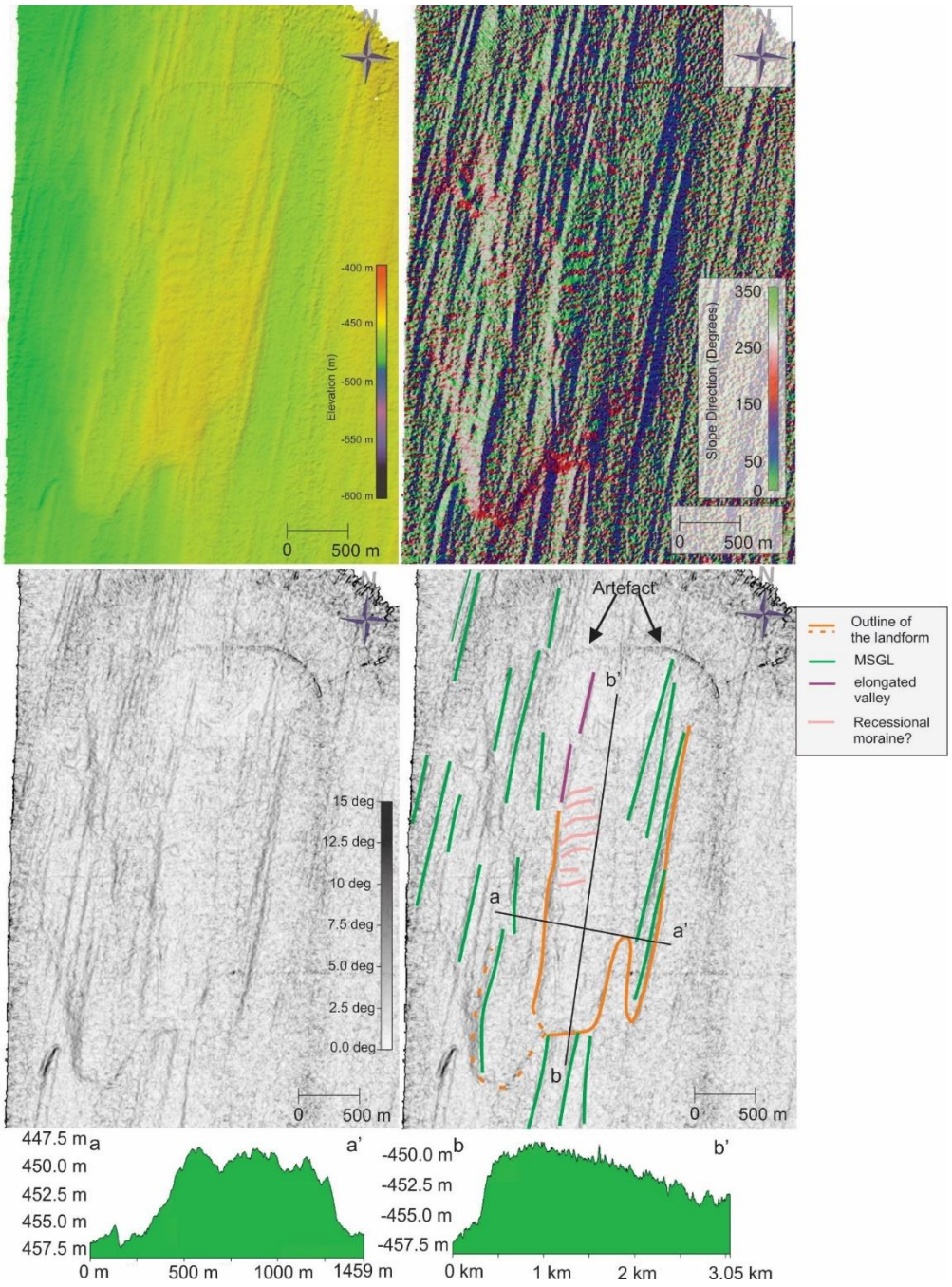

Figure 5.30. Bathymetric images large positive relief feature in northwestern Dove Bugt. Images include the feature relative to water depth (top left), slope dip direction (top right) and angle of dip (bottom left). The image on the bottom right contains interpretation of the landform/surrounding landforms as well as cross sections across and perpendicular along the landform.

5.2 Lithostratigraphy

5.2.1 Lithostratigraphic overview

Three gravity cores were collected from the study area (Fig. 5.31; Table 5.2). Within Bessel Fjord, core HH17-1289-GC-TUNU was collected in Section 1 along a lobe like feature and HH17-1290-GC-TUNU was collect in a basin in Section 3, close to the basin's southern sidewall. Gravity core HH17-1309-GC-TUNU was retrieved from the Store Bælt region of southwestern Dove Bugt, in an elongated channel-like feature (Fig. 5.25). The methodology described in Chapter 3 was used to analyze these cores in an attempt to interpret their depositional environment. The results from the visual core description, sediment grain size analysis, MSCL, XRF and radiocarbon dating can be found below. A summary of the minimum, maximum and mean values of MSCL, XRF and sediment grain size analysis results can be found in Table 5.2. Elements used in XRF ratio plots were chosen based on how well they responded to the XRF scan and their possible usefulness in analysis of the cores (see Chapter 3 for additional information). The calibrated results from radiocarbon dating, and the corresponding calculated sedimentation rates, can be found in Table 5.3.

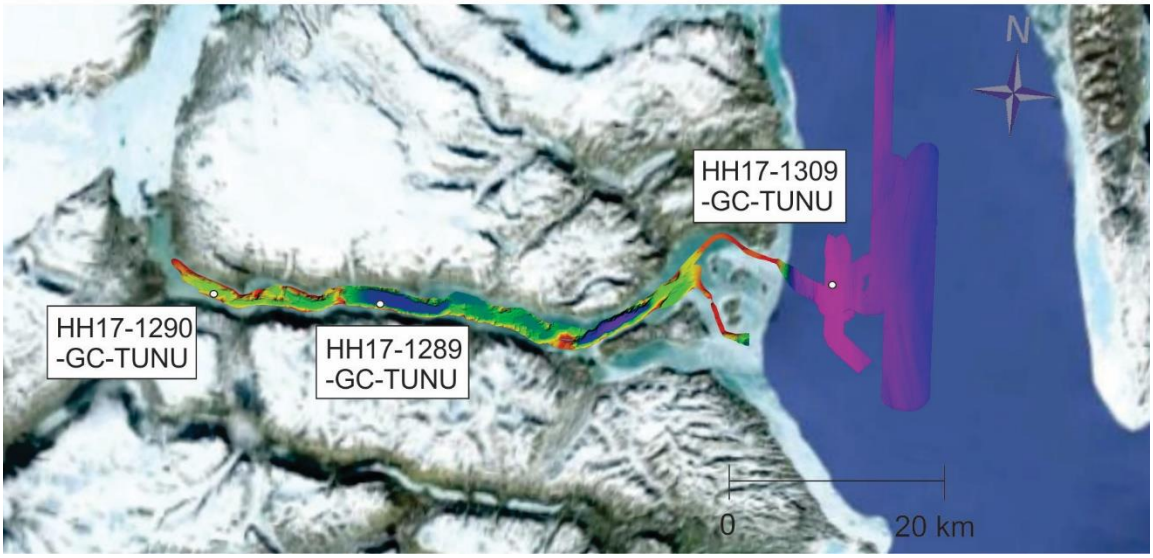

Figure 5.31. Location of gravity cores across the study area.

Table 5.2. Summary of gravity core locations and the resulting laboratory measurements.

Location	Inner Bessel Fjord			Mid-Bessel Fjord			Southeastern Dove Bugt		
Coring station	HH17-1290			HH17-1289			HH17-1309		
Latitude [N]	75° 58' 34.5907"			75° 58' 11.4928"			76° 01' 34.0387"		
Longitude [W]	21° 07' 13.1055"			21° 41' 48.0278"			19° 34' 31.3190"		
Water depth [m]	372			225			512		
Recovery [cm]	534.5			245.5			474.55		
	Min	**Max**	**Mean**	**Min**	**Max**	**Mean**	**Min**	**Max**	**Mean**
MS [SI x 10^{-5}]	1.03	229.33	148.40	38.46	191.12	81.65	21.33	151.41	100.78
P-wave [m/s]	1479.65	2479.82	1517.31	1487.82	1849.76	1631.15	1404.42	1690.32	1482.48
Density [g/cm^3]	1.54	2.10	1.79	1.78	2.18	1.99	1.40	2.06	1.64
Ca/Fe ratio	0.126	0.523	0.278	0.092	0.401	0.179	0.096	0.515	0.199
Al/Sum ratio	0.003	0.019	0.013	0.005	0.021	0.012	0.004	0.021	0.013
Zr/Rb ratio	0.724	6.978	2.056	1.326	5.151	2.205	0.979	8.192	1.626
Fe/Sum ratio	0.376	0.668	0.510	0.343	0.652	0.515	0.382	0.686	0.542
Ti/Sum ratio	0.036	0.084	0.047	0.037	0.108	0.057	0.032	0.073	0.047
Ca/Sum ratio	0.084	0.196	0.140	0.051	0.172	0.090	0.064	0.211	0.104
K/Sum ratio	0.077	0.130	0.117	0.091	0.160	0.130	0.084	0.136	0.122
Si/Sum ratio	0.062	0.252	0.156	0.081	0.355	0.169	0.062	0.261	0.151
Grain size sample #		4			8			37	
Grain size [µm]	8.30	11.20	9.93	15.40	203.50	84.57	3.63	137.66	9.47

5.2.2 Gravity Core HH17-1290-GC-TUNU (Inner Fjord)

Gravity core HH17-1290-GC-TUNU was collected in the inner part of Bessel Fjord at a water depth of -225 m (Fig. 5.31; Table 5.2). The total length of this core is 534.5 cm. Three units were identified within this core and were largely determined by the quantity and style of lamination (which generally decreases up core).

5.2.2.1 Unit 1.1 (411-534.5 cm)

Description

Unit 1.1 mostly consists of mud with high quantities of sand laminations and occasional large clasts (Fl-d) (Fig. 5.32). Partial and full sand layer are composed of fine-grained sand (or coarse-grained sand in the sand layer at ~412 cm) and appear to decrease in quantity up core. Laminations are typically <1 cm and faintly visible in split core but clearly identifiable in x-ray

Table 5.3. Summary of ^{14}C lab results and calibrated ages. + very small quantities of stainforthia feylingi also present. ^ very small quantities of islandiella norcrossi.

Coring station	Sampling Depth [cm]	Lab nr.	Species	^{14}C age BP	Cal yr BP Calib 7.10 1σ range	Cal yr BP Calib 7.10 2 σ range	Cal yr BP Calib 7.10 1 σ mean	Linear sedimentation interval [cm]	Linear sedimentation rate [cm/ka]
HH17-1290-GC-TUNU	97	5158.1.1	Melonis barleeanus^	6,800 ± 80	7059 - 7258	6943 - 7340	7160	0-97	13.55
HH17-1289-GC-TUNU	35	5154.1.1	Yoldiella lenticula	688 ± 34	103 - 244	46 - 262	174	0-35	201.73
HH17-1289-GC-TUNU	71	5155.1.1	Hiatella arctica	1,747 ± 28	1096 - 1208	1047 - 1247	1147	35-71	31.39
HH17-1289-GC-TUNU	125.5	5156.1.1	Bivalve frag.	3,809 ± 36	3481 - 3607	3433 - 3678	3544	71-125.5	15.38
HH17-1309-GC-TUNU*	377	5157.1.1	Islandiella norcrossi+	10,357 ± 95	11075 - 11308	10921 - 11592	11190	0-377	33.69

images (Fig. 5.32). Colors alternate between Gley 1 4/5 Gy and Gley 5/10 Gy throughout the entirety of the unit. Large clasts have been identified both in split core and in x-ray images throughout the unit (e.g. at ~340 cm) (Fig. 5.32). Microfractures have also been identified in x-ray images oriented in different directions (Fig. 5.32). A single sample was taken from this unit for sediment grain size analysis. This sample was taken near the top of the unit, at 455 cm, above the sand laminations. The resulting sample was determined to be a very poorly sorted medium silt composed of 5.9% sand, 755 silt and 19.1% clay. More specifically, the sample contains 0.01% fine sand, 5.8% very fine sand, 14.1 % very coarse silt, 18.5% coarse silt, 17.5% medium silt, 14.1% fine silt, 10.7% very fine silt and 19.1% clay. The bottom 10 cm of the core, where wavy sand layers have been identified, is believed to have experienced disturbance during the coring process.

Physical Properties

The average magnetic susceptibility of Unit 1.1 is 164.5 SI x 10^{-5} and values tend to fluctuate around this mean for the entirety of the unit (Fig. 5.33). The bulk density, P-wave velocity and acoustic impedance values tend to increase down core, particularly at the bottom where the core has experienced increased disturbance. The bulk density and P-wave velocities appear to have peaks at 413, 521 & 531 cm.

Elemental Geochemistry

Through the length of the unit Fe/Sum and Ti/Sum ratios tend to increase up core (Fig. 5.34). Conversely, Ca/Fe and Zr/Rb tend to decrease up core. At ~474 cm, there are positive peaks in Zr/Sum, Ti/Sum and Ca/Sum, and negative peaks in K/Sum and at 412 cm there is a small drop in Fe/Sum and Ti/Sum, and a positive peak in Al/Sum ratios across from a coarse sand layer.

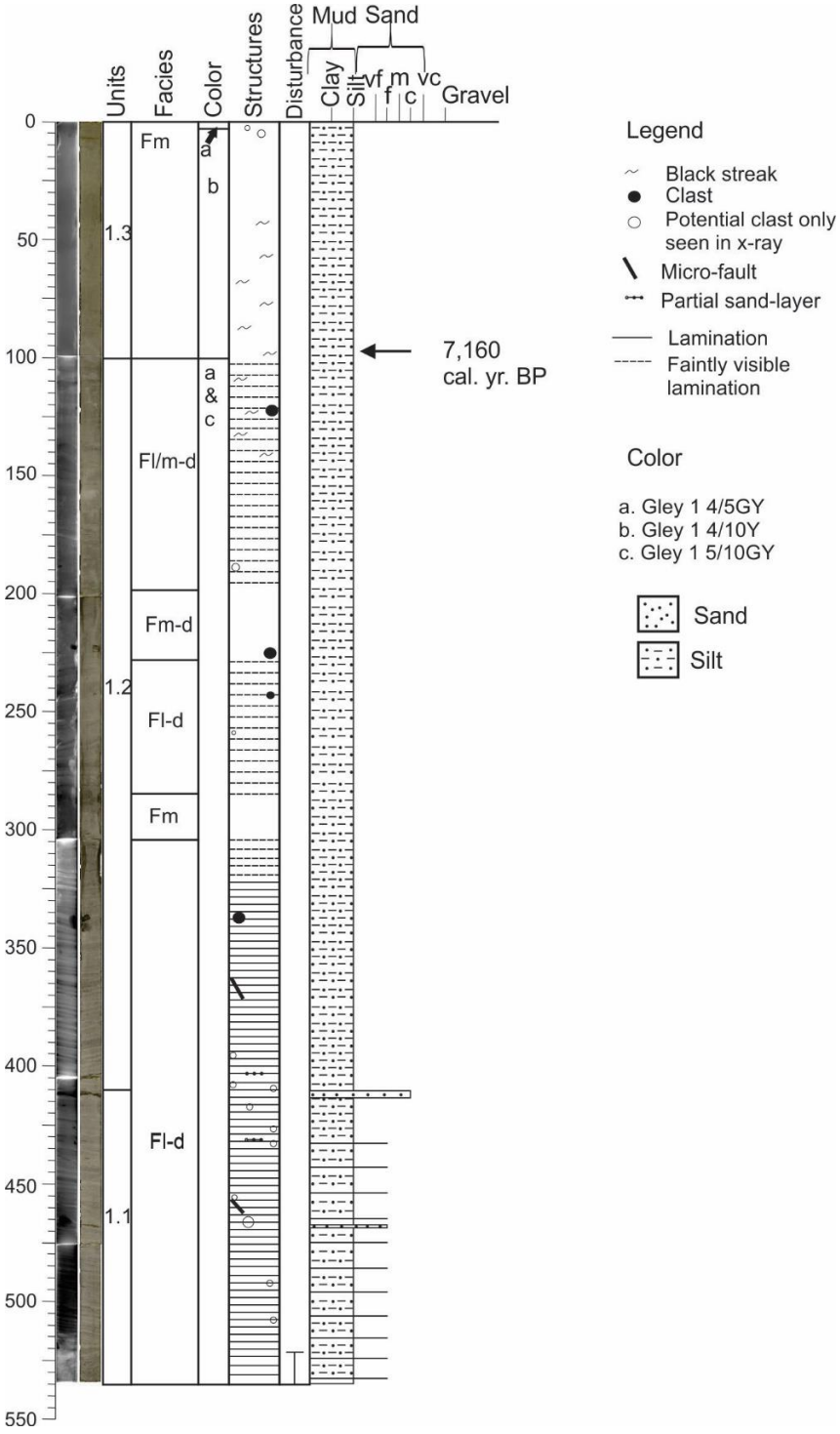

Figure 5.32. Lithological core log of HH17-1290-GC-TUNU. Includes the unit divisions, facies, color, structures and disturbance.

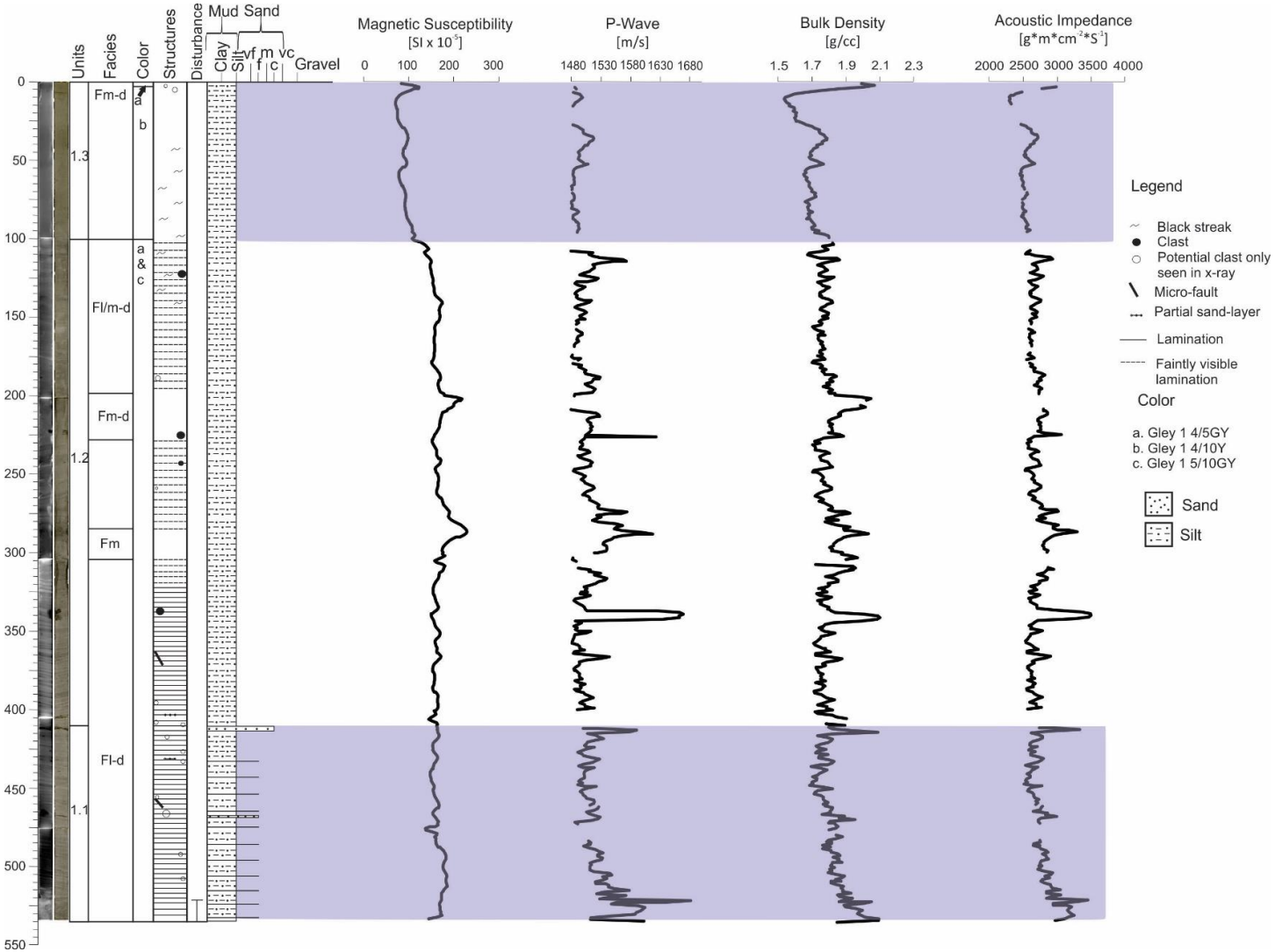

Figure 5.33. Results from the Multi Sensor Core Logger (MSCL) on gravity core HH17-1290-GC-TUNU. Blue sections encompass Unit 1.1 and 1.3.

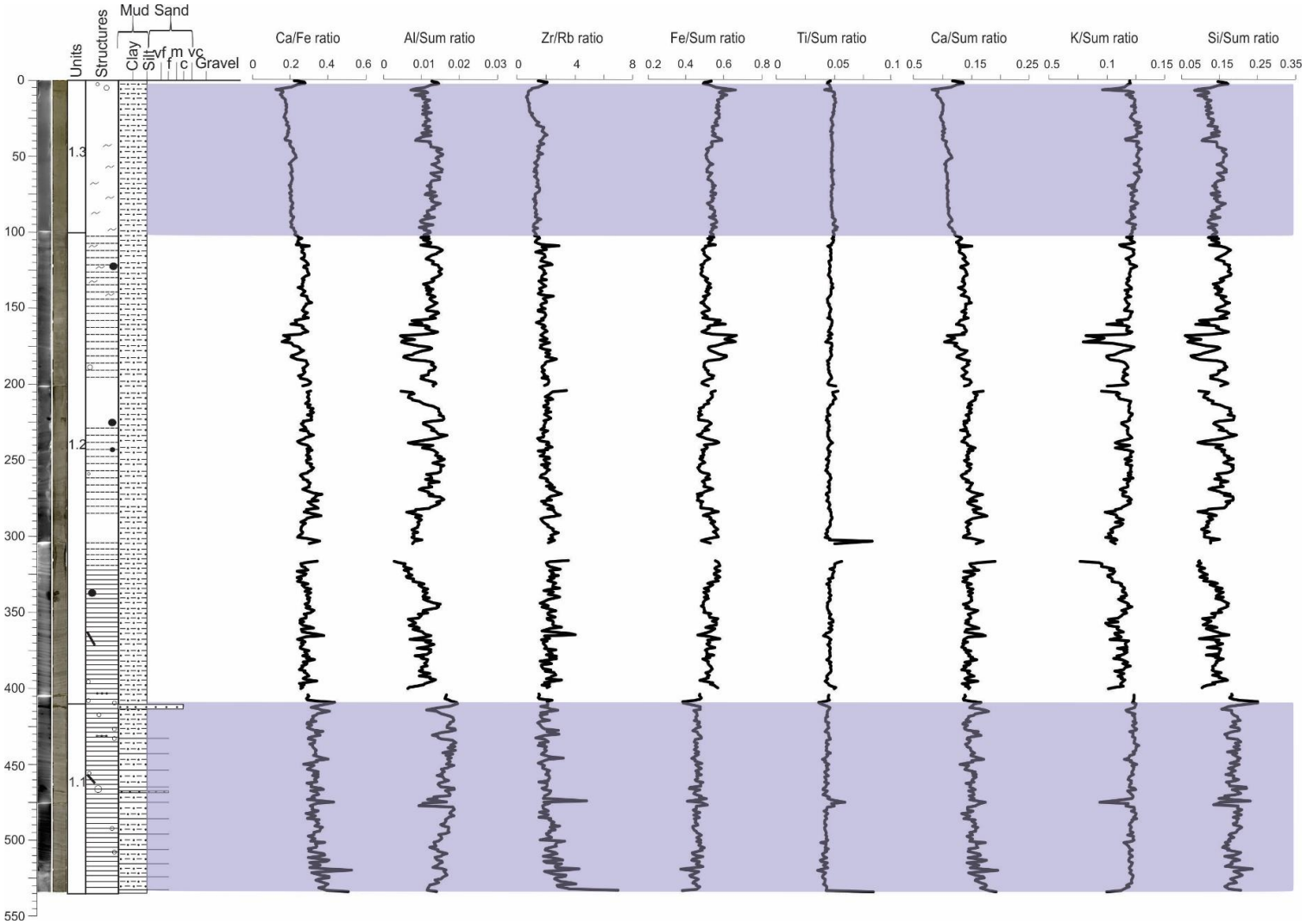

Figure 5.34. Results of select elemental ratios using the X-Ray Fluorescence (XRF) equipment on gravity core HH17-1290-GC-TUNU. Blue sections encompass Unit 1.1 and 1.3.

5.2.2.2 Unit 1.2 (~99.5-411 cm)

Description

Unit 1.2 contains mud with faint laminations (Fl) (Fig. 5.32). These faint laminations are clearly visible in x-ray images; however, they show little or no visual expression in the split core (Fig. 5.36). Between 317 to 411 cm these laminations appear in regular intervals, often <1 cm thick. A few partial sand layers appear near the bottom of this unit, the upper most being at ~368 cm. Scattered clasts have been identified through this area, including one particularly large clast at ~340 cm. Between ~262-327 cm the sediment became "sticky" and contains a notable absence of laminations in the center of this section of the core. Between 158 to 317 cm laminations appear less often (Fm) and when they are present, they occur in small intervals or as an independent faint lamination. It is possible that these sections have previously contained laminations but through deformation they appear absent. Between 100-158 cm laminations appear in 2 to 4 cm intervals, alternating between a darker and lighter material. Sediment grain size analysis of these two areas reveal that they are both very poorly sorted medium silt. The lighter material in x-ray imaging appears to have a larger mean grain size average (10.45 μm as opposed to the 9.78 μm seen in the darker section) and containing 2.2% more sand. The alternating silt layers are irregularly shaped and oriented both horizontal and diagonal across the axis of the core. At times these layers also contain faint inner laminations (Fig. 5.32). Large clasts can be found throughout the entire core (e.g. Fig. 5.35).

Physical Properties

The magnetic susceptibility generally appears to stay around its average of 165.2 SI x 10^{-5}, however there are two positive peaks around 261 and 203 cm (Fig. 5.33). P-wave and bulk density values tend to decrease up core, likely due to compaction. A large positive peak in p-wave and bulk density has been observed at ~341 cm, which happens to be across from a large clast. Other positive peaks in p-wave velocity have also been identified at 287, 273, 225 and 212 cm up core.

Figure 5.35. Large clasts identified in the gravity core HH17-1290. Left: A subrounded dark green gneiss (or metagabbro) identified at 223.5-225.5 cm (Unit 1.2); right: Subrounded dark green gneiss (or metagabbro) 340-343.5 cm (Unit 1.1).

Elemental Geochemistry

Geochemical ratios of Ca/Fe, Ca/Sum and Zr/Rb tend to decrease up core, where Fe/Sum and K/Sum appear to increase (Fig. 5.34). The Zr/Rb ratio, however, appears to fluctuate with greater intensity down core. Al/Sum, K/Sum and Si/Sum are particularly low in the bottom of the unit, where there is a dense concentration of thin laminations. Beginning around ~150 cm there are lower than average Ca/Fe, Al/Sum, K/Sum, Ca/Sum and Si/Sum ratios, as well as higher Fe/Sum ratios have been identified. At the top of unit two small peaks are observed in Al/Sum and Si/Sum concentrations.

5.2.2.3 Unit 1.3 (0-99.5 cm)

Description

This unit is composed of mud (Fm) that is the same color throughout the unit (excluding the top 4 cm of the core) (Fig. 5.32). Two potential clasts have been identified in the top of the unit in x-ray images but were not visible on the surface when logging the unit. The bottom half of the unit contains small organic streaks at approximately 57-99.5 cm and 43 cm. This unit does not appear to contain any laminations.

Physical Properties

The magnetic susceptibility and bulk density appear to decrease throughout the unit but have a positive peak near the top of the unit (Fig. 5.33). The p-wave velocity remains near its average but has positive peaks around 53 and 36 cm (which match peaks that are also visible in magnetic susceptibility and bulk density).

Elemental Geochemistry

The smallest amount of geochemical fluctuations can be observed in this portion of the core (Fig. 5.34). Ca/Fe appears to decrease up core, and K/Sum, Fe/Sum and Ti/Sum generally increase up core. Mid-way through the unit both Al/Sum and Si/Sum concentrations appear to increase slightly, and then decrease back to around the average for the remainder of the unit.

5.2.2.4 Chronology and sedimentation rate

A single sample of foraminifera was collected at 97 cm in Unit 1.3 and prepared for radiocarbon dating. Most of the species collected were *Melonis barleeanus*, but one or two *islandiella norcrossi* were also sampled. Notably, a high quantity of agglutinated species was also identified (but not sampled). A sample was also collected for radiocarbon dating at 310.5 cm for possibly dating but not enough material was recovered for analysis. Samples in the undated sample contained no agglutinated species or *Melonis barleeanus,* but only a few *islandiella norcrossi*. The calibrated age of the sample from Unit 1.3 is 7160 ± 101 cal. yr. BP (Table 5.3),

which may fall within the HTM (e.g. Briner et al., 2016). The calculated average sedimentation rate from 0-97 cm is 13.55 cm/ka.

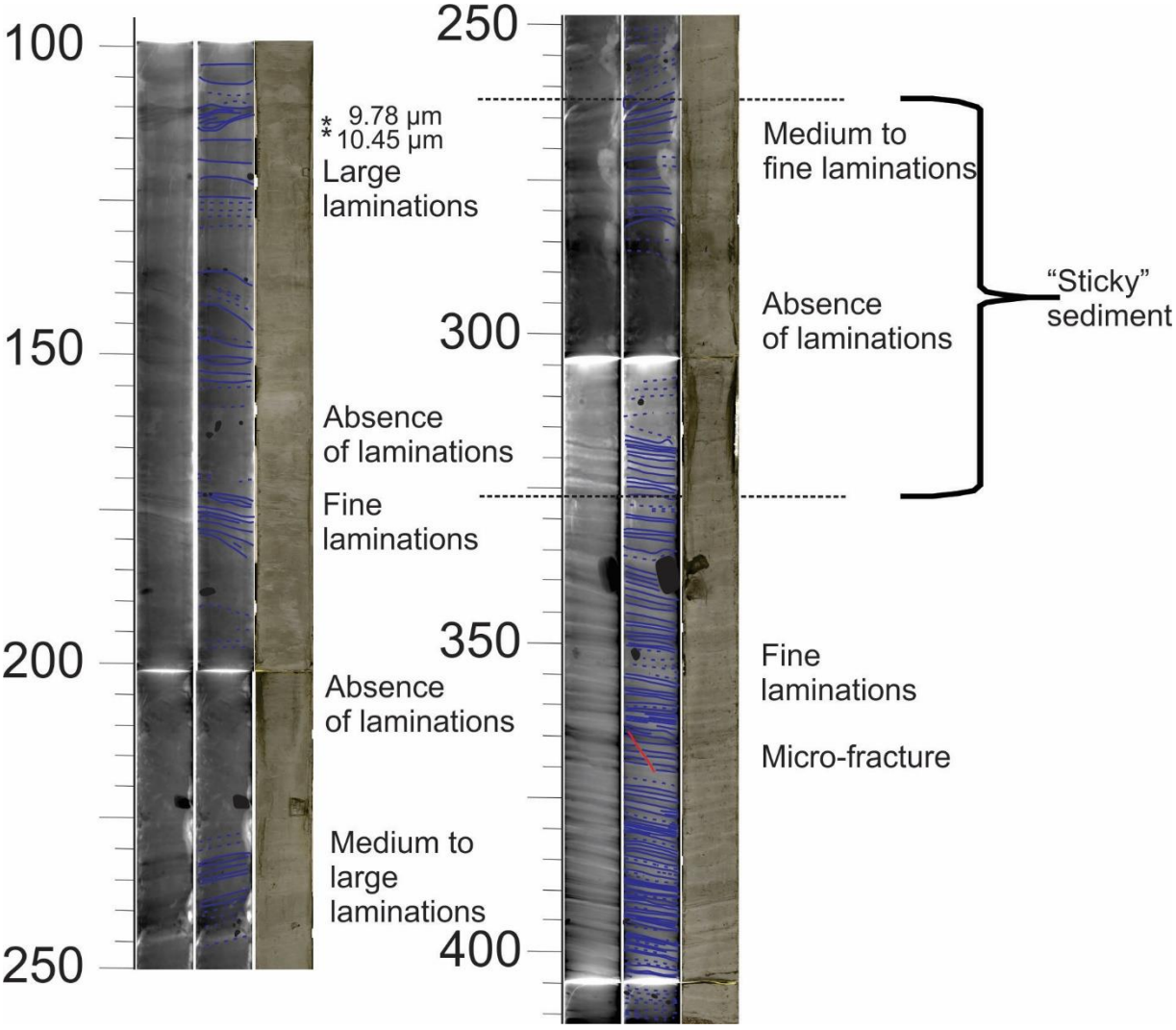

*Figure 5.36. X-ray image of Unit 1.2 with laminated layers highlighted in blue and a microfracture in red. Full blue lines trace a clearly visible lamination boundary and dashed blue lines trace barely visible lamination boundaries. Black circles mark large clasts. *- mark the position of sediment grain size analysis and the resulting mean grain size.*

5.2.2.5 Interpretation

The mud dominated Unit 1.1, with frequent sand laminates, is interpreted as developing from suspension settling from overflow plumes and turbidity-current activity (Cowan et al., 1999; Smith & Andrews, 2000; Ó Cofaigh et al., 2001). The appearance of large clasts through the unit, and core, has been interpreted as the deposition of IRD (Cowan et al., 1999; Forwick & Vorren, 2009). The presence of microfractures in Unit 1.1 has been interpreted as the hydrofracturing of subglacial or proglacial sand and silt by either Soranerbræen or by some other means (Passchier, 2000). The rhythmically laminated muds in Unit 1.2 are interpreted as being the result of ice-proximal suspension-settling from turbid overflow plumes, with additional input from iceberg related deposition (Mackiewicz et al., 1984; Cowan & Powell, 1990; Cowan et al., 1997; Ó Cofaigh et al., 2001). The rhythmic nature of the deposit may be related to alterations in the tidal regime and diurnal fluctuations in meltwater discharge (Cowan & Powell, 1990; Ó Cofaigh et al., 2001). Sections of sediment without laminations in Unit 1.2 may be the result from a brief switch to single sediment source for the area or the deformation of laminations that may have previously occupied that section of sediment. Sediment in Unit 1.3 is interpreted as being the result of suspension settling from overflow plumes from a single source.

5.2.3 Gravity Core HH17-1289-GC-TUNU (Mid-Fjord)

Gravity core HH17-1289-GC-TUNU was collected within a large basin in Section 3 at a water depth of -372 m. The cores length is 245.5 cm and comprises a complex assortment of sand and sandy silt layers. Laboratory results allowed for the division of the core into four broad units that are characterized by an underlying similar lithology. The core log (Fig. 5.37), MSCL data (Fig. 5.38) and XRF (Fig. 5.39) results can be found below.

5.2.3.1 Unit 2.1 (~145-245.5 cm)

Description

This bottom most unit is largely mud dominated (Fl) with laminations and layers of very fine to course grained sand (Sh) as well as sand interspersed throughout the muddy sections (Fig. 5.37).

The bottom 10 cm of the unit has experienced heavy disturbance, likely during the initial collection process. Above, most of the sand layers and lamina are found in the center of the unit. Sand layers often appear interbedded with mud. Layer contacts across the entire unit can be sharp and erosional or occasionally have gradational upper contacts with mud (e.g. ~234, 215, 174 cm). Sediment layers are generally horizontal or have a slight tilt. At times mud layers include increasing amounts of sand in its matrix without becoming sand dominated (e.g. 157 & 169 cm), which may be from post-depositional deformation of sand layers/lamina.

Soft sediment deformation (or load structures) has also been identified at the top of the two mud dominated sections (Fig. 5.40). This is likely due to the higher density of sand relative to the underlying mud. In split core, the top of these two soft sediment deformation structures contains a small clast and may be a diamict, although it is difficult to determine. The bottom of the core also appears to have a similar structure to the soft sediment deformation but is likely just a result of human disturbance (Fig. 5.37). Notably, there does not appear to be any additional depositional structures in unit (e.g. cross laminations, ripples). Two large clasts have also been identified at 192-195 & 226-228 cm within this unit as well (Fig. 5.41).

Sediment grain size analysis from four positions across the unit indicate that the unit coarsens upwards, except for a section of coarser sediment in the middle of the unit (Fig. 5.37). Near the bottom of the core, at 208 cm, a poorly sorted sediment sample with a mean grain size of medium silt was identified. This sample contains 12.6% clay, 64.7% silt and 22.7% sand. Above this, at 184 cm, the sediment transitions to a mean grain size of fine sand, with a drop-in clay and silt content to 1.9 and 19.4%, respectively. At 168 and 147 cm the sediment becomes very coarse silt, however the sorting transitions from very poorly sorted, to poorly sorted, between them. Clay content increases relative to the fine sand sample at 184 cm but decreases between the samples 168 and 147 cm (from 7.1 to 6.9%). The percentage of sand in these sediment samples also decrease between these samples, transitioning from 52.3 to 32.7%.

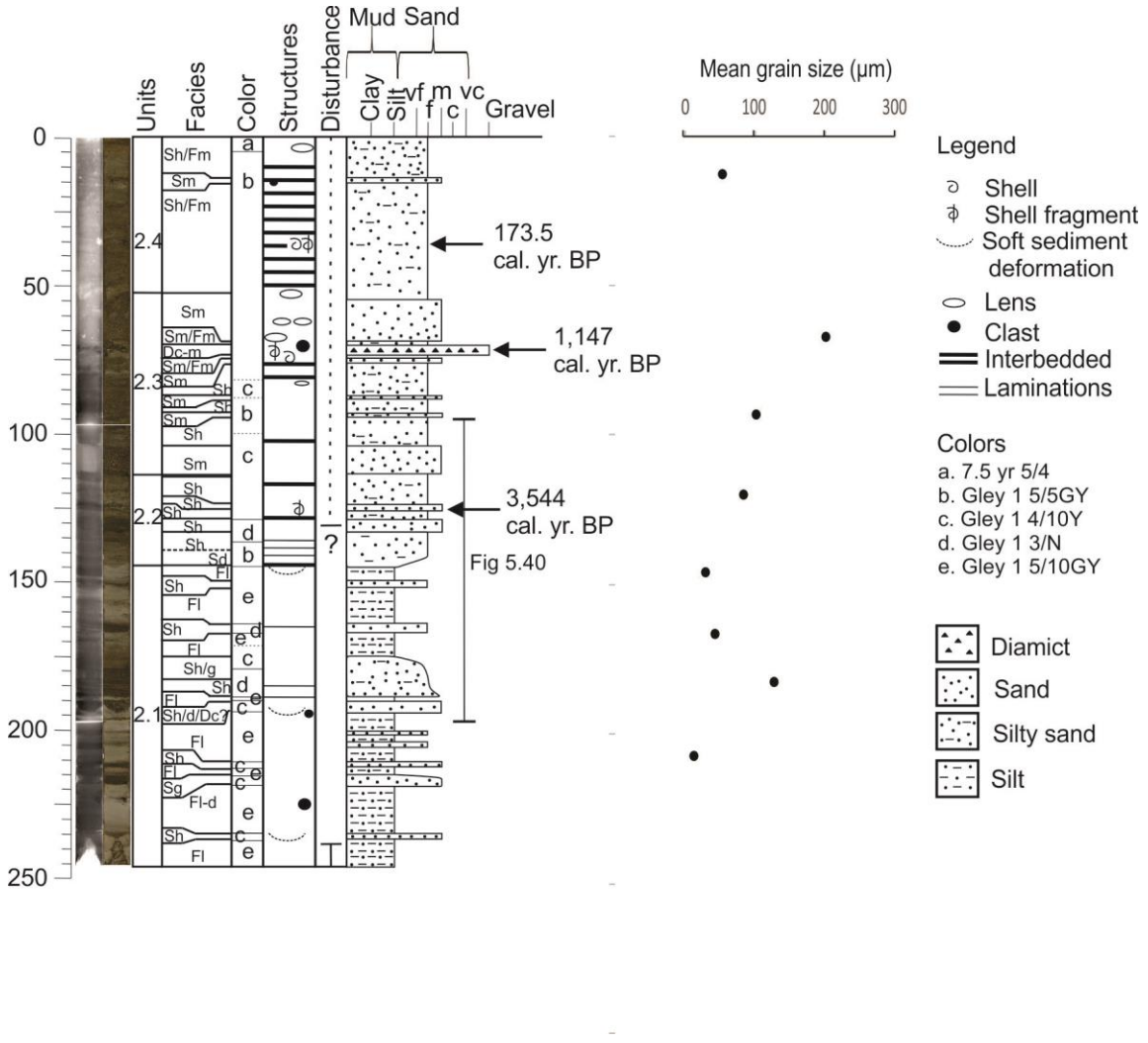

Figure 5.37. Lithological core log of HH17-1289-GC-TUNU. Includes the unit divisions, facies, color, structures, disturbance and mean grain size results for specific positions. The location of Figure 5.40 can be seen in brackets.

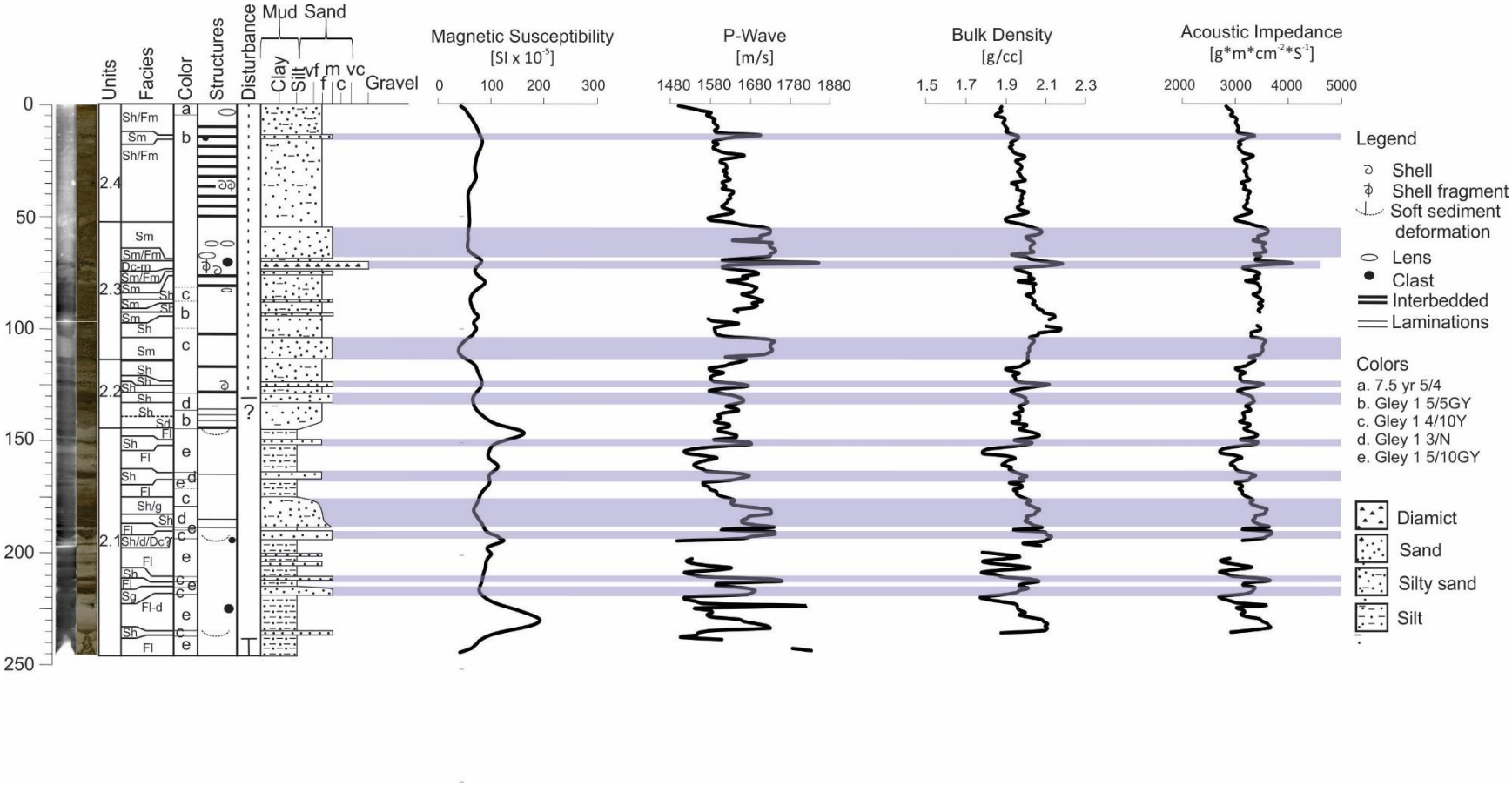

Figure 5.38. Results from the Multi Sensor Core Logger (MSCL) on gravity core HH17-1289-GC-TUNU. Blue lines outline specific sand and diamict layers.

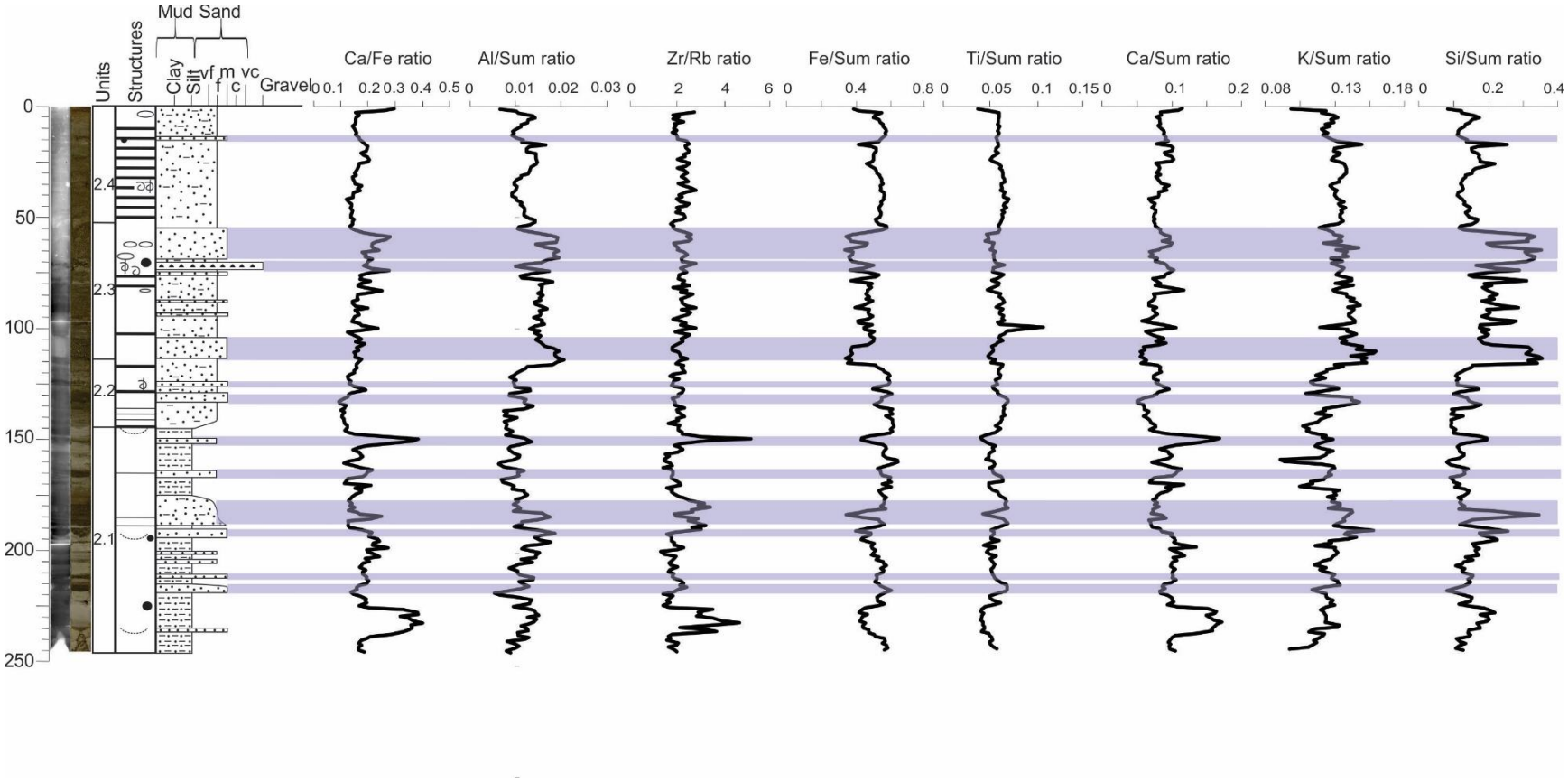

Figure 5.39. Results of select elemental ratios using the X-Ray Fluorescence (XRF) equipment on gravity core HH17-1289-GC-TUNU. Blue lines outline specific sand and diamict layers.

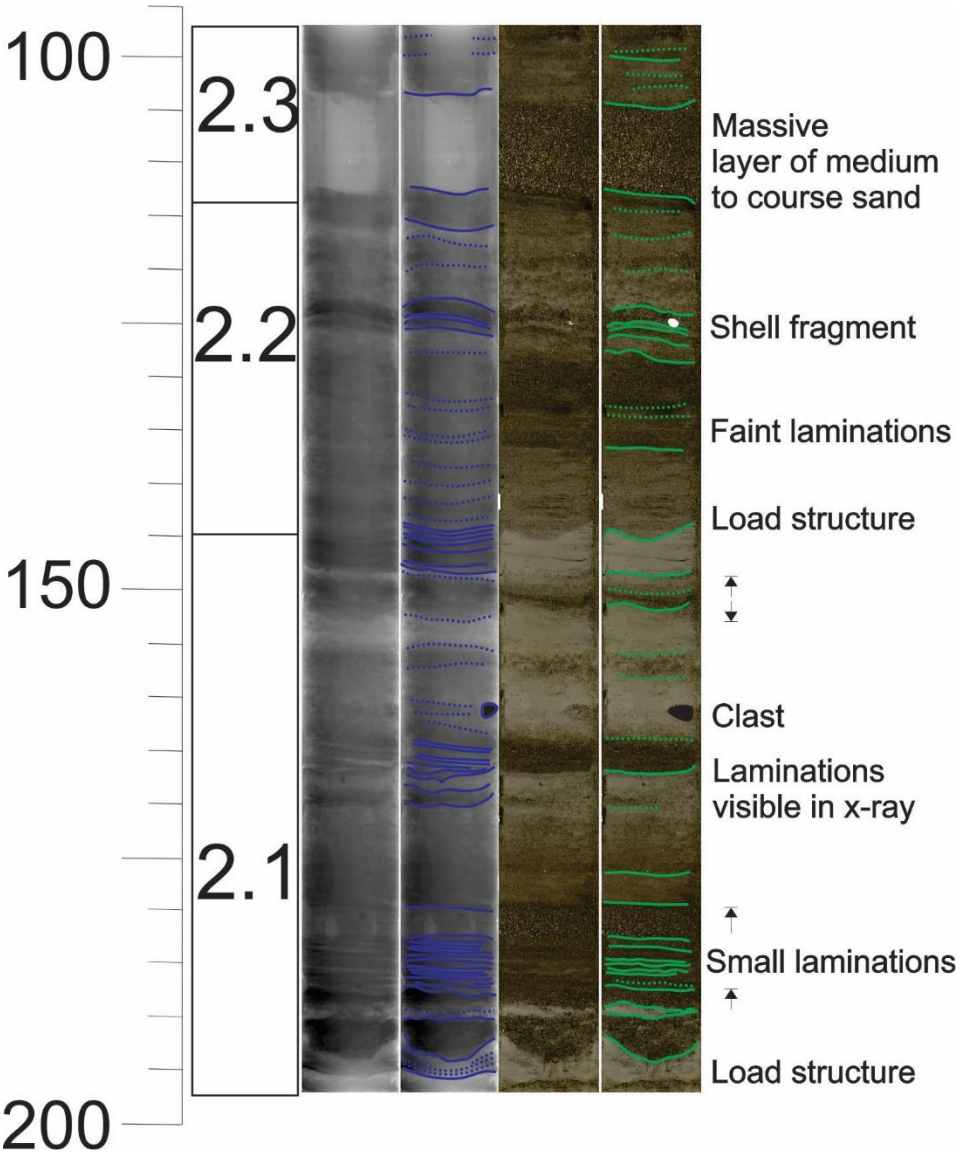

Figure 5.40. X-ray images of the full core and photographs of the split core of HH17-1289. Laminations visible in x-ray and in split core are highlighted in blue and green. Small arrows indicate if there is a gradational contact between layers (the arrow is pointing towards finer grains). Unit numbers are indicated on the left and notable features are indicated on the right. See Figure 5.37 for the location of this figure on the core log.

Figure 5.41. Large clasts identified in gravity core HH17-1289. Left: an angular to subangular, foliated dark green, potential metagabbro (or amphibolite) identified at 71-73 cm downcore (Unit 2.3); center: an angular to subangular porphyritic, or garnet rich, mafic to ultramafic rock collected at 192-95cm (Unit 2.1); right: an angular to subangular dark green (possible) gabbro identified at 223-226cm (Unit 2.1).

Physical Properties

Positive peaks in magnetic susceptibility have been identified at 231 cm (191.1 SI x 10^{-5}), 195 cm (123.4 SI x 10^{-5}), 162 cm (112.7 SI x 10^{-5}) and 147 cm (161.7 SI x 10^{-5}) (Fig. 5.38). It is noteworthy that some of the peaks in magnetic susceptibility can be found across from soft sediment deformation structures. The p-wave and bulk density result fluctuate frequently through this section. Positive or negative peaks in these attributes often coincide with a layer of sand or a clast in the mud-rich section. Local variations in p-wave velocities and bulk density are overprint by a slight downcore increasing trend in the top half of the unit. This can also be found in units 2.2 and 2.3 but not 2.4 and is likely the result of sediment compaction.

Elemental Geochemistry

Near the bottom of the unit, mostly in a mud dominated area, the concentrations of Ca/Fe, Zr/Rb, Ca/Sum and Si/Sum also have a prominent positive peak (Fig. 5.39). Across from the clast at 192-195 cm, a smaller positive peak in K/Sum and Si/Sum have also been observed. Near the center of the unit, in a sand rich region, values for Si/Sum ratios appear to increase substantially,

where Fe/Sum and Ti/Sum concentrations appear to drop. A positive peak in Ca/Fe, Zr/Rb, Ca/Sum, Si/Sum ratios and a negative peak in Fe/Sum and Ti/Sum ratios has been observed at a mud dominated region at the top of the unit, at ~151 cm.

5.2.3.2 Unit 2.2 (114-145 cm)

Description

Unit 2.2 is a complex assortment of muddy fine-grained sand that may have experienced some degree of disturbance, particularly in the upper section of the unit (Fig. 5.40). The unit is interbedded with sand layers, some of which are composed of medium darker grains. This can be predominantly seen in the bottom of the unit where faint laminations have been identified in x-ray images (Fig. 5.40). Sediment grain size analysis at ~121 cm down core reveal the material to be a very poorly sorted fine sand composed of 67.8% sand, 27.6% silt and 4.6% mud. The sand fractions are composed of 0.4% very coarse sand, 3.4% coarse sand, 18.9% medium sand, 26.5% fine sand and 18.6% very fine sand. The contact between beds appears more horizontal in the bottom of the unit but becomes increasingly irregular up core. No apparent depositional structures have been identified.

Physical Properties

Between 144 to 133 cm the magnetic susceptibility decreases from 125.3 to 65.6 SI x 10^{-5} (Fig. 5.38) and increases again at 125 cm. The magnetic susceptibility then appears to decrease in the top half of the unit (125 to 114 cm) from 82.3 to 53.1 SI x 10^{-5}. A small peak in p-wave velocity and bulk density of the sediment has been observed across from a sandy unit at 125-126 cm. Like in the other units, the p-wave and bulk density appear to increase slightly downcore.

Elemental Geochemistry

Throughout most of the unit Fe/Sum ratios appear to be higher than average, other than for two positions where the Fe/Sum concentration dip down beneath the unit's average (at 129 and 136 cm) (Fig. 5.39). At these two positions, Al/Sum, K/Sum and Si/Sum ratios also appear to have

positive peaks. At 125 cm, near the position of the identified shell fragment, Ca/Fe and Ca/Sum ratios increase positively.

5.2.3.3 Unit 2.3 (114-52 cm)

Description

This unit is largely characterized by layers of medium to coarse grained sand at the top and bottom of the unit. Sediment grain size analysis within the upper most medium to coarse sand section, at 68 cm depth, reveals that the sample is a poorly sorted fine sand composed of 10.9% very fine sand, 19.1% fine sand, 42.5 % medium sand, 11.3% coarse sand and 1.2% very coarse sand. Both coarser sections contain clearly visible quartz and biotite grains and appear to be massive structureless layers. This lower coarser layer has a sharp, slightly tilted lower contact with Unit 2.2. The upper coarser grained layer contains mud lenses in split core and anomalies in x-ray imaging. Both the upper and lower contacts of this bed are chaotic and irregular. Between these coarser layers is a section of fine-grained sand and mud with interbedded medium grained sand layer. Sediment grain size analysis of a sample from 94 cm revealed that the sample consists of poorly sorted very fine sand, with 31.5% fine sand, 18.9% medium sand and 3.4% coarse sand. At ~70-73.5 cm a poorly sorted diamict has been identified, containing larger clasts and shell fragments.

Physical Properties

Lower than average magnetic susceptibility values have been identified between 105-114 cm, at the bottom of the unit (Fig. 5.38). This coincides with an increase in the p-wave velocity and a general decrease in the bulk density. These values are observed across from a darker, more massive sand body that appears as a light, white color in x-ray imaging. P-wave and bulk density values are also particularly low at the top of the core, which may correspond to small mud rich inclusion or layer. The magnetic susceptibility appears to follow the average values for the unit for the top three-fourths of the unit, other than two small positive peaks that appear near a layer interpreted as a diamict at 70-73.5 cm. A sharp peak in p-wave and bulk density values have been identified within the same region.

Elemental Geochemistry

At 59 cm near the top of the unit, there is a positive peak in Ca/Fe ratios that declines through the remainder of the unit (excluding a few scattered positive peaks, such as the one at 69 cm) (Fig. 5.39). The top and bottom of the unit, where coarser sand beds have been observed, have higher ratios of Al/Sum and Si/Sum. A large positive peak in Ti/Sum and Ca/Sum, and a strong negative drop in K/Sum, has also been observed below the center of the unit.

5.2.3.4 Unit 2.4 (53- 0 cm)

Description

This unit is largely composed of course silt and fine-grained sand mixed with mud and is interbedded with other layers of sand that are a similar grain size (Fig. 5.37). Sediment grain size analysis of a sample from 13 cm down core resulted in a very poorly sorted very coarse silt, composed of 3.6% coarse sand, 17.3% medium sand, 21.9% fine sand, 13.4% very fine sand, 9.8% very coarse silt, 9.0% coarse silt, 8.2% medium silt, 6.6% fine silt, 4.5% very fine silt and 5.7% clay. It is quite likely that this unit has experienced a heavy amount of disturbance, especially on its flanks. At ~35-37 cm a round organic rich inclusion was identified, which contained plant material and intact and broken shells.

Physical Properties

Magnetic susceptibility appears to increase from the bottom of the unit to 19 cm and then decreases for the remainder (Fig. 5.38). Two peaks in p-wave values have been observed at 23 and 14 cm depth and the topmost of these two peaks appears to match the position of a coarser sand grain layer. The p-wave velocity and bulk density gradually increases throughout the entirety of this unit, likely due to compaction.

Elemental Geochemistry

Positive peaks in Al/sum, K/Sum and Si/Sum ratios have been found to match each other near the top of the unit, however these same ratios appear to decrease substantially across from the organic patch identified at 35-37 cm (Fig. 5.39). One of the above-mentioned positive peaks, at

17 cm downcore, may be related to the presence of a nearby a clast. Concentrations of Ca/Sum are high at the top of the core, but dramatically decrease within the first few centimeters. Fe/Sum and Ti/Sum concentrations appear to increase a few centimeters down core, but gradually decrease afterwards.

5.2.3.5 Chronology and sedimentation rate

Three mollusk samples were identified across HH17-1289 and were prepared for radiocarbon dating (Table 5.3; Fig. 4.4). The first of these samples was a full Yoldiella lenticula shell collected in an organic patch (surrounding by plant material and other shell fragments) at 35 cm depth in Unit 2.4. The calibrated mean radiocarbon age appears to be 173.5 ± 70.5 cal. yr. BP. This may place the deposition of this sample during the 'little Ice Age' (e.g. Jennings & Weiner, 1996). The second sample was collected at 71 cm in Unit 2.3 and was a large, 3 cm long half of a Hiatella arctica. Radiocarbon results indicate that this sample was deposited at 1147 ± 51 cal. yr. BP, which corresponds with the Medieval Warm Period (Jennings & Weiner, 1996; Wagner et al., 2008), although it could also potentially fall within the very end of the 'Dark Age Cold Period' (e.g. Helama et al., 2017). The third sample was a bivalve fragment that was collected at 125.5 cm in Unit 2.2. Lab results dated this fragment to 3544 ± 63 cal. yr. BP. This falls within a time frame in which the climatic conditions are not well constrained in east Greenland (e.g. Wagner et al., 2008; Briner et al., 2016) and will therefore be discussed in greater detail in the following chapter. Calculated average sedimentation rates from the top of the core and between these three samples resulted in 201.73 cm/ka, 31.39 cm/ka and 15.38 cm/ka for the core intervals between 0-35 cm, 35-71 cm and 71-125.5 cm. The clear trend in these results suggest that sedimentation rates have been increasing in modern times.

5.2.3.6 Interpretation

Between these four units, there is an overall upwards coarsening trend. The bottom most unit, Unit 2.1, contains sandy mud (with a mean grain size of silt where sampled) with sand layers interspersed periodically throughout it. It is likely that multiple processes are responsible for the formation of this unit. The sandy mud may be the result of suspension settling from overflows, sourced from glacial meltwater and/or fluvial activity (Benn & Evans, 2010). Larger sediment grains in the mud may be the product of iceberg or sea ice rafting, potentially from glacial,

aeolian, fluvial of colluvial sources (Benn & Evans, 2010). Large clasts identified in this unit are interpreted as Ice rafted debris (IRD) (e.g. Forwick & Vorren, 2009). The intermittent layers of sand in this unit likely developed from underflows, sourced from glacial and non-glacial streams and slope failures (Benn & Evans, 2010). The layers appear structureless, and at times relatively uniform, which suggests deposition in a rapid, instantaneous event. This, as well as the normally graded layers, are characteristic of the (A) layer of the Bouma sequence (Benn & Evans, 2010). Laminations seen in x-ray images of some sand layers are interpreted as being the result of short lived fluctuations in the sedimentation conditions of the area (Boggs Jr., 2012).

Sand layers from the overlying Unit 2.2, 2.3 and 2.4 are believed to have formed predominantly from similar underflow events. Horizontal Interbedded mud layers may represent periods of briefly returning to an environment where suspension settling was the dominant sedimentation process. Mud lenses may have become emplaced in sandy layers as a result of erosional forces related to a turbidity current (e.g. Postma et al., 2009; Li et al., 2017). It is difficult determine the origin of the diamict in Unit 2.3, however it may possibly be the result of sea ice or iceberg rafting/dumping (Benn & Evans, 2010). The organic patch identified in Unit 2.4 may have formed through a similar erosional mechanism as the mud lenses in Unit 2.3, however little attention has been given to the plant species in this inclusion, therefore it is difficult to confirm the true provenance of this material. Analysis of the bathymetric data at this coring site revealed that the core was collected near a sediment lobe, where it is possible that this one of the main sediment sources for the area (see Discussion).

5.2.4 Gravity Core HH17-1309-GC-TUNU (Southwest Dove Bugt)

Gravity core HH17-1309-GC-TUNU was collected outside of Bessel Fjord in southern Dove Bugt along the southwestern sloping sidewall of a large channel-like feature (Fig. 5.25). The core was collected in five sections and is a total length of 474.55 cm. This core has divided into four separate units: Unit 3.1 (380-474.55 cm), Unit 3.2 (87.5-380 cm), Unit 3.3 (28-87.5 cm) and Unit 3.4(0-28 cm). An larger quantity of sediment samples were collected from this core for sediment

grain size analysis (e.g. Table 5.2 & Fig. 5.42). See Appendix B for additional information on sediment grain size distribution across the core.

5.2.4.1 Unit 3.1 (380-474.55 cm)

Description

This unit consists of laminations of mud (Fl) with thin laminations of sand (Sh) (Fig. 5.42). The unit is predominantly a reddish-purple color (5R 3/1), often inner mixed with red (5R 4/4), light grey (N 8/) and grey (5Y 4/1) sediment (Figs. 5.45 & 5.46). Here, the orientation of the lamination's ranges from horizontal to wavy to irregular, sometimes shifted due to the presence of micro-fractures (Fig. 5.46). The top ~15 cm of Unit 3.1 contains a chaotic mix of different colors (Fig. 5.45). This includes the grey color seen in most of the remainder of the core above this unit (5Y 4/1) mixed with a reddish-purple (5R 3/1) with a few streaks of light grey (Fig. 5.45). This variation in color appears as horizontal to irregular laminations. This region between ~380 and 395 cm is referred to as a "transition zone" between a dominate reddish-purple color in the remainder of Unit 3.1 and the grey color observed in the overlying sediments.

Three sediment samples were collected for grain size analysis at 469.25 cm, 433.25 and 397.75 cm (Fig. 5.42). It was determined that each of these samples were very poorly sorted fine silt with a mean grain size of 6.1, 5.2 and 4.6 μm, respectively. Although the average grain size decreases up core, the quantity of sand grains in each sample (7.1%, 8.4 and 2.5% sand, respectively) does not appear to increase exponentially. The bottom of the unit contains a larger quantity of very fine-grained sand laminations than the top. A single large red mud lens was also identified at 452 cm and a single large clast was identified in x-ray images at 390 cm; however, it did not appear in the working half of the core (Fig. 5.45). Compared to the other units, it appears that Unit 3.1 contains in increased quantity of clay and a decreased quantity of silt (Fig. 5.42).

Physical Properties

The magnetic susceptibility of Unit 3.1 contains two postive peaks near the bottom of the unit (at 464 and 448 cm) and tends to increase to the top of the unit (Fig. 5.43). A peak in bulk density

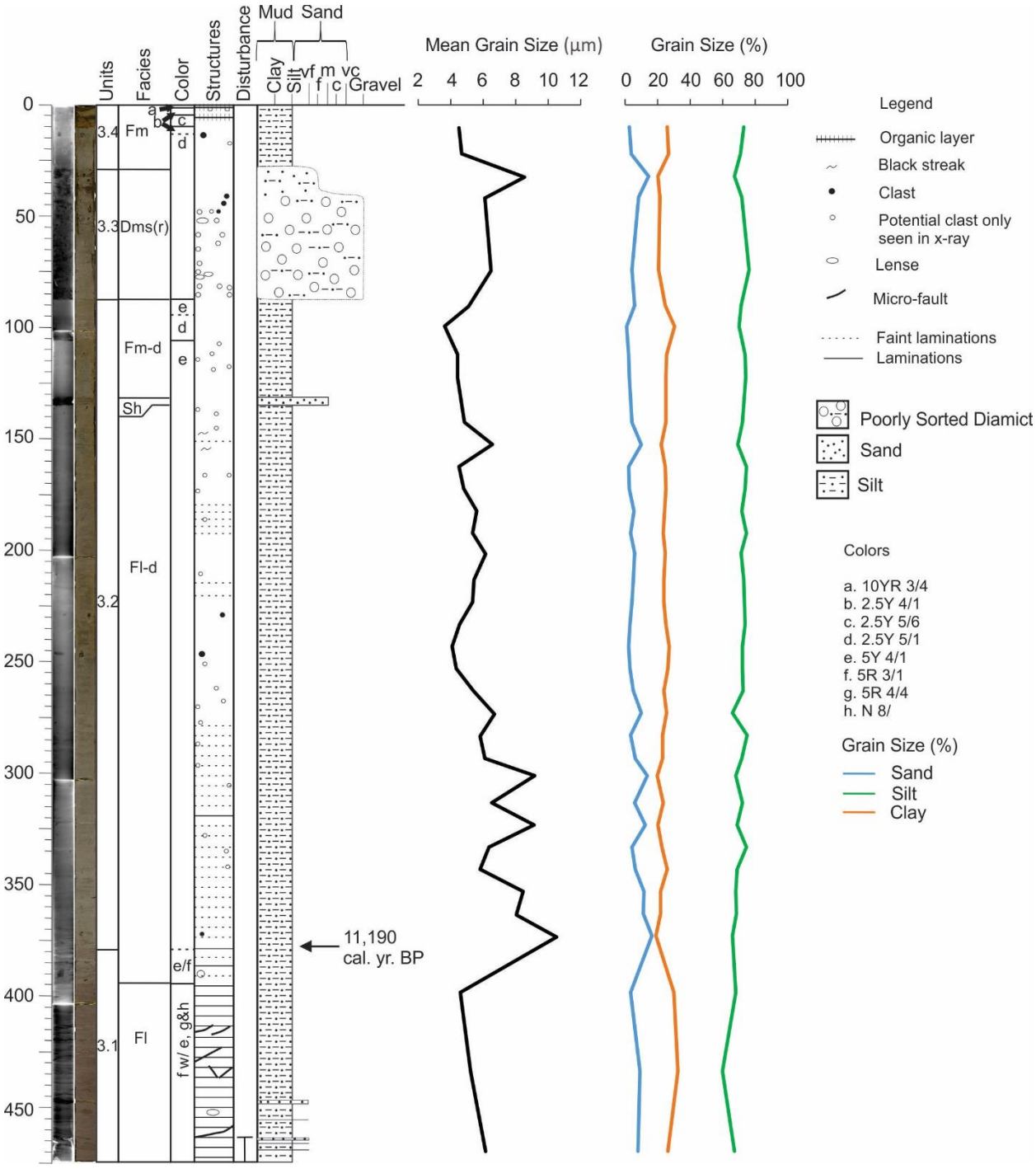

Figure 5.42. Lithological core log of HH17-1309-GC-TUNU. Includes the unit divisions, facies, color, structures and disturbance. Mean grain size and percentage of sand, silt and clay from sediment grain size analysis are presented to the right of the lithographical core log.

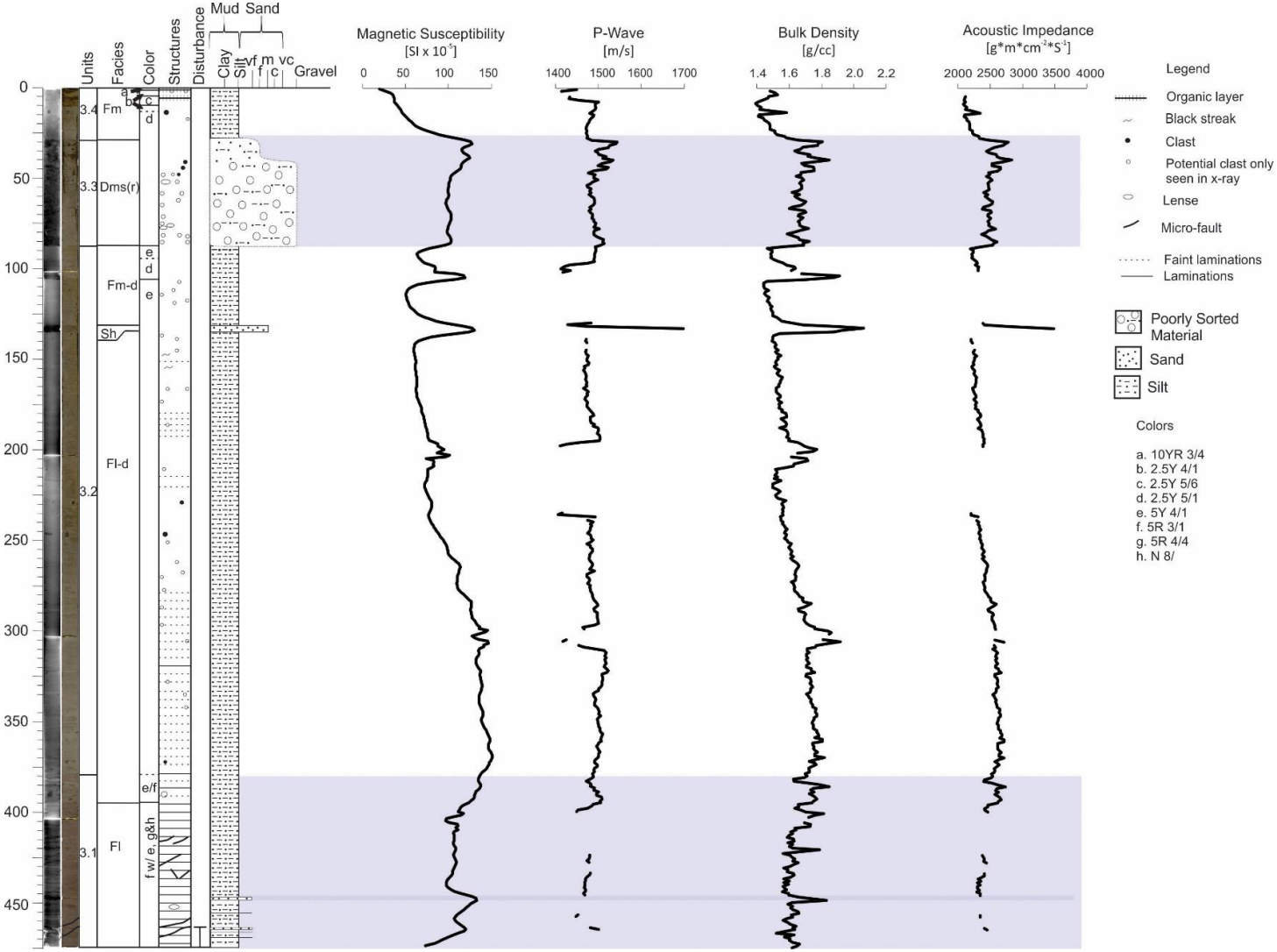

Figure 5.43. Results from the Multi Sensor Core Logger (MSCL) on gravity core HH17-1289-GC-TUNU. Blue sections encompass Unit 3.1 and 3.3.

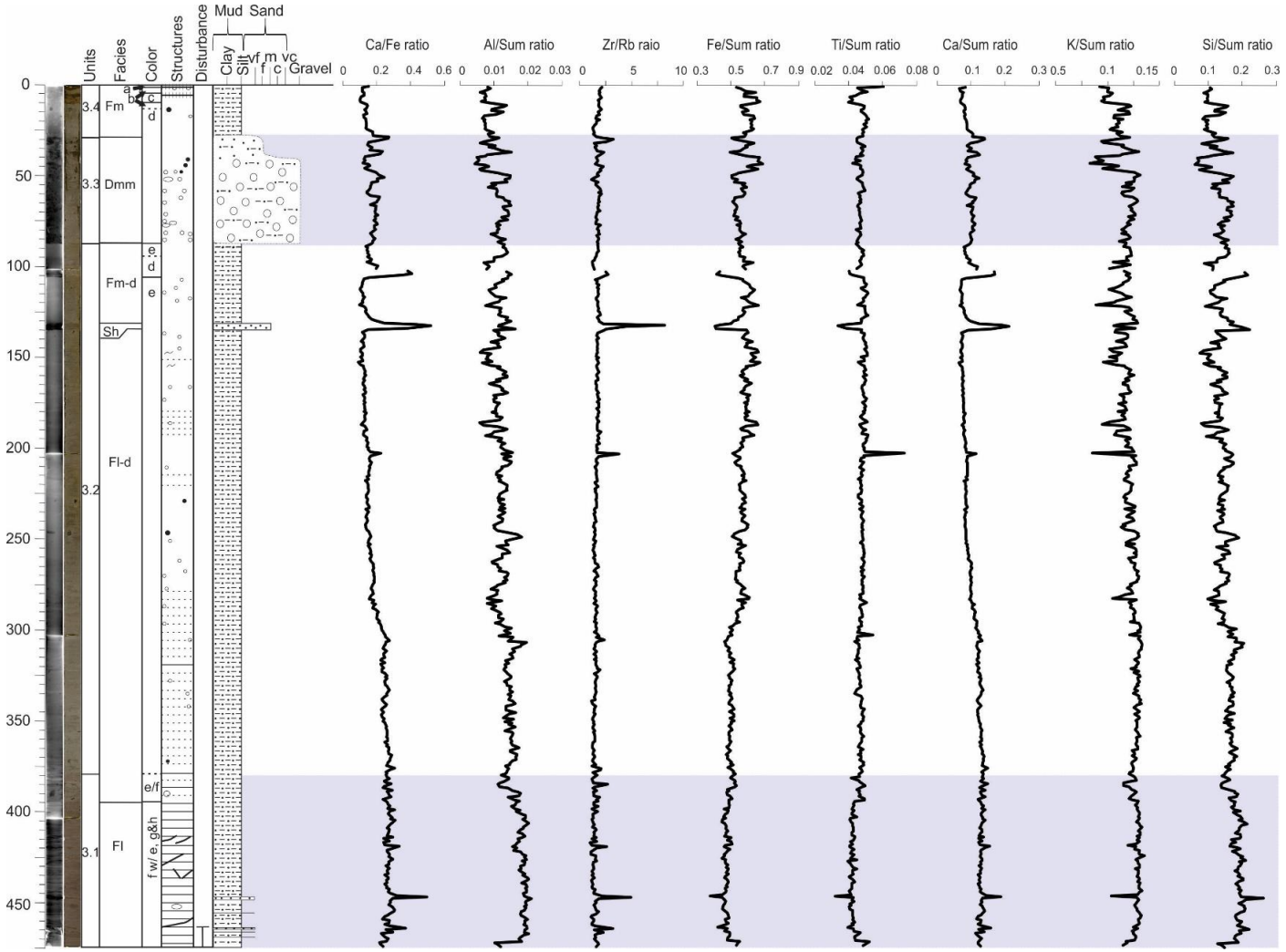

Figure 5.44. Results of select elemental ratios using the X-Ray Fluorescence (XRF) equipment on gravity core HH17-1309-GC-TUNU. Blue sections encompass Unit 3.1 and 3.3.

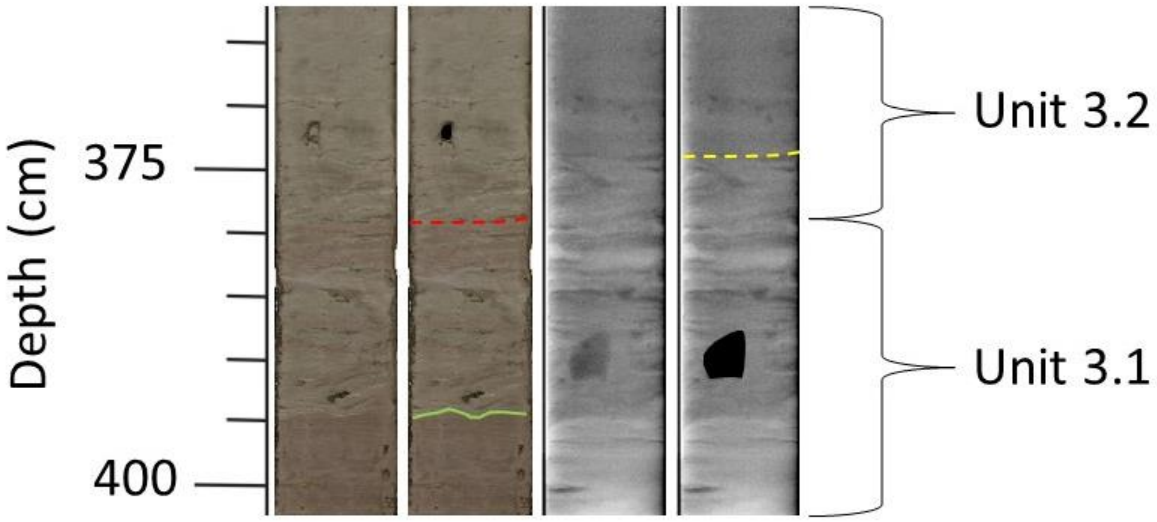

Figure 5.45. Split core and x-ray images of the "transition zone" at the top of unit 3.1. The redline represents the top of the unit, the yellow line represents the possible continuation of non-purplish red layers for an additional 5 cm up core and the green marks the lower boundary of the "transition zone". Black objects highlight the positions of large clasts.

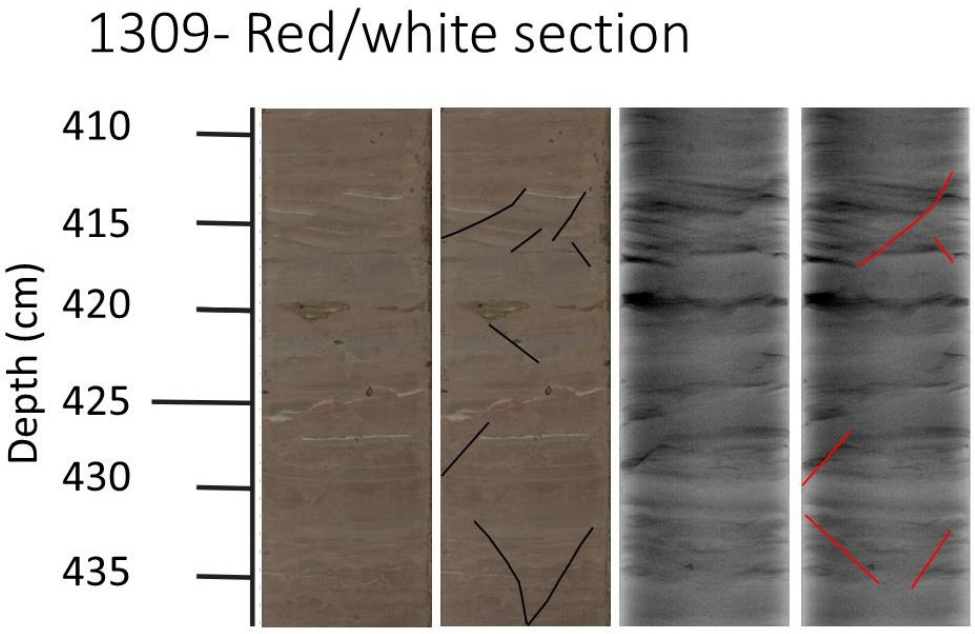

.

Figure 5.46. Split core and x-ray image of microfractures, irregular laminations and a sand layer. Observed microfractures in both split core and x-ray images are expressed in black and red.

has also been identified at 448 cm, which appears to corispond with a layer of sand. There is a small positve peak in the p-wave velocity at the top of the unit, however, beneath this there is very few p-wave values that contain high enough rates to be considered releable (and have therefore been excluded from this analysis).

Elemental Geochemistry

Throughout this unit there is a minor decrease in Al/Sum and Si/Sum concentrations up core (although there is a slightly drop in the concentraiton of these chemcail consitituents at the top of the unit), as well as an increase in Fe/Sum and Ti/Sum (Fig. 5.44). Positive peaks Zr/Rb, Ca/Sum and Si/Sum, and negative peaks in K/Sum, Ti/Sum and Fe/Sum can be seen occuring simultaneously, and might appear with the presence of sand grains. The wide range of colors seen in this section does not appear to be reflected in the geochemistry results.

5.2.4.2 Unit 3.2 (87.5-380 cm)

Description

Unit 3.2 is 292.5 cm in length and predominantly a grey (5Y 4/1) colored mud with occasional large clasts (Fl-d). The bottom of the unit contains a few streaks of grey that are a slightly different color (Fig. 5.47), however the color of the unit appears to vary very little in the remainder of the core. X-ray images also reveal that this small segment at the bottom of the core has internal characteristics that are similar to the top of Unit 3.1 (Fig. 5.46). The grey colors observed at the bottom of the unit also appear in a small 1.5 cm tall layer at ~322 cm depth and is underlined by a small reddish-purple irregular layer (Fig. 5.47). Near the top of the unit (~95-111 cm), the color appears to change briefly to a grey 2.5Y 5/1.

Sediment grain size analysis of this gravity core reveals that sediment is very poorly sorted to poorly sorted, with a mean grain size of fine silt. The exceptions are at the bottom of the unit, as well as at 322.75 and 300.75 cm, where the mean grain size is medium silt and at 322.75 cm and at the top of the unit where the mean grain size is very fine silt. The percentage of sand in the bottom of the unit is substantially higher at the bottom of the core as well as in one interval near the top of the core (Fig. 5.42). These peaks generally appear when there is a decrease in the

percentage of silt. The percentage of clay in the unit remains around its average, although there is a positive peak in clay near the top of the unit and drops in the quantity of clay when sand increases. It is noteworthy that the sample collected from 322.75 cm was on the light grey material shown in Fig. 5.47 rather than the typical 5Y 4/1 grey sediment. At ~132-135 cm a pronounced sand layer was sampled, and the resulting mean grain size was fine sand, composed of 78.3% sand and 21.7% mud. Two clasts have been identified within this unit in the split core (Fig. 5.48), while additional material assumed to be clasts have been identified in x-ray images and can be found throughout the unit (Fig. 5.42).

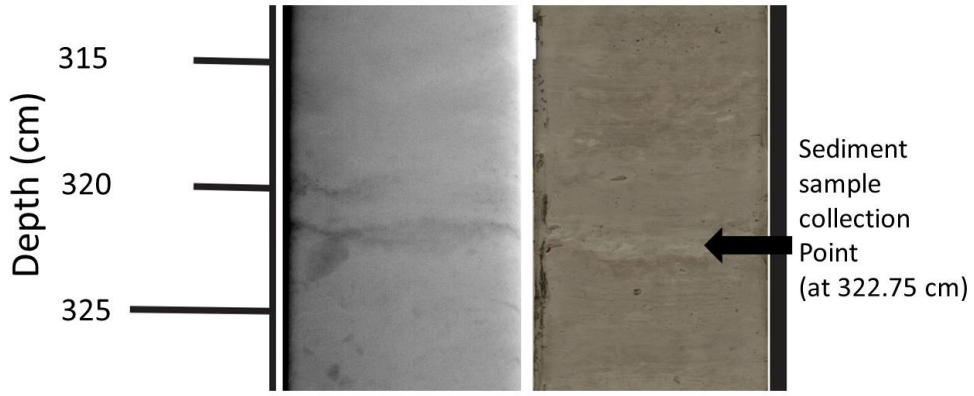

Figure 5.47. Image of the light grey and thin red layer identified within unit 3.2. The note on the side of the figure indicates the location of a single sample extracted for grain size analysis.

Physical Properties

The magnetic susceptibility, the p-wave velocity and bulk density tends to decrease up core, although both parameters appear to start increase slightly at the bottom of the unit (Fig. 5.43). Two postive peaks in magnetic susceptibility and bulk density have been identified near the top of the unit, one of which is a cross from a sand layer. In the center of the unit, at ~200 and ~300 cm, there also appears to be positive peaks in magnetic susceptibility and bulk density with a small dip in both of these reading in the middle of the peaks.

Figure 5.48. Large clasts extracted from HH17-1309-GC-TUNU. Left: angular to subangular dark green possible gabbro identified at 229.75-230.75 cm downcore; right: subrounded dark green and pink gneiss (or metamorphosed granite) identified at 244.25-247.25 cm.

Elemental Geochemistry

Ca/Fe and Al/Sum ratios appear to decrease up core where Ti/Sum ratios tend to increase. Two prominent positve peaks in Ca/Fe, Zr/Rb, Ca/Sum and Si/Sum, and negative peaks in Ti/Sum and Fe/Sum, have been observed at the top of the unit (near where there were also peaks in magnetic susceptiblity and bulk density) (Fig. 5.44). Concentraitons of K/Sum and Si/Sum appear more sporadic than unit 3.1, but more centered around the average thans units 3.3 and 3.4.

5.2.4.3 Unit 3.3 (28-87.5 cm)

Description

Unit 3.3 exhibits properties of matrix supported, stratified diamict with evidence of resedimentation (Dms(r)) with a sharp upper and lower boundary (Fig. 5.49). In split core it is

difficult to determine if the unit has any grading or structure, however through x-ray imaging internal characteristic become clearer.

The bottom of this unit is a section of assorted grain sizes (mud to gravel), that is (possibly) weakly stratified and contains pockets of mud and/or stringers of coarser sediment grains. Patches of mud observed in the split core appear to contain a different color relative to the surrounding material. A sediment sample collected from 74 cm reveal that the matrix is poorly sorted, and the mean grain size is a fine silt composed of 3.5% sand and 96.5% mud. Above this on the x-ray images there is a layer of lighter and darker material (found between the yellow lines in Fig. 5.49). A sediment sample taken at 41.5 cm (within the lighter material in x-ray imaging) reveals that this is poorly sorted mud (92.6%) with a mean grain size of fine silt. The top ~12 cm exhibits a wavy interlay of darker and lighter material which may represent convolute bedding. A sediment sample taken at 32 cm reveals that the sediment is very poorly sorted and is composed of 13.6% sand and 86.4% mud with a mean grain size of medium silt. Based on the sediment grain size analysis of these three samples it does not appear that this unit is grading in any direction, however additional sampling may be required to say this conclusively. Color variations in the core is not particularly obvious. The transition into the unit from Unit 3.2 is relatively clear as the material is no longer 5Y 4/1. At approximately 60 cm, and the top of the unit, the color may change slightly, however it is difficult to determine with visual observations.

Physical Properties

Magnetic susepitblity, p-wave and bulk density values all appear to increase throughout the length of the unit (Fig. 5.43). These parameters all have a positive peak at the top of the unit then tend in sharply decrease. These values differ from the normal expected trends in a core experiencing greater compaction with depth.

Elemental Geochemistry

The bottom half of the unit contains geochemical concentrations that are close to the average values for the dataset, and appear to have zero substantial positive or negative peaks (Fig. 5.44).

The upper half of the unit shows more diversity. There is an initial positive peak at ~30 cm in Ca/Fe, Zr/Rb and Ca/Sum and drop in Fe/Sum and K/Sum. Within the upper portion of the unit there are also three distinct peaks in Al/Sum, K/Sum and Si/Sum ratios have been identified at 29, 37 and 50 cm. Substially low ratio values of these three chemical consitutents can be seen between these positive peaks. Fe/Sum appears to show the reverse trend of Al/Sum, K/Sum and Si/Sum.

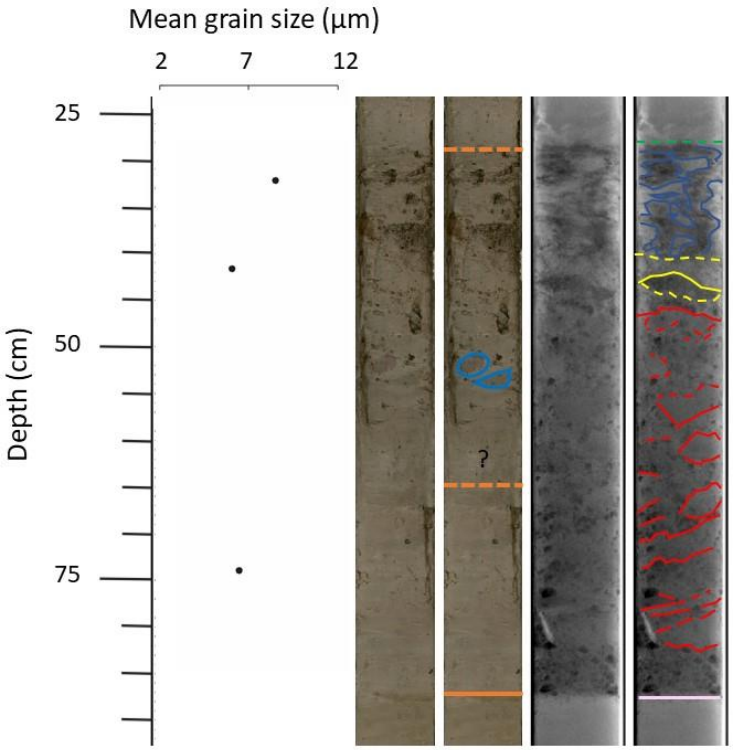

Figure 5.49. Photograph of Unit 3.3, highlighting unique features seen visually in split core and in x-ray images of the full core. Orange lines- potential changes in color; light blue- patches of mud; green line- beginning on the unit, containing "wavy" bedding (in dark blue); yellow line- boundary between "wavy " bedding and what appears to be homogenous section of mud and possibly sand; red lines- outline section of mud and potential faint bedding within the poorly sorted bottom half of the unit; pink- lower boundary of Unit 3.3. The graph to the left contains the mean grain size of three points across the unit, obtained using Folk & Ward (1957) *method of grain size analysis.*

5.2.4.4 **Unit 3.4 (0-28 cm)**

Description

This 28 cm long unit consists of grey mud (Fm) with a wide degree of color variation within the first half of the unit (Fig. 5.50). This transition includes 10YR 3/4 at the top of the core and

transition to 2.5Y 4/1 & 2.5Y 5/6 beneath it. At approximately 10 cm the unit changes to a grey, 2.5Y 5/1 color. The grain size throughout the entirety of the section appears consistent, excluding clasts that have been identified in split core and x-ray images (Fig. 5.50). Grain size analysis of sediment collected at 22 and 10 cm depth revealed that the material is a poorly sorted with a mean grain size of fine silt. Between these two samples, it appears that the percentage of sand increases from 3.1% at 22 cm to 1.9% at 10 cm. Along with this the average grain size increases from 4.670 to 4.482 μm up core. Generally, this section of the core resembles a similar lithology to Unit 3.2.

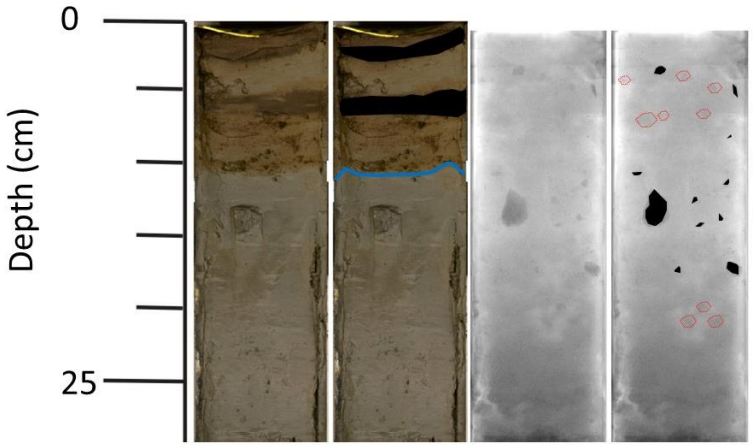

Figure 5.50. Split core and x-ray images of Unit 3.4. Core images with black lines indicate black material interpreted to be organic. The blue line denotes the transition from an orange oxidized section to a grey colored section. Black dots in x-ray images highlight larger clasts and red circles surround potential clasts not easily identifiable in x-ray images.

Physical Properties

All of the physical properties tend to decrease up core (Fig. 5.43). The p-wave velocity has a peak at the top of core, but then tends to decrease further down core. There are peaks in bulk density and p-wave at the top of the core, one of which appears across from a clast.

Elemental Geochemistry

Elemental concentrations generally follow trends seen in the remainder of the core. Zr/Rb, Fe/Sum and Ti/Sum tend to increase up core, where Ca/Fe tends to decrease (Fig. 5.44). There is

an increase in K/Sum, Si/Sum and Al/Sum concentrations mid-unit, however, near the bottom of the unit values tend to remain around the average for each geochemical constituent.

5.2.4.5 Chronology and sedimentation rate

A single foraminifera sample was obtained from 377 cm depth in Unit 3.2. Benthic *Islandiella norcrossi,* which were "rare to common" in the sample, were mostly collected for dating. One or two rare *stainforthia feylingi* were also identified and included into the sample. Notably, this sample was collected immediately above a "transition zone" mentioned in Unit 3.1. Calibrated lab results indicate that the foramina sample dates to 11,190 ± 115 cal yr. BP. This date indicates that these samples may have become deposited immediately after the Younger Dryas (e.g. Alley, 2000). The calculated average sedimentation rate between 0-377 cm is 33.69 cm/ka.

5.2.4.6 Interpretation

Similar to Unit 2.1 in HH17-1290-GC-TUNU, the mud dominated layers in Unit 3.1 have been interpreted as developing from suspension settling from overflow plumes, where sand laminations and layers may have developed from underflows, possibly related to turbidity-currents (e.g. Cowan et al., 1999; Smith & Andrews, 2000; Ó Cofaigh et al., 2001). Also similar to gravity core HH17-1290-GC-TUNU, the micro-fractures observed at the base of the core are believed to be the result of hydrofracturing of fine grained sediment due to the presence of a large nearby ice mass (e.g. Passchier, 2000). Coarse sediment grains found in muddy sections of Unit 3.4 have been interpreted as being a result of IRD or mass wasting processes (Eyles et al., 1985). Large independent clasts identified across the entirety of the core have also been interpreted as being the product of IRD (Gilbert, 1990; Reeh et al., 1999). The change in color between upper Unit 3.1 and 3.2 likely markers a shift into a different sediment source for the area (e.g. Forwick & Vorren, 2009) (see Discussion). Fine grained sediments in Unit 3.3 and 3.1 are also believed to be primarily derived from suspension settling from overflows (e.g. Ó Cofaigh et al., 2001), where the diamict in Unit 3.3 has been interpreted as a product of a density flow (e.g. Mulder & Alexander, 2001), although the exact mechanism behind its deposition is speculative (see Discussion).

6 Discussion

Findings outlined in the Results Chapter have been used here to reconstruct the palaeoenvironments of Dove Bugt and Bessel Fjord. Each section is divided into three stages: LGM, Deglaciation and Holocene. The implications of the results are discussed below, which is followed by a three-stage model of the area (Fig. 6.1). A basic age-depth model has been developed for each core, assuming constant sedimentation rates between the dated material and/or the surface (Fig. 6.1). Sedimentation rates likely fluctuated through these intervals; however, this acts as a "first approximation" for the age of certain core sections. Each core has also been correlated with the other cores in this study. The diamict from gravity core HH17-1309-GC-TUNU (Unit 3.3) was treated as a rapid event and has been excluded from this figure. Ages from HH17-1289-GC-TUNU may be less reliable due to perceived rapid fluctuations in the sedimentation rates and reworked sediments.

6.1 Palaeoenvironment of Dove Bugt

The following is a discussion based on finding from Dove Bugt. This has been broken down into three sections: LGM, Deglaciation and the Holocene. These sections are followed by a model for the changing environment and a brief summary.

6.1.1 Stage I: Last Glacial Maximum (LGM)

6.1.1.1 LGM Extent and Topographic controls

Stage I of this palaeoenvironmental reconstruction involves reconstructing the local conditions during the LGM. The orientation of streamlined landforms (e.g. MSGL) suggests that ice flowed to the south along the west coast of Store Koldewey and possibly into Dove Bugt Trough. This may suggest that the flow of the NGIS was controlled by the presence of topographic barriers in Dove Bugt. Despite the region's proximity to the Dove Bugt Trough, there is a topographic high in the center of the bay and a long N/NW-S/SE channel positioned in western Dove Bugt, immediately next to the outlet of Bessel Fjord. This topography shows that Dove Bugt does not appear to have the characteristic "trough" like shape that is common in all of the troughs further out on the continental shelf (e.g. Fig. 6.2). This is theorized to be related to the topography of the underlying bedrock. It is also possible that the ice stream partially flowed around this

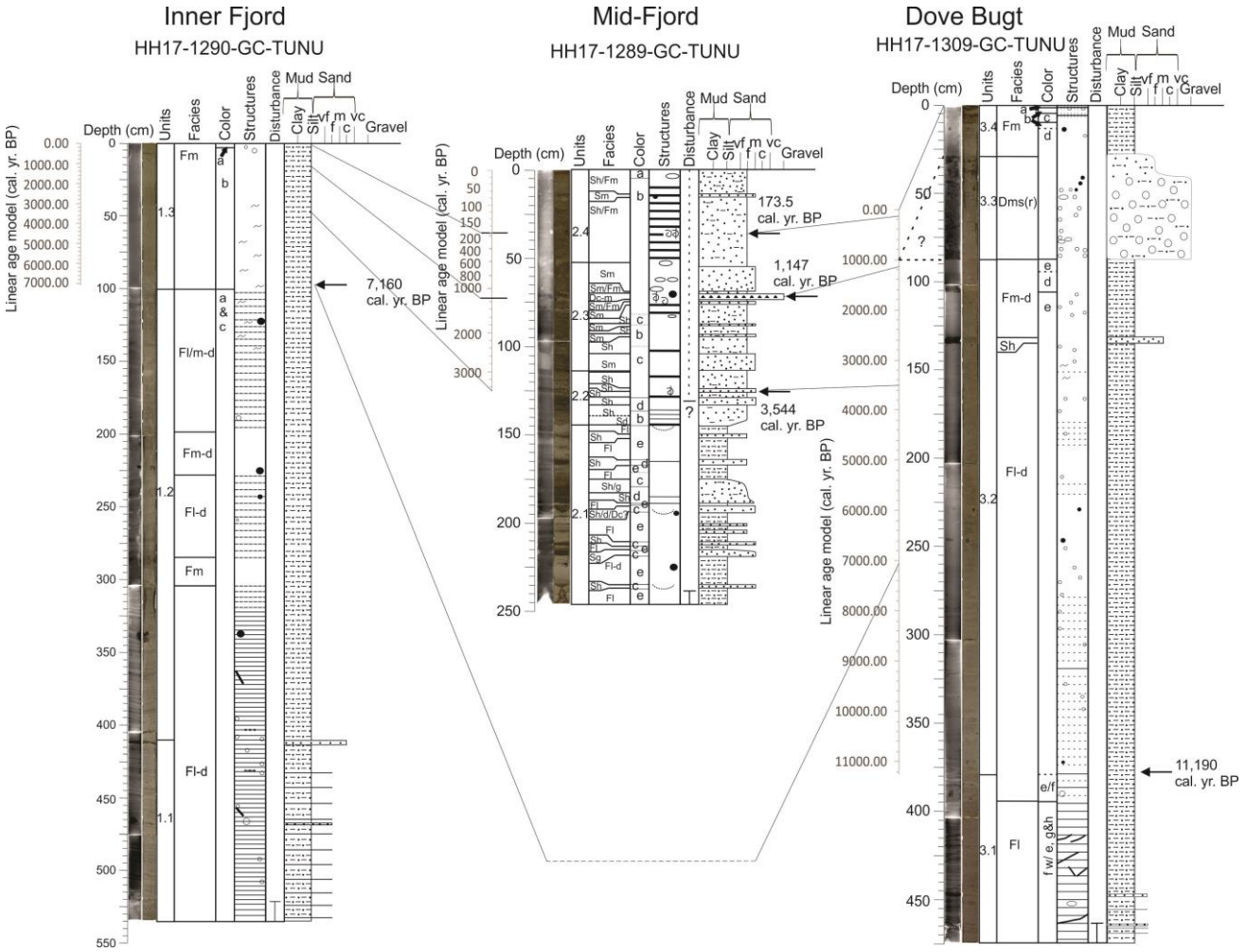

Figure 6.1. A linear age-depth model created for the three gravity cores in Dove Bugt and Bessel Fjord. Dates between cores are correlated as a "first approximation". This first approximation works significantly better for cores HH17-1290-GC-TUNU and HH17-1309-GC-TUNU, and less so for HH27-1289-GC-TUNU due to reworked sediment. Dashed lines between the unconformity at the bottom of Unit 3.3 and its top indicate this this likely formed in a rapid event(s) and is not being included in the linear age-depth model. Lines between cores connect similar dates rather than lithological similarities.

topographic high, which may explain why the MSGL appear to curve. Additionally, it may also be possible that as the ice stream flowed to the southwest as it became compressed against the sidewall of Dove Bugt, which eroded out the deep channel (Fig. 5.25). Given the orientation of the channel compared to the MSGL this does not seem particularly likely. Theoretically ice from an ice cap north of Bessel Fjord could have also come down to carve out this channel, however the mechanism behind how that would occur does not seem realistic. Therefore, until more data in collected, this channel feature has been interpreted as being non-glacial in origin.

Findings from numerous localities across the outer continental shelf of Northeast Greenland suggest that glacial ice reached the shelf break during the LGM (Fig. 6.2) (e.g. Winkelmann et al., 2010; Arndt et al., 2015, 2017; Laberg et al., 2017; Olsen et al., in review). To the east of Dove Bugt and Store Koldewey is the Store Koldewey Trough, a seaward deepening trough that is the only trough on Northeast Greenland's continental shelf that is not connected to a fjord continuation (Olsen et al., in review). Studies on this trough also found geomorphological evidence (i.e. MSGL, transverse ridges, GZW) for the presence of grounded, fast-flowing ice reaching the shelf break (Laberg et al., 2017; Olsen et al., in review). Due to the presence of these features and the unique position of the trough outside of Germania Land and Store Koldewey, Olsen et al. (in review) suggested the Storstrømmen ice stream acted as a "pure" ice streams (e.g. Bentley, 1987; Stokes and Clark, 1999) and overrode the underlying topography. To do this the ice stream would have needed to reach a substantial thickness to override the regions of modern day Storstrømmen and Germania Land (Olsen et al., in review). The ice stream was then theorized to become influenced by the topography of the deep trough and stabilize (Boulton et al., 2003; Olsen et al., in review). At a later phase of the last glacial, the ice sheet is theorized to begin conforming to the underlying topography as the ice sheet thinned and began draining northwards to Jøkelbugten and southwards to Dove Bugt (Olsen et al., in review).

Findings from this study can confirm the theorized southeast drainage of fast-flowing ice through Dove Bugt but there is no evidence to support the notion of an earlier "pure" ice stream that was not topographically bound in this dataset. These findings do not discredit the presence of a non-topographically controlled ice stream but suggest there may be some validity to the theorized later southwards draining ice stream as the ice sheet thinned. Topographic observations on

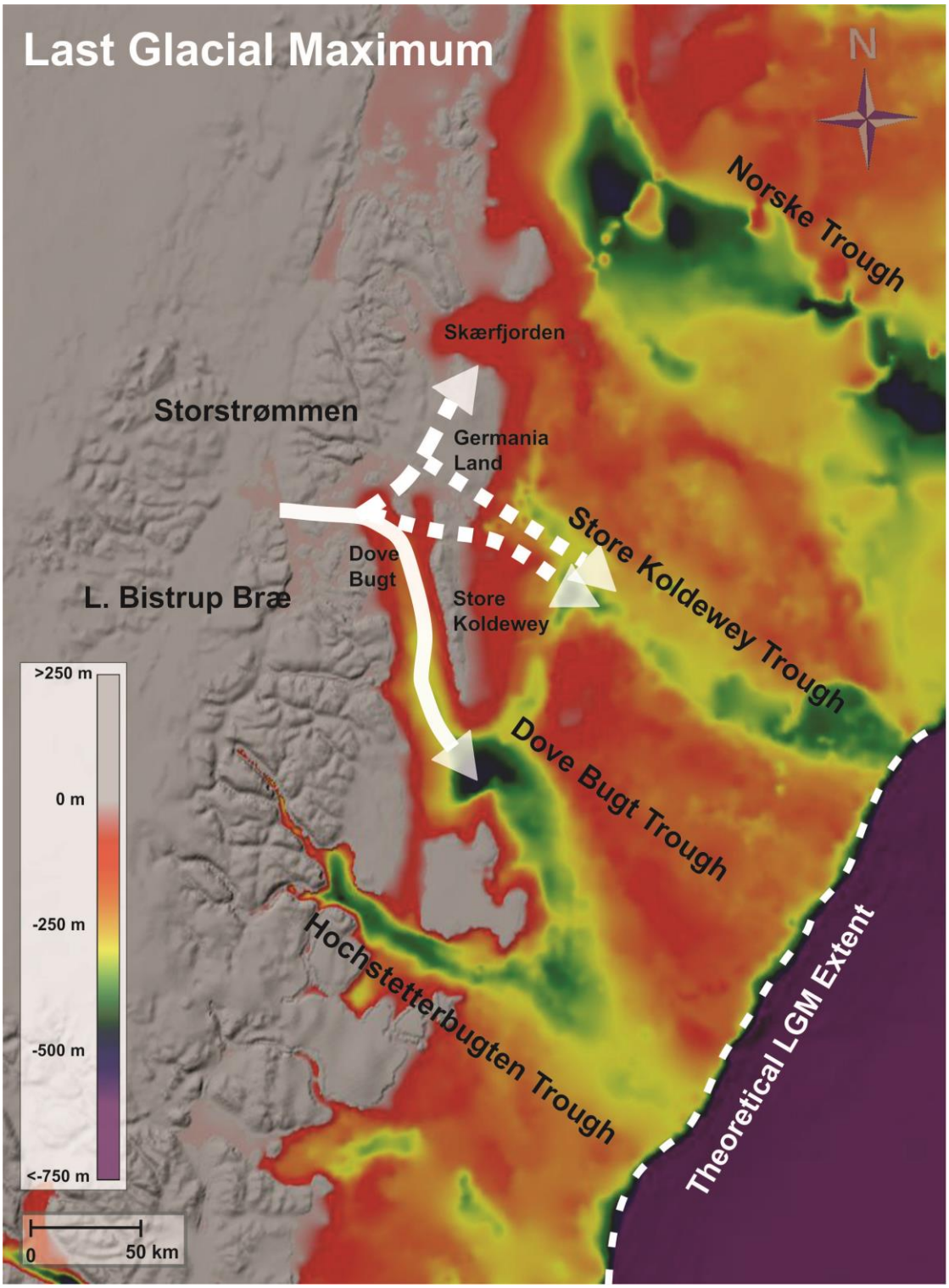

Figure 6.2. Map of the perceived flow path the ice stream during the LGM. Dashed lines with arrows indicate other potential ice stream flow paths reconstructed by Olsen et al. (in review).

Germania Land, north of Dove Bugt, suggested that ice drained north towards Skærfjorden as a tributary to Norske Trough (Fig. 6.2; Landvik, 1994; Arndt et al., 2015). The geomorphological evidence from the continental shelf and terrestrial areas around Germania Land do suggest that the ice stream may have had multiple outlets oriented in different directions.

6.1.1.2 Thermal Regimes of the Ice Stream

The presence of a hill-hole pair structure adjacent to MSGL may suggest that the thermal regime of the ice stream either changed over time or was polythermal (e.g. Wohlleben et al., 2009). Hill-hole pair features are generally associated with cold-based, slow flowing ice (Klages et al., 2013, 2015), where MSGL with length to width ratios > 10 are believed to have formed beneath fast-flowing ice with a warm-based sole (Stokes & Clark, 1999; Rydningen et al., 2013). The ice thickness would also impact the thermal properties of the ice stream. Thick ice would have greater insulation and frictional heat potential, which would allow enhanced basal meltwater production and a lubricated bed, creating a positive feedback mechanism for fast flowing ice (Paterson, 1994; Rydningen et al., 2013). This would also theoretically create increased deformation and enhance flow rates as ice viscosity relies on temperature (Clarke et al., 1977; Rydningen et al., 2013). In Dove Bugt, the ice would have needed to be thick enough to form MSGL yet thin enough to be bound be the topography of the area (see above).

Additionally, shifts in basal thermal conditions have frequently been associated with surging glaciers (e.g. Clarke et al., 1984; Sevestre et al., 2015). Modern day Storstrømmen and L. Bistrup Bræ are believed to be two of the largest surge-type glaciers in the world (Higgins, 1991) and Olsen et al. (in review) theorized that the palaeo-ice stream of Storstrømmen may have undergone surging behavior under full glacial conditions. As Olsen et al (in review) has also pointed out, surging activity during ice retreat has been suggested for other palaeo-ice streams, such as the Bjørnøyrenna Ice Stream (Andreassen et al., 2014) and the Irish Ice Sheet (Delaney et al., 2018), in addition to modern West-Antarctic ice streams (Hughes, 1973; Bindschadler et al., 1976). Conversely, in the context of glaciers in Svalbard, Severste et al. (2015) did assert that large tidewater glaciers remain warm during surge cycles (except for narrow cold zones along the glaciers margins) and that thermal switching can only explain the surge-like behavior of small glaciers but not larger, warm-based glaciers. Nonetheless, the appearance of these features

across Dove Bugt demonstrates the complex basal thermal regime beneath the palaeo-ice stream. Additional information may be required to understand the basal thermal properties of this ice stream.

6.1.2 Stage II: Deglaciation

6.1.2.1 Timing of the Deglaciation of Dove Bugt

The dated formainifera sample in HH17-1309-GC-TUNU yielded an age of 11,190 ± 115 cal yr. BP, which is close in age to dated material from Store Koldewey and Hochstetter Forland (Bennike & Weidick, 2001; Skov et al., 2020). This date is directly above the "transition zone" between two distinctly different sedimentological units. The underlying purple-red, red, white and dark grey sediments (Unit 3.1) are not only a different color than the overlying material, which is a grey-green color, but appears to have a slightly higher percentage of clay (Fig. 5.42). As these different colors appear in laminations, this suggests that the region has undergone numerous short-lived, fluctuations in sedimentation conditions. This drastic change in sediment input may be attributed to the absence of a large ice body in southern Dove Bugt. Increased quantities of sand, IRD and faulting in Unit 3.1 does suggest that sediments were deposited ice proximally. Up core in Unit 3.2, the decreasing quantity of laminations and fewer sand sized particles may reflect a retreating ice stream. Therefore, it is theorized that the sedimentological change at 11,190 ± 115 cal yr. BP marks a period of deglaciation in the region. This would suggest that southern Dove Bugt became deglaciated during the Early Holocene.

Prior to this study, dates constraining the timing of deglaciation in Dove Bugt are restricted to terrestrial regions. The most recent terrestrial study produced a deglaciation age of ca. 12.7 ka at Store Koldewey and ca. 9.8 ka at Pusterdal (Fig. 6.3) with the application of cosmogenic nuclide dating on low to mid-elevation (100-460 m) bedrock (Skov et al., 2020). The calculated retreat rate of the ice sheet between these two positions is ~22 m yr^{-1} (Skov et al., 2020). Lake studies on Store Koldewey appear to closely resemble these results (Klug et al., 2009). Bennike & Weidick (2001) presented a collection of previously published radiocarbon dates which represented the minimum date for deglaciation across Northeast Greenland. Here, a minimum age of 9.5 ka BP was presented for the southern coast of Germania Land (Bennike & Weidick,

2001). Earlier studies on Germania Land suggest that the ice front may have been east of the modern coastline until 19 ka BP and retracted to its present position by 7.5 ka BP (Landvik, 1994; Weidick et al., 1996). Bennike & Weidick (2001) also provided a minimum date for deglaciation on Hochstetter Forland at 11.2 ka. Later, Klug et al. (2016) presented a wider range of deglaciation ages for Hochsterr Foland and adjacent regions (Fig. 6.4).

These deglaciation ages largely match findings in this study. Chronologically, it appears that Store Koldewey may have become at least partially deglaciated prior to the retreat of the ice stream from southern Dove Bugt. Terrestrial regions on Hochstetter Forland may have remained fully or partially glaciated after the ice stream retreated further north.

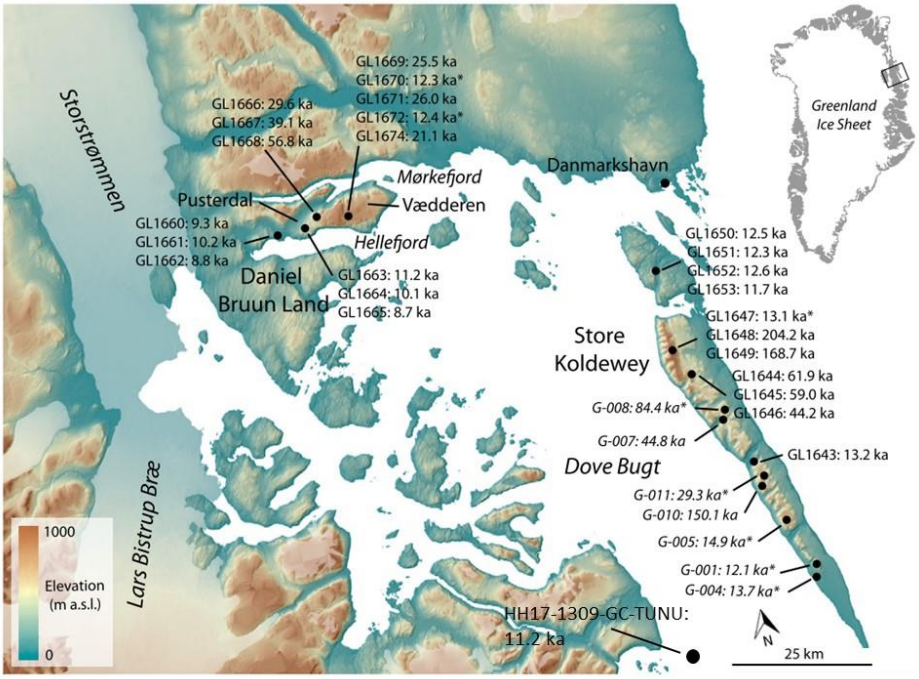

Figure 6.3. Cosmogenic nuclide dates collected across Dove Bugt. Taken and modified from Skov et al. (2020) to include HH17-1309-GC-TUNU.

6.1.2.2 Correlation between southwestern Dove Bugt and Hochstetterbugten Trough

In 1994 a Polarstern cruise collected gravity cores within Ardencaple Fjord and the trough south of Shannon Ø (Hubberten, 1995), regions that are immediately south of Dove Bugt (Fig. 6.4). Hubberten et al. (1995) released results from gravity core PS2623, which has been used in follow up studies (Funder et al., 1998; Andrews et al., 2016). Seeing as the Dove Bugt Trough appears to join with the Hochstetterbugten Trough (Fig. 6.2), cores collected from this region may act as the best analogue to gravity core HH17-1309-GC-TUNU (although there are some noticeable differences). Magnetic susceptibility reading from PS2621 (the core that is most geographically similar) and PS2623 (the core with the most published results) appear to correlate with HH17-1309-GC-TUNU (Fig. 6.5), as well as each other (Fig. 6.6). The lithology of core PS2623 has been broken into the following units: Unit A, an upper dark grayish-brown bioturbated silty clay; Unit B, a silty-clay with abundant 0.24.8-cm-thick sand layers intercalated every 0.5 to 2 cm and no IRD; Unit C, a olive, dark olive-gray, and dark grayish-brown silty clay, intercalated with layers/horizons of dark olive-gray and dark reddish-gray, sandy, silty clay with IRD and mudclasts and Unit D, a diamict, with dark olive-gray, sandy, silty clay and IRD.

The top two units have been observed in PS2621 and may appear in the other cores as well (Fig. 6.7). Additionally, HH17-1309-GC-TUNU appears to contain similar lithological trends, but with some notable distinctions. Like PS2623, a transition from lamination free sediments near the surface to laminated sediment with sand layers in HH17-1309-GC-TUNU has been observed. Within the laminated sediments a change in sediment color has also been identified. Unlike PS2623, HH17-1309-GC-TUNU does not reach a lower diamict beneath the surface. Additionally, the timing in which these units' transition does not appear to match HH17-1309-GC-TUNU (Fig. 6.5). IRD appears in faintly laminated regions of HH17-1309-GC-TUNU but are absent in Unit B of PS2623. Faint laminations also appear at various points mid-core (most notably at ~180 cm) in the equivalent section refered to as Unit A. These are absent in core PS2621, but have a closer resemblace to Unit A in PS2619 (Fig. 6.7), which is substantially closer to the mainland of Greenland (Fig. 6.4).

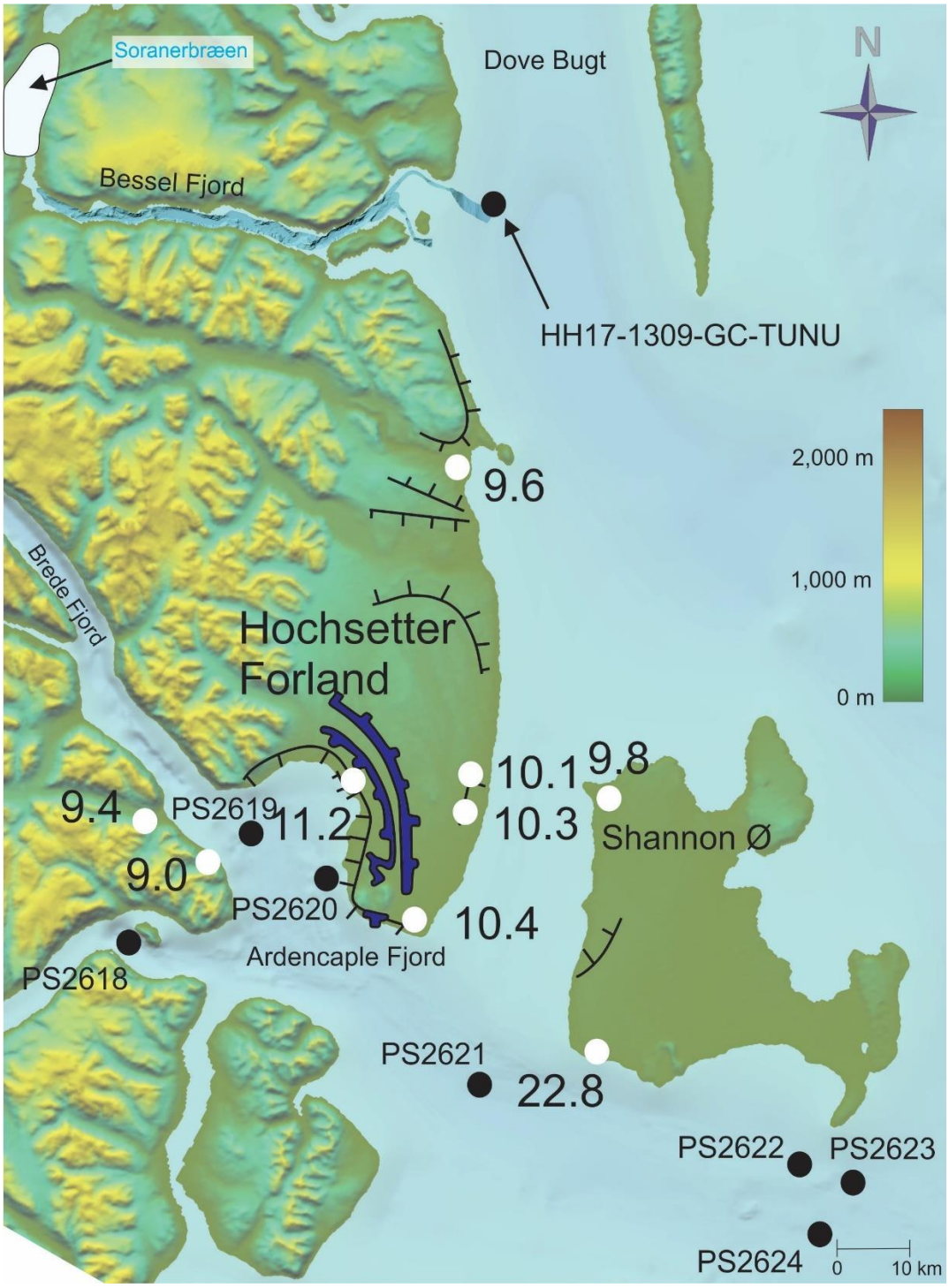

Figure 6.4. Mapped moraines on Hochsetter Forland based on a combination of maps from Hjort (1981), Hjort & Björck (1983) & Björck et al., (1994). Note: a moraine was also mapped from southern Hochsetter Forland, across the ocean to Shannon Ø in Hjort & Björck (1983) but was not included in this map. Blue lines- Muschelbjerg moraines, black lines- Nanok moraines. Black circles- the position of gravity cores from Hubberten et al., (1995) & Andrews et al. (2016).White circles- minimal ages for the last deglaciation from (Klug et al., 2016).

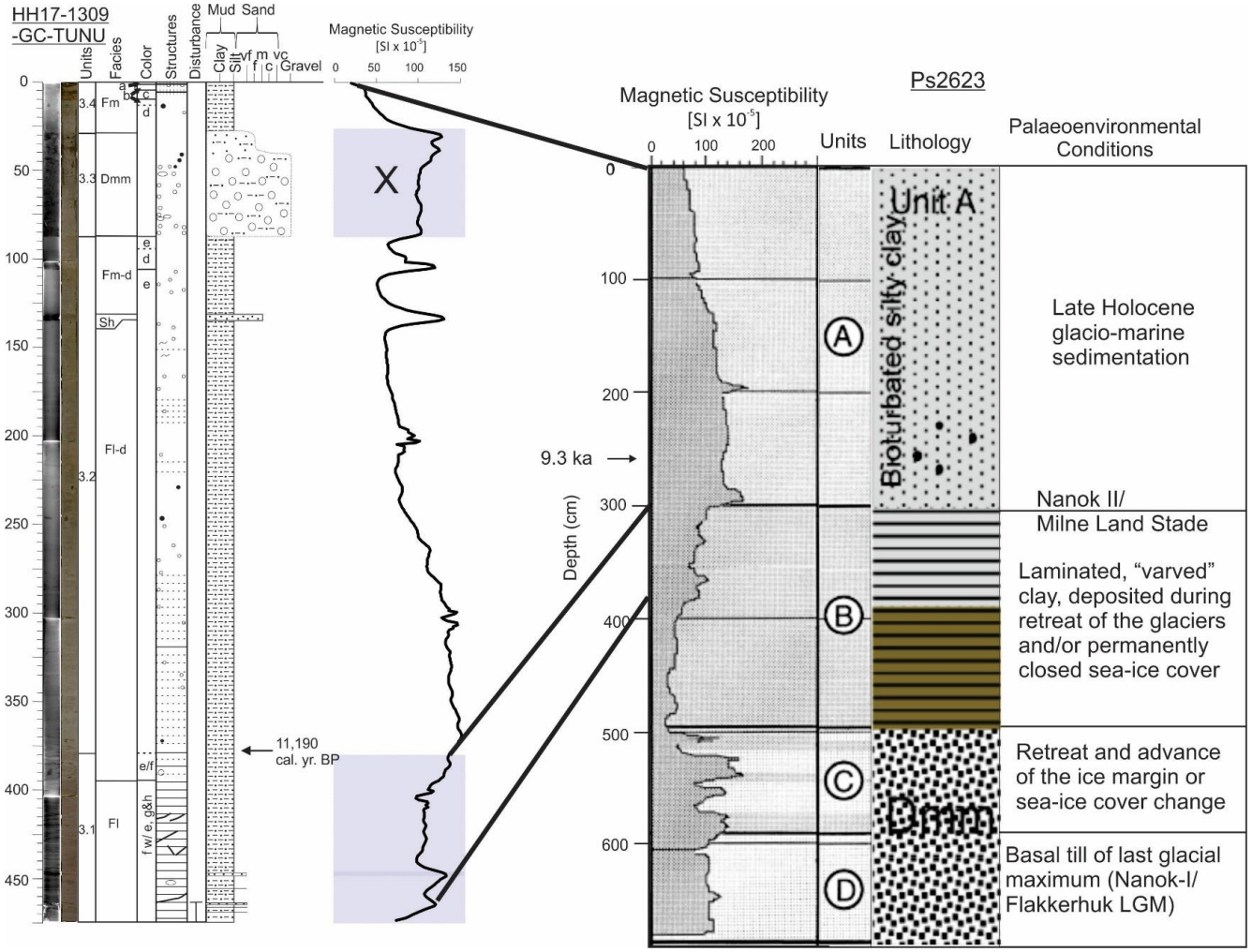

Figure 6.5. Correlation of HH17-1309 and PS2623 using magnetic susceptibility measurements. Information taken from Hubberten et al. (1995), Funder et al. (1998) & Andrews et al., (2016). An "X" has been placed through unit 3.3 because it is probably a local event and would not appear in the magnetic susceptibility readings of PS2623.

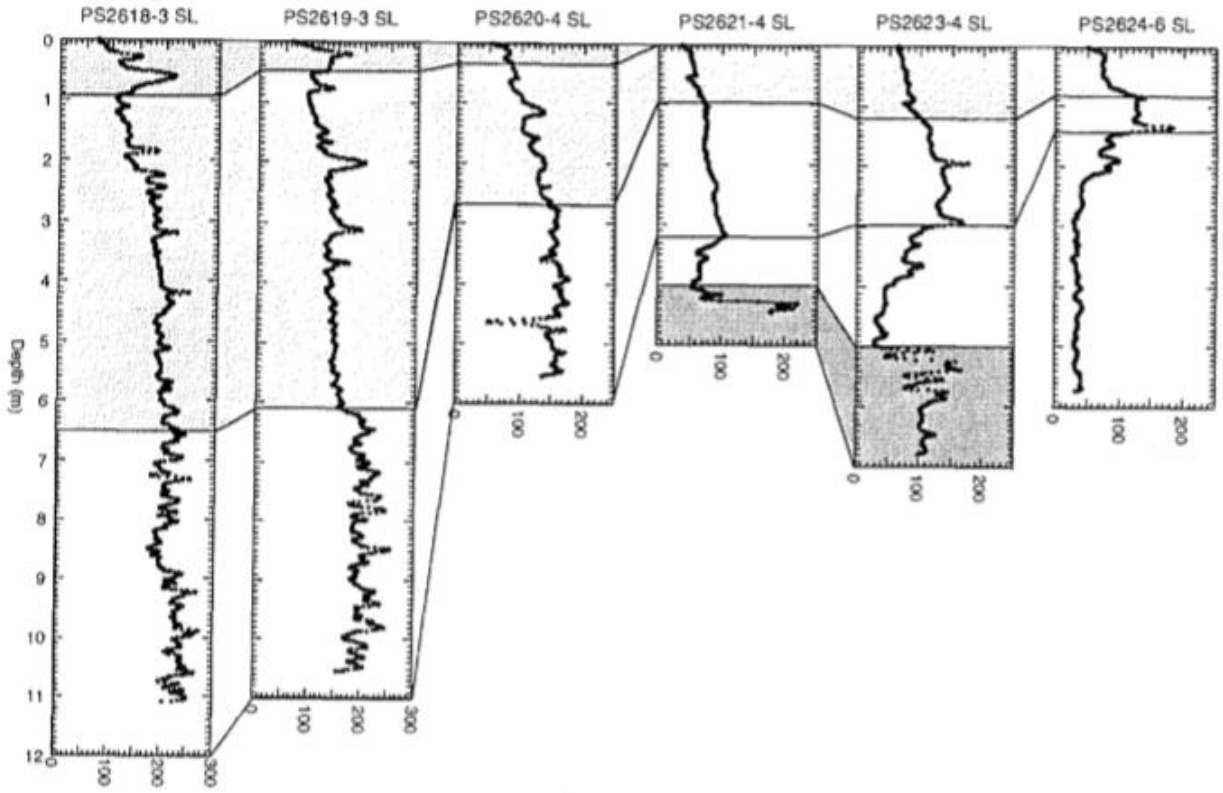

Figure 6.6. Lateral core correlation of cores from Hochstetterbugten using magnetic susceptibility. Figure taken from Hubberten (1995) *and positions of each core can be seen in Fig. 6.4. Shaded areas represent diamicts.*

The differences between units are likely linked to local variations in environmental conditions, including their relative position off the coast of mainland Greenland, their proximity to a glacial outlet and the composition of the local bedrock. The full length of magnetic susceptibly readings in PS2623, as well as Units C and D, do reflect the fact that much of the ice streams retreat through Dove Bugt may not appear at the bottom of HH17-1309-GC-TUNU. This may imply that the sediments in HH17-1309-GC-TUNU represents just the ice streams final retreat from the area. The transition in 'varved' sediment color mid-Unit B of PS2623 rather than at the Unit B and Unit A transition (which is where this shift occurs in HH17-1309-GC-TUNU) may suggest an earlier change in sediment sources for the Hochstetterbugten Trough region than southwestern Dove Bugt (Fig. 6.5).

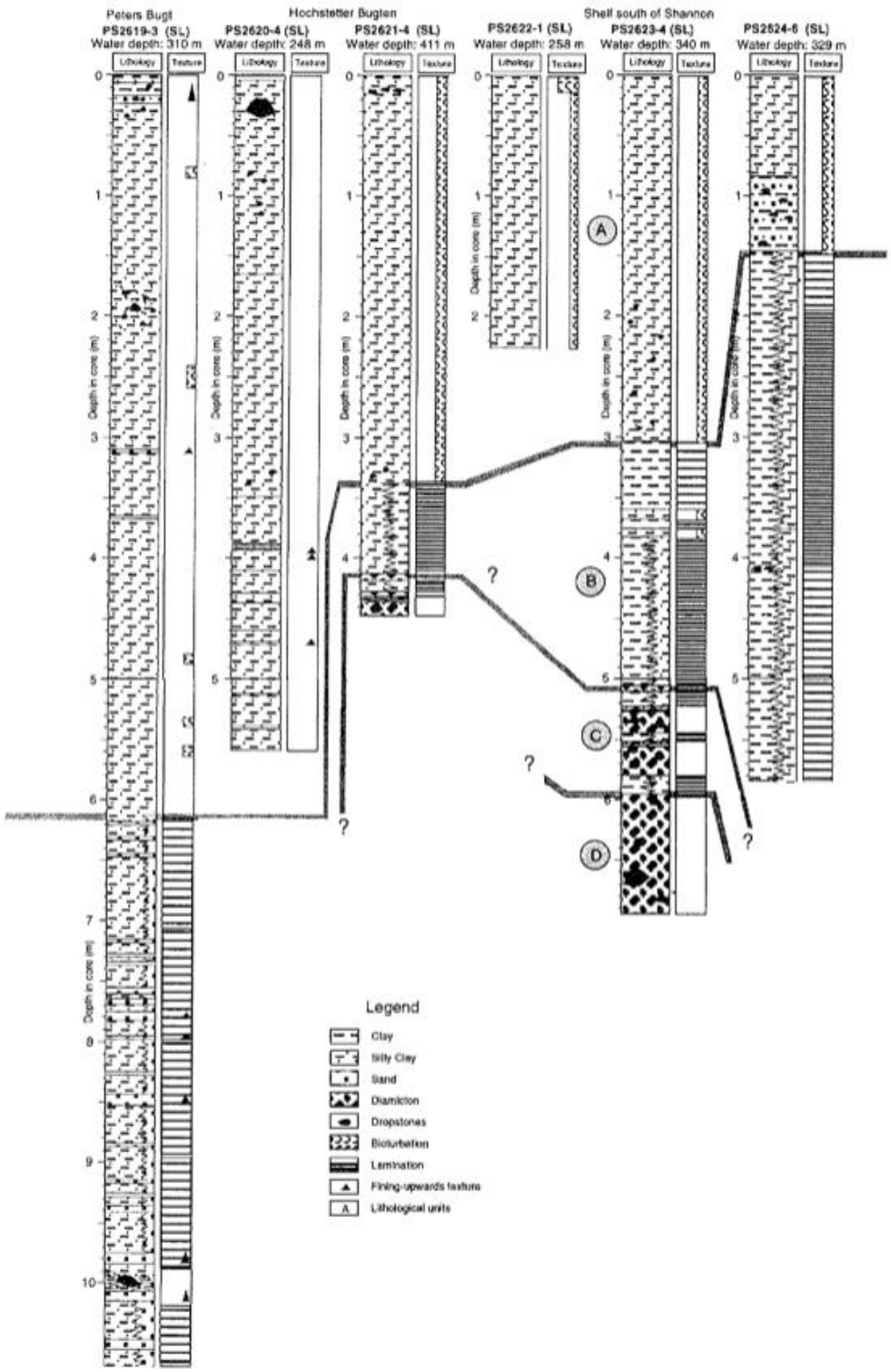

Figure 6.7. Lithological core description of cores from Peters Bugt, Hochstetterbugten and south of Shannon Ø. Taken from Hubberten (1995).

Nonetheless, assuming Units 3.1 and 3.2 of HH17-1309-GC-TUNU can be correlated with Unit B and A of PS2623 (Fig. 6.5), this transition has been previously interpreted as the Nanok II/Milne Land Stade (Funder et al., 1998). Sets of moraines mapped in the area and presented in older publications were proposed to be Saalian (or pre-Saalian) in age (Muschelbjerg moraines) and of Last Glacial Maximum age (Nanok moraines). The Nanok moraines had been divided into Nanok I and Nanok II stadials, the second of which has been proposed to correspond to the Preboreal Oscilllation (ca. 11,300– 11,150 cal. yr BP) (Fig. 6.4) (Hjort, 1979; Hjort & Björck, 1983; Funder, 1989; Johnsen et al., 1992; Larsen et al., 1995; Björck et al., 1997; Funder et al., 1998; Wagner et al., 2008). The Preboreal Oscilllation, as well as the an event marked at 9.3 ka BP and the 8.2 ka BP event in Greenland ice core records, mark short-lived cold reversals in the Early Holocene (Rasmussen et al., 2007). Vasskog et al. (2015) has asserted that Milne Land stade moraines (which correlates to the Nanok II moraines) are actually from the Younger Dryas and they represent the only well-developed onshore moraine system that formed during this time in Greenland (Funder et al., 1998).

Although some regions experienced an ice halt or readvanced during the Younger Dryas, it is believed that the total extent and volume of the Ice Sheet gradually decreased during this colder period (Vasskog et al., 2015). Marine studies, however, have found evidence for stabilization or readvancement of ice during the Younger Dryas (Ó Cofaigh et al., 2013; Hogan et al., 2016; Sheldon et al., 2016; Arndt et al., 2017) following the warmer Allerød–Bølling interstadial. The proposed deglaciation age of 11.2 cal. kyr BP of Hochstetter Forland (Bennike & Björck, 2002) implies terrestrial ice retreated soon after the formation of the moraines, although other publications point to a later last deglaciation age for the area (Fig. 6.4). Sedimentological data from HH17-1309-GC-TUNU does not provide any strong evidence for a Younger Dryas or Preboreal Oscillation readvancement. Microfractures at the base of HH17-1309-GC-TUNU may, however, suggest that an ice mass may have overrode the sediment (Fig. 5.46). Although, these features can form both in subglacial or proglacial environments (Passchier, 2000), therefore this alone may not be enough to conclusively determining if there was a readvancement.

6.1.2.3 Sediment Sources and Implications for Ice Flow into Dove Bugt

As it has been noted, the purple-red, red and dark grey sediments of Unit 3.1 are distinctly different from the remaining units in the core as well as the two gravity cores collected in Bessel Fjord. The paleoenvironmental setting of this unit was interpreted as being ice-proximal, as fine-grained sediment became deposited from suspension settling from overflow plumes and sand layers from turbidites. Therefore, sediments within Unit 3.1 are possibly the result of long-distance sediment transport across Dove Bugt via the NGIS.

Based purely on the color of the sediments, four potential options for their provenance were determined. The first option is the Trekant 'series' (Figs. 6.8 & 6.9). This 520 m thick series has been correlated to the Independence Fjord Group in Northern Greenland and contains grey-green and purple-red akosic and quartzitic sandstones that are interbedded with siltstones and quartz pebble conglomerates. The Trekant 'series' has been identified on Dronning Louise Land and other parts of the Western thrust belt (Henriksen & Higgins, 2009).

The second provenance option are gneisses and associated rocks (Figs. 6.8 & 6.9). Orthogneisses are widespread across Dove Bugt and appear mostly in a grey color in the Nørreland and Western Thrust Sheet (Henriksen & Higgins, 2009). In numerous places, gneisses are cut by foliated metagranitiod sheets, where in western Dove Bugt they appear as subconcordant, pink-colored sheets (Chadwick & Friend, 1994). Layers and lenses of gabbroic, gabbro-anorthositic, megacrystic anorthositic and ultramafic igneous rocks occur within the gneisses. Locally, east of L. Bistrup Bræ, leucogabbroic and gabbro-anorthositic layers and lenses are common. Anorthositic rocks have also been identified on an isolated nunatak in southwestern inner Bessel Fjord (Henriksen et al., 1989; Stecher & Henriksen, 1994). In western Dronning Louise Land, granitoid orthgneisses have been identified with minor occurrences of amphibolite, anorthosite and ultrabasic rocks (Henriksen & Higgins, 2009).

The third option are sediments derived from the Eleonore Bay Supergroup (Figs. 6.8 & 6.9). These are in a décollement-bounded enclave centered on Ardencaple Fjord and Bredefjord (Fig. 6.9). Here the Nathorst Land Group [NG], which consists of alternating units of quartz arenite, interbedded sandstone and mudstone and black silty mudstone, has been identified north and

south of Bredefjord, with isolated out-crops in southern Hochstetter Forland. This supergroup also includes the Lyell Land Group, which is composed of six 240 to 700 m thick units of white, brown and purple weathering quartz arenites and dark green, brown and deep red silty mudstones. The units are divided into Kempe Fjord [KF], Sandertop [ST], Berzelius Bjerg [BZ], Kap Alfred [KA], Vibeke Sø [VS] and Skjoldungebræ [SB] Formations. These have been identified north and south of inner Ardencaple Fjord and between Bredefjord and Smallefjord (Fig. 6.9) (Henriksen & Higgins, 2009).

The fourth provenance option are granites (Fig. 6.8 & 6.9). Granites appear in the Smallefjord and Eleonore Bay Supergroup as Caledonian intrusions, sheets and lenses (Fig. 6.9; Henriksen & Higgins, 2009). It has been suggested that the intrusions are the result of the partial melting of metasedimentary rocks belonging to the Smallefjord sequence. Caledonian granitic intrusions have been identified in the Grandjean Fjord – Bessel Fjord region (75°–76°N) (Hansen et al., 1994; Strachan et al., 2001) but have not been identified north of Bessel Fjord (Henriksen & Higgins, 2009).

These findings point to possibly two (or three) regions where this sediment may have originated from. Geomorphological evidence from this study suggests that a large ice stream was moving in a N-S direction through Dove Bugt (e.g. streamlined glacial lineations), thus sediment sourced from either west of the modern-day position of Storstrømmen and L. Bistrup Bræ or from around Dove Bugt, north of gravity core HH17-1309-GC-TUNU, seems the most likely. Therefore, the transportation of sedimentary rocks from the Trekant ‘series’/ Independence Fjord Group and/or gneisses and anorthosite (and associated rocks) from Dronning Louise Land (or other nunatooks) or from Rechnitzer Land, Ad. S. Jensen Land, Daniel Brunn Land and/or Germania Land is possible. This is supported by Landvik (1994) which notes the appearance of red sandstone and red sandstone erratics (Wegener, 1930) in northern Dove Bugt. This suggests that sediment may have been transport a substantial distance to reach the gravity core site.

Beyond geomorphic evidence, however, the color of the sediment appears to match photos taken Henriksen & Higgins (2009) of the Eleonore Bay Supergroup in Ardencaple Fjord and Bredefjord (Fig. 6.8). It is possible that ice caps south of Bessel Fjord expanded, transporting the

Figure 6.8. Images of locations across Northeast Greenland that may be the origin of sediment in Unit 3.1. All images are taken from Henriksen & Higgins (2009). A: Image of the upper Eleonore Bay Supergroup on the north-east side of Ardencaple Fjord. NG, Nathorst Land Group; KF, Kempe Fjord Formation; ST, Sandertop Formation. The profile height is about 1200 m. B: Image of the lowermost Zebra 'series' [Z] overlying sandstones and siltstones of the Trekant 'series' [T] in northern Dronning Louise Land Cliff height about 120 m. Photo: J.D. Friderichsen. C: Photograph of basement orthogneisses [gn1] within the Hagar Bjerg thrust sheet looking north at the north wall of innermost Grandjean Fjord at the front of Heinkel Gletscher. At the left side of the photograph is a thick zone of black, podded amphibolite [a]. Cliff height about 1200 m. D: Image of Caledonian granite [gi] cutting dark sedimentary rocks of the Nathorst Land Group [NG]. The photo was taken at the head of Bredefjord, looking north and the highest summits are 1200 m above the fjord.

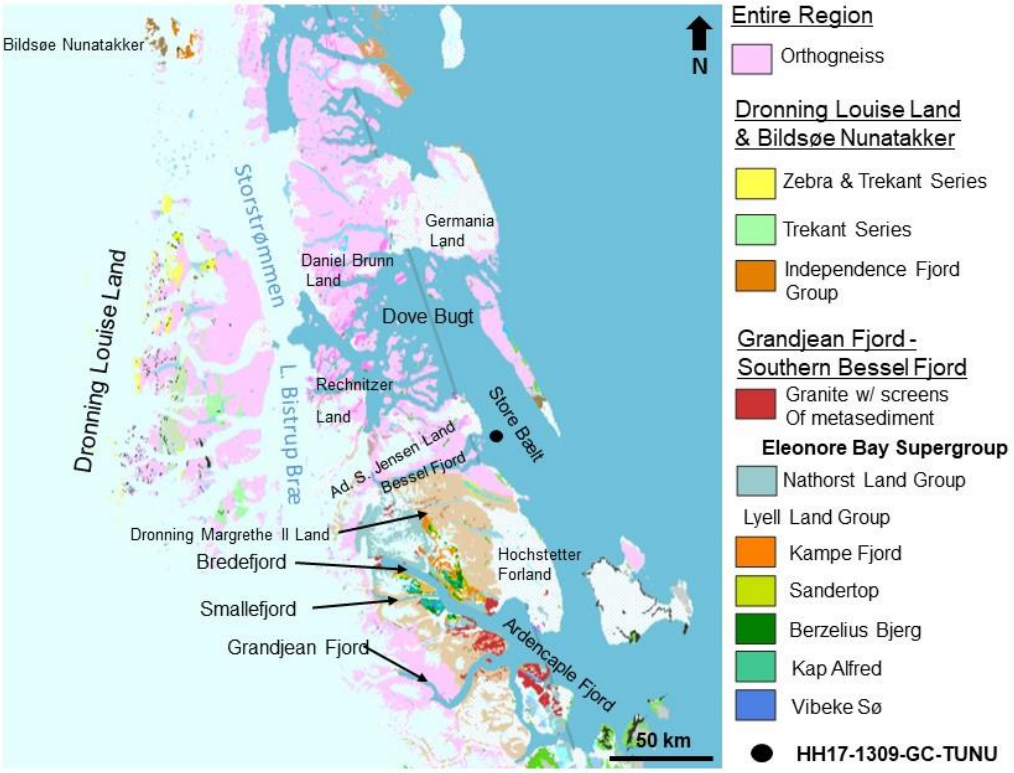

Figure 6.9. Simplified bedrock geology map of Northeast Greenland. For a more detailed map see Figure 2.4.

material northeast towards southern Dove Bugt. Geomorphological evidence does suggest an advance of ice from south of Bessel Fjord northeast to the outer section of the fjord (see below). The lack of similar characteristics in sediments from gravity core HH17-1290-GC-TUNU may imply that this ice cap expansion would not have encroach on Bessel Fjord or that the fjord was fully glaciated during an ice cap expanse, restricting sediment deposition in the fjord. The same speculation can be said about the granite which also appears mostly south of Bessel Fjord, although the sediments in Unit 3.4 have less of a resemblance to this material. Given the orientation of the MSGL in Dove Bugt this sediment source seems less likely, however it cannot be entirely ruled out. XRF results do not appear to suggest either one source may be a more likely option than the other. The collection and analysis of additional gravity cores and interpretation of the previously collected chirp data may be required to be a better understand the provenance of the sediments in southern Dove Bugt.

6.1.2.4 Ice Retreat

Dove Bugt is largely absent of any landforms that would suggest is halts or readvancements during deglaciation. A small number of retreat moraines have been observed on the eastern side of the study area (Fig. 5.28), but other moraine-like features appear in isolated regions of Dove Bugt, often only faintly visible. It has also been noted that a "large transverse ridge", which has been interpreted as a resistant bedrock layer, may be a GZW. GZWs have been identified across the continental shelf of Northeast Greenland (e.g. Evans et al., 2002a; Winkelmann et al., 2010; Arndt et al., 2015, 2017, 2018; Olsen et al., in review), therefore it is possible that one may be present in Dove Bugt. The issue with this interpretation, however, is the fact that this feature only appears in one location rather than crossing the entire trough. The West Antarctic Ice Sheet appears to have meandered through time (Jacobel et al., 1994; Eittreim et al., 1995; Powell & Alley, 1997), therefore a non-uniform NGIS ice front is certainly possible. This would imply that the ice front would be retracted in some regions and protrude others. This does not seem likely, however, as there does not seem to be a reason for lobes to form on the ice front and protrude outwards. Additional mapping of the area may be required to verify this, however, at this time the feature is believed to be an erosional feature rather than a depositional one.

Dowdeswell et al. (2008) proposed that ice streams in high latitude continental shelves have three retreat styles based on their seafloor geomorphology (Fig. 6.10). This includes a rapid, episodic and a slow retreat. Since southern Dove Bugt mostly consists of streamlined lineations, most of which are MSGL, this would suggest that retreat was likely rapid. The appearance of small moraines, however suggest, that retreat may have been at times slow (Fig. 6.10). Since these features are not widespread, however, it is possible that the retreating ice stream had brief periods of slower retreat that may have not been uniform across the entire grounding zone of the ice stream. Based on these results, it is theorized that Dove Bugt primarily experienced rapid retreat but may have also had short periods of slow retreat, which may have not been uniform across the ice stream.

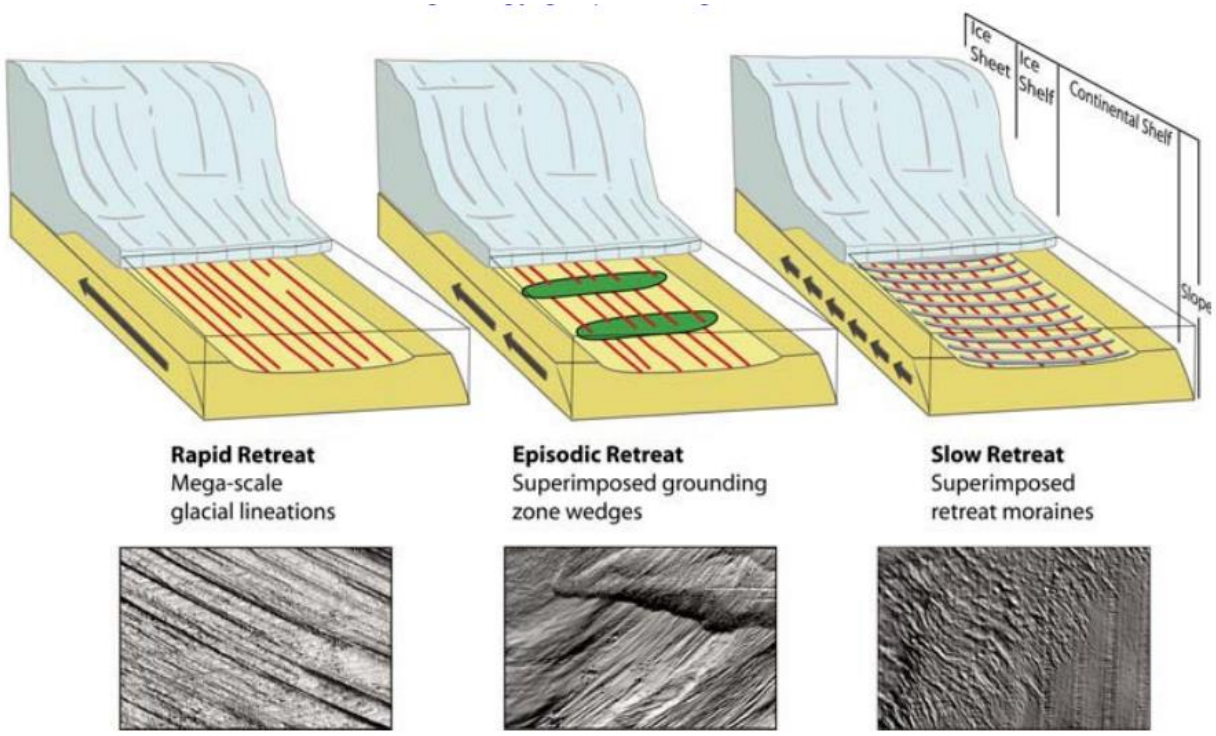

Figure 6.10. Three different ice stream retreat scenarios based on landform assemblages. Taken from Dowdeswell et al. (2008).

6.1.3 **Stage III: Holocene (Post-Ice Stream Deglaciation)**

Stage three of the model reflects a time in which the NGIS would be largely retreating from and/or absent from southern Dove Bugt. In gravity core HH17-1309-GC-TUNU this time period mostly consists of fine-grained sediment from suspension settling. The bottom of Unit 3.2 transitions away from a purple-red dominated sediment with sandy turbidites to a silty grey-green mud with faint laminations. It is likely that after 11,190 ± 115 cal yr. BP local sediment input from the surrounding ice caps and/or Soranerbræen became the dominate sediment source. Findings from this study do suggest that Soranerbræen and local ice caps did expand far beyond their modern-day position (see below). The continuation of sediment delivery from the NGIS seems unlikely, as Pusterdal was deglaciated by 9.5 ka BP (Skov et al., 2020) and Storstrømmen retreated to its present day position by 7.5 ka BP (Weidick et al., 1994).

Higher quantities of sand and IRD have been identified at the bottom of Unit 3.2. Andrews et al. (2016) examination of the mineralogical content of Kejser Franz Joseph Fjord, the adjacent continental shelf area and the region south of Shannon Ø (i.e. PS2623) noted little sediment that could be ascribed to ice-rafting for sediment <9.5 cal. ka BP. This was theorized to be due to the absence of a tidewater (calving) ice front, prolonged annual to multi-year landfast sea ice (which restricts iceberg transport) and melting of icebergs within fjords (Reeh, 2004). Despite the proximity to Dove Bugt and prolonged periods of sea ice, this does not appear to be the case for Dove Bugt. Other work on glacimarine sedimentation in East Greenland have established the importance of sedimentation related to icebergs and the abundance of iceberg-rafted sediments in East Greenland (Dowdeswell et al., 1994; Jennings & Weiner, 1996; Syvitski, Andrew, et al., 1996; Ó Cofaigh et al., 2001), therefore the presence of IRD near an outlet of an ice stream is expected. An increase in the quantity of IRD may be related to an increase of iceberg production due to an advance, the break-up of land sea ice and release of icebergs or the melting of icebergs due to the influx of warm water (Andrews et al., 2016).

Further up core, small red and white layers of mud at 322.75 cm, that are similar in character to sediment Unit 3.1, have been identified (Fig. 5.47). Presumably this material would have been deposited as suspension setting rather than from iceberg rafting due to the sediments grain size. Using the linear age-depth model (Fig. 6.1), this sediment appears to come in around 8,900 cal. yr. BP. This approximate date appears near two cold reversals seen in Greenland ice cores (i.e. 9.3 ka BP and the 8.2 ka BP) (Rasmussen et al., 2007). In southwest Greenland, ^{10}Be ages suggest that the GrIS margin re-advances or were at a stillstand around 11.6 ka, 10.4 ka, 9.1 ka, 8.1 ka, and 7.3 ka (Young et al., 2020). It is possible that these layers represent the advancement of the ice stream, however, if this was the case, one would expect to also see the ice stream advancement reflected in other studies in the area (e.g. Skov et al., 2020).

The age-depth model suggests that the faint laminations, visible only in x-ray images, occur in core HH17-1309-GC-TUNU from the onset of deglaciation at 11,190 cal. yr. BP (at 377 cm) to ~278 cm and cease around 7,500 cal. yr. BP. The formation of rhythmically-laminated muds in Scoresby Sund in East Greenland have been attributed to a changing tidal regime and diurnal fluctuations in meltwater discharge of an ice-proximal glacimarine environment (Cowan &

Powell, 1990; Ó Cofaigh et al., 2001). This suggests that Dove Bugt experienced ice-proximal settings throughout the Early Holocene (11.7–8.2 ka BP) (Vasskog et al., 2015).

Further up core, these laminations that are only visible in x-ray images have also been observed in smaller intervals at 214-220, 180-193 and 152 cm. These punctuated laminated areas correspond to 5500-5700, 4200-4800 and 3200 cal. yr. BP on the age-depth model, respectively. Assuming a consistent sedimentation rate, the first of these two intervals fall within the HTM. Lake studies on Store Koldewey suggest that the warmest period on the island may have occurred between -~8 and 4 ka (or as early as 10 ka) where studies on Hochstetter Forland suggest that it was from 8.8 to 5.6 ka (Briner et al., 2016). Warmer than present temperatures are supported in models of the GrIS during the Holocene, which position the ice sheet behind its present-day location in numerous regions (Fig. 6.11). Knowing this, it seems unlikely that these laminations formed through glacigenic events. Perhaps more simply, this reflects the fact that sedimentation rate fluctuated quite pronouncedly, rather than continuously, proving that the age-depth model for core HH17-1309-GC-TUNU may not be entirely accurate.

Despite this issue, the sedimentation rate of Dove Bugt (33.7 cm/ka) matches that of Greenlandic fjords (e.g. Evans et al., 2002; Olsen, 2015). Comparing it to other East Greenland shelf settings in the Holocene, however, it appears to have received more sediment (e.g. Evans et al., 2002). Compared to ice proximal settings in East Greenland (Syvitski et al., 1996) or areas near meltwater dominated temperate ice (e.g. Alaska) (Cowan & Powell, 1991; Ó Cofaigh et al., 2001), this sedimentation rate appears substantially lower. This broadly reflects the gravity cores position immediately outside the fjord, where glacier and ice cap meltwater played a much larger role in sediment deposition than a position further out on the shelf.

In summary, after 11,190 ± 115 cal yr. BP sediment is theorized to have been sourced from local regions rather than the NGIS. High quantities of sand at the bottom of Unit 3.2 is interpreted as being the result of increased ice rafting in Dove Bugt. A small layer of red and white mud found further up core resembles sediment believed to be ice stream derived, however it is difficult to account for the appearance of these layers. Laminated sediments observed in Unit 3.2 are believed to be glacially derived, however, dates produced from the linear age-depth model do not

always coincide with climatically cooler periods. Therefore, it is possible that the linear age-depth model does not accurately account for fluctuations in sedimentation in Dove Bugt, which may place the presence of these laminations in a different climatic period.

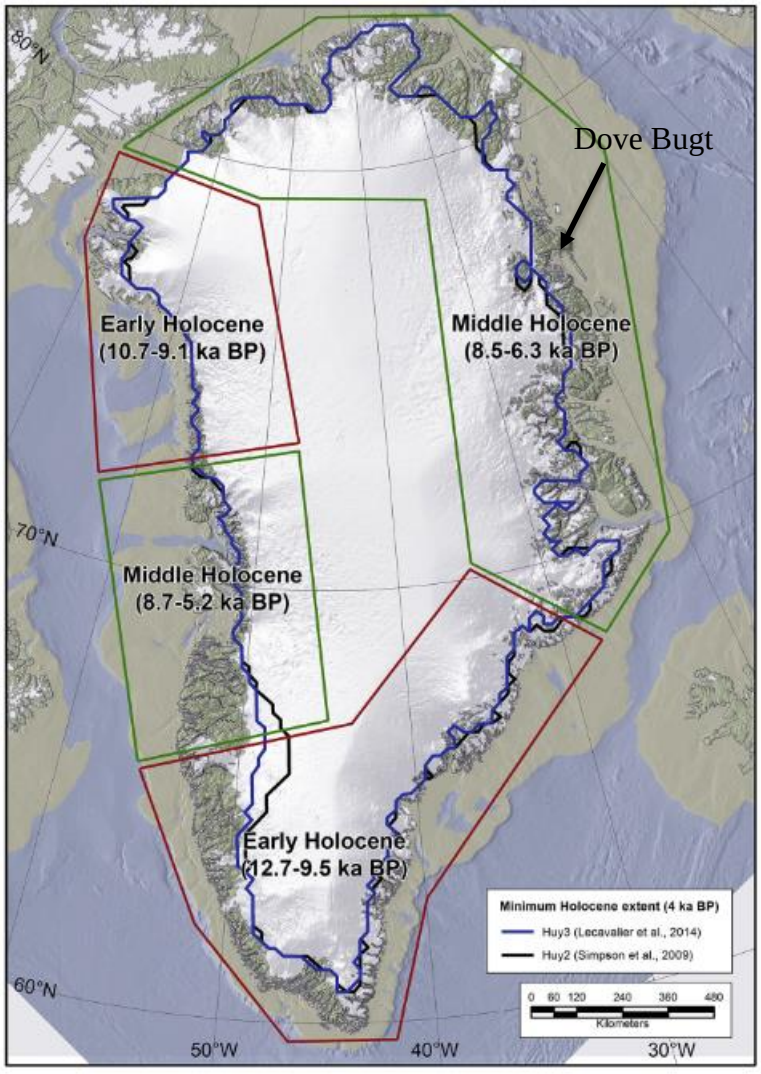

Figure 6.11. Two models of the minimum Holocene extent of the GrIS. The Huy2 model (Simpson et al., 2009) represented by a black line and the Huy3 model (Lecavalier et al., 2014) represented by a blue line. Both of these models contain a minimum extent and volume around 4 ka BP. Areas of the ice sheet margin that retreat behind its Late Holocene maximum, mostly in the Early Holocene, are enclosed in red, where regions where this mostly occurred during the Middle Holocene are enclosed around a green line. Map taken and modified from Vasskog et al. (2015).

6.1.3.1 Diamict in Unit 3.3

The diamict in Unit 3.3 contains an erosional lower boundary, semi-ordered structure and sediment grains that range in size from clay to gravel (Fig. 6.12). The bottom half of the unit contains a mixture of patches of mud, often surrounded by clasts, that may (or may not) be aligned with weakly visible stratigraphic layers. Two semi-planar layers, one of which is composed of mud, have been identified above this section. This is followed by an overlying section of assorted sand grains that form a wavy, possibly convolute, bedding with a relatively homogenous mud-rich section about it.

Based on these characteristics, this unit is interpreted as density flow deposit (Mulder & Alexander, 2001). Lithological observations suggest that it formed as the result of either a debris flow or turbidity current. A debris flow is particularly dense flow that contains high quantities of clay, which allows coarse grains to become transported in its matrix (Middleton & Hampton, 1976). This typically results in a massive poorly sorted deposit as the mud matrix holds coarse grains in place, restricting them from settling, after they have been mixed during transport (Pratson et al., 2000).

Within turbidity currents, fine grained particles are kept above the bed of a flow body by turbulence suspension (Kneller & Buckee, 2000; Mulder & Alexander, 2001). This may move down a slope and along a bed if the suspended particles make the flow denser than the surrounding liquid medium (Benn & Evans, 2010). They can develop for multiple reasons, including the discharge of sediment-laden meltwater from meltstreams or submerged conduit openings (as hyperpycnal underflows, frequently in lakes), from intense sediment fallout from suspension plumes (common in proximal glacimarine environments) and from debris flow dilution as it progresses down slope (associated with areas with high sedimentation rates, e.g. ice-proximal or ice-contact depo-centers) (Syvitski & Farrow, 1989; Nemec, 1990a, 1995; Benn & Evans, 2010). An idealized turbidity current sequence was developed by Bouma (1962) and is often used as an aid in identifying turbidity current deposits.

These three beds appear to match (perhaps roughly) with beds witnessed in an idealized Bouma Sequences (Fig. 6.12) , although issues with interpreting turbidity current deposits based on this

sequence has been noted by other authors (i.e. Shanmugam, 2002). From bottom up, this would encompass the A, B and C divisions in the sequence. Given the large number rip up clasts and chaotic structure in the bottom of the unit (Fig. 6.12; 1- between the red and white lines), this can alternatively be interpreted as a muddy debris flow that is overlain by part of a turbidite. In either scenario, the deposit may have characteristics of a 'base cut-out' distal turbidite (Fig. 6.12; 2), with convolute laminations and rip-up clasts (e.g. Benn & Evans, 2010). Regardless of the mechanism that causing the grains to become emplaced, it is possible that the coarse sediment was originally deposited onto the continental shelf as ice-rafted debris and had later undergone resedimentation.

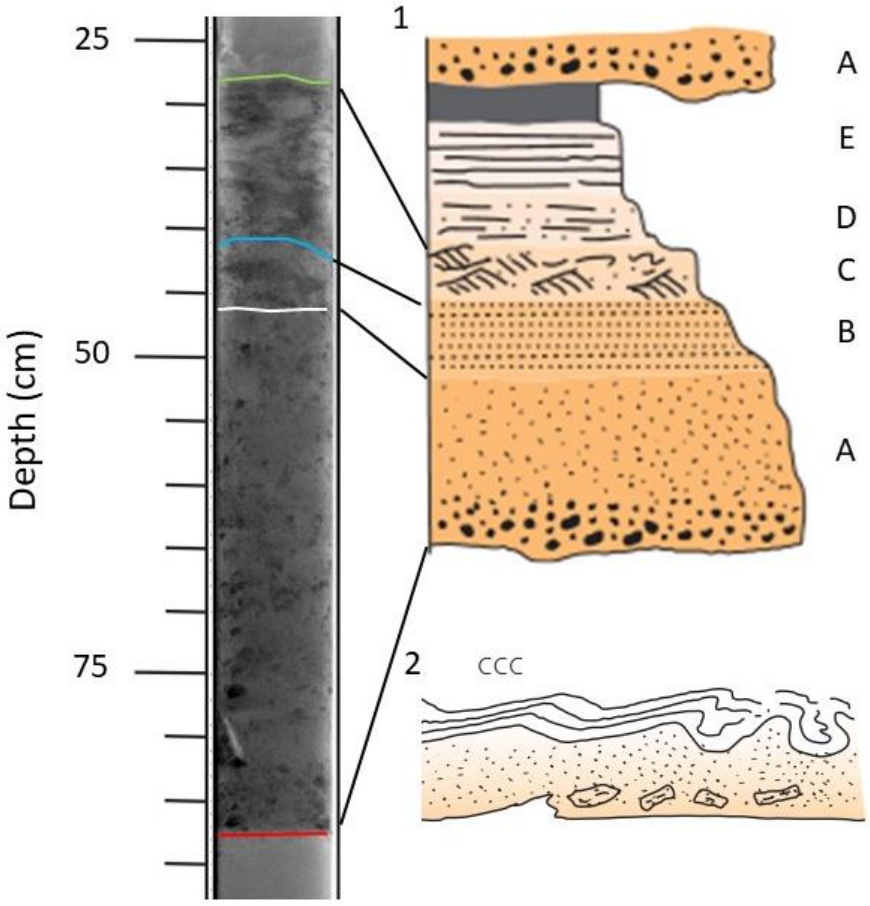

Figure 6.12. An x-ray image of Unit 3.3 from HH17-1309-GC-TUNU correlated with layers of the Bouma Sequence (1). (2) An image of a 'base cut-out' distal turbidite, which contains similar characteristic to Unit 3.3. Images taken from Benn & Evans (2010).

6.1.4 Model of Dove Bugt

A model for the palaeoenvironment is presented below (Fig. 6.13). As it has been previously discussed, this has primarily been divided into three stages: LGM, deglaciation and Holocene. As this thesis analyzed marine data, interpretations on land are entirely hypothetical. Here, ice cap expansion has been included into the models, however it is possible that the terrestrial areas around Dove Bugt had become covered by ice from the ice stream and/or a general expansion of the GrIS, or some combination of these three phenomena. The timing of ice cap expansion may or may not coincide with migration of the NGIS either, therefore their inclusion in the model simply suggests the expansion or retreat of terrestrial ice during corresponding stage.

Stage I: LGM

Geomorphological evidence (e.g. MSGLs) suggests that the NGIS was topographically bound by terrestrial areas in Dove Bugt and flowed to the south (Fig. 6.13; Stage I: LGM). It likely followed the Dove Bugt Trough, eventually merging with ice in the Hochstetterbergten Trough (Arndt et al., 2015). Along with other areas of the Northeast Greenland Ice Sheet, this converged ice may have reached the shelf break (Laberg et al., 2017). MSGL's in Dove Bugt would likely have formed during the LGM, although ascertaining why their geomorphological dimensions vary throughout this period is not clear. Nonetheless, these landforms suggest that fast-flowing ice, with a warm-based sole, that maintained some degree of thickness, would have been present in the area. A hill-hole pair identified in the region suggests that the ice stream was partially cold-based, either during the LGM or some point during a readvancement mid-deglaciation. Terrestrial areas would have likely been glaciated, although evidence form this study cannot state whether they were glaciated before, during or after the NGIS flowed south through southern Dove Bugt. Glacial ice in Bessel Fjord would have contributed to the ice stream as a tributary channel.

Stage II: Deglaciation (≥11.2 ka BP)

The lack of well-defined moraines or GZW overriding streamlined glacial lineation across the entire region suggests that deglaciation was mostly rapid (Fig. 6.13; Stage II: Deglaciation).

Small, mostly isolated, moraines (and a feature that may be a GWZ) do however suggest that rapid retreat may not have been uniform, and that sections of the ice stream retreated slower than others. Sedimentation in Dove Bugt would have been dominated by glacially derived overflow plumes and turbidites from the ice stream, resulting in laminated mud and sand layers. IRD from icebergs, formed from the calving ice front of the ice stream, would also supply sediment to the area. Ice proximal plumes from the ice stream ceased depositing sediment in front of outer Bessel Fjord by 11,190 cal. yr. BP as the ice stream retreated towards its modern-day position.

Stage II: Holocene (<11.2 ka BP)

As it was mentioned above, the deglaciation of Dove Bugt would have encompassed the Early Holocene (11.7–8.2 ka BP) and would largely have involved the retreat of terrestrial ice and the NGIS from Dove Bugt. Sedimentological evidence suggests suspension settling from glacial input would have dominated southwestern Dove Bugt and would have likely come from a non-ice stream source (e.g. Soranerbræen or ice caps).Climatically, despite the Northern Hemisphere summer insolation reaching a maximum around 11 ka BP (Berger and Loutre, 1991; Laskar et al., 2004), a negative feedback mechanism is theorized to have caused a gradual warming in the Northern Hemisphere (Kaufman et al., 2004; Carlson et al., 2008b; Renssen et al., 2009, 2012), punctuated by several short lived, cold reversals (i.e. ~11.4, 9.3, and 8.2 ka BP) (Rasmussen et al., 2007; Vasskog, 2015). Therefore, it is possible that Soranerbræen, or more likely the ice caps north of Bessel Fjord, had a delayed response to warming and/or readvancement during cold reversals, allowing for the deposition of glacimarine sediment in Dove Bugt.

Following the 8.2 event in the beginning of the Middle Holocene (~8.2–4.2 ka), the HTM would have caused warmer than present temperatures across Greenland, at times causing glaciers to reach their minimum extent. The ice stream is believed to have retreated beyond its current position between 6 to 1 ka BP, creating the Storstrømmen Sound (Weidick et al., 1994). Although laminations appear less frequently in core HH17-1309-GC-TUNU during this period, they are not absent. Therefore, it is hard to account for the HTM in Dove Bugt with the available sedimentological data. During the following Late Holocene (4.2 ka BP–present) colder temperatures returned to Greenland. Storstrømmen is believed to have expanded to its modern

day position during the Little Ice Age (Weidick et al., 1994). A gravity driven mass wasting event occurred during this period in southwestern Dove Bugt, possibly related to the onset of colder conditions in the region. Where sea ice and the presence of icebergs were presumably reduced during the HTM, it was like renewed during this period.

Sedimentation during the Holocene would have been the result of a range of processes that are typical of near shore shelf environments. Sediment input from Storstrømmen and L. Bistrup Bræ would have waned throughout the Holocene, likely only introducing sediment into the area via IRD. It is possible that sediment transport from local ice caps and/or Soranerbræen would have deposited sediments from suspension settling throughout the Holocene, most likely having the greatest impact in the Early Holocene. Likely under accounted for in this study, sea ice probably played a large role in sedimentation in the region. Allochthonous sediments can also be transported to the shelf by means of fluvial or estuarine processes, coastal jets, hyperpycnal flows, hypopycnal plumes or tidal fluxes (Suter, 2006). Longshore currents and downwelling storm flows can also transport sediments along shorelines (Suter, 2006), although the presence of Store Koldewey on the east side of the bay likely shelters most of the region from depositional and erosional effects of the EGC. Fluctuations in sea-level (transgressive-regressive coastal development) can also allow for the deposition of sediments across a shelf and has been used to explain the appearance of isolated gravel and sand depositions far from the present-day coastline (Suter, 2006). Mass wasting would have also occurred along the periphery of the bay as well as in select regions in the subsurface (as seen in Unit 3.3).

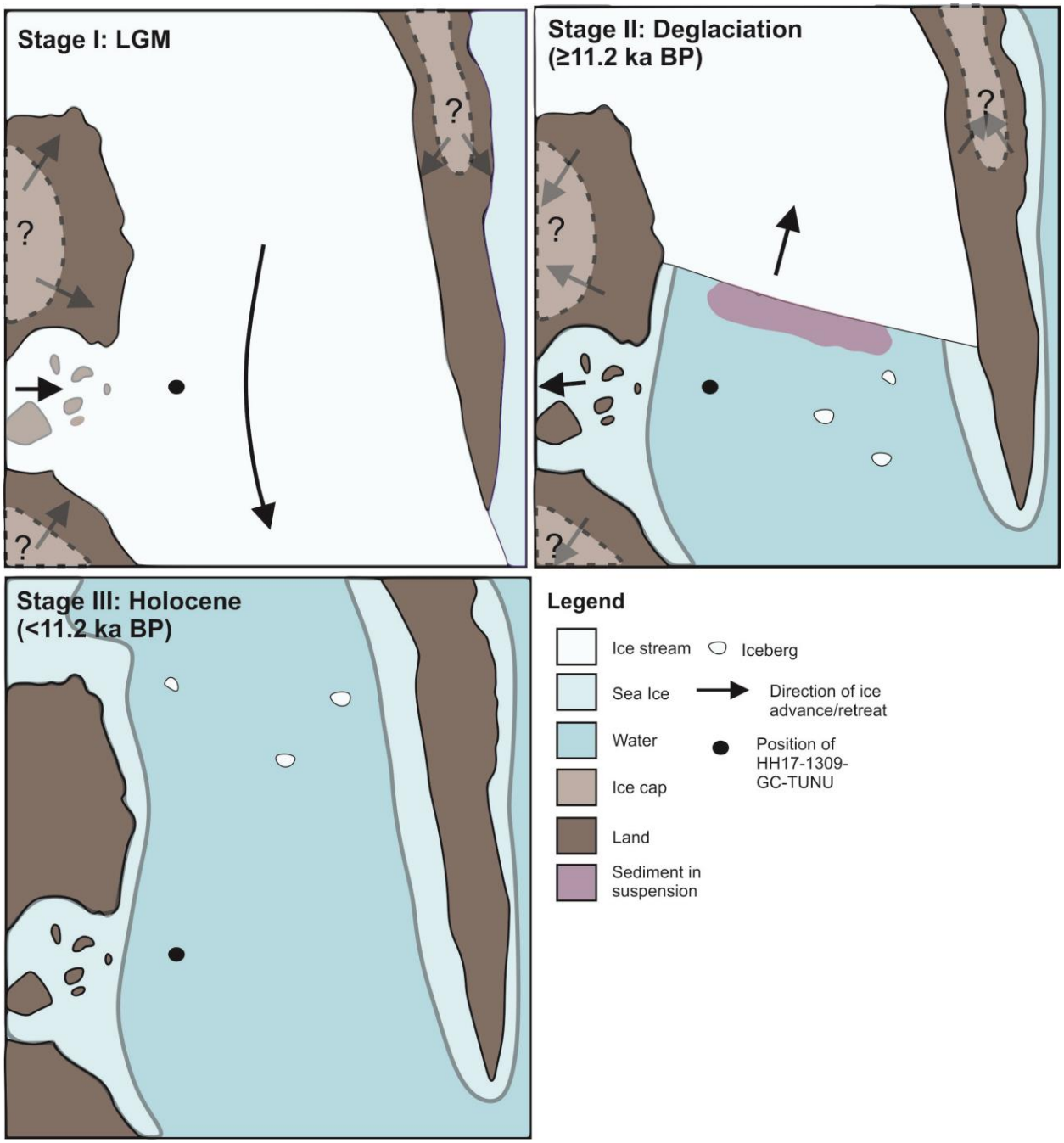

Figure 6.13. Model of the evolution of southern Dove Bugt from the LGM to modern times.

6.2 Palaeoenvironment of Bessel Fjord

Like the preceding section, the palaeoenvironmental reconstruction of Bessel Fjord consists of three stages: LGM, Deglaciation and the Holocene. This includes a discussion of each of these stages, followed by a presentation of a model for the region and an explanation and summary of the discussed material.

6.2.1 Stage I: Last Glacial Maximum (LGM)

6.2.1.1 LGM extent, topographic controls and ice cap expansion

During the LGM Bessel Fjord would have likely been fully glaciated. This glaciation would have seen an expansion of Soranerbræen to or beyond the fjord's outer sill as well as the expansion of local ice caps around terrestrial areas and possibly into the fjord. Geomorphologically, this is supported by the presence of glacigenic features near the mouth of the fjord (e.g. streamlined landforms, possible crevasse squeeze ridge and a possible medial moraine). Deep basins and base-level flattening likely reflects multiple ice advances into the fjord (e.g. Barnes et al., 2016).

Characteristics of the fjord also suggest that Soranerbræen was topographically bound, at least during its initial expansion (e.g. Fig. 5.4). Deepened sub-basins (SB 1-3) identified south of a large bedrock mound (M1) in Section 2 has been interpreted as being the result of Soranerbræen flowing around this bedrock feature before eventually flowing over the mound (Figs. 5.11 & 5.15). This is supported by the raised sub-basin to the north (SB 4) which may have been initially shielded from advancing ice. The presence of a streamlined landform on the eastern side of this large mound supports the theory that the mound was eventually overcome by the ice. This is believed to also be the case for the large mound between Sections 3 - 4 and Sections 4 - 5.

This is further supported by the orientation and shape of the basin in Section 5 (Fig. 6.14). As the fjord walls open to a bay, the over deepened basin appears to orient itself to the NE-SW north of Trums Ø. There does not appear to be any evidence of glacial erosion of the southern wall of Section 5 which leads around the southern passage of Trums Ø (Fig. 6.14). This suggests that ice was, at least initially, topographically bound and that the southern region between Trums Ø and the southern side of the fjord is composed of resistant bedrock.

Immediately east of this, the seafloor is divided into two regions that are at different elevations and separated by a small ridge and an elongated bedrock or glacigenic feature (Figs. 5.8 & 6.15). There are several theories to explain how these two flat lying regions formed. In Scenario I (Fig. 6.15) Soranerbræen continues to follow topographic controls to the northeast. Ice also begins to fill Langsødalen, either from Enjer Mikkelsen Gletscher, a branch of Soranerbræen via Vandrepasset (Fig. 2.1) and/or another outlet of Inland Ice. Ice in this glaciated valley eventually began intruding on the southern side of outer Bessel Fjord. In Scenario II there are two phases (P1 & P2, respectively). In the first phase (P1), Soranerbræen follows topographic controls, similar to Scenario I. In phase two (P2), however, Soranerbræen over comes regions of higher topography (i.e. western Trums Ø) and enters southern Outer Bessel Fjord at a later date. In Scenario III, local ice caps build up on terrestrial regions (Scenario IIIA) and eventually expand into marine areas (Scenario IIIB).

Scenario I is the least likely of these scenarios, because ice would need to cross multiple areas of raised topography to reach this position in Outer Bessel Fjord. In the time it would take ice to overcome topographic barriers and travel down valley, Soranerbræen would likely have been able to cross much lower topography in Bessel Fjord (i.e. Trums Ø). Therefore, the multi-phase Scenario II is far more likely. As it has been stated before, it has been theorized that mounds that acted as "topographic controls" in Inner and Mid-Fjord regions have eventually become overcome, which is supported by limited geomorphic evidence (e.g. streamlined landforms and sub-basins). Here, it is presumed that the entirety of Trums Ø and low-lying regions in outer Bessel Fjord would have been eventually covered by ice.

Scenario III assumes that either existing ice caps and/or new ice caps developed and expanded across mountain tops north and south of Bessel Fjord, eventually encroaching on the marine environment. In northern modern Bessel Fjord, ice lobes from a local ice cap appear nearby fjord water (e.g. Figs. 2.9, 5.4 & 5.5), therefore it is easy to imagine that in climatically colder periods these lobes (or similar lobes developed in other section of the fjord) would expand into Bessel Fjord. Possible further evidence for ice cap expansion can be found in Section 4, where large quantities of sediment and what are interpreted as sediment lobes appears nearby two valleys north and south of Bessel fjord (Fig. 6.14). It is possible that these valleys previously acted as a

conduit for ice lobes (and possibly a path for meltwater during periods of deglaciation). This is further supported by the presence of a single streamlined landform in Section 4 which is oriented at in a northwest-southeast direction. In the previous section this feature has interpreted as a crevasse squeeze ridge, however given its orientation relative to the northern most of these potential ice lobe conduits, it may be the result of an ice lobe expanding into Bessel Fjord. The lack of these features in the inner part of the fjord may be the result of Soranerbræen already occupying that section of the fjord by the time ice lobes started entering the fjord. In that case, the ice lobes would have joined the glacier ice and migrated eastwards.

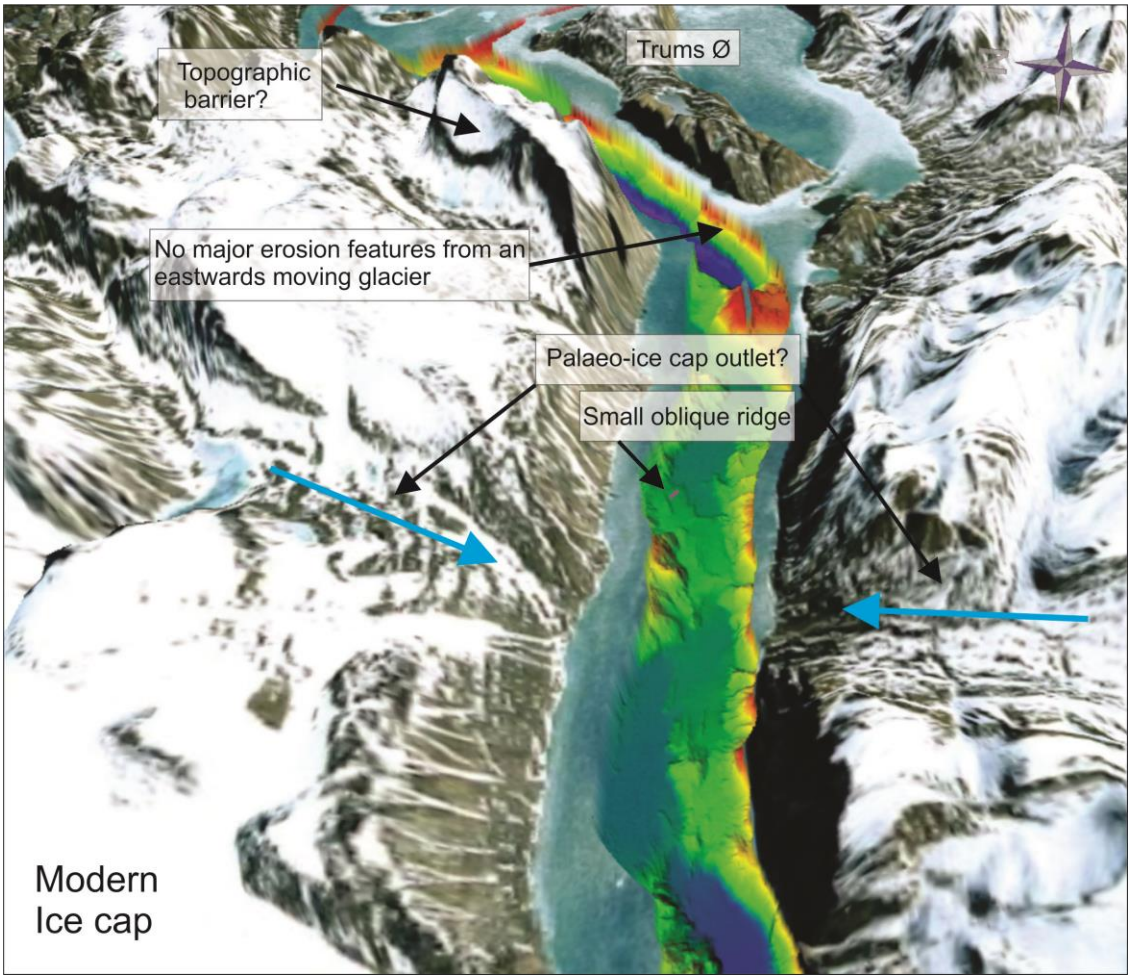

Figure 6.14. Image of Section 4 and western Section 5 in Bessel Fjord highlighting notable geomorphological features.

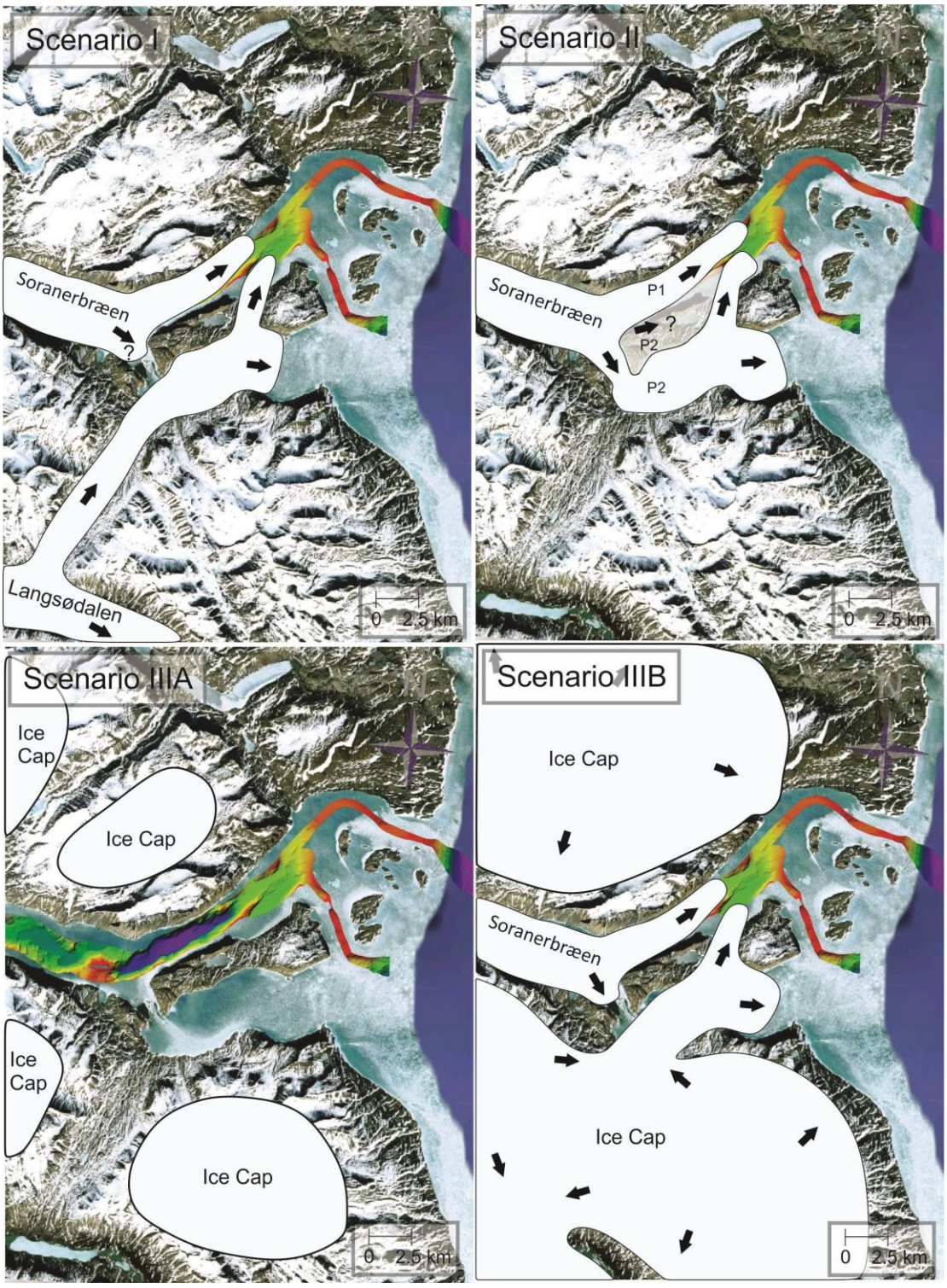

Figure 6.15. Different scenarios for the glaciation of the outer fjord region of Bessel Fjord. Scenario I- valleys are filled by glacial ice and expand into Outer Bessel Fjord. Scenario II- Soranerbræen glaciates the entire region in two different phases. Scenario III- Ice caps expand and glaciate the region along with Soranerbræen.

The expansion of terrestrial ice has been observed in Hochstetter Forland (Fig. 6.4; Hjort, 1981; Hjort & Björck, 1983; Björck et al., 1994) and remains unexplored on Ad. S. Jensen Land, north of Bessel Fjord. Therefore, it is likely that ice caps, either alone or with a larger body of terrestrial ice from the GrIS, aided in the formation of these features. It is theorized here that if terrestrial ice was able to reach the shores of Hochstetter Forland, it is possible that terrestrial ice could have migrated into the Outer Fjord region of Bessel Fjord and formed this secondary flat lying region.

6.2.2 Stage II: Deglaciation

6.2.2.1 Timing of Deglaciation

The exact timing of deglaciation within Bessel Fjord is difficult to constrain based on available data. As it was previously discussed, immediately outside of Bessel Fjord it is theorized that the NGIS retreated from southern Dove Bugt by 11,190 cal yr. BP. Evidence for continued glacial activity in Outer Bessel Fjord can be found in Unit 3.2 of HH17-1309-GC-TUNU, although it is difficult to attribute this to Soranerbræen or local ice caps. The similar and later deglaciation ages on Hochstetter Forland suggest that terrestrial ice (i.e. possible ice caps) south of Bessel Fjord would have either been in retreat at the same time as the ice stream or remained on land until a much later date. Therefore, it is possible that Bessel Fjord was still filled with ice after the ice stream retreated from southern Dove Bugt. In gravity core HH17-1290-GC-TUNU, in the Inner Fjord region of Bessel Fjord, the final appearance of laminations has been identified immediately prior to 7,160 cal yr BP (Fig. 6.1). This corresponds to the Middle Holocene (Fig. 6.11). The lithology of the preceding units does suggest that sediments were deposited in a glacimarine environment, becoming increasingly ice distal up core (see the following section for more details). Without additional datable material it is impossible to say when or exactly how quickly this material was deposited. This does suggest, however, that Soranerbræen, and possibly ice from local ice caps, were retreating through the Inner Fjord during the Early Holocene and into the beginning of the Middle Holocene. This provides a “minimum” age for deglaciation of the Inner Fjord.

6.2.2.2 Recessional Moraines and Topographic Controls on Deglaciation

Features interpreted as recessional moraines have been identified across Bessel Fjord, suggesting that Soranerbræen experienced a stepwise deglaciation. Recessional moraines are relatively common in shallow shelf and fjord setting where there is a slow retreat of a grounded tidewater glacier margin (Boulton, 1986; Ottesen & Dowdeswell, 2006; Dowdeswell et al., 2008) and can form through minor winter readvances, possibly induced by a lack of iceberg calving in the presence of sea ice (Dowdeswell et al., 2016).

The large moraine between Section 2 and 3 has been interpreted as forming during a major ice readvance. This interpretation is favored because of the size of the moraine relative to other moraines in the fjord. The age of 7,160 cal yr BP from core HH17-1290-GC-TUNU provides Soranerbræen with the latest possible age for retreat, therefore it likely formed prior to this date. Although there are multiple cold reversals between the LGM and modern times, the most pronounced was the Younger Dryas. However, if this moraine formed during the Younger Dryas, Soranerbræen would not have occupied the entirety of Bessel Fjord when the ice stream left Dove Bugt. This would imply that sedimentation in Dove Bugt after 11,190 cal. yr. BP would have been primarily from local ice caps. Bessel Fjord becoming ice free while Dove Bugt was still covered in ice seems less likely, however, therefore, it is theorized that this moraine likely formed during a different cold reversal during the Holocene. More data may be required to confirm this theory. Like in core HH17-1309-GC-TUNU in Dove Bugt, microfractures in the Mid-Fjord core HH17-1290-GC-TUNU act as the only evidence for an ice body overriding the sediment. However, as it has been stated before, these features may not have formed subglacially, therefore it is not definitive proof of overriding ice.

Smaller moraines appear to follow topographic boundaries at times (e.g. Section 2; Fig. 5.15), suggesting that the retreat of Soranerbræen was also topographically controlled. If the deglaciated ice followed topographic barriers, this may have caused sections of ice to become detached from the main glacial body. If this were to occur, these sections of dead ice may explain the presence of raised sub-basin in Section 2 (SB 5) and Section 4 (SB 6). In Telemark in southern Norway, Eilertsen et al. (2016) identified similar geomorphic features and also attributed their appearance to dead ice (although features in Bessel Fjord are “raised”, where

their features were directly on the seafloor). They suggested that although these features have been identified in sub-aerial proglacial areas (e.g. Kjær & Krüger, 2001) the processes behind their formation in marine environments are likely quite different (Eilertsen et al., 2016)

Additionally, ice caps and local glaciers have been theorized to be more responsive to local paleoclimatic fluctuations than inland Greenland ice (Kelly & Lowell, 2009). Since Soranerbræen is an extension of Inland Ice, it is possible that some smaller moraines are the result of ice cap expansion (e.g. S2TR1 in Section 2; Fig. 5.15), which may have advanced or retreated out of sync with Soranerbræen. Further evidence for ice cap expansion can be seen in Section 4, where large quantities of sediment lobes have been observed (Fig. 6.14). It is possible that ice cap expansion and/or retreat in the section caused the deposition of sediments along the side wall of the fjord. This may either be caused by glacifluvial activity and/or increased mass wasting associated with the presence of an ice body north and south of the fjord.

6.2.2.3 Evolution of Landforms in Western Section 3

A complex set of geomorphological features have been identified east of a large moraine in western Section 3 (Fig. 6.16). Below is the theorized chronology of these landforms:

A. Esker formation

It is theorized that first sub- and/or englacial channels became filled with glacial debris (Fig. 6.16A). This region of Bessel Fjord was likely covered in ice when these landforms developed. The presence of this landform confirms that larger quantities of subglacial water was once present beneath Soranerbræen.

B. Soranerbræen and ice cap moraine formation

An ice advance to what may be a bedrock threshold between basin 1 and 2 allowed for the formation of a large moraine (Fig. 6.16B). Given the concaved shape of the eastern side of the moraine, it may have been much larger but experienced a collapse in its center. During this time ice cap lobes may have also expanded into the fjord. Sediment lobe-like features at the mouth of the ice lobe may represent moraines.

C. Glacigenic mass wasting processes

Moraine gullies and other erosional features are believed to have formed as the result of the release of meltwater and sediment from the glacier and ice caps front (Fig. 6.16C).

D. Sediment waves

Although it is not entirely clear how these sediment waves formed, their orientation and relationship with other landforms suggest that they likely formed during this period (Fig. 6.16D). They appear to be mostly parallel to the moraine in the west, although some of the northern most sediment waves appear oriented parallel to the ice lobe. See below for additional information about these landforms.

E. Channel formation

A large channel identified cross cutting the sediment waves is believed to have formed next in succession (Fig. 6.16E). Given the channels orientation it is possible that it formed from a terrestrial landslide northwest of this region or from a possible collapse of the northern portion of the moraine. A small indent on the western side of the channel does suggest that the channel may have also been eroded in the middle of the channel from a different mass wasting event. However, the well-preserved esker to the west of this landform suggest that this may not have been the result of a turbidity current related to a collapse of the moraine wall to the west.

F. Fjord sidewall slide scars and gullies

The final stage involves the formation of slide scars and gullies from sidewall collapse of the fjord (Fig. 6.16F). Failures along the sidewall may have been the result of rapid suspension settling of sediment from the nearby ice cap, which may have increased the shear stressed beyond the critical shear strength of the sediments.

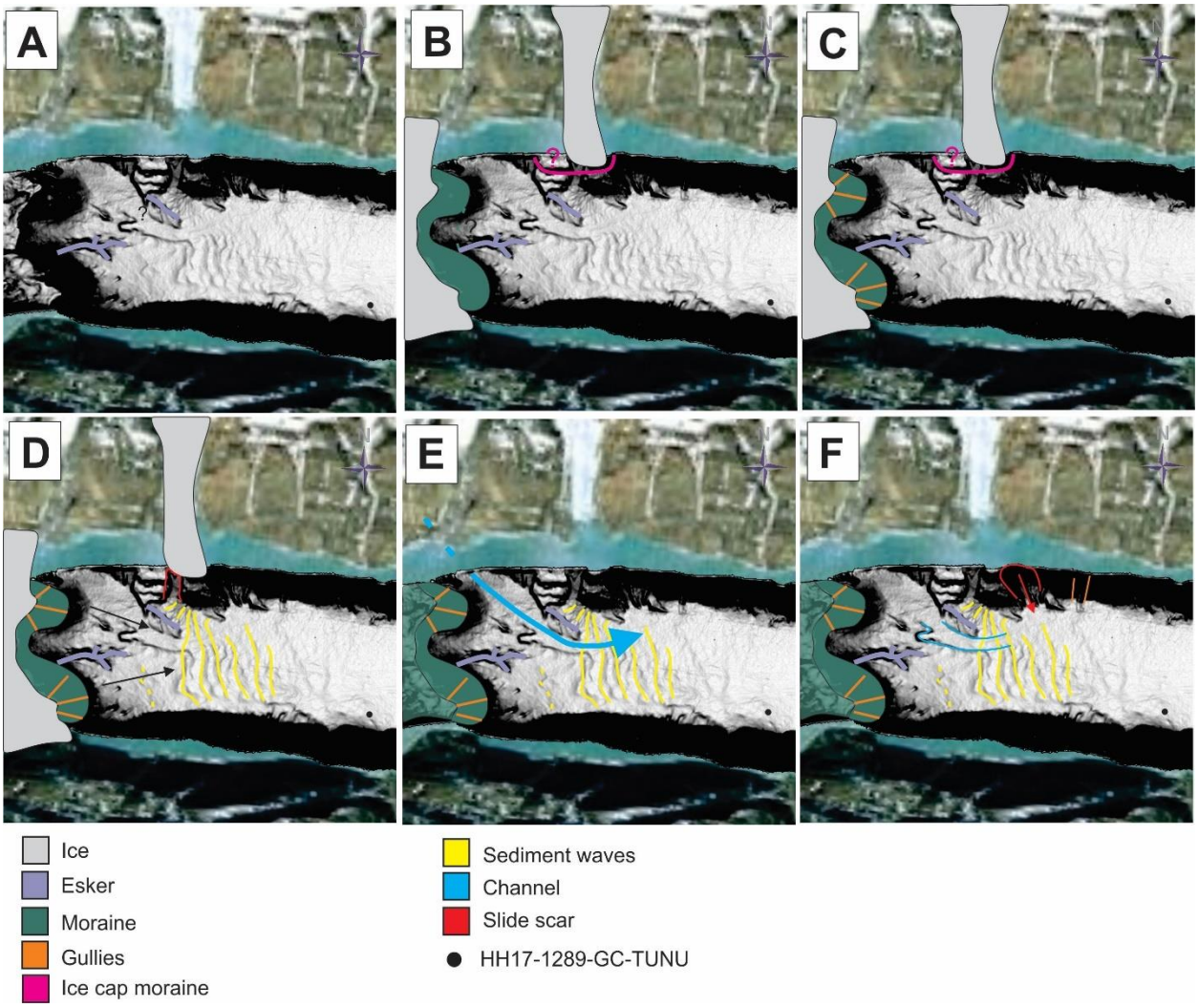

Figure 6.16. Potential chronological evolution of landforms in western Section 3 of Bessel Fjord. A: Esker formation. B: Moraine development by Soranerbræen and ice cap lobe. C: Moraine mass wasting. D: Sediment wave formation. E: Channel Formation. F: Sidewall mass wasting.

6.2.2.4 Sediment Waves

The orientation of sediment waves perpendicular to the large moraine between Section 2 and 3, and to some degree the ice cap lobe for the northern most sediment waves, suggest that these features may have aided in their formation (Fig. 6.17). Given the presence gullies on the moraine, it seems likely that the formation of these features is related to some ice induced mass wasting process, possibly related to the release of meltwater. The presence of eskers adjacent to the moraine do suggest that subglacial channels were once beneath local ice bodies. Two possible mechanisms behind the formation of sediment waves discussed by other authors are considered below. Bottom current processes have also been theorized to be responsible for forming sediment waves (e.g. Flood et al., 1993), however given the orientation of the northern most waves toward the ice cap this seems unlikely and will not be discussed here.

Cyclic steps

Based on surface level observations these features do appear to resemble cyclic steps described in other publications (Fig. 6.17) (e.g. Smith et al., 2005; Cartigny et al., 2011; Zhong et al., 2015; Normandeau et al., 2016; Trottier et al., 2020). The steep lee slope and low-angled stoss side typical of cyclic steps (Zhong et al., 2015). can be observed here. The formation of cyclic steps have been attributed to the upwards migration of waves as the result of turbidity flows from deltaic and glacifluvial deltaic systems (Stacey & Hill, 2016; Trottier et al., 2020).

In a very general sense, these sediment waves appear to have a steep lee slope and a low-angled stoss side typical of cyclic steps (Zhong et al., 2015). In determining if these features are cyclic it is particularly important to determine the features migration direction. Normandeau et al (2016) states that migration direction is not to be determined unambiguously without repeated bathymetric surveys or imaging of the internal termination. Despite this, Cartigny et al. (2011) provided a geometric framework for determining migration direction, however based on the positioning of these two sets of sediment waves (as well as the crescent geometry of the moraine to the west) it is difficult to determine if these features meet their given specifications. Many have also tied cyclic step formation to supercritical density flows, which can form on slopes steeper than 0.6° (Komar, 1971; Hand, 1974; Sequeiros, 2012) or 0.7° (Fricke et al., 2015;

Normandeau et al., 2016). Both the northern and southern sediment waves have slopes that meet these criteria, and the moraine to the west of the southern sediment wave (the most likely culprit for density flow development) slopes at ~12°. Based on all of the above observations it is possible that these landforms also developed as an upslope migrating product of density flows, although more data may be required to confirm this. As it was stated above, the southernmost feature likely developed from failures along the large recessional moraine to the west, where smaller sediment waves to the north formed in relation to the ice cap lobe that sits directly above it. Densimetric Froude number, the mean grain size, availability of sediment for erosion, slope, inflow concentration of sediment, as well as other factors, all effect the formation and evolution of cyclic steps (Kostic, 2011; Normandeau et al., 2016).

The position of these features adjacent to a moraine and ice cap would suggest that Soranerbræen and the ice lobe would have needed to produce a significant quantity of water to cause these features to form. The formation of eskers at the base of the moraine, as well as numerous gullies along the moraine, do support the theory that meltwater played a large role in shaping the area. However, there is no evidence that the glacier and moraine acted similar to a "delta" while also being able to maintain its position at the moraine. Given the steady quantity of water required to form these features this seems less likely.

Sediment Creep

An alternative mechanism to describe the formation of these features is gravity-driven downslope collapse or creep. Mass movements in submarine environments may be caused by high sedimentation rate, storm waves, earthquakes and biological processes, either increasing the applied shear stress or reducing the critical shear strength of the sediments (Lee & Chough, 2001). Sediment stability is also impacted by sediment lithology, pore-pressure, the slope angle and interrelated factors (Sultan et al., 2004; Shillington et al., 2012). Lee & Chough (2001) noted that the amplitude of the waves tends to increase downslope, where the slope decreases. In Bessel Fjord, there is no uniform change in amplitude (Fig. 6.17A). The amplitude of waves in the northern portion of the field site appear so small they are difficult to capture in profile (Fig. 6.17B). Forwick et al. (2010) has identified sediment waves in the Arctic near chutes and

attributed the formation of waves to mass wasting. As it has been previously discussed, evidence for mass wasting has been observed along the moraine to the west (e.g. gullies). Therefore, sediment creep brought about by mass wasting processes appears to be the more probable mechanism behind the formation of these features. This mass wasting may be attributed to the release of meltwater from nearby ice bodies, which would have caused instability along the slopes of the moraine and in front of the ice cap lobe. This is an initial theory, however, and additional investigations into the stratigraphy may be required to understand their origin.

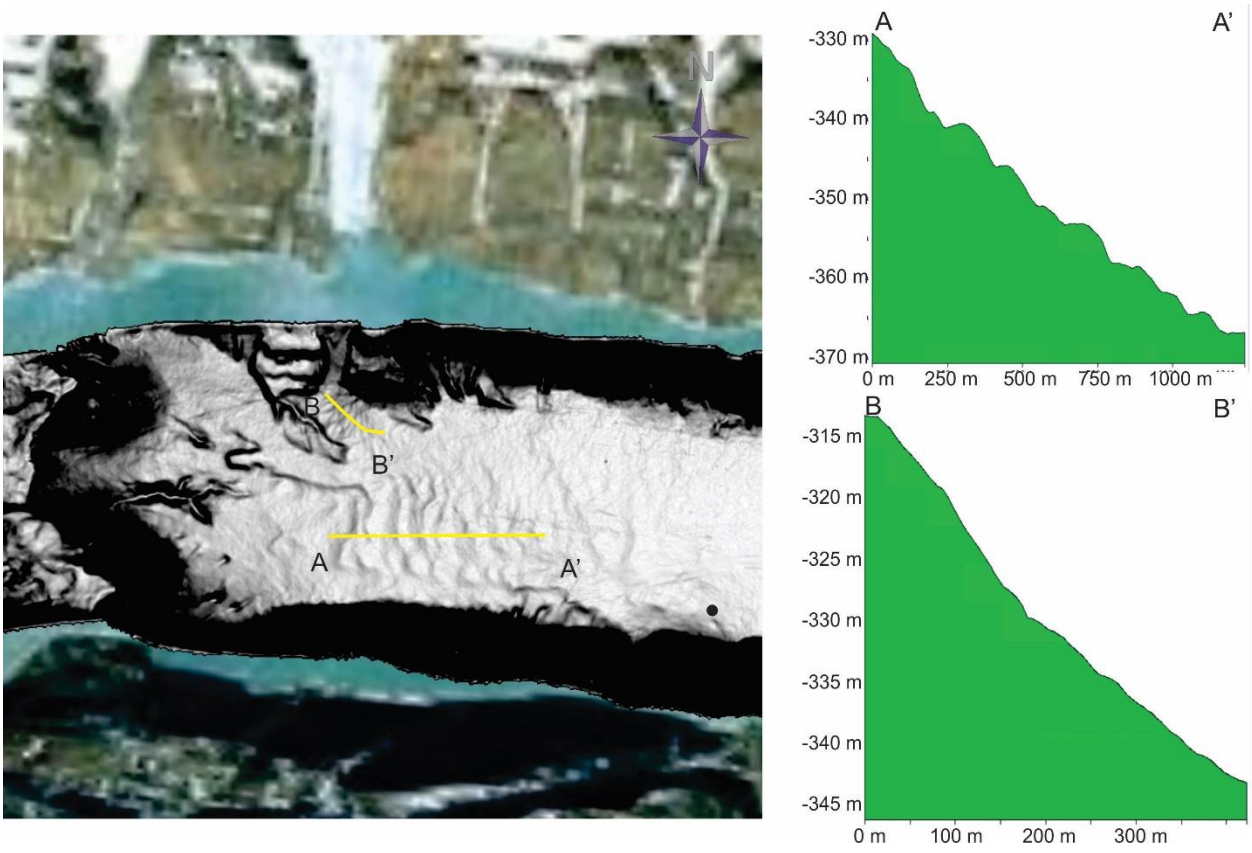

Figure 6.17. Sediment waves in Section 3. A-A' cross section profile of the prominent sediment waves that are oriented parallel to the moraine in the west. B-B' cross section profile of sediment waves oriented obliquely to the ice lobe. Note: B-B' small amplitude.

6.2.3 Stage III: Holocene

6.2.3.1 Implications of Sediment in HH17-1290-GC-TUNU

The third evolutionary stage of Bessel Fjord consists of the Holocene, which partially overlaps with the "Deglaciation Stage". The consistent laminations of mud and sand at the bottom of the core HH17-1290-GC-TUNU to ~317 cm have been interpreted as sediment plumes and turbidites from an ice proximal, glacimarine environment. Above this, Unit 1.2 consists of sections of punctuated laminations with IRD (Fig. 5.36). Like Unit 1.1, a lack of datable material makes it difficult to determine the exact timing of sedimentation, however radiocarbon dating suggests that these muddy laminations cease around 7,160 cal yr BP. These punctuated laminations have been interpreted as a brief return to a more ice proximal setting in the area, although with the available dataset it is difficult to determine if this is from an advance from Soranerbræen or a local ice cap. Microfractures near the base of the core support an ice advance, although it is difficult to assign these features to a single event. After 7,160 cal yr BP sedimentation becomes slow, and the sediment source(s) become more consistent. This uniform sediment reflects a depositional environment that experienced very little change, which may imply that there was little to no change in sea ice cover during this period.

XRF results do support the retreat of Soranerbræen prior to 7,160 cal yr BP and a consistent sediment source after this dated interval. As Ca concentrations appear higher downcore, where K and Fe concentrations increase up core, it is apparent that as Soranerbræen retreats sediment with a different chemical composition contributes more sediment to the area. This relationship between Ca and ice proximity has also been observed in Moskusoksefjord further south in East Greenland (Olsen, 2015). The dominant rock types in the area often given unspecific names like "orthogneiss", "Quaternary cover" and "metasediments" (Fig. 6.18) making it is difficult to pinpoint what the chemical composition of the source rock would have been. Therefore, a detail examination of provenance will not be discussed here. Fig. 6.18 shows multiple possible ice cap fed fluvial sources (B, C, D) that likely contributed sediment to the core after Soranerbræen (A) retreated.

After 7,160 cal yr BP (Unit 1.3), the chemistry of the sediment becomes more uniform, but is noticeably different than the sediment beneath it (Fig. 5.34) with particularly low Ca and Zr/Rb concentrations. This suggests that sediment input from Soranerbræen and glacifluvial streams remained relatively constant during the remainder of the Holocene. Assuming Ca can be used to interpret Soranerbræen ice front proximity, it does not appear that the glacier expanded into the Inner Fjord for the remainder of the Holocene. A peak in Ca has been observed near the top of the core, however it is difficult to attribute this to glacial input or biological activity. After the HTM, heavy sea ice cover may have also masked advances made by local ice caps or Soranerbræen during the Late Holocene. Satellite imagery from modern day Bessel Fjord show glacifluvial sediment being released directly from Soranerbræen and ice cap fed fluvial channels (Fig. 6.19), which suggests that sediment from HH17-1290-GC-TUNU is composed of fine sediment from multiple sources.

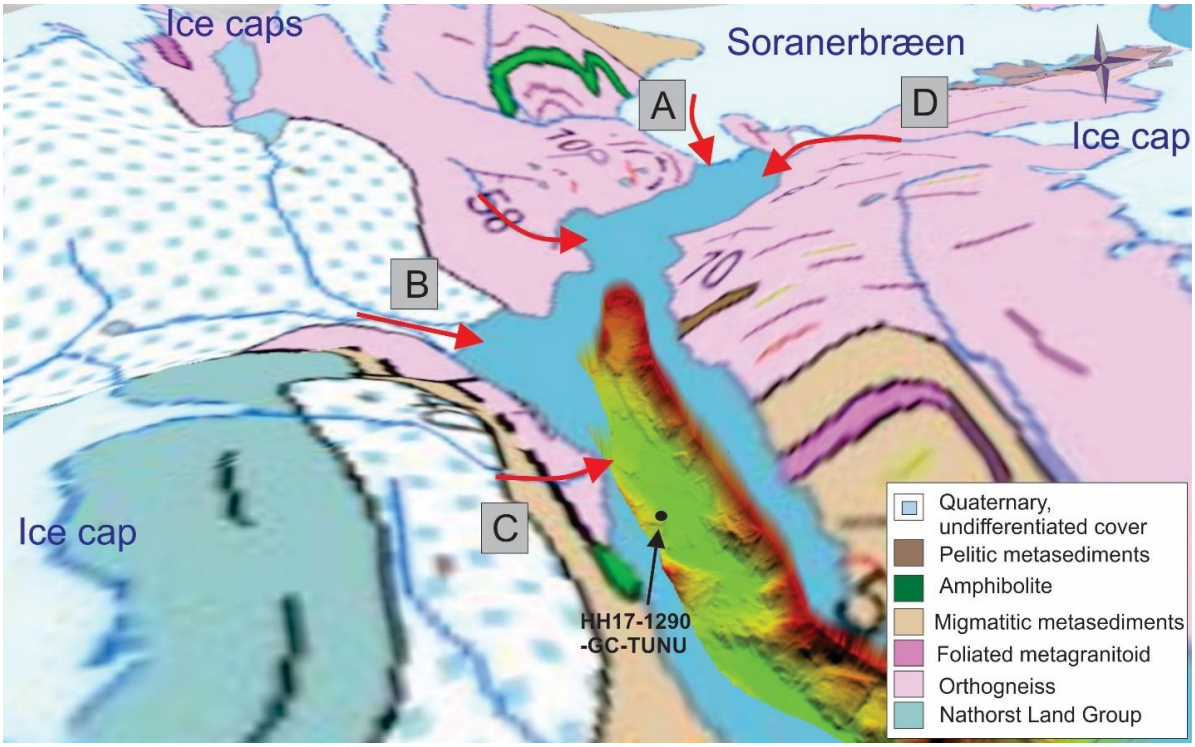

Figure 6.18. Bedrock map and bathymetry dataset of Section 1 of Bessel Fjord. Bedrock data taken from GEUS database. Red Arrows- modern (glaci)-fluvial input.

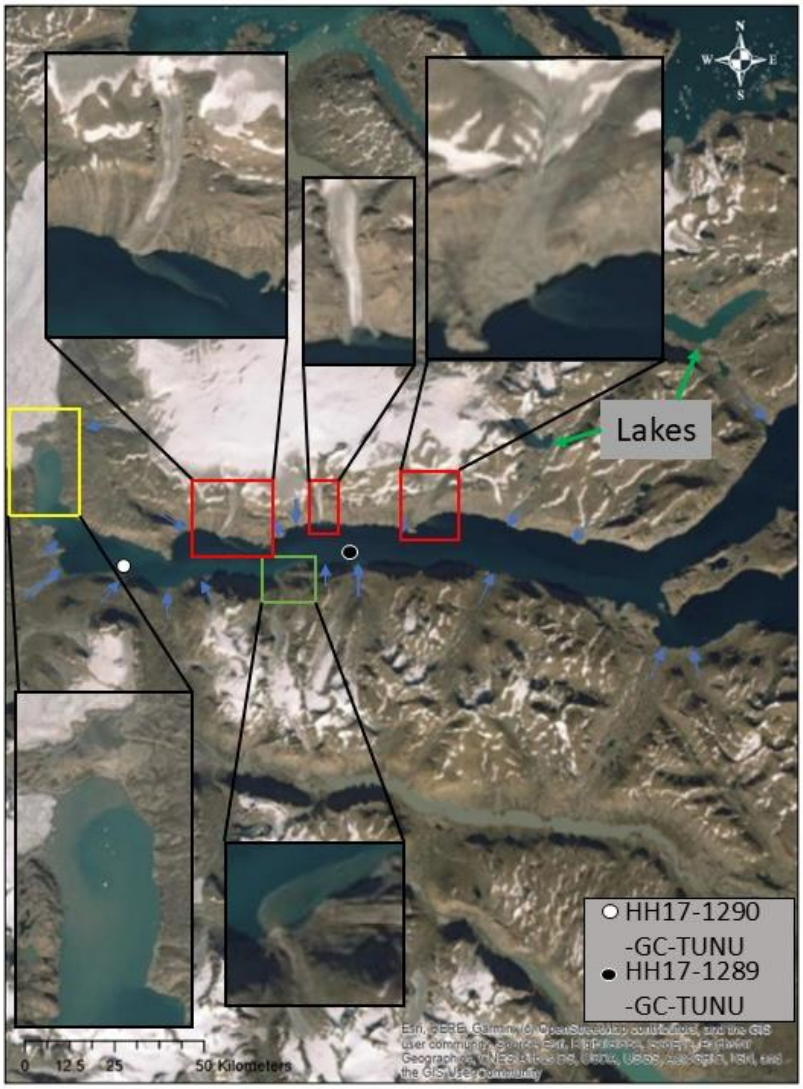

Figure 6.19. Satellite image of Bessel Fjord during the summer, with visually observed glacial and glacifluvial sedimentation magnified. Blue arrows mark the positions of mapped fluvial channels from GEUS bedrock map. Yellow box- Soranerbræen; red boxes- three larger outlets for the northern ice cap; green box- a fluvial outlet from southern ice cap drainage releasing a particularly large amount of sediment.

6.2.3.2 **Implications of Sediment in HH17-1289-GC-TUNU**

The bottom most unit of HH17-1289-GC-TUNU (Unit 2.1) is believed to have formed through suspension settling from glacifluvial sources, with the occasional turbidite layer introducing sand into the core. In the modern environment surface water has been observed flowing to the east (Fig. 6.19), therefore it is theorized that sediment forming this unit either came from west of the

coring location or from a position immediately adjacent to the coring site. A modern river is positioned south of the coring site and may have contributed to the deposition of much of the coarser material (Fig. 6.20). Given the units position beneath material dated to 3,544 cal yr BP, it can be assumed that at least part of this unit was deposited during the Middle Holocene, possibly during the HTM.

Just prior to 3,544 cal yr BP, at the bottom of Unit 2.2, sand deposition becomes the dominant sedimentation processes in the area and continues to be so until modern times. Along with this shift in sediment grain size, the sedimentation rates across Units 2.2, 2.3 and 2.4 appear to increase significantly up core. Therefore, at ~4,000 yr BP there is a change in the depositional environment. As it has been discussed above, the HTM likely ended in the region between 5.6-4 yr BP (Briner et al., 2016), which may imply that this shift in sedimentation was climatically driven. Although, more dated material may be required in order to confirm this interpretation.

Although colder temperatures during the Holocene may imply an ice advance, evidence from HH17-1290-GC-TUNU suggests that Soranerbræen did not readvance into the fjord during this period. However, ice caps that are more sensitive to climatic changes may have advanced and/or retreated. Northwest of HH17-1289-GC-TUNU, a lobe from the northern ice cap has been observed in modern times (Fig. 6.21C) and northeast there appears to be a potential conduit in which an ice lobe could follow. Multiple ice cap fed rivers can also be found south of coring site (Fig. 6.21A & B). Sediment lobes identified in bathymetric images suggests that a steep sloped -Gilbert-type delta- may have formed south of the core site. Deltas that form in the Arctic undergo numerous processes that differ from deltas that develop in more temperate climates. For example, rivers in the Arctic are frozen throughout most of the year in the Arctic, therefore river discharge only occurs during a brief time of the year, where poorly sorted coarse material is often transported (Nielsen, 1994). Since the core is also positioned nearby sediment waves, it is possible that processes involved in creating these features also deposited sediment in HH17-1289-GC-TUNU.

As it has been expressed about core HH17-1290-GC-TUNU, determining provenance based on XRF is quite challenging due to generalities made about rock types (Fig. 6.21). Nonetheless,

XRF can be used to make some inferences about certain layers. Since Zr happens to be relatively heavy and Rb is more typical in clays (Rothwell & Croudace, 2015), authors have used a ratio of these elements to indicate flood events (Wang et al., 2011) and the base of turbidites (Rothwell et al., 2006). In this core, peaks in Zr/Rb values can be found in some sand layers (and a section of mud) in Unit 2.1. The trend in this ratio also tends to (mostly) increase up core. Individual layers with high Zr/Rb ratios have been interpreted as resulting from rapid transport to the fjord (e.g. turbidite), where gravitational processes did not remove Zr from suspension. Si and Al, both indicators for terrigenous content (Rothwell & Croudace, 2015), have been identified in particularly high quantities in massive coarser sand layers at the top and bottom of Unit 2.3. These similar geochemical properties, as well as lithology, suggest a similar provenance and depositional processes. Here they are interpreted as being the result of rapid deposition, possible Layer (A) of the Buoma Sequence (Fig. 6.12; Benn & Evans, 2010).

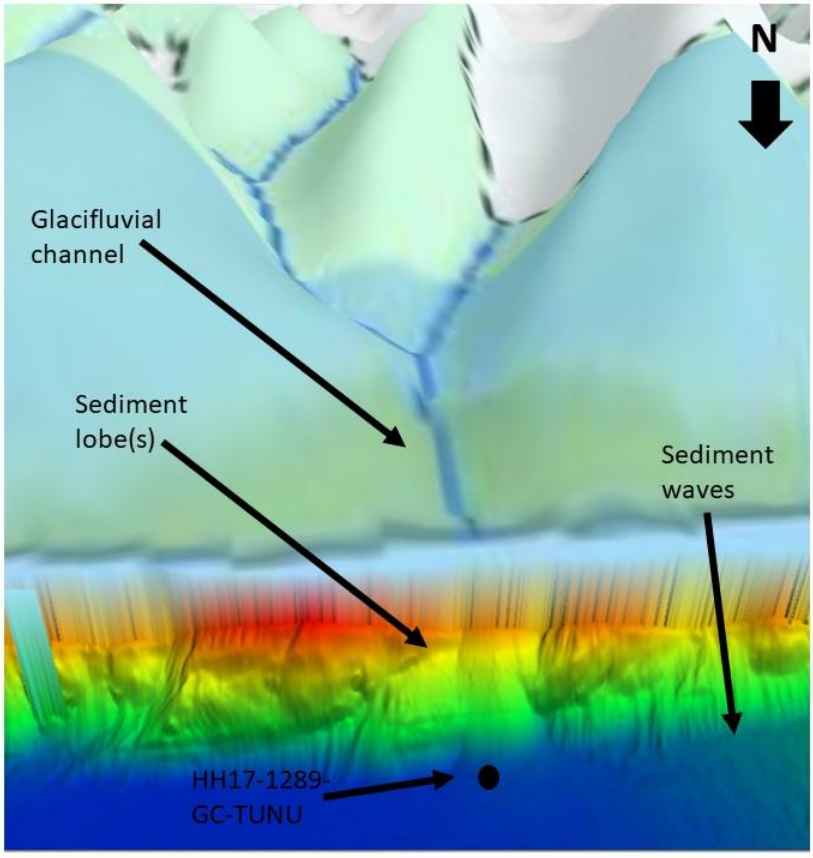

Figure 6.20. Image of the position of HH17-1289-GC-TUNU in Section 3 of Bessel Fjord.

A small diamict identified between these two coarser layers dated to 1,147 cal. yr. BP. This roughly falls within the Medieval Warm Period (Jennings & Weiner, 1996; Wagner et al., 2008), or by some accounts the end of the 'Dark Age Cold Period' (e.g. Helama et al., 2017). Nonetheless, this may suggest an ice advance during this period. Concentrations of heavier elements (i.e. Zr and Ti) are low in the diamict. This may reflect a source rock that lacked heavier minerals (e.g. sandstone or shale) or the material had undergone some degree of erosion. More likely, however, given the small quantity of material, it was iceberg derived.

Sediment grain size analysis revealed substantial mud content in each of the sand samples. In some instances, grain size distributions of sand samples were polymodal (e.g. Fig. 5.37; first sample), bimodal (e.g. Fig. 5.37; second sample) and trimodal (e.g. Fig. 5.37; seventh sample; see Appendix B). This likely reflects instantaneous sediment deposition with a mixed composition and/or suspension settling from various sources. Layers of mud have been observed interbedded and interspersed with sand around the diamict in Unit 2.3 to the top of the core. Interbedded layers of mud can very well be the result of a period with almost entirely sedimentation from suspension settling. The sand/mud mixture of Unit 2.4 is harder to account for due to the increased sedimentation rate up core. XRF values from Unit 2.4 are relatively uniform, suggesting that the source of sediment became relatively constant between ~600 cal yr. BP (using the age/depth model; Fig. 6.1) to modern times. Since this core has been collected near a sediment lobe (possibly a delta), it is possible that sedimentation here is the result of fluvial activity with a large input from suspension settling. This switch to "modern" conditions could theoretically be climatically related or a product of a fluvial distributary channel shifting (Hansen, 2004). Sedimentation in this deposit may have also been significantly faster, as the "organic patch" of plant and shell material could be similar to a "rip up clast" and may have been deposited here during a storm event, possibly during the summer season where there is no sea ice.

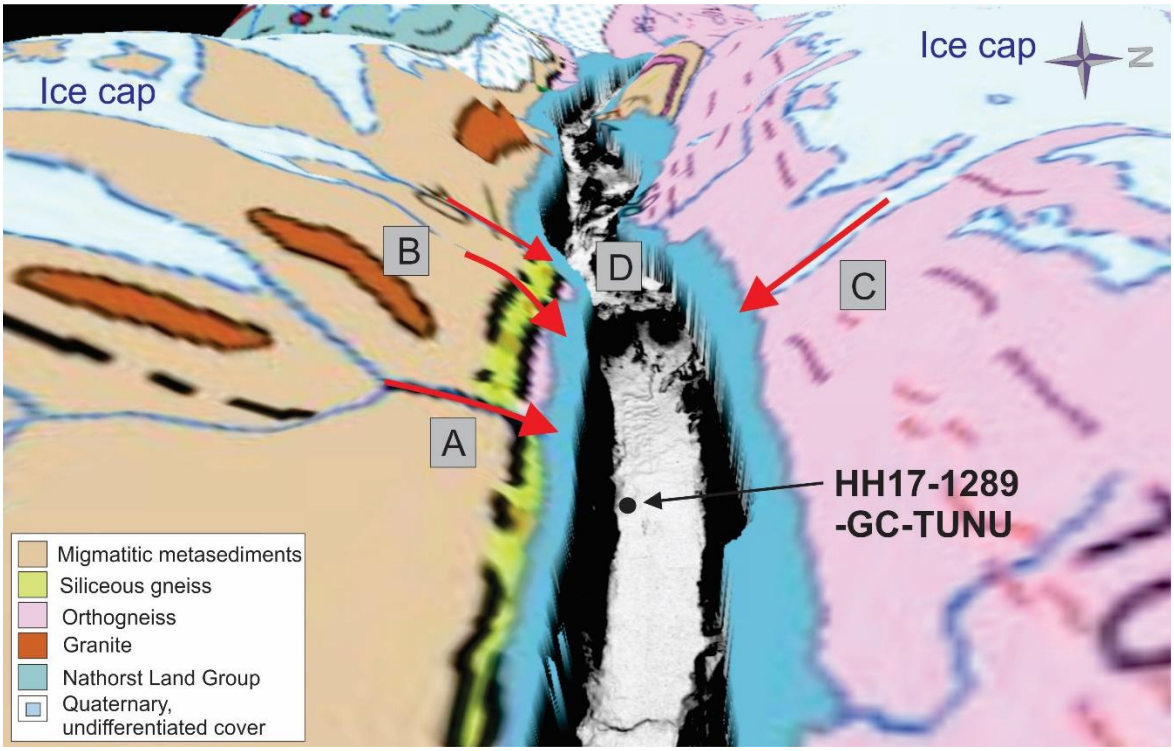

Figure 6.21. Bedrock map of Bessel fjord and bathymetry data from Section 3 of Bessel Fjord. Map taken from GEUS database.

6.2.4 **Model of Bessel Fjord**

Stage I: LGM

It is theorized that during the LGM ice (i.e. Soranerbræen, and likely ice caps) expanded due to palaeoclimatic conditions, largely following topographic controls in the fjord (Fig. 6.22; Stage I: LGM- Phase I). Soranerbræen eventually overcame initial topographic barriers, such as the mounds in Section 2, and continued to occupy the width of the fjord (Fig. 6.22; Stage I: LGM: Phase II). As ice filled Bessel Fjord, fast flowing ice formed streamlined lineations on the seabed. Ice is believed to have extended to the outer sill, likely meeting and merging with the ice stream in Dove Bugt. Terrestrial areas likely became glaciated as well and contained ice that possibly expanded into the fjord.

Stage II: Deglaciation

The deglaciation of Bessel Fjord likely occurred in a stepwise regression, as is suggested by the presence of numerous recessional moraines, especially in Section 2 through Section 4. As Soranerbræen retreated meltwater channel released sediment east of the glacier, either as plumes that cause sediment to become suspended and/or as turbulent underflows that deposited material ice-proximally. Meltwater channels became infilled with sediment, forming eskers between Section 2 and Section 3 (Fig 6.22; Stage II: Deglaciation: Phase I). A major ice advance or halt caused the formation of a large moraine to the west of the esker. Rapid and constant release of meltwater from sub- and englacial channels (and possible calving) on the eastern side of the moraine likely caused rapid, turbulent flow, forming moraine gullies (Fig 6.22; Stage II: Deglaciation: Phase I). Sediment waves may have formed as a result of mass wasting events associated meltwater discharge from Soranerbræen and a local ice cap to the north. A channel later developed, overriding sediment waves, possibly as a result of terrestrial mass wasting. Given the orientation of the recession, it is probable that it is also followed topographic controls during its retreat (Fig. 6.22; Stage II: Deglaciation: Phase II). As the ice caps around Bessel Fjord may have been more sensitive to climatic changes than Soranerbræen (which is an outlet for Inland Ice), they may have expanded during brief cold reversals anytime between the LGM to modern times.

Stage III: Holocene

During the Early Holocene (11.7–8.2 ka BP) Bessel Fjord would have largely been experiencing deglaciation (Fig 6.22; Stage III: Holocene). Sedimentation would have predominantly been in the form of suspension settling from overflow plumes and turbidity currents, although large quantities of glacial derived material would have been deposited during glacial standstills or advances. Infrequent lamination in Unit 1.2 suggest a fluctuating ice front during what is perceived to be the end of the Early Holocene/beginning of the Middle Holocene (~8.2–4.2 ka). Dated material suggests that glacial ice is absent from the Inner Fjord position by at least 7,160 cal yr BP. This roughly corresponds to the HTM, where Soranerbræen and local ice caps may have retreated behind their present-day positions. A sudden shift in sediment from fine grained

silt to predominantly sand at ~4,000 cal. yr. BP in a gravity core from the Mid-Fjord may suggest that local ice caps reacted to climatic changes by either expanding and/or causing additional meltwater to be released. Slide scars and gullies would have developed throughout much of the fjord during the Holocene, potentially enhanced due to the deposition of suspended sediment from ice cap meltwater entering the fjord.

Stage I: LGM - Phase I

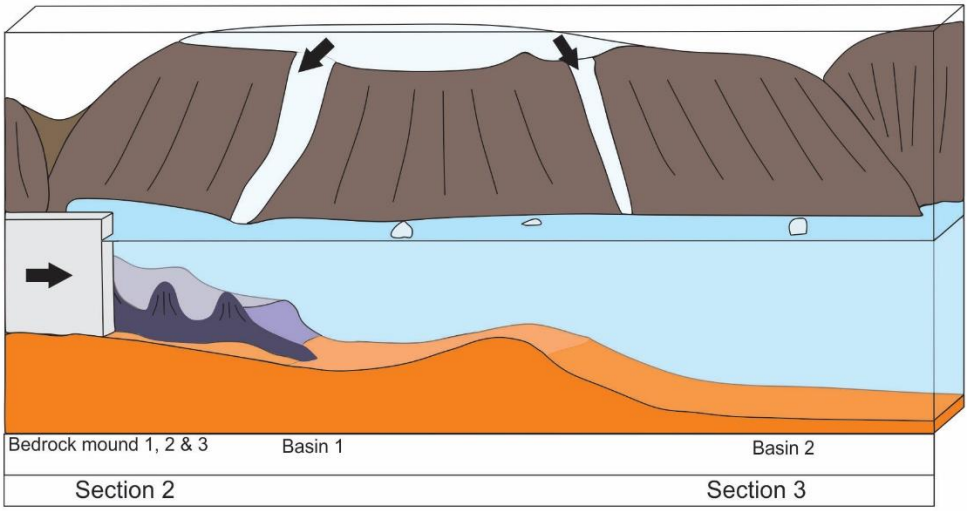

Stage I: LGM - Phase II

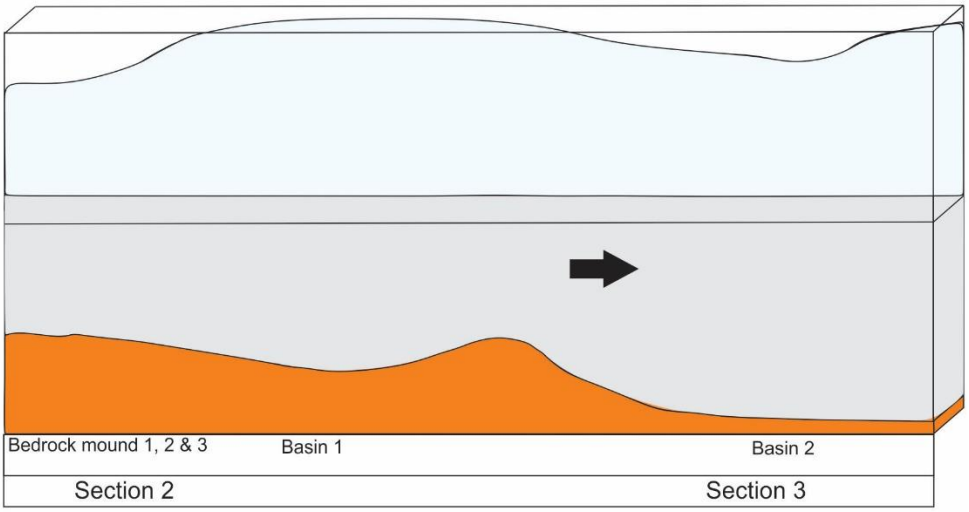

Stage II: Deglaciation - Phase I

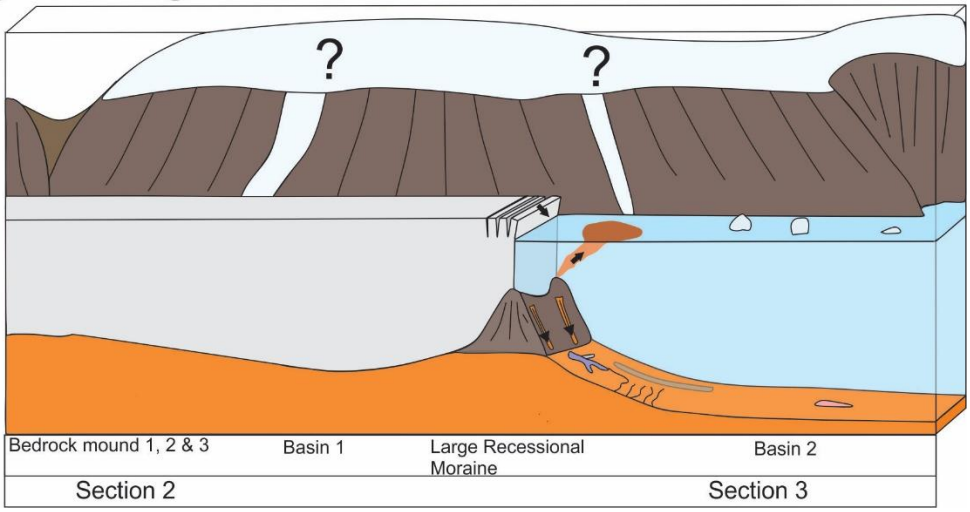

Stage II: Deglaciation - Phase II

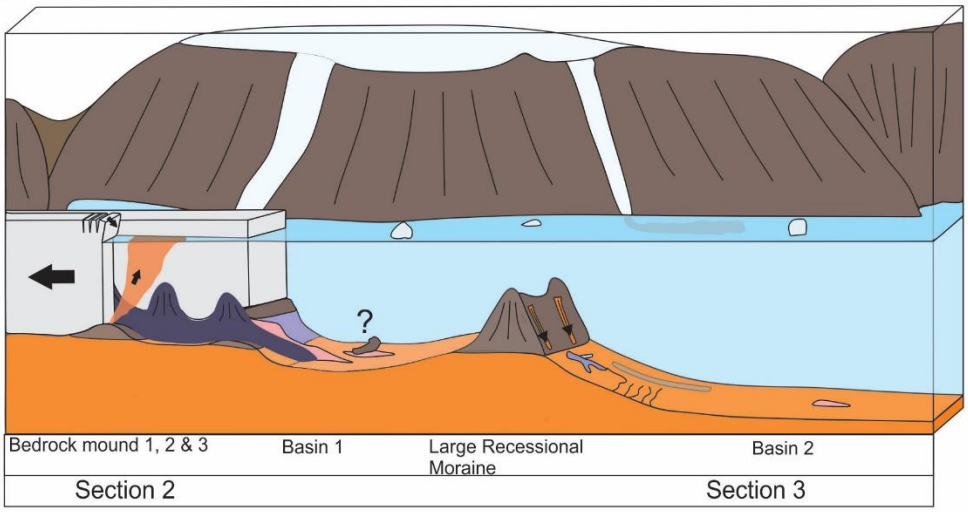

Stage II: Deglaciation - Phase III - Possible Scenario

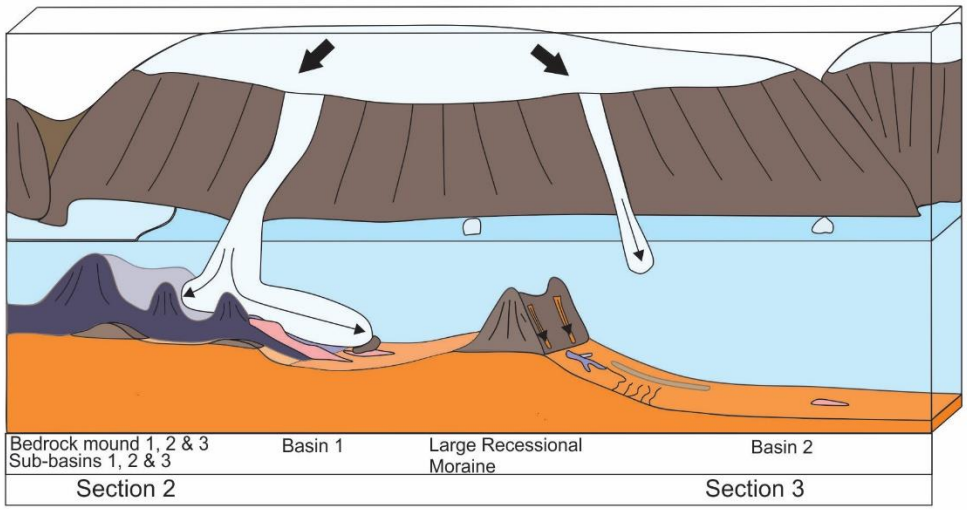

Stage III: Holocene

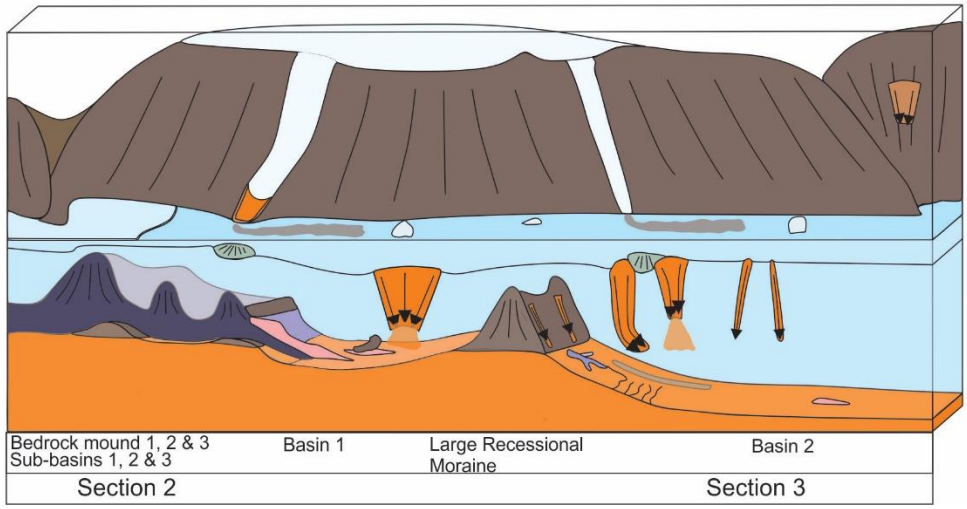

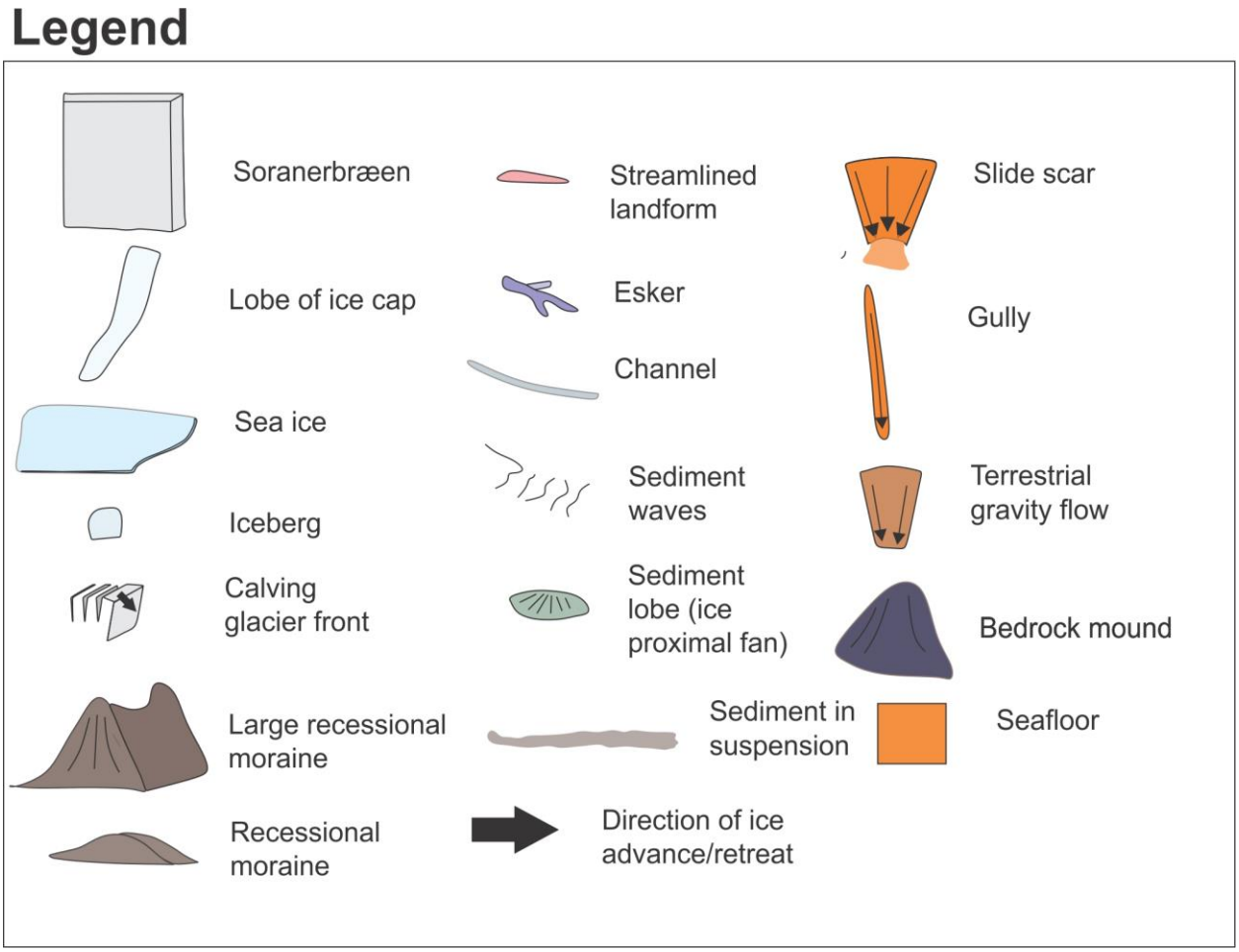

Figure 6.22. Model of the evolution of Bessel Fjord from the LGM to modern times. This model is schematically drawn and may not represent the correct thickness for certain features. Stage II: Deglaciation – Phase II is drawn with one side of Soranerbræen retreating further than the other. This is included into the model not to imply that one side retreated first, but rather to illustrate a topographically controlled deglaciation. Stage II: Deglaciation – Phase III represent a possible scenario where ice caps expand into the Mid-Fjord region without Soranerbræen readvancing into the area.

7 Conclusion

Swath bathymetry and three sediment cores were used to reconstruct the sedimentary environment and the glacial history of southwestern Dove Bugt and Bessel Fjord. The following conclusions can be drawn based on the analysis of this data:

- Geomorphological evidence suggests that fast flowing, topographically controlled glacial ice (i.e. a branch of the NGIS) flowed south through southern Dove Bugt.
- A deglaciation age of 11,190 cal yr. BP for southern Dove Bugt has been proposed based on sedimentological data and ^{14}C AMS dating results. This date coincides with proposed deglaciation ages on Store Koldewey (e.g. Skov et al., 2020) to the east. To the south, proposed deglaciation ages on Hochstetter Forland suggest that deglaciation either occurred at the same time as southern Dove Bugt or at a slightly later date (e.g. Klug et al., 2016).
- The absence of abundant recessional features (e.g. moraines, GZW) across Dove Bugt suggests that deglaciation of the NGIS was rapid.
- After 11,190 cal. yr. BP glacial marine sedimentation from Soranerbræen and/or local ice caps on Adolf S. Jensen Land and/or Dronning Margrethe II Land dominated the area. Fluctuations in the presence of laminations in a gravity core during this period may imply the advance and retreat of local ice bodies, possibly in response to climatic changes.
- Geomorphological features identified across Bessel Fjord suggest that the fjord was fully glaciated during the LGM and that Soranerbræen likely expanded through the Outer Fjord. Local ice caps may have also expanded, possibly also contributing to ice flow.
- The orientation of geomorphological features suggest that ice was topographically controlled during its initial expansion and likely overcame topographic barriers at a later stage in the glaciation.
- The presence of recessional moraines suggest that deglaciation likely had multiple halts/readvances. The position of moraines also suggests some halts may have been topographically controlled.
- Uniform sediment in gravity core HH17-1290-GC-TUNU after 7,160 cal yr BP in the Inner Fjord suggests that Soranerbræen and local ice caps retreated to or beyond their modern positions.
- There is a shift from mud to muddy sand dominated sediment around ~4,000 yr BP Mid-Fjord in gravity core HH17-1289-GC-TUNU. This change in depositional environment may be the product of increased sediment input from ice caps on northern Dronning Margrethe II Land and Adolf S Jensen Land in response to climatic fluctuations.

8 Future Work

The analysis of bathymetric data and gravity cores has allowed for the development of the first glacial and marine palaeoenvironmental reconstruction of southwestern Dove Bugt and Bessel Fjord. Recommendations have been developed for those who would wish to study this region further. These recommendations are as followed:

- Use existing chirp data in Dove Bugt and Bessel Fjord to better understand the nature of geomorphologic landforms and stratigraphy of the region.
    - Examine the small and large transverse ridges in Dove Bugt to determine if they are composed of bedrock or if they are glacigenic in origin.
    - Examine the channel-like feature in western Dove Bugt to help understand how the feature developed.
    - Investigate whether transverse ridges and mounds in Bessel Fjord are composed of bedrock or glaciogenic/marine sediment.
    - Examination of the stratigraphy of Bessel Fjord and Dove Bugt to attempt to quantify sedimentation in these regions during different climatic periods.
    - Determine whether the rounded depressions in the Outer Fjord are pockmarks or crevasse squeeze ridges.
- Improve the understanding of ice flow patterns through additional bathymetric mapping of Dove Bugt, Store Bælt, Dove Bugt Trough and Danmarkshavn.
- Additional bathymetric mapping of landforms that are partially visible in this study (e.g. the large channel-like feature and lateral moraines in western Dove Bugt) to better understand the evolution of the region.
- Collect additional gravity cores and sample for more datable material to obtain better age controls on the deglaciation of Dove Bugt and Bessel Fjord.
- From this; determine ice retreat rates for the area.
- Establish a better understanding of sediment provenance by conducting a detailed geochemical analysis of surrounding terrestrial rock in order to compare it to results obtained in this study. Determining sediment provenance can improve our understanding

of ice cap and glacier fluctuations during the Holocene by identifying the source of increased sediment input.

- Conduct lacustrine studies and cosmogenic nuclide dating of material in terrestrial regions near the study area to better understand the glacial history of the region. On northern Dronnings Margrethe II and Adolf S. Jensen Land this could better constrain the timing of deglaciation and determine the extent to which ice caps and local glaciers expanded during the Holocene. Studies on Trums Ø in outer Bessel Fjord may be used to determine when the fjord first became deglaciated.

References

Aarseth, I. (1997). Western Norwegian fjord sediments: age, volume, stratigraphy, and role as temporary depository during glacial cycles. *Marine Geology*, *143*, 39–53.

Adrielsson, L., & Alexanderson, H. (2005). Interactions between the Greenland Ice Sheet and the Liverpool Land coastal ice cap during the last two glaciation cycles. *Journal of Quaternary Science*, *20*(3), 269–283. https://doi.org/10.1002/jqs.900

Alexanderson, H., & Håkansson, L. (2014). Coastal glaciers advanced onto jameson land, east greenland during the late glacial-early holocene milne land stade. *Polar Research*, *33*(1), 20313. https://doi.org/10.3402/polar.v33.20313

Alfred-Wegener-Institut. (2019). *MICADAS - Mini Carbon Dating System*. https://www.awi.de/en/science/geosciences/marine-geochemistry/micadas.html

Alley, R. B. (2000). The younger dryas cold interval as viewed from central Greenland. *Quaternary Science Reviews*, *19*, 213–226.

Alley, R. B., Andrews, J. T., Brigham-Grette, J., Clarke, G. K. C., Cuffey, K. M., Fitzpatrick, J. J., Funder, S., Marshall, S. J., Miller, G. H., Mitrovica, J. X., Muhs, D. R., Otto-Bliesner, B. L., Polyak, L., & White, J. W. C. (2010). History of the Greenland Ice Sheet: paleoclimatic insights. *Quaternary Science Reviews*, *29*(15–16), 1728–1756. https://doi.org/10.1016/j.quascirev.2010.02.007

Andersen, T. B., Torsvik, T. H., Eide, E. A., Osmundsen, P. T., & Faleide, J. I. (1999). Permian and Mesozoic extensional faulting within the Caledonides of central South Norway. *Journal of the Geological Society, London*, *156*, 1073–1080.

Andreassen, K., Winsborrow, M. C. M., Bjarnadóttir, L. R., & Rüther, D. (2014). Ice stream retreat dynamics inferred from an assemblage of landforms in the northern Barents Sea. *Quaternary Science Reviews*, *92*, 246–257.

Andrews, J. T., Stein, R., Moros, M., & Perner, K. (2016). Late Quaternary changes in sediment composition on the NE Greenland margin (~73° N) with a focus on the fjords and shelf. *Boreas*, *45*(3), 381–397. https://doi.org/10.1111/bor.12169

Arndt, J. E. (2018). Marine geomorphological record of Ice Sheet development in East Greenland since the Last Glacial Maximum. *Journal of Quaternary Science*, *33*(7), 853–864. https://doi.org/10.1002/jqs.3065

Arndt, J. E., Jokat, W., & Dorschel, B. (2017). The last glaciation and deglaciation of the Northeast Greenland continental shelf revealed by hydro-acoustic data. *Quaternary Science Reviews*, *160*, 45–56.

Arndt, J. E., Jokat, W., Dorschel, B., Myklebust, R., Dowdeswell, J. A., & Evans, J. (2015). A new bathymetry of the Northeast Greenland continental shelf: Constraints on glacial and other processes. *AGU Publications: Geochemistry Geophysics Geosystems*, *16*(1), 267–300. https://doi.org/10.1002/2014GC005684.Key

Azetsu-Scott, K., & Syvitski, J. P. M. (1999). Influence of melting icebergs on distribution, characteristics and transport of marine particles in an East Greenland fjord. *Journal of Geophysical Research: Oceans*, *104*(C3), 5321–5328. https://doi.org/10.1029/1998jc900083

Azetsu-Scott, K., & Tan, F. C. (1997). Oxygen isotope studies from Iceland to an East Greenland Fjord: Behaviour of glacial meltwater plume. *Marine Chemistry*, *56*(3–4), 239–251.

https://doi.org/10.1016/S0304-4203(96)00078-3
Barnes, P. M., Pickrill, R. A., & Bostock, H. C. (2016). Thompson and Bradshaw sounds, Fiordland, New Zealand: a relict, mid-latitude, temperatue glacier system. In J.A. Dowdeswell, M. Canals, M. Jakobsson, B. J. Todd, E. K. Dowdeswell, & K. A. Hogan (Eds.), *Atlas of Submarine Glacial Landforms: Modern, Quaternary and Ancient* (pp. 45–46). The Geological Society of London.
Bartholomaus, T. C., Larsen, C. F., & O'Neel, S. (2013). Does calving matter? Evidence for significant submarine melt. *Earth and Planetary Science Letters*, *380*, 21–30.
Batchelor, C. L., & Dowdeswell, J. A. (2015). Ice-sheet grounding-zone wedges (GZWs) on high-latitude continental margins. *Marine Geology*, *363*, 65–92.
Batchelor, C. L., Dowdeswell, J. A., & Rignot, E. (2018). Submarine landforms reveal varying rates and styles of deglaciation in North-West Greenland fjords. *Marine Geology*, *402*, 60–80.
Batchelor, C. L., Dowdeswell, J. A., Rignot, E., & Millan, R. (2019). Submarine moraines in southeast Greenland fjords reveal contrasting outlet-glacier behavior since the Last Glacial Maximum. *Geophysical Research Letters*, *46*, 3279–3286.
Benn, D. I., & Evans, D. J. A. (2010). *Glaciers & glaciation* (2nd ed.). Hodder Arnold Publication - Routledge. https://doi.org/10.5860/choice.35-6240
Bennike, O., & Björck, S. (2002). Chronology of the last recession of the Greenland Ice Sheet. *Journal of Quaternary Science*, *17*(3), 211–219. https://doi.org/10.1002/jqs.670
Bennike, O., & Wagner, B. (2012). Deglaciation chronology, sea-level changes and environmental changes from Holocene lake sediments of Germania Havn Sø, Sabine Ø, northeast Greenland. *Quaternary Research*, *78*, 103–109.
Bennike, O., & Weidick, A. (2001). Late Quaternary history around Nioghalvfjerdsfjorden and Jøokelbugten, North-East Greenland. *Boreas*, *30*(3), 205–227. https://doi.org/10.1111/j.1502-3885.2001.tb01223.x
Berger, A., & Loutre, M. F. (1991). Insolation values for the climate of the last 10 million years. *Quaternary Science Reviews*, *10*, 297–317.
Bindschadler, R., Harrison, W. D., Raymond, C. F., & Gantet, C. (1976). Thermal Regime of a Surge-Type Glacier. *Journal of Glaciology*, *16*(74), 251–259. https://doi.org/10.3189/s0022143000031579
Björck, S., & Persson, T. (1981). Late Weichselian and Flandrian biostratigraphy and chronology from hochstetter forland, northeast Greenland. *Medd. Om. Grønl. Geosci.*, *5*, 1–19.
Björck, S., Rundgren, M., Ingólfsson, Ó., & Funder, S. (1997). The Preboreal oscillation around the Nordic Seas: terrestrial and lacustrine responses. *Journal of Quaternary Science*, *12*(6), 455–465. https://doi.org/10.1002/(sici)1099-1417(199711/12)12:6<455::aid-jqs316>3.3.co;2-j
Björck, S., Wohlfarth, B., Bennike, O., Hjort, C., & Persson, T. (1994). Revision of the early Holocene lake sediment based chronology and event stratigraphy on Hochstetter Forland, NE Greenland. *Boreas*, *23*(4), 513–523. https://doi.org/10.1111/j.1502-3885.1994.tb00619.x
Blikra, L. H., & Nemec, W. (1998). Postglacial colluvium in western Norway: depositional processes, facies and palaeoclimatic record. *Sedimentology*, *45*(5), 909–959. https://doi.org/10.1046/j.1365-3091.1998.00200.x

Blystad, P., Brekke, H., Færseth, R. B., Larsen, B. T., Skogseid, J., & Tørudbakken, B. (1995). Structural elements of the Norwegian continental shelf. Part II- the Norwegian Sea region. In *Structural elements of the Norwegian continental shelf. Park II: the Norwegian Sea Region. Norwegian Petroleum Directorate Bulletin* (Vol. 8).

Boggs Jr., S. (2012). *Boggs Jr., S., 2012, Principles of sedimentology and stratigraphy* (5th Editio). Pearson Education, Ltd.

Boulton, G. S. (1986). Push-moraines and glacier contact fans in marine and terrestrial environments. *Sedimentology*, *315*, 677–698.

Boulton, G. S., Hagdorn, M., & Hulton, N. R. J. (2003). Streaming flow in an ice sheet through a glacial cycle. *Annals of Glaciology*, *36*(1985), 117–128. https://doi.org/10.3189/172756403781816293

Bouma, A. (1962). *Sedimentology of some Flysch deposits.*

Bradley, R. S. (2015). *Paleoclimatology: Reconstructing climates in the Quaternary* (Third Edit). Elsevier.

Brekke, H. (2000). The tectonic evolution of the Norwegian Sea Continental Margin with emphasis on the Vøring and Møre Basins. In A. Nøttvedt (Ed.), *Dynamics of the Norwegian Margin* (Vol. 167, pp. 327–378). Geological Society, London, Special Publications.

Brett, C. P., & Zarudzki, E. F. K. (1979). Project Westmar: a shallow marine geophysical survey on the West Greenland continental shelf. *Gronlands Geol. Unders., Rapp.*, *87*, 27.

Briner, J. P., Håkansson, L., & Bennike, O. (2013). The deglaciation and neoglaciation of Upernavik Isstrøm, Greenland. *Quaternary Research*, *80*, 459–467.

Briner, J. P., McKay, N. P., Axford, Y., Bennike, O., Bradley, R. S., de Vernal, A., Fisher, D., Francus, P., Fréchette, B., Gajewski, K., Jennings, A., Kaufman, D. S., Miller, G., Rouston, C., & Wagner, B. (2016). Holocene climate change in Arctic Canada and Greenland. *Quaternary Science Reviews*, *147*, 340–364. https://doi.org/10.1016/j.quascirev.2016.02.010

Budéus, G., Schneider, W., & Gerhard, K. (1997). Distribution and exchange of water masses in the Northeast Water Polynya (Greenland Sea). *Journal of Marine Systems*, *10*, 123–138.

Cappelen, J., Jørgensen, B. V., & Laursen, E. V. (2001). The observed climate of Greenland, 1958-99 - with climatological standard normals, 1961-90. In *Danish Meteorological Institute Ministry of Transport Technical Report 00-18*.

Carlson, A. E., LeGrande, A. N., Oppo, D. W., Came, R. E., Schmidt, G. A., Anslow, F. S., Licciardi, J. M., & Obbink, E. A. (2008). Rapid early Holocene deglaciation of the Laurentide ice sheet. *Nature Geoscience*, *1*, 620–624.

Carlson, A. E., Winsor, K., Ullman, D. J., Brook, E. J., Rood, D. H., Axford, Y., Legrande, A. N., Anslow, F. S., & Sinclair, G. (2014). Earliest Holocene south Greenland Ice Sheet retreat within its late Holocene extent. *Geophysical Research Letters*, *41*, 5514–5521.

Cartigny, M. J. B., Postma, G., Berg, J. H., & Mastbergen, D. R. (2011). A comparative study of sediment waves and cyclic steps based on geometries, internal structures and numerical modeling. *Marine Geology*, *280*, 40–56.

Chadwick, B., & Friend, C. R. L. (1994). Reaction of Precambrian high-grade gneisses to mid-crustal ductile deformation in western Dove Bugt, North-East Greenland. In A. K. Higgins (Ed.), *Geology of North-East Greenland. Rapport Grønlands Geologiske Undersøgelse* (Vol. 162, pp. 53–70).

Christiansen, J. S. (2012). The TUNU-Programme : Euro-Arctic Marine Fishes — Diversity and Adaptation. In *Adaptation and Evolution in Marine Environments* (Vol. 1, Issue 9037, pp. 35–50). https://doi.org/10.1007/978-3-642-27352-0

Christianson, K., Peters, L. E., Alley, R. B., Anandakrishnan, S., Jacobel, R. W., Riverman, K. L., Muto, A., & Keisling, B. A. (2014). Dilatant till facilitates ice-stream flow in northeast Greenland. *Earth and Planetary Science Letters*, *401*, 57–69. https://doi.org/10.1016/j.epsl.2014.05.060

Clark, C. D. (1993). Mega-scale lineations and cross-cutting ice-flow landforms. *Earth Surface Processes and Landforms*, *18*, 1–29.

Clark, C. D., Hughes, A. L. C., Greenwood, S. L., Spagnolo, M., & Ng, F. S. L. (2009). Size shape characteristics drumlins derived from large sample associated scaling laws. *Quaternary Science Reviews*, *28*, 677–692.

Clark, C. D., & Stokes, C. R. (2003). Palaeo-ice stream landsystem. In D. J. A. Evans (Ed.), *Glacial Landscapes* (pp. 204–227). Edward Arnold, London.

Clarke, G. K.C., Collins, S. G., & Thompson, D. E. (1984). Flow, thermal structure, and subglacial conditions of a surge- type glacier. *Canadian Journal of Earth Sciences*, *21*(2), 232–240. https://doi.org/10.1139/e84-024

Clarke, Garry K.C., Nitsan, U., & Paterson, W. S. B. (1977). Strain heating and creep instability in glaciers and ice sheets. *Reviews of Geophysics*, *15*(2), 235–247. https://doi.org/10.1029/RG015i002p00235

Corner, G. D., Nordhal, E., Munch-Ellingsen, K., & Robertsen, K. R. (1990). Morphology and sedimentology of an emergent fjord-head Gilbert-type delta: Alta delta Norway. In *Coarse-Grained Deltas* (Vol. 10, pp. 155–168). Int. Assoc. Sedimentol. Spec. Publ.

Cottier, F. R., Nilsen, F., Skogseth, R., Tverberg, V., Skardhamar, J., & Svendsen, H. (2010). Arctic fjords: A review of the oceanographic environment and dominant physical processes. *Geological Society Special Publication*, *344*(November 2014), 35–50. https://doi.org/10.1144/SP344.4

Cowan, E. A., Cai, J., Powell, R. D., Clark, J. D., & Pitcher, J. N. (1997). Temperate glacimarine varves: an example from Disenchantment Bay, southern Alaska. *Journal of Sedimentary Research*, *67*, 536–549.

Cowan, E. A., & Powell, R. D. (1990). Suspended sediment transport and deposition of cyclically interlaminated sediment in a temperate glacial fjord, Alaska, USA. *Glacimarine Environments: Processes and Sediments*, *53*, 75–89.

Cowan, E. A., & Powell, R. D. (1991). Ice-proximal sediment accumulation rates in a temperate glacial fjord, southeastern Alaska. In J. B. Anderson & G. M. Ashley (Eds.), *Glacial marine sedimentation; Paleoclimatic significance.* (pp. 61–73). Geological Society of America, Boulder, Colorado, Special publication.

Cowan, E. A., Seramur, K. C., Cai, J., & Powell, R. D. (1999). Cyclic sedimentation produced by fluctuations in meltwater discharge, tides and marine productivity in an Alaskan fjord. *Sedimentology*, *46*(6), 1109–1126. https://doi.org/10.1046/j.1365-3091.1999.00267.x

Cremer, H., Bennike, O., & Wagner, B. (2008). Lake sediment evidence for the last deglaciation of eastern Greenland. *Quaternary Science Reviews*, *27*(3–4), 312–319. https://doi.org/10.1016/j.quascirev.2007.09.004

Dahl-Jensen, D., Bamber, J. L., Bøggild, C. E., Buch, E., van den Broeke, M., Christensen, J. H.,

Dethloff, K., Fahnestock, M., Marshall, S., Rosing, M., Steffen, K., Thomas, R., Truffer, M., & van der Veen, C. (2009). *The Greenland Ice Sheet in a Changing Climate: Snow, Water, Ice and Permafrost in the Arctic (SWIPA), Arctic Monitoring and Assessment Programme (AMAP)*.

Dansgaard, W., Johnsen, S. J., Clausen, H. B., Dahl-Jensen, D., Gundestrup, N. S., Hammer, C. U., Hvidberg, C. S., Steffensen, J. P., Sveinbjörnsdottir, A. E., Jouzel, J., & Bond, G. (1993). Evidence for general instability of past climate from a 250-kyr ice-core record. *Nature*, *364*(6434), 218–220. https://doi.org/10.1038/364218a0

Davis, P. T., Menounos, B., & Osborn, G. (2009). Holocene and latest Pleistocene alpine glacier fluctuations: a global perspective. *Quaternary Science Reviews*, *28*, 2021–2033.

Delaney, C. A., McCarron, S., & Davis, S. (2018). Irish Ice Sheet dynamics during deglaciation of the central Irish Midlands_ Evidence of ice streaming and surging from airborne LiDAR. *Geomorphology*, *306*, 235–253.

Dmitrenko, I. A., Kirillov, S. A., Rysgaard, S., Barder, D. G., Babb, D. G., Pedersen, L. T., Koldunov, N. V., Boone, W., Crabeck, O., & Mortensen, J. (2015). Polynya impacts on water properties in a Northeast Greenland fjord. *Estuarine, Coastal and Shelf Science*, *153*, 10–17.

Domack, E. W., & Mcclemen, C. E. (1996). Accumulation of glacial marine sediments in fjords of the Antarctic Peninsula and their use as Late Holocene Paleoenvironmental indicators. Foundations for ecological research west of the Antarctic Peninsula. *Antarctic Research Series*, *70*, 135–154.

Doré, A. G., Lundin, E. R., Jensen, L. N., Birkeland, Ø., Eliassen, P. E., & Fichler, C. (1999). Principal tectonic events in the evolution of the northwest European Atlantic margin. In A. J. Fleet & S. A. R. Boldy (Eds.), *Petroleum Geology of Northwest Europe: Proceedings of the 5th Conference* (p. 41+61). Geological Society, London.

Dowdeswell, E. K., Todd, B. J., & Dowdeswell, J. A. (2016a). Crag-and-tail features: convergent ice flow through Eclipse Sound, Baffin Island, Arctic Canada. In K. A. Dowdeswell, J. A., Canals, M., Jakobsson, M., Todd, B. J., Dowdeswell, E. K. & Hogan (Ed.), *Atlas of Submarine Glacial Landforms: Modern, Quaternary and Ancient* (Memoir 46, pp. 55–56). Geological Society.

Dowdeswell, E. K., Todd, B. J., & Dowdeswell, J. A. (2016b). Ice-proximal fans in Dexterity Fjord, Buchan Gulf, Baffin Island, Canadian Arctic. In K. A. Dowdeswell, J. A., Canals, M., Jakobsson, M., Todd, B. J., Dowdeswell, E. K. & Hogan (Ed.), *Atlas of Submarine Glacial Landforms: Modern, Quaternary and Ancient.* (Memoirs, 4, pp. 89–90.). Geological Society of London.

Dowdeswell, E. K., Todd, B. J., & Dowdeswell, J. A. (2016c). Submarine medial moraines and convergent ice flow, Scott Inlet, Baffin Island, Arctic Canada. In K. A. Dowdeswell, J. A., Canals, M., Jakobsson, M., Todd, B. J., Dowdeswell, E. K. & Hogan (Ed.), *Atlas of Submarine Glacial Landforms: Modern, Quaternary and Ancient.* (Vol. 46, pp. 193–194).

Dowdeswell, J. A., Canals, M., Jakobsson, M., Todd, B. J., Dowdeswell, E. K., & Hogan, K. A. (2016). The variety and distribution of submarine glacial landforms and implications for ice-sheet reconstruction. *Geological Society Memoir*, *46*(1), 519–552. https://doi.org/10.1144/M46.183

Dowdeswell, J. A., Hogan, K. A., Ó Cofaigh, C., Fugelli, E. M. G., Evans, J., & Noormets, R.

(2014). Late Quaternary ice flow in a West Greenland fjord and cross-shelf trough system: submarine landforms from Rink Isbrae to Uummannaq shelf and slope. *Quaternary Science Reviews*, *92*, 292–309.

Dowdeswell, J. A., Ottesen, D., Evans, J., Cofaigh, C. Ó., & Anderson, J. B. (2008). Submarine glacial landforms and rates of ice-stream collapse. *Geology*, *36*(10), 819–822. https://doi.org/10.1130/G24808A.1

Dowdeswell, J. A., & Vásquez, M. (2013). Submarine landforms in the fjords of southern Chile: Implications for glacimarine processes and sedimentation in a mild glacier-influenced environment. *Quaternary Science Reviews*, *64*, 1–19. https://doi.org/10.1016/j.quascirev.2012.12.003

Dowdeswell, J. A., Villinger, H., Whittington, R. J., & Marienfeld, P. (1993). Iceberg Scouring in Scoresby Sund and on the East Greenland continental shelf. *Marine Geology*, *111*, 37–53.

Dowdeswell, J.A., Whittington, R. J., & Marienfeld, P. (1994). The origin of massive diamicton facies by iceberg rafting and scouring, Scoresby Sund, East Greenland. *Sedimentology*, *41*, 21–35.

Dowdeswell, Julian A., Hogan, K. A., Arnold, N. S., Mugford, R. I., Wells, M., Hirst, J. P. P., & Decalf, C. (2015). Sediment-rich meltwater plumes and ice-proximal fans at the margins of modern and ancient tidewater glaciers: Observations and modeling. *Sedimentology*, *62*(6), 1665–1692. https://doi.org/10.1111/sed.12198

Dowdeswell, Julian A., Ó Cofaigh, C., & Pudsey, C. J. (2004). Thickness and extent of the subglacial till layer beneath an Antarctic paleo-ice stream. *Geology*, *32*(1), 13–16. https://doi.org/10.1130/G19864.1

Dyke, L. M., Hughes, A. L. C., Murray, T., Hiemstra, J., Andresen, C. S., & Rodes, A. (2014). Evidence for the asynchronous retreat of large outlet glaciers in southeast Greenland at the end of the last glaciation. *Quaternary Science Reviews*, *99*, 244–259.

Eilertsen, R.S., Longva, O., & Corner, G. D. (2016). A Younger Dryas moraine ridge and fjord delta in Valldal, Norddalsfjorden, Møre og Romsdal, Norway. In K. A. Dowdeswell, J. A., Canals, M., Jakobsson, M., Todd, B. J., Dowdeswell, E. K. & Hogan (Ed.), . *Atlas of Submarine Glacial Landforms: Modern, Quaternary and Ancient* (Memior, 46, pp. 95–96). Geological Society, London.

Eilertsen, Raymond S, Bøe, R., Hermanns, R., Longva, O., & Dahlgren, S. (2016). Kettle holes, "dead-ice" topography and eskers on a lake floor in Telemark, southern Norway. In J.A. Dowdeswell, M. Canals, M. Jakobsson, B. J. Todd, E. K. Dowdeswell, & K. A. Hogan (Eds.), *Atlas of Submarine Glacial Landforms: Modern, Quaternary and Ancient* (pp. 113–114). The Geological Society of London.

Eittreim, S. L., Cooper, A. K., & Wannesson, J. (1995). Seismic stratigraphic evidence of ice sheet advances in the Wilkes Land margin of Antarctica. *Sedimentary Geology*, *96*, 131–156.

Eldholm, O., Tsikalas, F., & Faleide, J. I. (2002). The continental margin off Norway 62-75°N: Palaeogene tectono-magmatic segmentation and sedimentation. In D. W. Jolley & B. R. Bell (Eds.), *The North Atlantic Igneous Province: stratigraphy, tectonics, volcanic and magmatic processes* (Vol. 197, pp. 39–68).

Elmore, D., & Phillips, F. M. (1987). Accelerator Mass Spectrometry for Measurement of Long-

Lived Radioisotopes. *Science*, *236*(4801), 543–550.
Evans, David J A, & Rea, B. R. (1999). Geomorphology and sedimentology of surging glaciers: a land-systems approach. *Annals of Glaciology*, *28*(1999), 75–82.
Evans, J., Dowdeswell, J. A., Grobe, H., Niessen, F., Stein, R., Hubberten, H. W., & Whittington, R. J. (2002). Late Quaternary sedimentation in Kejser Franz Joseph Fjord and the continental margin of East Greenland. *Geological Society Special Publication*, *203*, 149–179. https://doi.org/10.1144/GSL.SP.2002.203.01.09
Evans, J., Ó Cofaigh, C., Dowdeswell, J. A., & Wadhams, P. (2009). Marine geophysical evidence for former expansion and flow of the Greenland Ice Sheet across the north-east Greenland continental shelf. *Journal of Quaternary Science*, *24*(3), 279–293.
Eyles, C. H., Eyles, N., & Miall, A. D. (1985). Models of Glaciomarine sedimentation and their application to the interpretation of ancient glacial sequences. *Palaeogeography, Palaeoclimatology, Palaeoecology*, *51*, 15–84.
Eyles, N., Eyles, C. H., & Niall, An. D. (1983). Lithofacies types and vertical profile models; an alternative approach to the description and environmental interpretation of glacial diamict and diamictite sequences. *Sedimentology*, *30*, 393–410.
Fahnestock, M. A., Joughin, I., Scambos, T. A., Kwok, R., Krabill, W. B., & Gogineni, S. (2001). Ice-stream-related patterns of ice flow in the interior of northeast Greenland. *Journal of Geophysical Research Atmospheres*, *106*(D24), 34035–34045. https://doi.org/10.1029/2001JD900194
Farmer, D. M., & Freeland, H. J. (1983). The physical oceanography of Fjords. *Progress in Oceanography*, *12*(2), 147–220. https://doi.org/10.1016/0079-6611(83)90004-6
Field, M. E., Gardner, J. V., & Prior, D. B. (1999). Geometry and significance of stacked gullies on the northern California slope. *Marine Geology*, *154*, 271–286.
Flood, R. ., Shor, A. N., & Manley, P. L. (1993). Morphology of abyssal mudwaves at Project MUDWAVES site in the Argentine Basin. *Deep-Sea Research Part II*, *40*(4/5), 859–888.
Folk, R. L. (1954). The Distinction between Grain Size and Mineral Composition in Sedimentary-Rock Nomenclature. *The Journal of Geology*, *62*(4), 344–359.
Folk, R. L., & Ward, W. (1957). Brazos river bar, a study in the significance of grain size parameters. *Journal of Sedimentary Petrology*, *27*, 34–59.
Forwick, M. (2013). *How to use XRF core scanner data acquired with the Avaatech XRF core scanner at the Department of Geology, University of Tromsø* (pp. 1–9).
Forwick, M., Kempf, P., & Laberg, J. S. (2016). Eskers in deglacial sediments of three Spitsbergen fjords. In J. A. Dowdeswell, M. Canals, M. Jakobsson, B. J. Todd, E. K. Dowdeswell, & K. A. Hogan (Eds.), *Atlas of Submarine Glacial Landforms: Modern, Quaternary and Ancient* (Memoirs, 4, pp. 85–86).
Forwick, M., & Vorren, T. O. (2009). Late Weichselian and Holocene sedimentary environments and ice rafting. *Palaeogeography, Palaeoclimatology, Palaeoecology*, *280*, 258–274.
Forwick, Matthias, Baeten, N. J., & Vorren, T. O. (2009). Pockmarks in Spitsbergen fjords. *Norsk Geologisk Tidsskrift*, *89*(1–2), 65–77.
Forwick, Matthias, Vorren, T. O., Hald, M., Korsun, S., Roh, Y., Vogt, C., & Yoo, K. C. (2010). Spatial and temporal influence of glaciers and rivers on the sedimentary environment in Sassenfjorden and Tempelfjorden, Spitsbergen. *Geological Society Special Publication*, *344*, 163–193. https://doi.org/10.1144/SP344.13

Fricke, A. T., Sheets, B. A., Nittrouer, C. A., Allison, M. A., & Ogston, A. S. (2015). An examination of froude-supercritical flows and cyclic steps on a subaqueous lacustrine delta, Lake Chelan, Washington, U.S.A. *Journal of Sedimentary Research*, *85*, 754–767.

Funder, S. (1982). *14C-dating of samples collected during the 1979 expedition to North Greenland.: Vol. The Geolog*.

Funder, S. (1989). Quaternary geology of the ice free areas and adjacent shelves of Greenland. In R. J. Fulton (Ed.), *Quaternary geology of Canada and Greenland. Geological Survey of Canada, Toronto* (pp. 743–792).

Funder, S., Hjort, C., Landvik, J. Y., Nam, S. Il, Reeh, N., & Stein, R. (1998). History of a stable ice margin - East Greenland during the middle and upper pleistocene. *Quaternary Science Reviews*, *17*(1–3), 77–123. https://doi.org/10.1016/S0277-3791(97)00082-6

Funder, S., Kjeldsen, K. K., Kjær, H. K., & Ó Cofaigh, C. (2011). The Greenland Ice Sheet During the Past 300,000 Years: A Review. *Developments in Quaternary Science*, *15*, 699–713. https://doi.org/10.1016/B978-0-444-53447-7.00050-7

García, M., Dowdeswell, J. A., Ercilla, G., & Jakobsson, M. (2012). Recent glacially influenced sedimentary processes on the East Greenland continental slope and deep Greenland Basin. *Quaternary Science Reviews*, *49*, 64–81. https://doi.org/10.1016/j.quascirev.2012.06.016

GEOTEK. (2016). *Manuel; Multi-Sensor Core Logger* (Version No).

Gilbert, R. (1990). Rafting in glacimarine environments. *Glacimarine Environments: Processes and Sediments*, *53*, 105–120.

Gilotti, J. A. (1993). Discovery of a medium-temperature eclogite province in the Caledonides of North-East Greenland. *Geology*, *21*, 523–526.

Gilotti, J. A., Jones, K. A., & Elvevold, S. (2008). Caledonian metamorphic patterns in Greenland. In A. K. Higgins, J. A. Gilotti, & M. P. Smith (Eds.), *The Greenland Caledonides: evolution of the northeast margin of Laurentia* (Vol. 202, pp. 201–225). Geological Society of America Memoir.

Gilotti, J. A., & McClelland, W. C. (2008). Geometry, kinematics, and timing of extensional faulting in the Greenland Caledonides – a synthesis. In A. K. Higgins, J. A. Gilotti, & M. P. Smith (Eds.), *The Greenland Cale donides: evolution of the northeast margin of Laurentia.* (Vol. 202, pp. 251–271). Geological Society of America.

Gjessing, J. (1956). Om iserosjon, fjorddal – dalendedannelse. *Norsk Geografisk Tidsskrift*, *15*, 243+269.

Grove, J. M. (2001). The initiation of the “Little Ice Age” in regions round the North Atlantic. *Clim. Chang.*, *48*, 53–82.

Haarpaintner, J., Gascard, J.-C., & Haugan, P. M. (2001). Ice production and brine formation in Storfjorden, Svalbard. *Journal of Geophysical Research: Oceans*, *106*(C7), 14001–14013. https://doi.org/10.1029/1999jc000133

Håkansson, S. (1973). University of Lund Radiocarbon Dates VI. *Radiocarbon*, *15*(3), 493–513.

Hall, B., Caroni, C., & Denton, G. H. (2010). Relative sea-level changes, Schuchert Dal, East Greenland, with implications for ice extent in late-glacial and Holocene times. *Quaternary Science Reviews*, *29*, 3370–3378.

Hall, B., Caroni, C., Denton, G., Kelly, M. A., & Lowell, T. (2008). Relative sea-level change, Kjove Land, Scoresby Sund, East Greenland: implications for seasonality in Younger Dryas time. *Quaternary Science Reviews*, *27*, 2283–2291.

Hamann, N. E., Whittaker, R. C., & Stemmerik, L. (2005). Geological development of the Northeast Greenland Shelf. In A. G. Dore & B. A. Vining (Eds.), *Petroleum Geology: North-West Europe and Global Perspectives- Proceedings of the 6th Petroleum Geology Conference* (Petroleum, pp. 887–902). Geological Society, L.

Hambrey, M. (1994). *Glacial Environments*.

Hand, B. M. (1974). Supercritical flow in density currents. *Journal of Sedimentary Petrology*, *44*(3), 637–648.

Hansen, B. T., Henriksen, N., & Kalsbeek, F. (1994). Age and origin of Caledonian granites in the Grandjean Fjord – Bessel Fjord region (75°–76°N), North-East Greenland. In A. K. Higgins (Ed.), *Geology of North-East Greenland. Rapport Grønlands Geologiske Undersøgelse* (Vol. 162, pp. 139–151).

Hansen, L. (2004). Deltaic Infill of a Deglaciated Arctic Fjord, East Greenland: Sedimentary Facies and Sequence Stratigraphy. *Journal of Sedimentary Research*, *74*, 422–437.

Helama, S., Jones, P. D., & Briffa, K. R. (2017). Dark Ages Cold Period: A literature review and directions for future research. *The Holocene*, *27*(10), 1600–1606. https://doi.org/10.1177/0959683617693898

Henricksen, N., & Higgins, A. K. (2009). *Descriptive text to the Geological map of Greenland, 1:500 000, Dove Bugt, Sheet 10.* Geological Survey of Denmark and Greenland Map Series 4.

Henriksen, N., Friderichsen, J. D., Strachan, R. A., Soper, N. J., & Higgins, A. K. (1989). Caledonian and pre-Caledonian geology of the region between Grandjean Fjord and Bessel Fjord (75°–76°N). In *North-East Greenland. Rapport Grønlands Geologiske Undersøgelse* (Vol. 145, pp. 90–97).

Henriksen, Niels, & Higgins, A. K. (2009). Descriptive text to the Geological map of Greenland, 1:500 000, Lambert Land, Sheet 9. In *Geological Survey of Denmark and Greenland Map Series* (Series 4). Geological Survey of Denmark and Greenland Map Series.

Higgins, A. K. (1991). North Greenland Glaeier Velocities and Calf lce Production. *Polarforschung*, *60*(1), 1–23.

Hill, P. R. (2012). Changes in submarine channel morphology and strata development from repeat multibeam surveys in the Fraser River delta, western Canada. In M. Z. Li, C. R. Sherwood, & P. R. Hill (Eds.), *Sediments, Morphology and Sedimentary Processes on Continental Shelves* (44th ed., pp. 47–70). Blackwell Science, International Association of Sedimentologists.

Hjort, C. (1979). Glaciation in northern East Greenland during the Late Weichselian and Early Flandrian. *Boreas*, *8*(3), 281–296. https://doi.org/10.1111/j.1502-3885.1979.tb00812.x

Hjort, C. (1981). A glacial chronology for northern East Greenland. *Boreas*, *10*(3), 259–274.

Hjort, C., & Björck, S. (1983). A re-evaluated glacial chronology for Northern East Greenland. *Gff*, *105*(3), 235–243. https://doi.org/10.1080/11035898309452590

Hogan, K. A., Ó Cofaigh, C., Jennings, A. E., Dowdeswell, J. A., & Hiemstra, J. F. (2016). Deglaciation of a major palaeo-ice stream in Disko Trough, West Greenland. *Quaternary Science Reviews*, *147*, 5–26.

Holland, M. M., & Bitz, C. M. (2003). Polar amplification of climate change in coupled models. *Climate Dynamics*, *21*, 221–232.

Holtedahl, H. (1967). Notes on the formation of fjords and fjord-valleys. *Geografiska Annaler*

Series A, Physical Geography, *49*, 188–203.
Hopkins, T. S. (1991). The GIN Sea-A synthesis of its physical oceanography and literature review 1972-1985. *Earth Science Reviews*, *30*(3–4), 175–318. https://doi.org/10.1016/0012-8252(91)90001-V
Hovland, M., Gardner, J. V., & Judd, A. G. (2002). The significance of pockmarks to understanding fluid flow processes and geohazards. In *Geofluids* (Vol. 2, Issue 2, pp. 127–136). https://doi.org/10.1046/j.1468-8123.2002.00028.x
Howe, J., Austin, W., Forwick, M., Paetzel, M., Harland, R., & Cage, A. (2010). Fjord systems and archives: a review. In *Fjord Systems and Archives* (344th ed., pp. 5–15). London: Special Publications.
Hubberten, H., Grobe, H., Jokat, W., Melles, M., Niessen, F., & Stein, R. (1995). Glacial History of East Greenland Explored. *Eos*, *76*(36), 353–364.
Hubberten, H. W. (1995). *Die Expedition ARKTIS-X/2 mit FS 'Polarstern' 1994. Berliner Polarforschung*. *174*.
Hughes, A. L., Rainsley, E., Murray, T., Fogwill, C. J., Schnabel, C., & Xu, S. (2012). Rapid response of Helheim Glacier, southeast Greenland, to early Holocene climate warming. *Geology*, *40*, 427– 430.
Hughes, T. (1973). Is the West Antarctic ice sheet disintegrating? *Journal of Geophysical Research*, *78*(33), 7884–7910.
Inall, M. E., & Gillibrand, P. (2010). The physics of midlatitude fjords: a review. In J. A. Howe, W. E. N. Austin, M. Forwick, & M. Paetzel (Eds.), *Fjord Systems and Archives* (Vol. 344, pp. 17–33). Geological Society, London, Special Publications.
Jacobel, R. W., Dorsey, C. W., & Harner, A. M. (1994). Ice velocities near a relict flow feature on Siple Dome. *Antarctic J. U.S.*, *29*, 62–66.
Jennings, A. E., Andrews, J. T., Knudsen, K. L., Hansen, C. V., & Hald, M. (2002). A mid-Holocene shift in Arctic sea-ice variability on the East Greenland Shelf. *Holocene*, *12*(1), 49–58. https://doi.org/10.1191/0959683602hl519rp
Jennings, A. E., & Weiner, N. J. (1996). Environmental change in eastern Greenland during the last 1300 years: Evidence from foraminifera and lithofacies in Nansen Fjord, 68°N. *Holocene*, *6*(2), 179–191. https://doi.org/10.1177/095968369600600205
Johnsen, S. J., Clausen, H. B., Dansgaard, W., Gundestrup, N. S., Hansson, M., Jonsson, P., & Steffensen, J. P. S. A. (1992). A 'deep' ice core from East Greenland. *Meddel Grønl Geosci*, *29*, 29.
Judd, A. G., Long, D., & Shankey, M. (1994). Pockmark formation and activity, U.K. Block 15/25, North Sea. *Bulletin Ofthe Geological Society OfDenmark*, *14*, 34–49.
Kalsbeek, F., Nutman, A. P., & Taylor, P. N. (1993). Palaeoproterozoic basement province in the Caledonian fold belt of North-East Greenland. *Precambrian Research*, *63*, 163+178.
Kaufman, D. S., Ager, T. A., Anderson, N. J., Anderson, P. M., Andrews, J. T., Bartlein, P. J., Brubaker, L. B., Coats, L. L., Cwynar, L. C., Duvall, M. L., Dyke, A. S., Edwards, M. E., Eisner, W. R., Gajewski, K., Geirsdóttir, Á., Hu, F. S., Jennings, A. E., Kaplan, M. R., Kerwin, M. W., … Wolfe, B. B. (2004). Holocene thermal maximum in the western Arctic (0-180°W). *Quaternary Science Reviews*, *23*, 529–560.
Kearey, P., Brooks, M., & Hill, I. (2002). *An Introduction to Geophysical Exploration* (3rd Editio). Blackwell Science.

Kelly, M. A., & Lowell, T. V. (2009). Fluctuations of local glaciers in Greenland during latest Pleistocene and Holocene time. *Quaternary Science Reviews*, *28*, 2088–2106.
Kelly, M. A., Lowell, T. V., Hall, B. L., Schaefer, J. M., Finkel, R. C., Goehring, B. M., Alley, R. B., & Denton, G. H. (2008). A 10Be chronology of lateglacial and Holocene mountain glaciation in the Scoresby Sund region, east Greenland_ implications for seasonality during lateglacial time. *Quaternary Science Reviews*, *27*, 2273–2282.
Khan, S. A., Kjær, K. H., Bevis, M., Bamber, J. L., Wahr, J., Kjeldsen, K. K., Bjørk, A. A., Korsgaard, N. J., Stearns, L. A., Van Den Broeke, M. R., Liu, L., Larsen, N. K., & Muresan, I. S. (2014). Sustained mass loss of the northeast Greenland ice sheet triggered by regional warming. *Nature Climate Change*, *4*(4), 292–299. https://doi.org/10.1038/nclimate2161
Kikuchi, T., Hatakeyama, K., & Morison, J. H. (2004). Distribution of convective Lower Halocline Water in the eastern Arctic Ocean. *Journal of Geophysical Research C: Oceans*, *109*(12), 1–10. https://doi.org/10.1029/2003JC002223
Kjær, K. H., & Krüger, J. (2001). The final phase of dead-ice moraine development: processes and sediment architecture, Kötlujökull, Iceland. *Sedimentology*, *48*, 935–952.
Klages, J. P., Kuhn, G., Graham, A. G. C., Hillenbrand, C.-D., Smith, J. A., Nitsche, F. O., Larter, R. D., & Gohl, K. (2015). Palaeo-ice stream pathways and retreat style in the easternmost Amundsen Sea Embayment, West Antarctica, revealed by combined multibeam bathymetric and seismic data. *Geomorphology*, *245*, 207–222.
Klages, J. P., Kuhn, G., Hillenbrand, C.-D., Graham, A. G. C., Smith, J. A., Larter, R. D., & Gohl, K. (2013). First geomorphological record and glacial history of an inter-ice stream ridge on the West Antarctic continental shelf. *Quaternary Science Reviews*, *61*, 47–61.
Klug, M., Bennike, O., & Wagner, B. (2009). Repeated short-term bioproductivity changes in a coastal lake on Store Koldewey, northeast Greenland: An indicator of varying sea-ice coverage? *Holocene*, *19*(4), 653–663. https://doi.org/10.1177/0959683609104040
Klug, M., Bennike, O., & Wagner, B. (2016). Late Pleistocene to early Holocene environmental changes on Store Koldewey, coastal north-east Greenland. *Polar Research*, *35*(2016). https://doi.org/10.3402/polar.v35.21912
Klug, M., Schmidt, S., Melles, M., Wagner, B., Bennike, O., & Heiri, O. (2009). Lake sediments from Store Koldewey, Northeast Greenland, as archive of Late Pleistocene and Holocene climatic and environmental changes. *Boreas*, *38*(1), 59–71. https://doi.org/10.1111/j.1502-3885.2008.00038.x
Kneller, B., & Buckee, C. (2000). The structure and fluid mechanics of turbidity currents: A review of some recent studies and their geological implications. *Sedimentology*, *47*(SUPPL. 1), 62–94. https://doi.org/10.1046/j.1365-3091.2000.047s1062.x
Komar, P. D. (1971). Hydraulic Jumps in Turbidity Currents. *Geological Society of America Bulletin*, *82*(June), 1477–1487.
Kongsberg Maritime. (2017). *EM® 302: 30 KHZ MULTIBEAM ECHO SOUNDER* (Issue February). https://doi.org/10.19009/jjacg.31.5_390
Kostic, S. (2011). Modeling of submarine cyclic steps: Controls on their formation, migration, and architecture. *Geosphere*, *7*(2), 294–304. https://doi.org/10.1130/GES00601.1
Krabbendam, M., Eyles, N., Putkinen, N., Bradwell, T., & Arbelaez-Moreno, L. (2016). Streamlined hard beds formed by palaeo-ice streams: A review. *Sedimentary Geology*, *338*,

24–50.
Laberg, J. S., Eilertsen, R. S., & Vorren, T. O. (2009). The paleo – ice stream in Vestfjorden, north Norway, over the last 35 k.y .: Glacial erosion and sediment yield. *GSA Bulletin*, *121*(3), 434–447. https://doi.org/10.1130/B26277.1
Laberg, J. S., Forwick, M., & Husum, K. (2017). New geophysical evidence for a revised maximum position of part of the NE sector of the Greenland ice sheet during the last glacial maximum. *Arktos*, *3*(1). https://doi.org/10.1007/s41063-017-0029-4
Landvik, J. Y. (1994). The last glaciation of Germania Land and adjacent areas, northeast Greenland. *Journal of Quaternary Science*, *9*(1), 81–92. https://doi.org/10.1002/jqs.3390090108
Larsen, E., Sejrup, H. P., Johnsen, S. J., & Knudsen, K. L. (1995). Do Greenland ice cores reflect NW european interglacial climate variations? *Quaternary Research*, *43*, 125–132.
Larsen, H. C. (1984). Geology of the East Greenland shelf. In A. M. Spencer (Ed.), *Petroleum Geology of the North European Margin* (pp. 329–339). Norwegian Petroleum Society.
Larsen, H. C. (1990). The East Greenland Shelf. In A. Grant, L. Johnson, & J. F. Sweeney (Eds.), *The Arctic Ocean region* (pp. 185–210). Geological Society of America.
Larsen, N.K., Funder, S., Kjær, K. H., Kjeldsen, K. K., Knudsen, M. F., & Linge, H. (2014). Rapid early Holocene ice retreat in West Greenland. *Quaternary Science Reviews*, *92*, 310–323.
Larsen, Nicolaj K., Kjær, K. H., Lecavalier, B., Bjørk, A. A., Colding, S., Huybrechts, P., Jakobsen, K. E., Kjeldsen, K. K., Knudsen, K. L., Odgaard, B. V., & Olsen, J. (2015). The response of the southern Greenland ice sheet to the Holocene thermal maximum. *Geology*, *43*(4), 291–294. https://doi.org/10.1130/G36476.1
Laskar, J., Robutel, P., Joutel, F., Gastineau, M., Levrard, B., Laskar, J., Robutel, P., Joutel, F., Gastineau, M., Correia, A. C. M., Laskar, J., Robutel, P., Joutel, F., Gastineau, M., Correia, A. C. M., & Levrard, B. (2004). A long term numerical solution for the insolation quantities of the Earth. *Astron. Astrophys.*, *428*, 261–285.
Lecavalier, B. S., Milne, G. A., Simpson, M. J. R., Wake, L., Huybrechts, P., Tarasov, L., Kjeldsen, K. K., Funder, S., Long, A. J., Woodroffe, S., Dyke, A. S., & Larsen, N. K. (2014). A model of Greenland Ice Sheet deglaciation constrained by observations of relative sea level and ice extent. *Quaternary Science Reviews*, *102*, 54–84.
Lee, S. H., & Chough, S. K. (2001). High-resolution 2-7 (kHz) acoustic and geometric characters of subamarine creep deposits in the South Korea Plateau, East Sea. *Sedimentology*, *48*(3), 629–644. https://doi.org/10.1046/j.1365-3091.2001.00383.x
Li, S., Li, S., Shan, X., Gong, C., & Yu, X. (2017). Classification, formation, and transport mechanisms of mud clasts. *International Geology Review*, *59:12*, 1609–1620. https://doi.org/10.1080/00206814.2017.1287014
Long, D., Lammers, S., & Linke, P. (1998). Possible hydrate mounds within large sea-floor craters in the Barents Sea. In J. P. Henriet & J. Mienert (Eds.), *Gas Hydrates: Relevance to World Margin Stability and Climate Change, Geological Society of London Special Publication No. 137* (pp. 223–37).
Lønne, I., & Nemec, W. (2004). High-arctic fan delta recording deglaciation and environment disequilibrium. *Sedimentology*, *51*(3), 553–589. https://doi.org/10.1111/j.1365-3091.2004.00636.x

Løseth, T. M. (1999). *Submarine massflow sedimentation: computer modelling and basin-fill stratigraphy*. Springer.

Luckman, A., Benn, D. I., Cottier, F., Bevan, S., Nilsen, F., & Inall, M. (2015). Calving rates at tidewater glaciers vary strongly with ocean temperature. *Nature Communications*, *6*, 1–7. https://doi.org/10.1038/ncomms9566

Mackiewicz, N. E., Powell, R. D., Carlson, P. R., & Molnia, B. F. (1984). Interlaminated ice-proximal glacimarine sediments in Muir Inlet, Alaska. *Marine Geology*, *57*, 113–147.

Mann, M. E., Zhang, Z., Rutherford, S., Bradley, R. S., Hughes, M. K., Shindell, D., Ammann, C., Faluvegi, G., & Ni, F. (2009). Global signatures and dynamical origins of the Little Ice Age and Medieval Climate Anomaly. *Science*, *326*, 1256–1260.

Marcott, S. A., Shakun, J. D., Clark, P. U., & Mix, A. C. (2013). A reconstruction of regional and global temperature for the past 11,300 years. *Science*, *339*, 1198–1201.

Marienfeld, P. (1991). 14C dates of glacimarine sediments from Scoresby Sund, East Greenland. In P. Möller, C. Hjort, & O. Ingolfsson (Eds.), *The Last Interglacial-Glacial Cycle: Jameson Land and Scoresby Sund, East Greenland* (Lundqua Re, pp. 165–167).

Masson-Delmotte, V., Kageyama, M., Braconnot, P., Charbit, S., Krinner, G., Ritz, C., Guilyardi, E., Jouzel, J., Abe-Ouchi, A., Crucifix, M., Gladstone, R. M., Hewitt, C. D., Kitoh, A., LeGrande, A. N., Marti, O., Merkel, U., Motoi, T., Ohgaito, R., Otto-Bliesner, B., … Yu, Y. (2006). Past and future polar amplification of climate change: Climate model intercomparisons and ice-core constraints. *Climate Dynamics*, *26*(5), 513–529. https://doi.org/10.1007/s00382-005-0081-9

Mees, F., Swennen, R., van Geet, M., & Jacob, P. (2003). Applications of X-ray computed tomography in the geosciences. In *Applications of X-ray Computer Tomography in the Geosciences* (Vol. 215, pp. 1–6).

Micallef, A., & Mountjoy, J. J. (2011). A topographic signature of a hydrodynamic origin for submarine gullies. *Geology*, *39*(2), 115–118. https://doi.org/10.1130/G31475.1

Middleton, G. V., & Hampton, M. A. (1976). Subaqueous sediment transport and deposition by sediment gravity flows. In *Marine sediment transport and environmental management* (pp. 197–218). John Wiley, New York.

Miller, G. H., Alley, R. B., Brigham-Grette, J., Fitzpatrick, J. J., Polyak, L., Serreze, M. C., & White, J. . (2010). Arctic amplification: can the past constrain the future? *Quaternary Science Reviews*, *29*, 1779–1790.

Motyka, R. J., Hunter, L., Echelmeyer, K. A., & Connor, C. (2003). Submarine melting at the terminus of a temperate tidewater glacier, LeConte glacier, Alaska, USA. *Annals of Glaciology*, *36*, 57–65.

Mouginot, J., Bjørk, A. A., Millan, R., Scheuchl, B., & Rignot, E. (2018). Insights on the Surge Behavior of Storstrømmen and L. Bistrup Bræ, Northeast Greenland, Over the Last Century. *Geophysical Research Letters*, *45*(20), 11,197-11,205. https://doi.org/10.1029/2018GL079052

Mugford, R. I., & Dowdeswell, J. A. (2011). Modeling glacial meltwater plume dynamics and sedimentation in high-latitude fjords. *Journal of Geophysical Research: Earth Surface*, *116*(1), 1–20. https://doi.org/10.1029/2010JF001735

Mulder, T. (2011). Gravity Processes and Deposits on Continental Slope, Rise and Abyssal Plains. In *Developments in Sedimentology* (63rd ed., pp. 26–125).

Mulder, T., & Alexander, J. (2001). The physical character of subaqueous sedimentary density flow and their deposits. *Sedimentology*, *48*(2), 269–299. https://doi.org/10.1046/j.1365-3091.2001.00360.x

Murray, T., Scharrer, K., Selmes, N., Booth, A. D., James, T. D., Bevan, S. L., Bradley, J., Cook, S., Llana, L. C., Drocourt, Y., Dyke, L., Goldsack, A., Hughes, A. L., Luckman, A. J., & McGovern, J. (2015). Extensive Retreat of Greenland Tidewater Glaciers, 2000-2010. *Arctic, Antarctic, and Alpine Research*, *47*(3), 427–447. https://doi.org/10.1657/AAAR0014-049

Myhre, A. M., Eldolm, O., Skogseid, J., Faleide, J. I., Gudlaugsson, S. T., Planke, S., Stuevold, L. M., & Vågnes, E. (1992). The Norwegian continental margin. In C. W. Poad & P. C. Graciansky (Eds.), *Geologic evolution of Atlantic Continental Rises* (pp. 157–185).

Nemec, W. (1990a). Aspects of sediment movement on steep delta slopes. In A. Colella & D. B. Prior (Eds.), *Coarse-Grained Deltas: International Association of Sedimentologists, Special Publication* (Vol. 10, pp. 29–73).

Nemec, W. (1990b). Deltas – remarks on terminology and classification. *Spec. Publs. Int. Ass. Sediment*, *10*, 3–12.

Nemec, W. (1995). The dynamics of deltaic suspension plumes. In M. N. Oti & G. Postma (Eds.), *Geology of Deltas* (pp. 31–93).

Nesje, A., & Whillans, I. M. (1994). Erosion of the Sognefjord. *Geomorphology*, *9*, 33+45.

Nielsen, N. (1994). View of Geomorphology of a Degrading Arctic Delta, Sermilik, South-East Greenland. *Geografisk Tiddskrift, Danish Journal of Geography*, *94*.

Nilsen, F., Cottier, F., Skogseth, R., & Mattsson, S. (2008). Fjord-shelf exchanges controlled by ice and brine production: The interannual variation of Atlantic Water in Isfjorden, Svalbard. *Continental Shelf Research*, *28*(14), 1838–1853. https://doi.org/10.1016/j.csr.2008.04.015

Normandeau, A., Lajeunesse, P., Poire, A. G., & Francus, P. (2016). Morphological expression of bedforms formed by supercritical sediment density flows on four fjord-lake deltas of the south-eastern Canadian Shield (Eastern Canada). *Sedimentology*, *63*, 2106–2129.

Ó Cofaigh, C. (2005). Flow Dynamics and till genesis associated with a marin-based Antarctic palaeo-ice stream. *Quaternary Science Reviews*, *24*, 709–740.

Ó Cofaigh, C., Dowdeswell, J. A., Evans, J., & Larter, R. D. (2008). Geological constraints on Antarctic palaeo-ice-stream retreat. *Earth Surface Processes and Landforms*, *33*, 513–525.

Ó Cofaigh, C., Dowdeswell, J. A., Jennings, A. E., Hogan, K. A., Kilfeather, A., Hiemstra, J. F., Noormets, R., Evans, J., McCarthy, D. J., Andrews, J. T., Lloyd, J. M., & Moros, M. (2013). An extensive and dynamic ice sheet on the west greenland shelf during the last glacial cycle. *Geology*, *41*(2), 219–222. https://doi.org/10.1130/G33759.1

Ó Cofaigh, Colm, Dowdeswell, J. A., & Grobe, H. (2001). Holocene glacimarine sedimentation, inner Scoresby Sund, East Greenland: The influence of fast-flowing ice-sheet outlet glaciers. *Marine Geology*, *175*(1–4), 103–129. https://doi.org/10.1016/S0025-3227(01)00117-7

Ohmura, A., & Reeh, N. (1991). New precipitation and accumulation maps for Greenland. *Journal of Glaciology*, *125*, 140–148.

Olsen, Ingrid L., Forwick, M., Laberg, J. S., & Rydningen, T. A. (in review). Last Glacial ice-sheet dynamics offshore NE Greenland – a case study from Store Koldewey Trough. In *The Cryosphere Discussions*.

Olsen, Ingrid Leirvik. (2015). *Sedimentary processes and paleoenvironments in Moskusoksefjord and Nordfjord, North-East Greenland*. *May*.

Orsi, T. H., Edwards, C. M., & Anderson, A. L. (1994). X-ray computed tomography: a nondestructive method for quantitative analysis of sediment cores. *Journal of Sedimentary Research*, *64*, 690–693.

Ottesen, D., Dowdeswell, J. A., Bellec, V. K., & Bjarnadóttir, L. R. (2017). The geomorphic imprint of glacier surges into open-marine waters: Examples from eastern Svalbard. *Marine Geology*, *392*, 1–29.

Ottesen, D., Dowdeswell, J. A., Benn, D. I., Kristensen, L., Christiansen, H. H., Christensen, O., Hansen, L., Lebesbye, E., Forwick, M., & Vorren, T. O. (2008). Submarine landforms characteristic of glacier surges in two Spitsbergen fjords. *Quaternary Science Reviews*, *27*(15–16), 1583–1599. https://doi.org/10.1016/j.quascirev.2008.05.007

Ottesen, Dag, & Dowdeswell, J. A. (2006). Assemblages of submarine landforms produced by tidewater glaciers in Svalbard. *Journal of Geophysical Research: Earth Surface*, *111*(1), 1–16. https://doi.org/10.1029/2005JF000330

Ottesen, Dag, & Dowdeswell, J. A. (2009). An inter-ice-stream glaciated margin: Submarine landforms and a geomorphic model based on marine-geophysical data from Svalbard. *Bulletin of the Geological Society of America*, *121*(11–12), 1647–1665. https://doi.org/10.1130/B26467.1

Passchier, S. (2000). Soft-Sediment Deformation Features in Core from CRP-2 / 2A , Victoria Land Basin, Antarctica. *Terra Antarctica*, *7(3)*, 401–412.

Paterson, W. S. B. (1994). *The Physics of Glaciers.* Pergamon Press, Oxford.

Pedersen, J. B. T., Kaufmann, L. H., Kroon, A., & Jakobsen, B. H. (2010). The Northeast Greenland Sirius Water Polynya dynamics and variability inferred from satellite imagery. *Geografisk Tidsskrift*, *110*(2), 131–142. https://doi.org/10.1080/00167223.2010.10669503

Plassen, L., & Vorren, T. O. (2003). Fluid flow features in fjord-fill deposits, Ullsfjorden, North Norway. *Norsk Geologisk Tidsskrift*, *83*(1), 37–42.

Postma, G., Cartigny, M., & Kleverlaan, K. (2009). Structureless, coarse-tail graded Bouma Ta formed by internal hydraulic jump of the turbidity current. *Sedimentary Geology*, *219*, 1–6.

Powell, R. D. (1990). Glacimarine processes at grounding-line fans and their growth to ice-contact deltas. *Geological Society Special Publication*, *53*(53), 53–73. https://doi.org/10.1144/GSL.SP.1990.053.01.03

Powell, R. D., & Alley, R. B. (1997). Grounding-line Systems: Processes, Glaciological Inferences and the Stratigraphic Record. *Geology and Seismic Stratigraphy of the Antarctic Margin, Part 2, Antarctic Research Series*, *71*, 169–187.

Pratson, L. F., Imran, J., Parker, G., Syvitski, J. P. M., & Hutton, E. (2000). Debris Flows versus Turbidity Currents: A Modeling Comparison of their Dynamics and Deposits. In A. H. Bouma & C. G. Stone (Eds.), *Fine-grained turbidite systems, AAPG Memoir 72* (SEPM Speci, Vol. 68, pp. 57–72). https://doi.org/10.1306/a9672b86-1738-11d7-8645000102c1865d

Prior, D., & Bornhold, B. (1990). The underwater development of Holocene fan deltas. In A. Colella & D. Prior (Eds.), *Coarse-grained deltas* (pp. 75–90).

Ramana, M. V, Ramprasad, T., Paropkari, A. L., Borole, D. V, Rao, B. R., Karisiddaiah, S. M., Desa, M., Kocherla, M., Joao, H. M., Lokabharati, P., Gonsalves, M., Pattan, J. N., Khadge,

N. H., Babu, C. P., Sathe, A. V, Kumar, P., & Sethi, A. K. (2009). Multidisciplinary investigations exploring indicators of gas hydrate occurrence in the Krishna – Godavari Basin offshore , east coast of India. *Geo-Marine Letters*, *29*, 25–38. https://doi.org/10.1007/s00367-008-0121-7

Rasmussen, S. O., Vinther, B. M., Clausen, H. B., & Andersen, K. K. (2007). Early Holocene climate oscillations recorded in three Greenland ice cores. *Quaternary Science Reviews*, *26*, 1907–1914.

Rea, B. R., & Evans, D. J. A. (2011). An assessment of surge - induced crevassing and the formation of crevasse squeeze ridges. *Journal of Geophysical Research*, *116*(January), 1–17. https://doi.org/10.1029/2011JF001970

Reeh, N. (2004). Holocene climate and fjord glaciations in Northeast Greenland: implications for IRD deposition in the North Atlantic. *Sedimentary Geology*, *165*(3–4), 333–342. https://doi.org/10.1016/j.sedgeo.2003.11.023

Reeh, N., Mayer, C., Miller, H., Thomsen, H. H., & Weidick, A. (1999). Present and past climate control on fjord glaciations in Greenland: Implications for IRD-deposition in the sea. *Geophysical Research Letters*, *26*(8), 1039–1042.

Renssen, H., Seppä, H., Crosta, X., Goosse, H., & Roche, D. (2012). Global characterization of the Holocene thermal maximum. *Quaternary Science Reviews*, *48*, 7–19.

Renssen, H., Seppa, H., Heiri, O., Roche, D. M., Goosse, H., & Fichefet, T. (2009). The spatial and temporal complexity of the Holocene thermal maximum. *Nature Geoscience*, *2*, 411–414.

Rignot, E., & Mouginot, J. (2012). Ice flow in Greenland for the International Polar Year 2008-2009. *Geophysical Research Letters*, *39*(11), 1–7. https://doi.org/10.1029/2012GL051634

Rise, L., Bellec, V. K., Ch, S., & Bøe, R. (2014). Pockmarks in the southwestern Barents Sea and Finnmark fjords. *Norsk Geologisk Tidsskrift*, *94*(4), 263–282. https://doi.org/10.17850/njg94-4-02

Roberts, D. G., Thompson, M., Mitchener, B., Hossack, J., Carmichael, S., & Bjørnseth, H.-M. (1999). Palaeozoic to Tertiary rift and basin dynamics: mid-Norway to the Bay of Biscay—a new context for hydrocarbon prospectivity in the deep water frontier. In: In *Petroleum Geology of Northwest Europe:Proceedings of the Fifth Conference* (pp. 7–40). Geological Society, London.

Rothwell, R. G., & Croudace, I. W. (2015). Twenty Years of XRF Core Scanning Marine Sediments : What Do Geochemical Proxies Tell Us ? In I. W. Croudace & R. G. Rothwell (Eds.), *Micro-XRF Studies of Sediment Cores* (pp. 25–102). https://doi.org/10.1007/978-94-017-9849-5

Rothwell, R. G., Hoogakker, B., Thomson, J., Croudace, I. W., & Frenz, M. (2006). Turbidite emplacement on the southern Balearic Abyssal Plain (western Mediterranean Sea) during Marine Isotope Stages 1-3: An application of ITRAX XRF scanning of sediment cores to lithostratigraphic analysis. *Geological Society Special Publication*, *267*(Haschke 2006), 79–98. https://doi.org/10.1144/GSL.SP.2006.267.01.06

Rudels, B., Anderson, L. G., & Jones, E. P. (1996). Formation and evolution of the surface mixed layer and halocline of the Arctic Ocean. *Journal of Geophysical Research C: Oceans*, *101*(C4), 8807–8821. https://doi.org/10.1029/96JC00143

Rutledge, A. K., & Leonard, D. S. (2001). OTC 12956 Role of Multibeam Sonar in Oil and Gas

Exploration and Development. *Offshore Technology Conference, Company, Exxonmobil Exploration*, 1–12.
Rydningen, T. A., Vorren, T. O., Laberg, J. S., & Kolstad, V. (2013). The marine-based NW Fennoscandian ice sheet: Glacial and deglacial dynamics as reconstructed from submarine landforms. *Quaternary Science Reviews*, *68*, 126–141. https://doi.org/10.1016/j.quascirev.2013.02.013
Schmidt, S., Wagner, B., Heiri, O., Klug, M., Bennike, O., & Melles, M. (2011). Chironomids as indicators of the Holocene climatic and environmental history of two lakes in Northeast Greenland. *Boreas*, *40*(1), 116–130. https://doi.org/10.1111/j.1502-3885.2010.00173.x
Schneider, W., & Budéus, G. (1997). Summary of the Northeast Water Polynya formation and development (Greenland Sea). *Journal of Marine Systems*, *10*, 107–122.
Seibert, J. A. (2004). *X-Ray Imaging Physics for Nuclear Medicine Technologists . Part 1 : Basic Principles of X-Ray Production* *. 139–148.
Sequeiros, O. E. (2012). Estimating turbidity current conditions from channel morphology : A Froude number approach. *Journal of Geophysical Research*, *117*(February), 1–19. https://doi.org/10.1029/2011JC007201
Serreze, M., Barrett, A., Stroeve, J., Kindig, D., & Holland, M. (2009). The emergence of surface based Arctic amplification. *Cryosphere*, *3*, 11–19.
Serreze, M. C., & Francis, J. A. (2006). The Arctic amplification debate. *Clim. Chang.*, *76*, 241–264.
Sevestre, H., Benn, D. I., Hulton, N. R. J., & Bælum, K. (2015). Thermal structure of Svalbard glaciers and implications for thermal switch models of glacier surging. *Journal of Geophysical Research F: Earth Surface*, *120*(10), 2220–2236. https://doi.org/10.1002/2015JF003517
Shanmugam, G. (2002). Ten Turbidite myths. *Earth-Science Reviews*, *58*, 311–341.
Sharp, M. (1985). "Crevasse-Fill " Ridges: A Landform Type Characteristic of Surging Glaciers? *Geografiska Annaler*, *67 A*(3–4), 213–220.
Shaw, J., & Lintern, D. G. (2016). Landforms in a Pacific fjord system: Douglas Channel, British Columbia, Canada. In K. A. Dowdeswell, J. A., Canals, M., Jakobsson, M., Todd, B. J., Dowdeswell, E. K. & Hogan (Ed.), *Atlas of Submarine Glacial Landforms: Modern, Quaternary and Ancient* (Memoirs 46, pp. 81–82). Geological Society of London.
Shaw, J., & Potter, D. P. (2016). A glacial landform assemblage in Placentia Bay, Newfoundland, eastern Canada. In K. A. Dowdeswell, J. A., Canals, M., Jakobsson, M., Todd, B. J., Dowdeswell, E. K. & Hogan (Ed.), *Atlas of Submarine Glacial Landforms: Modern, Quaternary and Ancient* (Memior 46, Vol. 46, pp. 139–142). Geological Society of London.
Sheldon, C., Jennings, A., Andrews, J. T., Ó Cofaigh, C., Hogan, K., Dowdeswell, J. A., & Seidenkrantz, M.-S. (2016). Ice stream retreat following the LGM and onset of the west Greenland current in Uummannaq Trough, west Greenland. *Quaternary Science Reviews*, *147*, 27–46.
Shillington, D. J., Seeber, L., Sorlien, C. C., Steckler, M. S., Kurt, H., Dondurur, D., Çifçi, G., Imren, C., Cormier, M. H., McHugh, C. M. G., Gürçay, S., Poyraz, D., Okay, S., Atgin, O., & Diebold, J. B. (2012). Evidence for widespread creep on the flanks of the sea of Marmara transform basin from marine geophysical data. *Geology*, *40*(5), 439–442.

https://doi.org/10.1130/G32652.1
Shreve, R. L. (1985). Esker characteristics in terms of glacier physics, Katahdin esker system, Maine. *Geological Society of America Bulletin*, *96*(5), 639–646. https://doi.org/10.1130/0016-7606(1985)96<639:ECITOG>2.0.CO;2
Simpson, M. J. R., Milne, G. A., Huybrechts, P., & Long, A. J. (2009). Calibrating a glaciological model of the Greenland ice sheet from the Last Glacial Maximum to present-day using field observations of relative sea level and ice extent. *Quaternary Science Reviews*, *28*(17–18), 1631–1657. https://doi.org/10.1016/j.quascirev.2009.03.004
Skogseth, R., Sandvik, A. D., & Asplin, L. (2007). Wind and tidal forcing on the meso-scale circulation in Storfjorden, Svalbard. *Continental Shelf Research*, *27*, 208–227.
Skov, D. S., Andersen, J. L., Olsen, J., Jacobsen, B. H., Knudsen, M. F., Jansen, J. D., Larsen, N. K., & Egholm, D. L. (2020). Constraints from cosmogenic nuclides on the glaciation and erosion history of Dove Bugt , northeast Greenland. *GSA Bulletin*, 1–13.
Smith, D. P., Ruiz, G., & Iampietro, P. J. (2005). Semiannual patterns of erosion and deposition in upper Monterey Canyon from serial multibeam bathymetry. *GSA Bulletin*, *117*(9/10), 1123–1133. https://doi.org/10.1130/B25510.1
Smith, L. M., & Andrews, J. T. (2000). Sediment characteristics in iceberg dominated fjords, Kangerlussuaq region, East Greenland. *Sedimentary Geology*, *130*(1–2), 11–25. https://doi.org/10.1016/S0037-0738(99)00088-3
Solheim, A., & Elverhøi, A. (1993). Gas-related sea floor craters in the Barents Sea. *Geo-Marine Letters*, *9*, 235–43.
Solheim, Anders, & Pfirman, S. L. (1985). Sea-floor morphology outside a grounded, surging glacier, Bravsvellbreen, Svalbard. *Marine Geology*, *65*, 127–143.
Sønderholm, M., Collinson, J. D., & Tirsgaard, H. (1989). Stratigraphic and sedimentological studies of the Eleonore Bay Group (Precambrian) between 73°30´ and 76°N in East Greenland. *Rapport Grønlands Geologiske Undersøgelse*, *145*, 97–102.
Sønderholm, M., & Tirsgaard, H. (1993). Lithostratigraphic framework of the Upper Proterozoic Eleonore Bay Supergroup of East and North East Greenland. *Bulletin Grønlands Geologiske Undersøgelse*, *167*, 38.
Sørensen, M. (2012). Walrus Island—a pivotal place for high Arctic palaeo-Eskimo societies in Northeast Greenland. *Etud Inuit*, *36*, 183−205.
Sørensen, M., & Gulløv, H. C. (2012). The prehistory of inuit in Northeast Greenland. *Arctic Anthropology*, *49*(1), 88–104. https://doi.org/10.1353/arc.2012.0016
Spagnolo, M., Clark, C. D., Hughes, A. L. C., Dunlop, P., & Stokes, C. R. (2010). The planar shape of drumlins. *Sedimentary Geology*, *232*, 119–129.
Spagnolo, Matteo, Clark, C. D., Ely, J. C., Stokes, C. R., Anderson, J. B., Andreassen, K., Graham, A. G. C., & King, E. C. (2014). Size, shape and spatial arrangement of mega-scale glacial lineations from a large and diverse dataset. *Earth Surface Processes and Landforms*, *39*(11), 1432–1448. https://doi.org/10.1002/esp.3532
St-Onge, G., Mulder, T., Francus, P., & Long, B. (2007). Chapter Two Continuous Physical Properties of Cored Marine Sediments. *Developments in Marine Geology*, *1*(07), 63–98. https://doi.org/10.1016/S1572-5480(07)01007-X
Stacey, C. D., & Hill, P. R. (2016). Cyclic steps on a glacifluvial delta, Howe Sound, British Columbia. In K. A. Dowdeswell, J. A., Canals, M., Jakobsson, M., Todd, B. J.,

Dowdeswell, E. K. & Hogan (Ed.), *Atlas of Submarine Glacial Landforms: Modern, Quaternary and Ancient* (Memoir 46, pp. 93–94). Geological Society of London.
Stecher, O., & Henriksen, N. (1994). Sm-Nd model age of an early Proterozoic gabbro-anorthosite from the Caledonian fold belt in North-East Greenland. In A. K. Higgins (Ed.), *Geology of North-East Greenland. Rapport Grønlands Geologiske Undersøgelse* (Vol. 162, pp. 135–137).
Steffensen, J. P., Andersen, K. K., Bigler, M., Clausen, H. B., Dahl-jensen, D., Fischer, H., Goto-azuma, K., Hansson, M., Johnsen, S. J., Jouzel, J., Masson-delmotte, V., Popp, T., Rasmussen, S. O., Röthlisberger, R., Ruth, U., Stauffer, B., Sveinbjörnsdóttir, Á. E., Svensson, A., & White, J. W. C. (2008). High-Resolution Greenland Ice Core Data Show Abrupt Climate Change Happens in Few Years. *Science*, *321*(5889), 680–684. https://doi.org/10.1126/science.1157707
Stemmerik, L., & Piasecki, S. (1990). Post-Caledonian sediments in North-East Greenland between 76° and 78°30´N. *Rapport Grønlands Geologiske Undersøgelse*, *148*, 123–126.
Stokes, C. R., & Clark, C. D. (1999). Geomorphological criteria for identifying Pleistocene ice streams. *Annals of Glaciology*, *28*(4), 67–74. https://doi.org/10.3189/172756499781821625
Stokes, C. R., & Clark, C. D. (2001). Palaeo-ice streams. *Quaternary Science Reviews*, *20*, 1437–1457.
Stoner, J. S., Channel, J. E. T., & Hillaire-Marcel, C. (1996). The magnetic signature of rapidly deposited detrital layers from the deep Labrador Sea: Relationship to North Atlantic Heinrich layers. *Paleoceanography*, *11*(3), 309–325.
Storrar, R. D., Ewertowski, M., Tomczyk, A. M., Barr, I. D., Livingstone, S. J., Ruffell, A., Stoker, B. J., & Evans, D. J. A. (2020). Equifinality and preservation potential of complex eskers. *Boreas*, *49*(1), 211–231. https://doi.org/10.1111/bor.12414
Strachan, R. A. (1994). Evidence in north-east Greenland for late Silurian-early Devonian regional extension during the Caledonian orogeny. *Geology*, *22*(10), 913–916. https://doi.org/10.1130/0091-7613(1994)022<0913:EINEGF>2.3.CO;2
Strachan, R. A., Holdsworth, R. E., Friderichsen, J. D., & Jepsen, H. F. (1992). Regional Caledonian structure within an oblique convergence zone, Dronning Louise Land, NE Greenland. *Journal - Geological Society (London)*, *149*(3), 359–371. https://doi.org/10.1144/gsjgs.149.3.0359
Strachan, R. A., Martin, M. W., & Friderichsen, J. D. (2001). Evidence for contemporaneous yet contrasting styles of granitic magmatism during extensional collapse of the northeast Greenland Caledonides. *Tectonics*, *20*, 458–473.
Strachan, R. A., Nutman, A. P., & Friderichsen, J. D. (1995). SHRIMP U-Pb geochronology and metamorphic history of the Smallefjord sequence: NE Greenland Caledonides. *Journal of the Geological Society (London)*, *152*, 779–784.
Straneo, F., Hamilton, G. S., Sutherland, D. A., Stearns, L. A., Davidson, F., Hammill, M. O., Stenson, G. B., & Rosing-Asvid, A. (2010). Rapid circulation of warm subtropical waters in a major glacial fjord in East Greenland. *Nature Geoscience*, *3*(3), 182–186. https://doi.org/10.1038/ngeo764
Stuiver, M. (1978). Carbon-14 Dating: A Comparison of Beta and Ion Counting. *Science*, *202*(4370), 881–883.
Sultan, N., Cochonat, P., Canals, M., Cattaneo, A., Dennielou, B., Haflidason, H., Laberg, J. S.,

Long, D., Mienert, J., Trincardi, F., Urgeles, Vorren, T. O., & Wilson, C. (2004). Triggering mechanisms of slope instability processes and sediment failures on continental margins. *Marine Geology*, *213*, 291–321.

Surlyk, F. (2003). East Greenland. *Geological Survey of Denmark and Greenland Bulletin*, *1*, 659–722. https://doi.org/10.2307/j.ctt1w1vmxd.8

Surpless, K. D., Ward, R. B., & Graham, S. A. (2007). Evolution and stratigraphic architecture of marine slope gully complexes- Monterey Formation (Miocene), Gaviota Beach, California. *Marine and Petroleum Geology*, *26*, 269–288.

Synal, H.-A., Stocker, M., & Suter, M. (2007). MICADAS: A new compact radiocarbon AMS system. *Nuclear Intruments and Method in Physics Research B 259*, 7–13.

Syvitski, J. P. M. (1989). On the deposition of sediment within glacier-influenced fjords: oceanographic controls. *Marine Geology*, *85*, 301–329.

Syvitski, J. P. M., Andrew, J. T., & Dowdeswell, J. A. (1996). Sediment deposition in an iceberg-dominated glacimarine environment, East Greenland: basin fill implications. *Global and Planetary Change*, *12*, 251–270.

Syvitski, J. P. M., Andrews, J. T., & Dowdeswell, J. A. (1996). Sediment deposition in an iceberg-dominated glacimarine environment, East Greenland: Basin fill implications. *Global and Planetary Change*, *12*(1–4), 251–270. https://doi.org/10.1016/0921-8181(95)00023-2

Syvitski, J. P. M., & Farrow, G. E. (1989). Fjord sedimentation as an analogue for small hydrocarbon-bearing fan deltas. In M. K. G. Whateley & K. T. Pickering (Eds.), *Deltas: Sits and Traps for Fossil FUels*. Geological Society Special Publication No. 41.

Syvitski, J. P. M., & Shaw, J. (1995). Sedimentology and geomorphology of fjords. In G. M. E. Perillo (Ed.), *Geomorphology and Sedimentology of Estuaries. Developments in Sedimentology* (Vol. 53, pp. 113–178).

Syvitski, J. P. M., Stein, A. B., Andrews, J. T., & Milliman, J. D. (2001). Icebergs and the sea floor of the East Greenland (Kangerlussuaq) continental margin. *Arctic, Antarctic, and Alpine Research*, *33*(1), 52–61. https://doi.org/10.1080/15230430.2001.12003404

Tanaka, A., Nakano, T., & Ikehara, K. (2011). X-ray computerized tomography analysis and density estimation using a sediment core from the Challenger Mound area in the Porcupine Seabight, off Western Ireland. *Earth Planets Space*, *63*, 103–110. https://doi.org/10.5047/eps.2010.12.006

Tirsgaard, H., & Sønderholm, M. (1997). Lithostratigraphy, sedimentary evolution and sequence stratigraphy of the Upper Proterozoic Lyell Land Group (Eleonore Bay Supergroup) of East and North-East Greenland. *Geology of Greenland Survey Bulletin*, *178*, 60.

Tonai, S., Kubo, Y., Tsang, M., Bowden, S., & Ide, K. (2019). A new method for quality control of geological cores by x-ray computed tomography: application in IODP expedition 370. *Froniers in Earth Science*, *7*(May), 1–13. https://doi.org/10.3389/feart.2019.00117

Trottier, A.-P., Lajeunesse, P., Gagnon-Poire, A., & Francus, P. (2020). Morphological signatures of deglaciation and postglacial sedimentary processes in a deep fjord-lake (Grand Lake, Labrador). *Earth Surface Professes and Landforms*, *45*, 928–947.

Tsikalas, F., Faleide, J. I., Eldholm, O., & Wilson, J. (2005). Late Mesozoic-Cenozoic structural and stratigraphic correlations between the conjugate mid-Norway and NE Greenland continental margins. In A. G. Doré & B. A. Vining (Eds.), *Petroleum Geology: North-West*

Europe and Global Perspectives—Proceedings of the 6th Petroleum Geology Conference (pp. 785–801). Geological Society, London.

Vallelonga, P., Christianson, K., Alley, R. B., Anandakrishnan, S., Christian, J. E. M., Dahl-Jensen, D., Gkinis, V., Holme, C., Jacobel, R. W., Karlsson, N. B., Keisling, B. A., Kipfstuhl, S., Kjær, H. A., Kristensen, M. E. L., Muto, A., Peters, L. E., Popp, T., Riverman, K. L., Svensson, A. M., … Winstrup, M. (2014). Initial results from geophysical surveys and shallow coring of the Northeast Greenland Ice Stream (NEGIS). *Cryosphere*, *8*(4), 1275–1287. https://doi.org/10.5194/tc-8-1275-2014

van der Veen, C. J. (1998). Fracture mechanics appraoch to penetration of bottom crevasses on glaciers. *Cold Regions Science and Technology*, *27*, 213–223.

Vasskog, K., Langebroek, P. M., Andrews, J. T., Nilsen, J. E. Ø., & Nesje, A. (2015). The Greenland Ice Sheet during the last glacial cycle: Current ice loss and contribution to sea-level rise from a palaeoclimatic perspective. *Earth-Science Reviews*, *150*, 45–67. https://doi.org/10.1016/j.earscirev.2015.07.006

Vorren, T. O. (2003). Subaquatic landsystems: continental margins. In D.J.A. Evans (Ed.), *Glacial Landsystems*. Arnold Publishers.

Wagner, B., Bennike, O., Bos, J. A. A., Cremer, H., Lotter, A. F., & Melles, M. (2008). A multidisciplinary study of Holocene sediment records from Hjort Sø on Store Koldewey, Northeast Greenland. *Journal of Paleolimnology*, *39*(3), 381–398. https://doi.org/10.1007/s10933-007-9120-3

Wang, M. J., Zheng, H. B., Xie, X., Fan, D. Du, Yang, S. Y., Zhao, Q. H., & Wang, K. (2011). A 600-year flood history in the Yangtze River drainage: Comparison between a subaqueous delta and historical records. *Chinese Science Bulletin*, *56*(2), 188–195. https://doi.org/10.1007/s11434-010-4212-2

Watts, A. (2010). *Greenland glaciers – melt due to sea current change, not air temperature. Retrieved August 18, 2019, from Watts Up With That?:* https://wattsupwiththat.com/2010/02/16/greenland-glaciers-melt-due-to-sea-current-change-not-air-temperature/

Weidick, A. (1995). Satellite Image Atlas of the Glaciers of the World: Greenland. In R. S. J. Williams & J. G. Ferrigno (Eds.), *U.S. Geological SUrvey Professional Paper 1386 - C* (p. 153). https://doi.org/10.1038/063215a0

Weidick, A., Andreasen, C., Oerter, H., & Reeh, N. (1994). Neoglacial glacier changes around Storstrommen, north-east Greenland. *Polarforschung*, *64*(3), 95–108.

Weidick, A., Bennike, O., Citterio, M., & Nørgaard-Pedersen, N. (2012). Neoglacial and historical glacier changes around Kangersuneq fjord in southern West Greenland. In *Geological Survey of Denmark and Greenland Bulletin* (Issue 27).

Weidick, B. A., Andreasen-, C., & Oerter, H. (1996). *Neoglacial Glacier Changes around Storstrommen, North-East Greenland*. *64*(3), 95–108.

Widell, K., Fer, I., & Haugan, P. M. (2006). Salt release from warming sea ice. *Geophysical Research Letters*, *33*(12), 1–5. https://doi.org/10.1029/2006GL026262

Wilken, M., & Mienert, J. (2006). Submarine glacigenic debris flows, deep-sea channels and past ice-stream behaviour of the East Greenland continental margin. *Quaternary Science Reviews*, *25*, 784–810.

Winkelmann, D., Jokat, W., Jensen, L., & Schenke, H. W. (2010). Submarine end moraines on

the continental shelf off NE Greenland - Implications for Lateglacial dynamics. *Quaternary Science Reviews*, *29*(9–10), 1069–1077. https://doi.org/10.1016/j.quascirev.2010.02.002
Winsor, K. (2014). *A Chronology of Late Quaternary Southwestern Greenland Ice Sheet Retreat Using Terrestrial and Marine Records*. University of Wisconsin–Madison.
Winsor, K., Carlson, A. E., Caffee, M. W., & Rood, D. H. (2015). Rapid last-deglacial thinning and retreat of the marine-terminating southwestern Greenland ice sheet. *Earth and Planetary Science Letters*, *426*, 1–12.
Wohlleben, T., Sharp, M., & Bush, A. (2009). Factors influencing the basal temperatures of a High Arctic polythermal glacier. *Annals of Glaciology*, *50*(52), 9–16. https://doi.org/10.3189/172756409789624210
Young, E., Briner, J. P., Miller, G. H., Lesnek, A. J., Crump, S. E., Thomas, E. K., Pendleton, S. L., Cuzzone, J., Lamp, J., Zimmerman, S., Caffee, M., & Schaefer, J. M. (2020). Deglaciation of the Greenland and Laurentide ice sheets interrupted by glacier advance during abrupt coolings. *Quaternary Science Reviews*, *229*.
Young, N. E., & Briner, J. P. (2015). Holocene evolution of the western Greenland Ice Sheet: Assessing geophysical ice-sheet models with geological reconstructions of ice-margin change. *Quaternary Science Reviews*, *114*, 1–17.
Zhang, P., Lee, Y. I., & Zhang, J. (2019). A review of high-resolution X-ray computed tomography applied to petroleum geology and a case study. *Micron*, *125*(102702).
Zhong, G., Cartigny, M. J. B., Kuang, Z., & Wang, L. (2015). Cyclic steps along the South Taiwan Shoal and West Penghu submarine canyons on the northeastern continental slope of the South China Sea. *GSA Bulletin*, *125*(5/6), 804–824. https://doi.org/10.1130/B31003.1

Appendix A

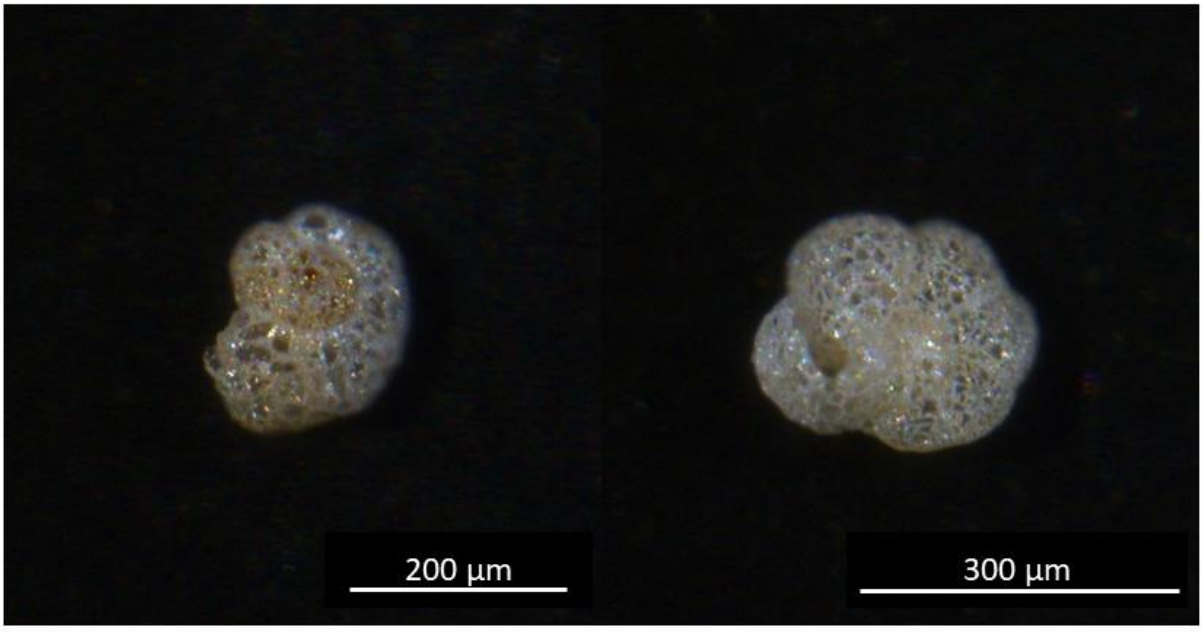

Figure A 1. Agglutinated foraminifera from HH17-1290-GC-TUNU 96 cm depth (left and right images).

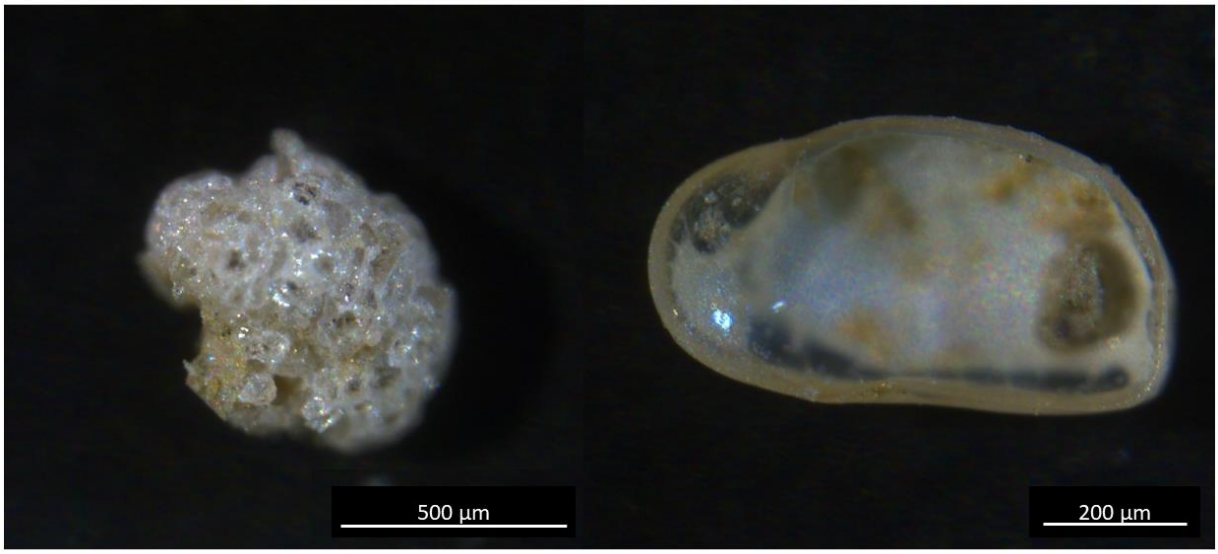

Figure A 2. A large agglutinated foraminifera fragment from HH17-1290-GC-TUNU 96 cm depth (left). An ostracod collected from HH17-1309-GC-TUNU at 176-178 cm.

Appendix B

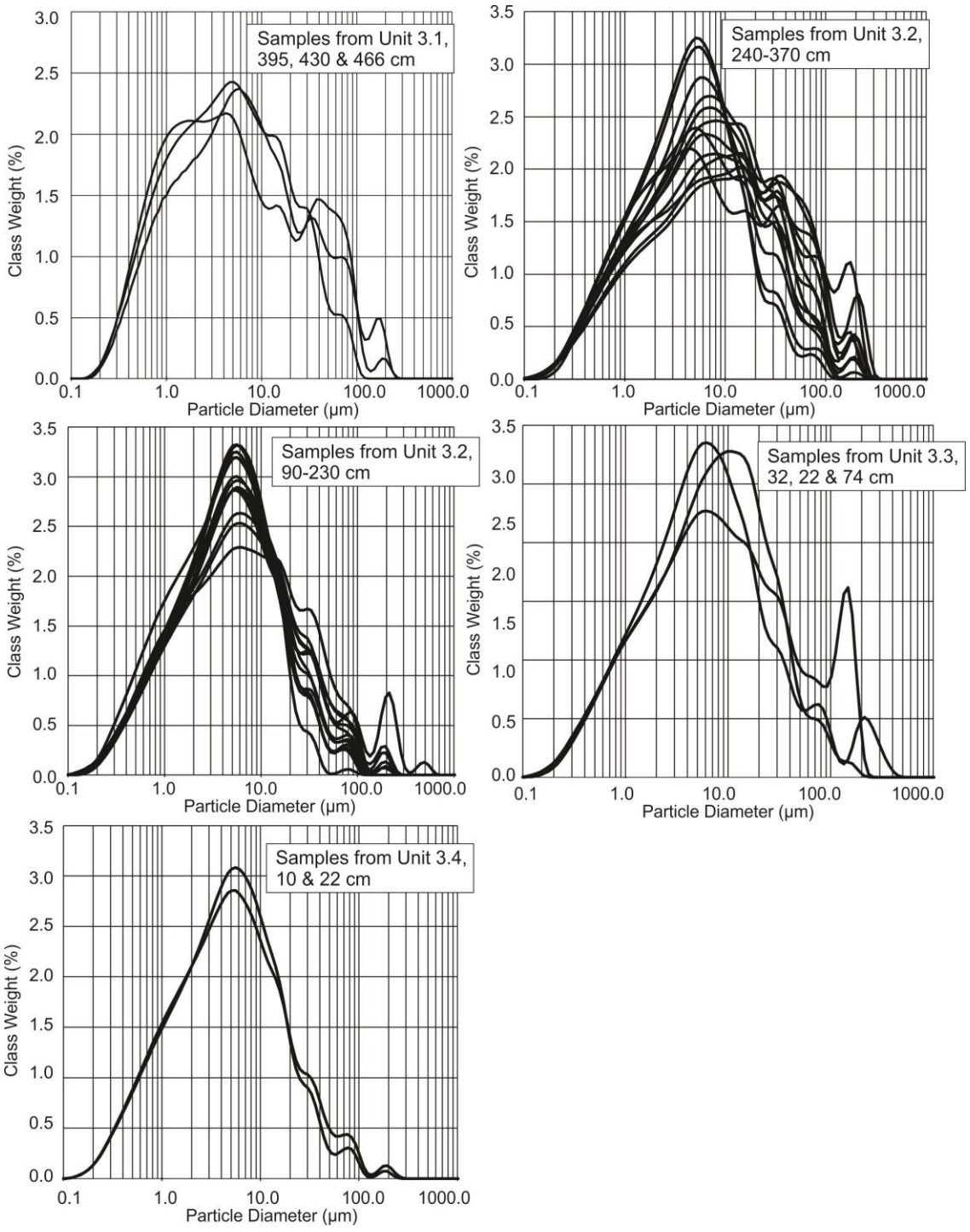

Figure B 1. Grain size distribution plots of sediment grain size analysis data from HH17-1309-GC-TUNU. Plots are divided into different units, except for unit 3.2 which has been divided into two separate plots.